Amorphization and Glass Formation of Metal-Organic Frameworks

Zhou, Chao

DOI (link to publication from Publisher):
10.5278/vbn.phd.eng.00070

Publication date:
2018

Document Version
Publisher's PDF, also known as Version of record

Citation for published version (APA):
Zhou, C. (2018). *Amorphization and Glass Formation of Metal-Organic Frameworks*. Aalborg Universitetsforlag. Ph.d.-serien for Det Ingeniør- og Naturvidenskabelige Fakultet, Aalborg Universitet
https://doi.org/10.5278/vbn.phd.eng.00070

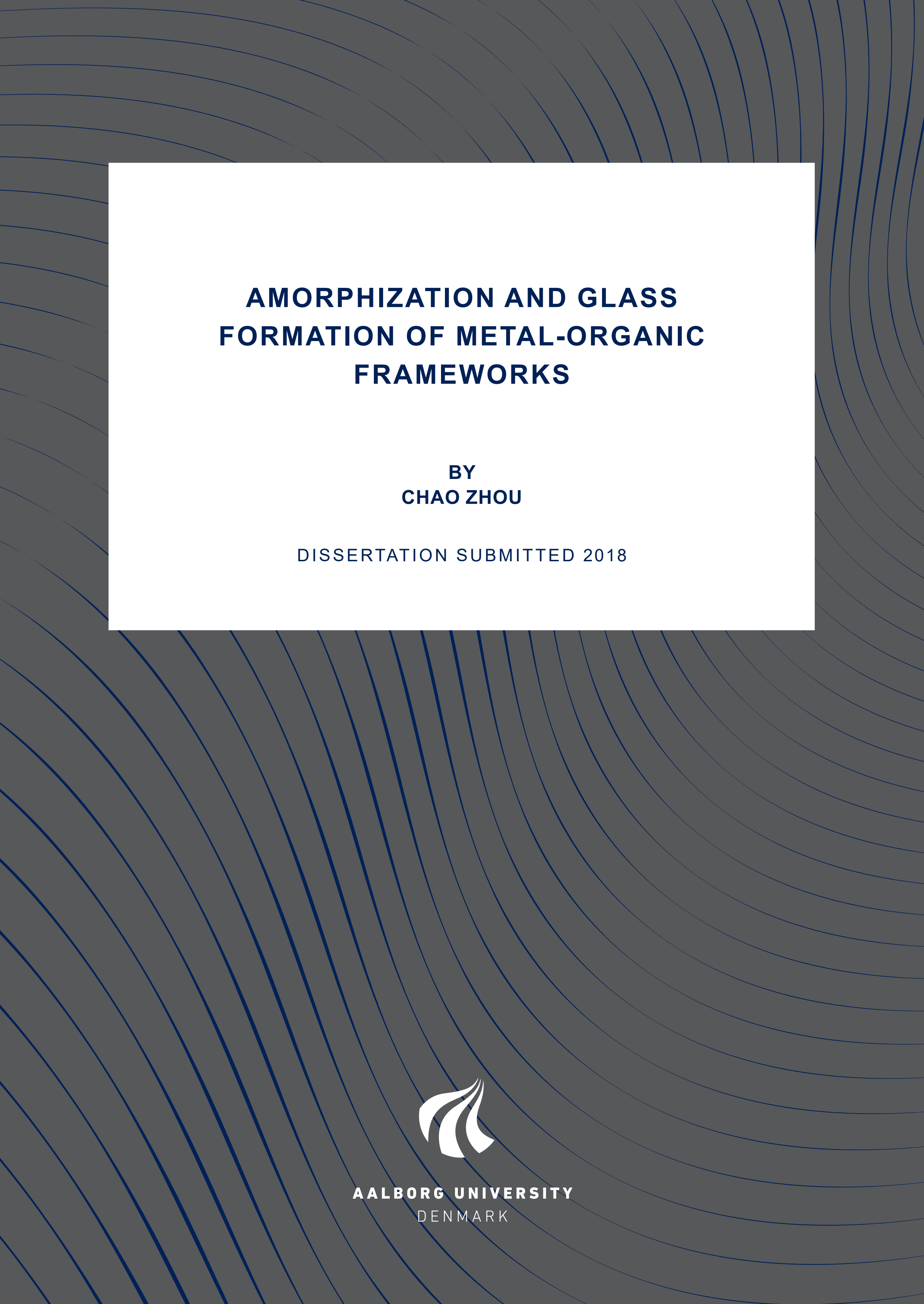

AMORPHIZATION AND GLASS FORMATION OF METAL-ORGANIC FRAMEWORKS

BY
CHAO ZHOU

DISSERTATION SUBMITTED 2018

AALBORG UNIVERSITY
DENMARK

AMORPHIZATION AND GLASS FORMATION OF METAL-ORGANIC FRAMEWORKS

by

Chao Zhou

AALBORG UNIVERSITY
DENMARK

Dissertation submitted 2018

Dissertation submitted: November 2018

PhD supervisor: Prof. Yuanzheng Yue,
Aalborg University, Denmark

PhD co-supervisor: Dr. Thomas Douglas Bennett,
University of Cambridge, UK

PhD committee: Professor Kim Lambertsen Larsen (chairman)
Aalborg University, Denmark

Professor Bo Brummerstedt Iversen
Aarhus University, Denmark

Professor Sabyasachi Sen
University of California, USA

PhD Series: Faculty of Engineering and Science, Aalborg University

Department: Department of Chemistry and Bioscience

ISSN (online): 2446-1636
ISBN (online): 978-87-7210-253-5

Published by:
Aalborg University Press
Langagervej 2
DK – 9220 Aalborg Ø
Phone: +45 99407140
aauf@forlag.aau.dk
forlag.aau.dk

Printed in Denmark by Rosendahls, 2018

CV

Mr. Chao Zhou was born in Qitaihe, Heilongjiang, P. R. China in March, 1991. He got his Bachelor's degree in Materials Engineering in Shandong University in 2012. He continued his study there and got his Master's degree in 2015. He started his PhD study at Department of Chemistry and Bioscience in Aalborg University in September, 2015. His research has been focused on amorphization and glass transition of metal-organic frameworks during the three-year PhD study at AAU. He was awarded the Elite Research Travel Scholarship by Danish Ministry of Science in 2017. He worked for 6 months with Dr. Thomas Bennett in University of Cambridge as an exchange student in 2017.

ENGLISH SUMMARY

Metal-organic frameworks (MOFs) have been extensively studied due to their large porosities and flexible chemical compositions, giving potentials for applications such as gas and liquid absorption, gas separation, catalysis, sensoring and detection, food storage etc. Amorphization and glass formation of MOFs with disordered structure induced by temperature, pressure, and ball-milling were recently discovered. This glass with hybrid structural units chemically differs from the inorganic, organic and metallic glass categories, making it a new glass family of glasses. In this thesis, crystal formation, physical and structural properties, and potential applications of the chemical functionalities have been investigated on amorphous MOFs.

Crystal synthesis of ZIF-4 isomorphs with $[Zn(Im)_2]$ composition was developed using solution mixing method. Synthesis time strongly influences the crystal phases, whereas synthesis temperature only affects the morphologies and porosities with regard to the crystal formation of ZIF-zec. High porosities of ZIF-zec and ZIF-nog phases (>500 $m^2\ g^{-1}$) are revealed. Moreover, both phases undergo amorphization, recrystallization to ZIF-zni, and melting upon heating, and MOF glasses can be achieved after quenching from the melts.

Dynamic features of a stable MOF glass - a_gZIF-62 were studied via sub-T_g enthalpy relaxation. The long relaxation time in the range of $0.93{\sim}0.99T_g$ and the wide range of the stretching exponent demonstrate the prominent structural heterogeneity in ZIF-62 glass.

Melting and glass forming ability of some MOFs were evaluated by calorimetric approach. Although most MOFs show no melting upon heating, ZIF-76 and the isomorph ZIF-76-mbIm have been discovered to be good MOF glass formers for the first time. Remarkably, vitrified a_gZIF-76-mbIm still possesses permanent accessible porosity especially for CO_2 and CH_4. In addition, a Zr-based MOF, DUT-67, exhibits an irreversible first-order phase transformation to a dense framework at 230 °C, while the transformation needs an activation energy of ~183 kJ mol^{-1} with an enthalpy release upon heating. The densified DUT-67-HT also exhibits enough pore volume for N_2 and CO_2 absorption.

The application potentials of MOF glasses were facilitated by the following investigations. Inspired by the liquid blending of miscible polymers, blends of ZIF-4 and ZIF-62 in liquid and amorphous state were achieved. This discovery provides a technique to tune the chemical structures and thus the functionalities of MOF glasses. Motivated by improving the porosity of MOF glasses, a post-synthetical modification (PSM) method was applied to ZIF-7 by imidazole. A kinetically stable ZIF-PSM composite was hence obtained, which is composed by the parent ZIF-7 phase and the modified ZIF-62 phase. This ZIF-PSM can be thermally driven to amorphous a_TZIF-

PSM at 500 ˚C. The a_TZIF-PSM preserves the porosity and shows a larger surface area from N_2 uptakes than other temperature-induced amorphous MOFs. This finding indicates that the PSM method is beneficial to tuning the framework structures for the retention of the porosity of MOFs after amorphization.

DANSK RESUME

Metalorganiske netværker (fra engelsk: *metal-organic frameworks*, forkortet MOF) har været studeret flittigt grundet deres store porøsitet og fleksible kemiske sammensætninger, der muliggør applikationer såsom gas- og væskeabsorption, gasseparation, katalyse, detektion, madopbevaring osv. Glasdannelse af MOF med uordnede strukturer fremkaldt af temperatur, tryk, og kuglemaling blev opdaget for nyligt. Disse glasser har hybride strukturelle enheder, og adskiller sig fra uorganiske, organiske og metalliske glasser, hvilket gør dem til en ny familie af glasser. I denne afhandling er krystaldannelse, fysiske og strukturelle egenskaber, samt potentielle anvendelser af kemiske funktionelle grupper af amorfe MOF blevet undersøgt.

Krystalsyntese af ZIF-4 isomofer med sammensætningen [Zn(Im)$_2$] blev udført vha. opløsningsblandingsmetoden. Syntesetid har en stærk indvirkning på krystalfaser, hvorimod syntesetemperaturen påvirker kun morfologi og porøsitet med hensyn til krystaldannelse af ZIF-zec. De store porøsiteter af ZIF-zec og ZIF-nog faser (>500 m^2 g^{-1}) er afdækkede. Derudover gennemgår begge faser amorfisering, krystallisation til ZIF-zni, og smeltning under opvarmning, mens MOF-glasser kan opnås via bratnedkøling fra smelterne.

Dynamiske funktioner af en stabil MOF-glas, a_gZIF-62, blev studerede via sub-T_g entalpirelaksation. Den lange relaksationstid i temperaturintervallet 0.93~0.99T_g og den brede spænd af strækningseksponenten demonstrerer den fremtrædende heterogenitet i ZIF-62 glas.

Smeltning og glasdannelsesevne af nogle MOF blev evaluerede fra en kalorimetrisk tilgangsvinkel. Selvom de fleste MOF ikke udviser smeltning under opvarmning, blev ZIF-76 og isomorfet ZIF-76-mbIm opdagede som gode glasdannende materialer for første gang. Bemærkelsesværdigt, vitrificeret a_gZIF-76-mbIm besidder fortsat permanent og tilgængelig porøsitet, særligt for CO$_2$ and CH$_4$. Derudover, udviser en Zr-baseret MOF, DUT-67, en irreversibel faseovergang til en kompakt netværk ved 230 °C, mens den overgang kræver en aktiveringsenergi på ~183 kJ mol^{-1} med en entalpifrigørelse under opvarmning. Den densificerede DUT-67-HT udviser også nok porevolumen for N$_2$ og CO$_2$ absorption.

Anvendelsespotentialer af MOF-glasser blev fremmet vha. følgende undersøgelser. Inspireret af væskeblanding af blandbare polymerer, blev blandinger af ZIF-4 og ZIF-62 i både væske- og amorf tilstand opnået. Denne opdagelse giver en teknik til at variere på den kemiske struktur og dermed funktionaliteter af MOF-glasser. For at forbedre porøsiteten af MOF-glasser, blev post-syntetisk modificering (PSM) anvendt på ZIF-7 med imidazol. En kinetisk stabil ZIF-PSM komposit, der består af ZIF-7 fasen og den modificerede ZIF-62 fase, blev dermed opnået. ZIF-PSM kan blive termisk drevet til en amorf a_TZIF-PSM ved 500 °C. Denne a_TZIF-PSM opretholder

porøsiteten og udviser et større overfladeareal fra N_2 optag end andre temperaturinducerede amorfe MOF. Denne opdagelse indikerer at PSM metoden er fordelagtig for at variere netværksstrukturerne til at opretholde porøsiteten af MOF-glasser efter en glasovergang.

ACKNOWLEDGEMENTS

I cannot imagine to accomplish my PhD study and research without the help of a great number of people. First and foremost, I would like to thank my supervisor Prof. Yuanzheng Yue. I met him seven years ago when I just started my research, and I was thrilled by his scientific knowledge after getting to know him afterwards. It makes me come to Denmark for pursuing my PhD degree with him in 2015. With his generous attitude, I feel comfortable to control and dominate my research outcomes independently. We shared many ideas and perspective during our coffee breaks in many 'hyggelige' moments. I am also very grateful for his help for applying the travel grant, with which I would have the opportunities to extend my academic network.

Secondly, I give my appreciation to my co-supervisor Dr. Tom Bennett. I felt very lucky to know him. His research creativity, scientific attitude and working efficiency inspire me on my work. It is always joyful to discuss and share insights with him, and his encouragements motivate me to overcome challenges. I benefited greatly from him. With his kind invitation, I could happily live and study in Cambridge for half a year. The experiences are so memorable that I will never forget the fantastic moments there.

Working in chemistry section is quite cozy, and my colleagues are so kind and helpful to me in various aspects including scientific discussions, experiments training and performing, and Danish assistance. I had a wonderful time especially with tons of cakes and coffee. I would like to thank everyone to express my gratitude: Assoc. Prof. Vittorio Boffa, Prof. Morten Smedskjær, Assoc. Prof. Donghong Yu, Dr. Hao Liu, Dr. Sonja Haastrup Merrild, Tobias Bechgaard, Martin Østergaard, Dr. Rasmus Peterson, Usuma Naknikham, Katie Kedwell, Dr. Nerea Mascaraque, Yang Shen, Dr. Laura Paraschiv, Dr. René Thomsen, Chengwei Gao, Jiayan Zhang, Dr, Zhengkun Du, Dr. Tainan Duan, Dr. Qiang Tao, Mikkel Bødker, Katarzyna Janowska, Jonas Nørgaard, Dr. Saurabh Kapoor, and Dr. Mouritz Svenson. I also highly appreciate our secretaries and lab technicians who could sort out my issues in any circumstances. I give my special appreciations to Kacper Januchta and Malwina Stępniewska for their tremendous supports.

I had a great time working in Cambridge because of many brilliant and easy-going co-workers. I am very grateful to Dr. Fengxia Wei and Dr. Yue Wu for training me on refinements. I also really enjoy working together with Louis Longley, no matter in Cambridge or in Didcot. I would like to extend my appreciation to all the scientists: Prof. Tony Cheetham, Dr. Shijing Sun, Dr. Zeyu Deng, Dr. Tiesheng Wang, Dr. Federico Brivio, Christopher Ashling, Sammy Shaker, Trevor Binford, Remo Widmer, Dr. Giulio Lampronti, Dr. Ilknur Eurçar, Dr. Ziyu Chen, Dr. David Keen. I hope everyone will enjoy their academic life and have a bright future.

I also appreciate my collaborators for their scientific assistance and helpful discussions, who are Dr. Ang Qiao in TU Wuhan, Assoc. Prof. Giuliana Magnacca in University of Turin, and Sixu Peng and Prof. Haibin Yu in HUST. Special mention goes to Dr. Jingwei Hou, who kindly gave me valuable advice. It is fabulous to collaborate with him.

I would like to thank the supports from China Scholarship Council. I am also grateful to the Elite Research Travel Scholarship (EliteForsk-Rejsestipendier) from the Danish Ministry of Higher Education and Science (Uddannelses- og Forskningsministeriet) for the travelling support. More acknowledgements go to the provision of synchrotron access at Diamond Light Source and ISIS in UK.

Furthermore, I would personally give my tremendous appreciation to my lovely friends: Suancaiyu group, Caney group, Edith, Russell, Kitty, Yunhui, Vivien, Vera, Zili, Yao, Emma, Linea, Jilin, Rongkuan, Rickie, Bo, Tianbao, Zhongxu, Yi, zyx etc.. I won't deny that it was tough to live abroad alone at the beginning. Fortunately, I got comfort from them every time I felt struggled and confused.

My heartfelt thanks belong to my parents. I could continue my study to pursue the PhD degree and come abroad owing to their endless love, encouragement and support. I love you forever!

At last, I would like to appreciate myself for my persistence and efforts through my PhD. There were so many remarkable events and places. Maybe after many years, I will still remember the nights working in the lab, the cycling along the harbor and across bridges on the Cam, the sunset views from the balcony in the department, and the emotions with the music of Mozart and Sodagreen.

LIST OF ABBRIVATIONS

MOF	Metal-organic framework
CP	Coordination polymer
ZIF	Zeolitic imidazolate framework
MIL	MOFs named after Matériaux de l'Institut Lavoisier
MCIF	Metal cyanoimidazole framework
TIF	Tetrahedral imidazolate framework
JUC	MOFs named after Jilin University
ZTIF	Zeolitic tetrazolate-imidazolate framework
DUT	MOFs named after Dresden University of Technology
UiO	MOFs named after University of Oslo
PSM	Post-synthetic modification
a_{g}ZIF-xx	ZIF glass from melt-quenching
a_{T}ZIF-xx	Amorphous ZIF from thermal treatment
R_{wp}	Weighted profile R-factor
R_{exp}	Expected R-factor
R_{p}	Profile R-factor
R_{Bragg}	Bragg R-factor
χ^2	Goodness of fit, $R_{\mathrm{wp}}/R_{\mathrm{exp}}$
cif	Crystallographic information file
T_{g}	Glass transition temperature
T_{m}	Melting point
T_{d}	Decomposition temperature
C_{p}	Heat capacity
$C_p^{sl}(T)$	Temperature dependence of C_{p} in supercooled liquid region
$C_p^{x}(T)$	Temperature dependence of C_{p} of crystal
T_a	Annealing temperature
t_a	Annealing time
τ_{a}	Characteristic relaxation time
β	Stretching exponent
m	Fragility index
ΔH_{f}	Enthalpy of fusion
ΔS_{f}	Entropy of fusion
$\Delta H^{sl-x}(T)$	Enthalpy difference between supercooled liquid and crystal
$\Delta S^{sl-x}(T)$	Entropy difference between supercooled liquid and crystal
$\Delta G^{sl-x}(T)$	Gibbs free energy difference between supercooled liquid and crystal
PXRD	Powder X-ray diffraction
DSC	Differential scanning calorimetry
TGA	Thermogravimetry
NMR	Nuclear magnetic resonance
SEM	Scanning electron microscopy
FT-IR	Fourier-transform infrared (spectroscopy)

SAXS/WAXS	Small/wide-angle x-ray scattering
SR-FIR	Synchrotron radiation far-infrared (spectroscopy)
HSQC	Heteronuclear single quantum coherence
AAU	Aalborg University
UCam	University of Cambridge
SI	Supporting information
S(Q)	Structural factor
D(r), PDF	Pair distribution function
FWHM	Full width at half maximum
FD, T/V	Framework density
ESD	Estimated standard deviation
PV_TCHZ	Thompson-Cox-Hastings Pseudo-Voigt (model)
ADP	Atomic displacement parameter
KWW	Kohlrausch-Williams-Watts (function)
PEL	Potential energy landscape
BET	Brunauer-Emmett-Teller (method)
HIm	Imidazole
HbIm	Benzimidazole
2-HmIm	2-Methylimidazole
HdcIm	4,5-Dichloroimidazole
5-HcbIm	5-Chlorobenzimidazole
2-HmbIm	2-Methylbenzimidazole
5-HmbIm	5-Methylbenzimidazole
HdcbIm	5,6-Dichlorobenzimidazole
5-Hmtz	5-Methyltetrazolate
2-HeIm	2-Ethylimidazole
HDCI	4,5-Dicyanoimidazole
HAc	Acetic acid
HFa	Formic acid
H_2tdc	2,5-Thiophenedicarboxylic acid
H_2bdc	Terephthalic acid; Benzene-1,4-dicarboxylic acid
H_3btc	Trimesic acid; Benzene-1,3,5-tricarboxylic acid
DMF	*N*,*N*-Dimethylformamide
DEF	*N,N*-Diethylformamide
DCM	Dichloromethane
MeOH	Methanol
EtOH	Ethanol
n-PrOH	n-Propanol
n-BuOH	n-Butanol
MeCN	Acetonitrile
NMP	*N*-Methyl-2-pyrrolidone
DMSO-d_6	Deuterated dimethyl sulfoxide
DCl	Deuterium chloride

TABLE OF CONTENTS

Chapter 1. Introduction..1

1.1. Background and Challenges... 1

1.2. Objectives.. 3

1.3. Thesis Content... 3

Chapter 2. Experimental..5

2.1. Synthesis 5

2.2. Characterizations and Methods 8

Chapter 3. Crystal Synthesis and Glass Formation $Zn(Im)_2$ Polymorphs.........13

3.1. Synthesis Conditions Influence of $Zn(Im)_2$ Polymorphs.............................. 13

3.1.1. Synthesis Time Influence... 14

3.1.2. Synthesis Temperature Influence... 17

3.2. Glass Formation of ZIF-zec and ZIF-nog 22

3.3. Summary.. 24

Chapter 4. Enthalpy Relaxation in ZIF-62 Glass...25

4.1. Glass Transition in ZIF-62 25

4.2. Thermodynamic Features of ZIF-62 26

4.3. Enthalpy Relaxation in a_gZIF-62 28

4.4. Structural Features after Relaxation.. 32

4.5. Summary.. 33

Chapter 5. Glass Forming Ability of MOFs...35

5.1. Glass Forming Ability of Some MOFs 35

5.1.1. ZIF-11 & ZIF-12.. 35

5.1.2. ZIF-71 & MCIF-1 37

5.1.3. TIF-5-Cl & JUC-160.. 38

5.1.4. ZTIF-1.. 39

5.2. Glass Formation of ZIF-76... 40

5.2.1. Glass Formaiton of ZIF-76.. 40

5.2.2. Porosity 43

5.3. Phase Transformation of DUT-67... 44

5.3.1. Phase Transformation of DUT-67 44
5.3.2. Structural Features 47
5.3.3. Thermodynamics 49
5.3.4. Porosity 51
5.4. Summary 52
Chapter 6. ZIF-4 and ZIF-62 Liquid Phase Blending in Thermodynamic Aspects 53
6.1. ZIF-4-Zn & ZIF-62 53
6.2. ZIF-4-Co & ZIF-62 55
6.3. Summary 58
Chapter 7. Post-Synthetic Modified MOF with Enhanced Porosity after Amorphization 59
7.1. Crystal Identity after Modification 59
7.2. Glass Formation and Structural Evolution 65
7.3. Morphology and Mechanical properties 67
7.4. Porosity of a_TZIF-PSM 69
7.5. Structural Features of a_TZIF-PSM 70
7.6. Summary 71
Chapter 8. Conclusions and Perspective 73
8.1. Conclusions 73
8.2. Perspective 74
Bibliography 75
List of Publications 89
Appendices 91

TABLE OF FIGURES

Figure 1-1 (a) Structural analogy of the building units between ZIFs (Zn-Im-Zn) and silica (Si-O-Si); (b) Unit cell of ZIF-4; (c) Representative view of a_TZIF-4 structure (5,6). 1
Figure 3-1 Schematic figure of the process of $Zn(Im)_2$ synthesis using solution mixing method. 13
Figure 3-2 Experimental PXRD patterns of the samples S1-S5 obtained after different synthesis time, and the corresponding simulated spectra (black). Synthesis durations: (a) 0.083 h; (b) 18 h; (c) 24 h; (d) 48 h; and (e) 120 h. 15
Figure 3-3 SEM micrographs of S1-S5 from left to right. Scale bar: 10 µm. 15
Figure 3-4 Thermogravimetric analysis of samples S1-S5. 16
Figure 3-5 N_2 absorption-desorption isotherms of samples S1-S5 synthesized for different durations (a) Solid symbols: Absorption; Open symbols: Desorption. (b) Pore size distribution. 16
Figure 3-6 PXRD patterns of samples S3 and S6-S9 obtained at different temperature for 24 hours. Simulated XRD pattern of ZIF-zec is also shown in black. 18
Figure 3-7 Rietveld refinement of the PXRD pattern of S6. 18
Figure 3-8 SEM micrographs of S6-S9 from left to right. Scale bar: 10 µm. 20
Figure 3-9 N_2 absorption-desorption isotherms of samples S3 and S6-S9 synthesized at different temperature. Solid and open symbols: Absorption and desorption, respectively. (b) Pore size distribution. 20
Figure 3-10 (a) Summary of crystal phases of synthesized for different time and at different temperature. (b) Framework densities (FD, *T/V*) of the polymorphic ZIFs from Table 3-3. The arrows give the FD of the corresponding crystals in literature (40). 22
Figure 3-11 (a) Heat flow of the crystals and glasses of ZIF-nog, ZIF-zec (S8) and ZIF-zni; (b) PXRD patterns of ZIF-nog annealed at different temperature, ZIF-nog glass, ZIF-zec glass, and simulated XRD patterns of ZIF-nog and ZIF-zni. 22
Figure 3-12 (a) Liquid-state ^{1}H NMR spectra and (b) FT-IR spectra of crystalline and glassy ZIF-nog and ZIF-zec. 23
Figure 4-1 (a) PXRD of the simulated and as-synthesized crystalline ZIF-62, and a_gZIF-62 with different cooling rates. (b) Temperature dependence of C_p and mass loss of crystalline and glass ZIF-62 upon heating, shown as red and blue curves, respectively. 26
Figure 4-2 Temperature dependence of the heat capacity in supercooled liquid, glass and crystalline states of ZIF-62, shown as red line (Eq. 4-1), blue diamond points and black line (Eq. 4-2), respectively. The green circles are the heat capacity in supercooled liquid obtained from the enthalpy relaxation results. 27
Figure 4-3 (a) ΔH_T^{sl-x} and ΔS_T^{sl-x} of ZIF-62. (b) ΔG_T^{sl-x} of ZIF-62, together with the data of some alloys from literature (55–57). 27
Figure 4-4 Temperature dependence of C_p of a_gZIF-62 annealed at 559 K for different durations t_a (in seconds). 29

Figure 4-5 The recovered enthalpy ($\Delta H(T_a, t_a)$) of a_gZIF-62 after annealing at different temperatures and time. Dashed lines: the fitted curves via Eq. 4-7. Inset: T_a dependence of β. 30
Figure 4-6 Structure factors S(Q) of a_gZIF-62 after melt quenching (red), annealing at 553 K with no duration (t_a=0) (purple), and annealing at 553 K for 72 hours (blue). 32
Figure 4-7 Corresponding pair distribution functions $D(r)$ in the regions (a) 0 Å < r < 7 Å and (b) 6.5 Å < r < 12 Å. 32
Figure 5-1 (a) Unit cell of ZIF-11 from the direction of *b* axis. Gray: C; Light blue: N; Dark blue: Zn. H atoms are omitted for clarity. (b) PXRD patterns of the as-synthesized and simulated ZIF-11. (c) DSC-TGA upscan curves of the as-synthesized ZIF-11. 36
Figure 5-2 (a) Unit cell of ZIF-12 from the direction of *b* axis. Gray: C; Light blue: N; Dark blue: Co. H atoms are omitted for clarity. (b) PXRD patterns of the as-synthesized and simulated ZIF-12. (c) DSC-TGA upscan curves of the as-synthesized ZIF-12. 36
Figure 5-3 (a) Unit cell of ZIF-71 from the direction of *b* axis. Gray: C; Light blue: N; Green: Cl; Dark blue: Zn. H atoms are omitted for clarity. (b) PXRD patterns of the as-synthesized and simulated ZIF-71. (c) DSC-TGA upscan curves of the as-synthesized ZIF-71 37
Figure 5-4 Unit cell of MCIF-1 from the direction of *a* axis (a) and *c* axis (b). Gray: C; Blue: N; Red: Cu. H atoms are omitted for clarity. (c) PXRD patterns of the as-synthesized and simulated MCIF-1. (d) DSC-TGA upscan curves of the as-synthesized MCIF-1. 37
Figure 5-5 (a) Unit cell of TIF-5-Cl from the direction of *b* axis. Gray: C; Light blue: N; Green: Cl; Dark blue: Zn. H atoms are omitted for clarity. (b) PXRD patterns of the as-synthesized and simulated TIF-5-Cl, and one preheated at 400 °C. (c) DSC-TGA upscan curves of the as-synthesized TIF-5-Cl. 38
Figure 5-6 (a) Unit cell of JUC-160 from the direction of *b* axis. Gray: C; Light blue: N; Dark blue: Zn. H atoms are omitted for clarity. (b) PXRD patterns of the as-synthesized and simulated JUC-160. (c) DSC-TGA upscan curves of the as-synthesized JUC-160 39
Figure 5-7 (a) Unit cell of ZTIF-1 from the direction of *b* axis. Gray: C; Light blue: N; Dark blue: Zn. H atoms are omitted for clarity. (b) PXRD patterns of the as-synthesized and simulated ZTIF-1. (c) DSC-TGA upscan curves of the as-synthesized ZTIF-1. 40
Figure 5-8 (a) Unit cell of ZIF-76 from the [1 0 1] orientation. Gray: C; Light blue: N; Green: Cl; Purple: Zn. H atoms are omitted for clarity. (b) DSC-TGA upscan curves of the as-synthesized ZIF-76 41
Figure 5-9 (a) PXRD patterns of the a_gZIF-76 and ones preheated at 400 °C and melting point (451 °C). (b) DSC-TGA upscan curves of the a_gZIF-76. 41
Figure 5-10 (a) PXRD patterns of the as-synthesized ZIF-76-mbIm and the one preheated at melting point (471 °C). (b) DSC-TGA upscan curves of the as-synthesized ZIF-76-mbIm. Inset: DSC upscans of a_gZIF-76 and a_gZIF-76-mbIm. . 42

Figure 5-11 (a) Unit cell of DUT-67 from the direction of *b* axis. Gray: C; Yellow: S; Red: O; Light blue: Zr. H atoms are omitted for clarity. (b) PXRD patterns of the as-synthesized and simulated DUT-67, and ones heat-treated at 230 ˚C, 260 ˚C and 300 ˚C in argon. (c) DSC-TGA upscan curves of the as-synthesized DUT-67. Inset: DSC upscan after preheated at 260 ˚C. 45

Figure 5-12 PXRD patterns of as-synthesized and simulated MOFs, and ones heat-treated at certain temperatures. (a) DUT-69, (c) UiO-66, and (e) MOF-808; DSC-TGA upscan curves of the as-synthesized (b) DUT-69, (d) UiO-66, and (f) MOF-808. .. 46

Figure 5-13 SEM micrographs of (a) DUT-67 and (b) DUT-67-HT. Scale bar: 2 μm. 47

Figure 5-14 (a) *In situ* SAXS profile of DUT-67. (b) Some SAXS data at characteristic temperatures. 47

Figure 5-15 Comparison of the structure of DUT-67 and DUT-67-HT characterized by (a) ^{1}H and ^{1}H-^{13}C HSQC liquid-state NMR, (b) Raman, and (c) FT-IR spectroscopy. 48

Figure 5-16 (a) DSC upscans of DUT-67 preheated at various temperatures. The red point on each scan indicates the preheated temperature. (b) DSC upscans at different heating rates R_h on the sample preheated to 220 ˚C. Inset: Linear fits of the characteristic onset, peak and end-set temperatures of the exothermic peak with heating rates. 50

Figure 5-17 (a) N_2 and (b) CO_2 absorption-desorption isotherms of DUT-67 and DUT-67-HT. Solid points: Absorption; Open points: Desorption. 51

Figure 6-1 Unit cell of ZIF-4-Zn (a) and ZIF-62 (b) from the direction of *b* axis. Light blue: Zn; Dark blue: N; black: C; H atoms are omitted for clarity. (c) DSC and TGA results of ZIF-4-Zn/ZIF-62(50/50) mixture (red line) and blended (ZIF-4-Zn)$_{0.5}$(ZIF-62)$_{0.5}$ (blue line). Upscan rate: 10 K min^{-1}. 53

Figure 6-2 PXRD results. Purple and orange lines correspond to the patterns of ZIF-62 and ZIF-4-Zn, respectively, and the dashed lines are the simulated patterns, respectively. Blue and red lines represent the patterns of ZIF-4-Zn/ZIF-62(50/50) mixture and blended (ZIF-4-Zn)$_{0.5}$(ZIF-62)$_{0.5}$, respectively. 54

Figure 6-3 (a) DSC upscans of the blended (ZIF-4-Zn)$_{1-x}$(ZIF-62)$_x$. The dashed arrow represents the shift of T_g. (b) T_g shift with the wt% of ZIF-62 in the blended (ZIF-4-Zn)$_{1-x}$(ZIF-62)$_x$. Predicted T_g based on the properties of the two ZIFs are shown as the dashed lines in terms the CK and GT models. 55

Figure 6-4 Unit cell of ZIF-4-Co (a) and ZIF-62 (b) from the direction of *b* axis. Green: Zn; Purple: Co; Dark blue: N; black: C; H atoms are omitted for clarity. (c) DSC and TGA results of ZIF-4-Co/ZIF-62(50/50) mixture (blue line) and blended (ZIF-4-Co)$_{0.5}$(ZIF-62)$_{0.5}$ (inset). The mixture was ball-milled for 5 minutes. Upscan rate: 10 K min^{-1}. 56

Figure 6-5 PXRD results. Purple and green lines correspond to the patterns of ZIF-62 and ZIF-4-Zn, respectively, and the dashed lines are the simulated patterns, respectively. Brown and red lines represent the patterns of ZIF-4-Co/ZIF-62(50/50) mixture and blended (ZIF-4-Co)$_{0.5}$(ZIF-62)$_{0.5}$, respectively. 56

Figure 6-6 DSC and TGA results of ZIF-4-Co/ZIF-62(50/50) mixture (blue line) and blended (ZIF-4-Zn)$_{0.5}$(ZIF-62)$_{0.5}$ (red line) from different pre-treatments. (a) The mixture was light grinded in a mortar and pestle; (b) The mixture was ball-milled for 20 minutes. Upscan rate: 10 K min^{-1}. 57
Figure 7-1 (a) Schematic modification process with mechanochemical method; (b) PXRD patterns of the ZIF-PSM crystal, together with the simulated ones of ZIF-7 and ZIF-62 phases; (c) Rietveld refinement of the PXRD pattern of the ZIF-PSM 60
Figure 7-2 Liquid-state ^{1}H NMR spectrum of the mixture of ZIF-7/ZIF-62(50/50) (a) and the ZIF-PSM (b) digested in DCl/D$_2$O/DMSO-d_6. 61
Figure 7-3 (a) PXRD patterns of modified ZIF-7 by imidazole and 75 μL DMF for different durations. (b) PXRD patterns of modified ZIF-7 by imidazole for 60 minutes with different volume of DMF. Note that the ZIF-PSM sample refers to the one specifically modified for 60 minutes with 75 μL DMF. 62
Figure 7-4 PXRD patterns of modified ZIF-7 by imidazole for 60 minutes with 75 μL of different types of solvent. 63
Figure 7-5 PXRD patterns of modified ZIF-7 by imidazole with DMF and n-BuOH using solvothermal method. 64
Figure 7-6 PXRD patterns of as-synthesized and modified ZIF-8 (a) and ZIF-14 (b) by imidazole for 60 minutes with 75 μL DMF. 65
Figure 7-7 (a) Heat flow of ZIF-7, ZIF-62, mixture (ZIF-7)(ZIF-62)(50/50), ZIF-PSM crystal and a_TZIF-PSM. Upscan rate: 20 K min^{-1}; (b) PXRD patterns of ZIF-7, ZIF-62, (ZIF-7)(ZIF-62)(50/50) and ZIF-PSM samples after preheated at 500 °C. 65
Figure 7-8 (a) Ex-situ PXRD measurements of the ZIF-PSM sample preheated at different temperature. (b) A comparison of the PXRD patterns of ZIF-7 and ZIF-PSM at room temperature and preheated at 600 °C. The star indicates the ZnO phase..... 66
Figure 7-9 Liquid-state ^{1}H NMR spectrum of the a_TZIF-PSM digested in DCl/D$_2$O/DMSO-d_6. 67
Figure 7-10 SEM micrographs of (a) ZIF-7, (b) ZIF-PSM, and (c) a_TZIF-PSM. Scale bar: 500 nm. 68
Figure 7-11 (a) Load-displacement curve from nanoindentation measurement of the a_TZIF-PSM. Inset: *E*-*H* relationship of ZIF-7, a_gZIF-62 and a_TZIF-PSM (11,37). (b) Elastic modulus (*E*) and hardness (*H*) as a function of indentation depth of a_TZIF-PSM. Error bars come from the standard deviation of 26 measurements. 68
Figure 7-12 (a) N$_2$ absorption-desorption isotherms of ZIF-7 crystal, ZIF-PSM, and a_TZIF-PSM at 77 K. Solid points: Absorption; Open points: Desorption. (b) Relations between BET surface area from N$_2$ uptake measurements and pycnometric density of some amorphous MOFs (8,11). 69
Figure 7-13 Synchrotron radiation far-infrared (SR-FIR) spectra of ZIF-7 crystal, ZIF-7/ZIF-62 (50/50) mixture, ZIF-PSM and a_TZIF-PSM. 70

TABLE OF TABLES

Table 3-1 Synthesis conditions (time and temperature), topology, space group, and yield of the product of each process.. 14

Table 3-2 Specific surface area (BET method), pore volume, N_2 uptakes (at P/P_0=0.9), and densities of samples S1-S5. The brackets give the standard error of the density from 10 cycle measurements.. 17

Table 3-3 Refinement parameters of PXRD patterns of S3, S6-S9. Space group: *C2/c*. Values in brackets give the estimated standard deviations (ESDs) from the refinements.. 19

Table 3-4 Specific surface area (BET method), pore volume, N_2 uptakes (at P/P_0=0.9), and densities of all ZIF-zec samples. 21

Table 3-5 Melting (T_m) and glass transition (T_g) temperature of the ZIF Zn(Im)$_2$ isomorphs, together with crystal porosity, the enthalpy of recrystallization (ΔH_{rc}) and the heat of fusion (ΔH_f) of the ZIF crystals.. 23

Table 4-1 Fitting parameters and standard errors from Eq. 4-7 in Figure 4-5.......... 30

Table 4-2 The glass transition temperature T_g, liquid fragility *m*, and the stretched exponent β from the KWW equation (Eq. 4-7) for different ranges of T_a/T_g. 31

Table 5-1 Characteristic temperatures of crystalline and glassy ZIF-76 and ZIF-76-mbIm.. 42

Table 5-2 Summary of the porous characteristics of ZIF-76, ZIF-76-mbIm and a_gZIF-76-mbIm. Surface area and pore volume are calculated from the NLDFT fitting of the CO_2 absorption isotherms. 43

Table 5-3 Surface area (BET method from N_2 uptakes), pore volume, N_2 uptakes (P/P_0=0.9), CO_2 uptakes (P/P_0=0.03), and densities of DUT-67 and DUT-67-HT. 51

Table 7-1 Refinement parameters of the PXRD pattern in Figure 7-1c. Values in brackets are ESDs from refinements.. 61

Table 7-2 Compositions of the PSM samples with different types of solvents, quantified by Rietveld refinements of the PXRD patterns in Figure 7-4. 63

Table 7-3 Elemental analysis of the ZIF-PSM and a_TZIF-PSM (based on the composition of (ZIF-7)$_{47.2}$(ZIF-62)$_{52.8}$, ZIF-7: $ZnC_{14}H_{10}N_4$; ZIF-62: $ZnC_7H_{6.5}N_4$).. 67

CHAPTER 1. INTRODUCTION

1.1. BACKGROUND AND CHALLENGES

Metal-organic frameworks (MOFs), or coordination polymers (CPs), have been a hot research topic in the last two decades, due to their large porosity and flexible chemical composition, giving various kinds of potentials for applications such as gas and liquid absorption, gas separation, catalysis, sensoring and detection, food storage etc. (1–4). Companies, such as BASF, MOF Technologies, and framergy, as well as a number of start-ups including novoMOF and MOFWORX, have commercialized some MOFs for industrial applications. Furthermore, over 60,000 MOF structures have been reported in literature according to the Cambridge Crystallographic Data Centre (CCDC) in 2017, showing the speed at which this hybrid inorganic-organic material research field broadens in structural chemistry and crystallography.

Amorphous MOFs obtained directly after synthesis, however, were rare reported before, as most of them are regarded as failures of the syntheses of crystalline MOFs. Amorphization of MOFs was first reported as an edge sub-topic in 2010 (5). The studied subject is ZIF-4, which is in the category denoted as zeolite imidazolate frameworks (ZIFs), a subfamily of MOFs. ZIF-4 [$Zn(Im)_2$], composed by Zn^{2+} as metallic center and imidazolate (Im) as organic linker, can be amorphized and recrystallized to ZIF-zni upon heating. The thermal-induced amorphous ZIF-4 (a_TZIF-4) has the angle of ~145° between the Zn-Im-Zn bond in the tetrahedral, analogues to that of Si-O-Si in silica (Figure 1-1).

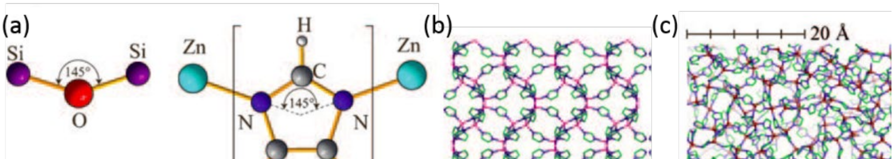

Figure 1-1 (a) Structural analogy of the building units between ZIFs (Zn-Im-Zn) and silica (Si-O-Si); (b) Unit cell of ZIF-4; (c) Representative view of a_TZIF-4 structure (5,6).

Amorphous MOFs could be categorized as three different types: liquid and melt-quenched glasses; non-melt quenched glasses; and amorphous non-glassy solids (7). Remarkably, melt-quenched glasses (also MOF glasses in this thesis) refer to the samples quenched after melting, which show a liquid-like state with glass transition behaviour on the DSC trace upon reheating (8). A number of 3D MOFs, especially some ZIFs such as ZIF-4, TIF-4 [$Zn(Im)_{1.5}(5\text{-mbIm})_{0.5}$], and ZIF-62 [$Zn(Im)_{1.75}(bIm)_{0.25}$], are revealed to form melt-quenched MOF glasses (9,10). Taken

TIF-4 as an example, the melting point (T_m) and the glass transition temperature (T_g) are 467 °C and 343 °C, respectively (10). It suggests the high thermal stability of 3D MOF glasses. The mechanism of ZIF-4 melting has been interpreted by an *in silico* study: the coordinated bond between Zn^{2+} and the linkers breaks and metal ions redirect to connect another linker in a short time scale (11,12). Furthermore, some 1D and 2D coordiCPs, such as $[Zn(H_2PO_4)_2(HTr)_2]$ (HTr: 1,2,4-triazole) are also discovered to form melt-quenched MOF glasses (13–18). These 1D and 2D CPs can be normally melted at $T_m < 200$ °C. As with the non-melt quenched MOFs glasses, they are mostly obtained by heating or ball-milling MOFs (6,19–21). A characteristic feature is that these glasses are structurally the same as those from melt-quenching with no broken coordination bonds (22). The third category points to those amorphous MOFs with considerable changes of the local environments of the metal center and the broken coordination bonds compared to their crystalline counterparts. They can be achieved by ball-milling, pressure, heating, or even direct synthesis (23–26). Considering the constituents and bonds, the coexistence of both ionic bonds and coordination bonds in hybrid MOFs is unique, compared to other glass formers such as oxide glasses, metallic glasses, and organic molecules and polymers. This discovery makes amorphous MOFs, especially MOF glasses, a new subfamily of glass.

The amorphous MOFs could be characterized by XRD spectroscopy, PDF analysis, DSC-TGA, and nanoindentation measurements. MOFs lose the long-range order structure after amorphization, which can be verified by the disappearance of Bragg peaks on XRD patterns and the PDF spectra. In particular, structural information with subtle differences of the local environments between crystalline and amorphous MOFs could be revealed by PDF and NMR or EXAFS results (10). Additionally, elastic modulus and hardness from nanoindentation measurements normally increases after amorphization of MOFs (27). It is ascribed to the loss of the crystal defects and the structural flexibility in the crystalline counterparts. More experimental approaches are applied to investigate the structural features and properties of amorphous MOFs, such as SAXS/WAXS, NMR, SR-FIR etc (9,21,28–30). Gas absorption measurements and positron annihilation lifetime spectroscopy (PALS) are also carried out to detect the pore size and volume of amorphous MOFs (31–33), although the pores might be disappeared due to the collapse of the framework.

Amorphous MOFs have shown practical advantages for potential applications. For instance, a_gZIF-8 has proved to permanently capture ratioactive waste such as iodine (34,35). Some MOFs are biodegradable, and hence amorphous MOFs can be regarded as biomaterials. As an example, amorphous UiO-66 via ball-milling exhibits a satisfactory period of time to release calcein (up to 30 days), which overcomes the fast release of the drug in the crystalline counterpart (36). With the amorphous features of homogeneous structure and casting possibility, it is possible to apply amorphous MOFs for diverse purposes such as ion conductivity and membrane selectivity (13,37).

As a new family of glasses, amorphous MOFs are far from being understood. Here are some intriguing questions: Do synthesis conditions kinetically affect the crystal phases and thus the glass forming ability? What is the mechanism of melting and glass transition in MOF glasses, compared to the conventional glass families? Can theories in amorphous materials be transferred to MOF glasses to explain the physical features of amorphous MOFs, such as structural relaxation? What is the connection between the crystalline and glassy MOFs in structures and properties? Can we predict MOF glass formers by their crystalline structures? Is it possible to control and design the structures of MOF glasses to facilitate their functionalities? These questions motivated the author to implement this PhD project on amorphization and glass formation of MOFs. Some of the mentioned questions are discussed in this thesis.

1.2. OBJECTIVES

The objectives of the Ph.D. thesis are summarized as follows:

1. Probe the crystalline MOF synthesis influence on the amorphization of MOFs.
2. Investigate the dynamic features, such as sub-T_g enthalpy relaxation, of a MOF glass with good glass forming ability (ZIF-62).
3. Explore more MOF glass formers, and discuss the structural features and functionalities after amorphization.
4. Facilitate chemical properties and porosities of MOF glasses by designing the structure of the crystal phases for potential applications.

1.3. THESIS CONTENT

The experiments of this thesis were conducted at Aalborg University and University of Cambridge. This thesis consists of an overview and four papers, of which three papers have been published in peer-reviewed journals, and one has been accepted. The four papers correspond to the content in Chapter 3, Chapter 4, Chapter 6, and Section 5.2, respectively. Specifically, in the joint paper III, the author conducted all DSC measurements, which are one of the main outcome in the paper. Moreover, in the joint paper IV, the author firstly discovered the glass formation of ZIF-76, which is one of the most prominent contribution in the manuscript. The author also contributed to all the DSC measurements and the manuscript writing, and involved in other characterizations. In addition, results in Section 5.1, 5.3 and Chapter 7 were mostly conducted by the author and independently analyzed by the author. The manuscripts regarding to the results will be submitted soon to journals in relative fields. The relations between the contents of chapters and those in the attached papers are also clarified in the footnotes in the first page of each chapter.

The papers are listed below and cited with roman numbers throughout the thesis:

I. **Zhou C.**, Stepniewska M., Sørensen J. M., Scarpa L., Magnacca G., Boffa V., Bennett T. D., Yue Y. Z., Polymorph Formation for a Zeolitic Imidazolate Framework Composition - $Zn(Im)_2$. *Microporous and Mesoporous Materials*, 265, 57-62 (2018).
II. **Zhou C.**, Stepniewska M., Longley L., Ashling C. W., Chater P. A., Keen D. A., Bennett T. D., Yue Y. Z., Thermodynamic Features and Enthalpy Relaxation in a Metal-Organic Framework Glass. *Physical Chemistry Chemical Physics*, 20, 18291-18296 (2018).
III. Longley L., Collins S. M., **Zhou C.**, Smales G. J., Norman S. E., Brownbill N. J., Ashling C. W., Chater P. A., Tovey R., Schönlieb C., Headen T. F., Terrill N. J., Yue Y., Smith A. J., Blanc F., Keen D. A., Midgley P. A., Bennett T. D., Liquid Phase Blending of Metal-Organic Frameworks. *Nature Communications*, 9, 2153 (2018).
IV. **Zhou C.**, Longley L., Krajnc A., Smales G. J., Qiao A., Erucar I., Doherty C. M., Thornton A. W., Hill A. J., Ashling C. W., Qazvini O. T., Lee S. J., Chater P. A., Terrill N. J., Smith A. J., Yue Y., Mali G., Keen D. A., Telfer S. G., Bennett T. D., Metal-Organic Framework Glasses with Permanent Accessible Porosity, *Nature Communications*, (in press).

CHAPTER 2. EXPERIMENTAL

In this Chapter, details of sample synthesis in this dissertation and the characterization methods are presented.

2.1. SYNTHESIS

Solvothermal and solvent mixing methods were mostly used for MOF synthesis in the present work. All syntheses were performed solely by the author in this thesis. All of the structures were verified by matching the PXRD patterns with the simulated ones.

2.1.1. ZIF-4 ZN(IM)$_2$

According to the previous synthesis process (9), 2.27 g zinc nitrate hexahydrate (7.63 mmol), and 1.5 g imidazole (HIm, 22.0 mmol) were dissolved in 50 ml DMF (*N*,*N*-dimethylformamide). The solvent was transferred into a 100 ml glass jar, which was sealed tightly and heated to 130 °C for 48 hours. Colorless prism-shaped crystals were collected and washed by DMF (30 ml × 3) and DCM (dichloromethane, 30ml × 1). The crystalline sample was activated at 100 °C for 20 hours in vacuum before use. The yield was 1.545 g (41 % based on the amount of zinc).

2.1.2. ZIF-62 ZN(IM)$_{1.75}$(BIM)$_{0.25}$

According to the previous synthesis process (38), 2.380 g zinc nitrate hexahydrate (8 mmol), 7.35 g imidazole (108 mmol), and 1.418 g benzimidazole (HbIm, 12 mmol) were dissolved in 75 ml DMF. The solvent was transferred into a 100 ml glass jar, which was sealed tightly and heated to 130 °C for 48 hours. Colorless prism-shaped sample was collected and washed by DMF (30 ml × 3) and DCM (30ml × 1). The crystals were activated at 100 °C in vacuum before use. The yield was 1.148 g (67 % based on the amount of zinc).

2.1.3. ZIF-11 ZN(BIM)$_2$ AND ZIF-12 CO(BIM)$_2$

According to the previous synthesis process (39), toluene-assisted method was applied for ZIF-11 and ZIF-12 synthesis. First, 120 mg benzimidazole (1 mmol) was dissolved in 4.8 g methanol (6.061 ml). Then 4.6 g toluene (5.287 ml, 50 mmol) was added into the solution. Ammonia hydroxide (60 mg, 66.7 μL, 1 mmol) was then dropped into the solution. After stirring at room temperature to obtain a homogeneous solution, 110 mg zinc acetate dehydrate (0.5 mmol) was added to synthesize ZIF-11 (or 125 mg cobalt(II) acetate tetrahydrate for ZIF-12 synthesis). After stirring for 3 hours, the samples were collected by centrifugation. Both crystals were washed by methanol 2 times and dried at room temperature in fume cupboard overnight. The yields of ZIF-

11 and ZIF-12 were 123.6 mg (81.6 %) and 107 mg of ZIF-12 (72.2 %), respectively, based on Zn.

2.1.4. ZIF-71 ZN(DCIM)$_2$

According to the previous synthesis process (40), a solution of 110 mg zinc acetate dehydrate (0.5 mmol) in 15 ml DMF, and another one of 220 mg 4,5-dichloroimidazole (HdcIm, 1.6 mmol) in 15 ml DMF, were mixed together in a sealed glass jar. The solution was mixed at room temperature for 24 hours via a stirring bar. The DMF was removed by a pipette and the crystals were soaked in chloroform (20 ml × 3) for 3 days. The sample was finally collected via centrifugation. The crystalline sample was evacuated at 100 °C for 24 hours in vacuum. The yield was 144.1 mg (85.5 % based on Zn).

2.1.5. MCLF-1 CU$_2$(DCI)$_2$·MECN

According to the previous synthesis process (41), 19 mg copper(I) iodide (0.1 mmol) and 12 mg 4,5-dicyanoimidazole (HDCI, 0.1 mmol) were dissolved in 5 ml MeCN. The solution was stirred for 10 minutes in a 20 ml glass vial and left it at room temperature for 3 days. The sample were filtered and immersed in fresh MeCN overnight. Then the product was collected by filtration, washed with MeCN three times, and dried in air. The yield was ~7.5 mg (18.6% based on Zn).

2.1.6. TIF-5-CL ZN(IM)(DCBIM)

According to the previous synthesis process (42), 1.785 g zinc nitrate hexahydrate (6 mmol), 408.5 mg imidazole (6 mmol) and 877.1 mg 5,6-dichlorobenzimidazole (HdcbIm, 6 mmol) were dissolved in 50 ml DMF. The mixture was transferred into a 100 ml glass vial, followed by heating to 100 °C for 72 hours. The product was filtered after synthesis, and washed by DMF (20 ml × 3) and DCM (20 ml × 2). After leaving in fume hood overnight, 872.1 mg crystalline sample was collected (yield: 53.3 % based on Zn).

2.1.7. JUC-160 ZN$_4$(2-MBIM)$_3$(BIM)$_5$

According to the previous synthesis process (43), 119 mg zinc nitrate hexahydrate (0.4 mmol), 52.8 mg 2-methylbenzimidazole (2-HmbIm, 0.4 mmol), and 59 mg benzimidazole (0.5 mmol) were dissolved in 11 ml of DMF. The solvent was transferred into a 23 ml autoclave, which was sealed tightly and heated to 180 °C for 48 hours. Pale-yellow crystals were collected and washed by DMF (30 ml × 2). The crystalline sample was activated at 100 °C in vacuum before use. The yield was 316 mg (60 % based on the amount of zinc).

2.1.8. ZTIF-1 ZN(5-MTZ)(2-EIM)

According to the previous synthesis process (41), 110 mg zinc acetate dihydrate (0.5 mmol), 43 mg 5-methyltetrazole (5-Hmtz, 0.5 mmol) and 48 mg 2-ethylimidazole (2-HeIm, 0.5 mmol) were dissolved in a mixed solvent with 2 ml DMF and 2 ml ethanol. The mixture was sealed tight in a 20 ml glass vail and heated up to 120 ˚C for 72 hours. The transparent polyhedral crystals were collected by filtration after washed by ethanol. The yield was 100 mg (81.4% based on Zn).

2.1.9. ZIF-76 ZN(IM)(5-CBIM)

According to the previous synthesis process (44),1.785 g zinc nitrate hexahydrate (6 mmol), 408.5 mg imidazole (6 mmol) and 915.5 mg 5-chlorobenzimidazole (5-HcbIm, 6 mmol) were dissolved in 50 ml DMF. The mixture was transferred into a 100 ml glass vial, followed by heating up to 100 ˚C for 72 hours. The samples was filtered after synthesis, and washed by DMF (20 ml × 3) and DCM (20 ml × 2). After leaving in fume hood overnight, 622.5 mg crystalline sample was collected (yield: 37.2 % based on Zn).

2.1.10. ZIF-76-MBIM ZN(IM)(5-MBIM)

According to the previous synthesis process (45), 117.5 mg imidazole (1.725 mmol) and 114.5 mg 5-methylbenzimidazole (5-HmbIm, 0.866 mmol) were dissolved in a mixed solvent with 5.75 ml DMF and 5.75 ml DEF (*N,N*-diethylformamide). Then 255.6 mg zinc nitrate hexahydrate (0.859 mmol) was added to this solution. 0.5184 ml NaOH solution (M = 2.5 mol/L) was added later according to the literature. The mixture was transferred into a 20 ml glass vial, followed by heating to 90 ˚C for 72 hours. The product was filtered after synthesis, and washed by DMF (20 ml × 3) and MeOH (20 ml × 2). After leaving in fume hood overnight, 622.5 mg crystalline sample was collected (yield: 37.2 % based on Zn).

2.1.11. DUT-67 [$ZR_6O_6(OH)_2(TDC)_4(AC)_2$]

According to the previous synthesis process (46,47), 233 mg $ZrCl_4$ (1 mmol) was dissolved in a mixed solvent of 9.5 ml DMF and 9.5 ml NMP (*N*-methyl-2-pyrrolidone) by sonication for 10 minutes. 86 mg 2,5-thiophenedicarboxylic acid (H_2tdc, 0.5 mmol) was added to the mixed solvent and the solution was sonicated for 5 minutes. Acetic acid (HAc, 15 ml) was then added and sonicated together for 10 minutes. The solution was transferred into a 50 ml autoclave and synthesized at 120 ˚C for 2 days. The resultant powders were collected via centrifugation and washed with DMF and ethanol (20 ml × 2). The product was dried at 60 ˚C overnight. The yield was 132 mg (70% based on tdc).

2.1.12. DUT-69 [$ZR_6O_4(OH)_4(TDC)_5(AC)_2$]

According to the previous synthesis process (46), 233 mg $ZrCl_4$ (1 mmol) was dissolved in DMF (33 ml) via sonication for 10 minutes. 115 mg H_2tdc (0.67 mmol) was added to the mixed solvent and sonicated for 5 minutes. Then acetic acid (HAc, 18.3 ml) was added and sonicated for 10 minutes. The solvent was transferred into a 100 ml glass jar and synthesized at 130 ˚C for 3 days. The samples were centrifuged and washed with DMF and ethanol (20 ml × 2). The resultant powders were collected via centrifugation and thoroughly washed with DMF and ethanol (20 ml × 2). The sample were dried at 60 ˚C overnight. The yield was 40 mg (19% based on tdc).

2.1.13. UIO-66 [$ZR_6O_4(OH)_4(BDC)_6$]

According to the previous synthesis process (48), 3.5 g $ZrCl_4$ (15 mmol) and 2.5 g terephthalic acid (H_2bdc; 15 mmol) were dissolved in DMF (155 ml). 1.5 ml of a 37 % solution of HCl was add to the solution. The mixture was transferred into a 250 ml glass jar and synthesized at 120 ˚C for 24 hours. The resultant powders were collected via centrifugation and thoroughly washed with DMF and ethanol (20 ml × 2). The sample were dried at 60 ˚C overnight. The yield was 3.726 g (91.5% based on Zr).

2.1.14. MOF-808 [$ZR_6O_4(OH)_4(BTC)_2(FA)_6$]

According to the previous synthesis process (49), 268 mg $ZrOCl_2·8H_2O$ (0.83 mmol) and 175 mg trimesic acid (H_3btc; 0.83 mmol) were dissolved in a mixed solvent of DMF (33 ml) and formic acid (HFa, 33 ml) DMF (155 ml). The solvent was transferred into a 100 ml glass jar and synthesized at 100 ˚C for 4 days. The resultant powders were collected via centrifugation and thoroughly washed with DMF and ethanol (20 ml × 2). The sample were dried at 60 ◦C overnight. The yield was 136 mg (63% based on Zr).

2.1.15. ZIF-7 $ZN(BIM)_2$

2.38 g zinc nitrate tetrahydrate (8 mmol) and 1.89 g benzimidazole (16 mmol) were well dissolved in 180 ml DMF after stirring 20 minutes by magnetic stirrers. The solvent was then transferred to a 200 ml glass jar. After heating to 130 ˚C for 48 hours, crystals were collected by centrifugation. The samples was washed by DMF (30 ml × 3) and methanol (30 ml × 3). 2.377 g crystalline sample was obtained after drying (yield: 88.5 % based on Zn).

2.2. CHARACTERIZATIONS AND METHODS

The author performed most of the experiments and analysed all results in this thesis. A co-author contribution is presented in the relevant section only if the measurements were not carried out by the author independently.

2.2.1. POWDER X-RAY DIFFRACTION (PXRD) SPECTROSCOPY

PXRD patterns of fine-grinded samples were collected on a PANalytical empyrean X-ray diffractometer (AAU) or a Bruker-AXS D8 diffractometer (UCam) in Bragg-Brentano geometry using Cu $K\alpha_1$ radiation ($\lambda = 1.54098$ Å) equipped with a Cu $K\alpha$ operated at 45 kV and 40 mA. PXRD patterns were collected in the 2θ range from 3 to 50° (or 70°) with a step size of 0.013°. Simulated PXRD patterns were obtained from Software Mercury 3.9 from the crystallographic information files (cif) of corresponding framework structures. Analysis of the data was carried out using the X'pert HighScore Plus, Topas-Commercial V3, or Topas-Academic V4 programs.

2.2.2. REFINEMENT DETAILS

The peak positions of the experimental PXRD data of a MOF sample were first compared to simulated patterns of MOFs with corresponding compositions to evaluate the possible crystalline phases. Note that there is no new crystalline structure reported in the present work, and the structural models were initiated according to the corresponding cifs from the CCDC (Cambridge Crystallographic Data Centre). However, the peak intensities and width of the PXRD pattern shall be refined in order to give the precise structural information. Therefore, Rietveld and Le Bail refinements were applied to some PXRD patterns to study the crystal structure (50,51). All refinements were carried out with Topas-Commercial V3 package using the fundamental parameters approach (50).

The background was fitted using the Chebyshev polynomial model. A Lorentz–polarization factor of 90, and a polarization correction of 1, and a refined axial convolution parameter and absorption coefficient parameter were also implemented. Space group, unit-cell dimension, and site occupancies were initially adopted from the corresponding cif file after the preliminary compaison between the experimental and simulated PXRD patterns. The peak positions were first refined by optimizing the unit cell parameters and the specimen displacement. The preferred orientation (March-Dollase parameter is in the range of 0.7~1), site occupancies, atomic coordinates, and isotropic ADPs (positive values) were applied to refine the relative peak intensities. The anisotropic displacement parameters were not modified as (1) preferred orientation parameters were applied during refinements; (2) the unit cells are quite large (>10000 Å^3), and the considerable atoms (e.g. 116 sites for ZIF-zec) give strong atomic motions; (3) the current model could yield good refinement results. Pesudo-Voigt model was applied to refine the peak profile. Regarding the least-squares Rietveld analysis, the R factors were expected to be $R_{\mathrm{wp}} < 20$, $R_{\mathrm{Bragg}} < 5$, $R_{\mathrm{p}} < 5$, and $\chi^2 < 5$, so as to verify the rationality of the structural model. Other details of the refine models and parameters with regard to the PXRD patterns of the relevant samples are presented in the corresponding sections.

2.2.3. DIFFERENTIAL SCANNING CALORIMETRY (DSC)

Differential scanning calorimetric and thermogravimetric (TGA) results were collected simultaneously with Netzsch STA 404 C (AAU), Netzsch STA 449 F1 Jupiter (AAU), and TA Q600 (UCam). Pt/Rh crucibles were used for both samples and the references. The sample mass was normally 7 ~ 15 mg. The direction of the enthalpy release, i.e. exothermic direction, points downwards in all figures in this thesis. Scanning rates were 10 K/min as default, whilst various upscan rates were also applied for determining activation energy. The isobaric heat capacity (C_p) curves (i.e. $C_p \sim T$ curve) were determined by comparing the DSC outputs with those of a reference sapphire at the same upscan rate.

2.2.4. LIQUID-STATE NUCLEAR MAGNETIC RESONANCE (NMR) SPECTROSCOPY

Liquid-state nuclear magnetic resonance (NMR) spectra were recorded on a Bruker DPX600 Advanced 600 MHz spectrometer. All the samples (8~15 mg) were dissolved in a mixed solvent (37 wt% DCl/D_2O: 100 *µ*l; DMSO-d_6: 500 µl). ^{1}H, ^{13}C, and 2D ^{13}C-HSQC were collected at 308.1 K. Spectral acquisition was controlled using the TopSpin 3.6 software (Bruker BioSpin). The spectra were also processed with the MestreNova Suite program. All liquid-state NMR results, except those in Paper IV, were collected and analysed by the author. Note that liquid-state NMR spectroscopy is commonly used for characterizing MOF structures due to small amount of samples (5~20 mg), short time for data collection, and high resolution data for analysis (52–55).

2.2.5. SCANNING ELECTRON MICROSCOPY (SEM)

Scanning electron microscopy (SEM) measurements were performed on Zeiss EVO 60 SEM using secondary electron mode. For observations, samples were coated by a thin gold layer with a thickness of ~15 nm. Alternatively, some SEM measurements were conducted by using FEI Nova Nano SEM 450. The samples were dried under 30 °C and then followed by chromium coating prior to imaging.

2.2.6. RAMAN SPECTROSCOPY

Raman spectra were collected in HORIBA LabRAM HR Evolution Raman microscope with a green laser with the wavelength of 532 nm. A typical power of 0.1 W was used to record the Raman shift in the range of 150 to 2000 cm^{-1}. Raman data in 5.3.2 were collected by Ang Qiao and analysed by the author.

2.2.7. FOURIER-TRANSFORM INFRARED (FT-IR) SPECTROSCOPY

Fourier transform-infrared (FT-IR) spectra were collected on a Varian 640 IR spectrophotometer in transmittance mode with the KBr technique (KBr:sample wt% = 100:1). Alternatively, some FT-IR measurements were performed by using Bruker Tensor II FT-IR Spectrometer in an attenuated total reflectance (ATR) mode. All data were collected in range of 4000~400 cm^{-1}.

2.2.8. GAS ABSORPTION

Gas absorption isotherms were measured on a Micromeritics ASAP 2020 instrument. About 100 mg sample was used for each measurement. Samples were degassed in vacuum for 3 hours at approximately 100 °C before starting the measurements. The N_2 and CO_2 absorption-desorption isotherms were conducted at 77 K and 273.1 K respectively. The surface area was estimated by the Brunauer-Emmett-Teller (BET) and Langmuir methods for the relative pressure range (P/P_0) of 0.06 to 0.2 from the N_2 uptake isotherms. The results in 3.1 and 5.4 were measured by Giuliana Magnacca and Jingwei Hou, respectively, and the ones in 7.4 were collected by the author and Jingwei Hou. All results were analysed by the author.

2.2.9. GAS PYCNOMETRY

Pycnometric measurements on the samples were performed using a Micromeritics Accupyc 1340 helium pycnometer, equipped with a 1.3 cm^3 insert. The typical mass used was ~150 mg. The mean values and standard deviations are calculated from a cycle of 10 measurements.

2.2.10. NANOINDENTATION

The Young’s modulus (E) and hardness (H) of the samples were measured using an MTS Nanoindenter XP at ambient conditions. Samples were mounted in an epoxy resin and polished using increasingly fine diamond suspensions up to 1/4 μm. Indentation experiments were performed under the dynamic displacement controlled mode, at a constant strain rate of 0.05 s^{-1}. All tests were conducted using a three-sided pyramidal (Berkovich) diamond indenter tip, to a maximum surface penetration depth of 500 nm. The collected load-displacement data were analysed using the Oliver & Pharr method (56). A Poisson’s ratio of 0.4 was used, in accordance with prior studies on ZIF materials (57). The results in 7.3 were measured and analysed by the author, and the relevant results in Paper III is not included in this thesis.

2.2.11. X-RAY TOTAL SCATTERING MEASUREMENTS

X-ray total scattering data were collected on the I15-1 beamline at the Diamond Light Source, Didcot, UK. Data were collected between $\sim 0.4 < Q < \sim 26$ Å^{-1} with the wavelength of λ = 0.161669 Å. Finely powdered samples were loaded into 1.17 mm (inner diameter) borosilicate capillaries, and data from an empty instrument and capillary were also collected for background subtraction. Corrections for background, multiple, container and Compton scattering, along with absorption were performed using the GudrunX program (58,59). The normalized reciprocal space data were then converted to the pair distribution functions (PDFs) via Fourier transform. The author took part in the sample preparation and data collection of the X-ray total scattering measurements, and the preliminary analysis of the data in Papers II, III, and IV.

2.2.12. SAXS/WAXS MEASUREMENTS

Synchrotron SAXS/WAXS data were collected on the SAXS beamline at the Australian Synchrotron (ANSTO), Clayton VIC, Australia. Dried powder samples were loaded into a 1.0 mm quartz capillary under argon protection in a glove box. The *in-situ* SAXS/WAXS measurements were carried out at 16 keV, 2675 mm camera length using a Pilatus 1M detector at a transmission mode. A line scan mode (3 mm) was conducted for each analysis at 0.3 mm/s. The data were processed on an in-house developed Scatterbrain software for averaging and background subtraction. The experiments were performed by Jingwei Hou, and the results were analysed by the author.

2.2.13. SYNCHROTRON RADIATION FAR-INFRARED SPECTROSCOPY

Synchrotron radiation far-infrared (SR-FIR) measurements were conducted on the THz/Far-IR Beamline at the Australian Synchrotron (ANSTO), Clayton VIC, Australia. The beamline was equipped using the attenuated total reflectance (ATR) sampling accessory. The resolution was 0.028927 THz (0.9642 cm^{-1}) and the spectra were collected in range of 30-700 cm^{-1}. The spectrometer was performed at a current of 200 mA with a total of 240 scans. The experiments were performed by Jingwei Hou, and the results were analysed by the author.

CHAPTER 3. CRYSTAL SYNTHESIS AND GLASS FORMATION ZN(IM)$_2$ POLYMORPHS

Polymorphism in metal-organic frameworks has been extensively studied (60,61), which can be observed by controlling synthesis conditions, such as synthesis temperature and time, concentration of reagents, pH values, post-synthetic processes, pressure etc. At the same time, the crystal size and morphology of the obtained crystalline MOFs are also influenced by these conditions, giving different properties such as porosities. The first-reported melt-quenched MOF glass was ZIF-4 [Zn(Im)$_2$] with a **cag** topology as the variscite $CaGa_2O_4$ in *P*bca space group (9). [Zn(Im)$_2$] polymorphs have various network topologies, such as **cag**, **coi**, **crb**, **dft**, **gis**, **mer**, **nog**, **zec** and **zni** (60). In literature, ZIF-4 and ZIF-zni were mostly studied (11,62), and only ZIF-4 and ZIF-gis were reported to form MOF glasses after melt-quenching in ZIF [Zn(Im)$_2$] polymorphs (9,10). Synthesis influence of the ZIF [Zn(Im)$_2$] frameworks and their glass forming ability is however not investigated in details. In light of this, the influence of synthesis conditions on the crystal formation of ZIF with Zn(Im)$_2$ composition was explored in this Chapter. Crystal size, morphology and porosity, glass formation of the polymorphs were discussed [1].

3.1. SYNTHESIS CONDITIONS INFLUENCE OF ZN(IM)$_2$ POLYMORPHS

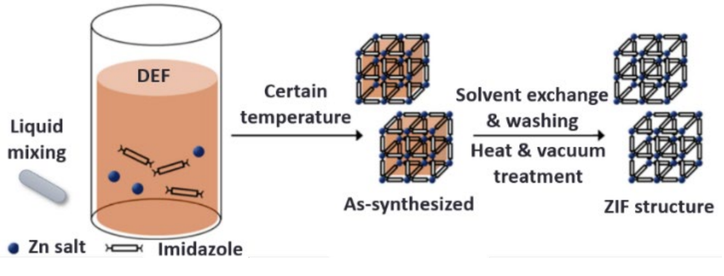

Figure 3-1 Schematic figure of the process of Zn(Im)$_2$ synthesis using solution mixing method.

A solution mixing method was applied to synthesize ZIF [Zn(Im)$_2$] to precisely control the conditions, instead of using the conventional solvothermal method as normally used for ZIF-4 synthesis (63). A solution of 1.1 g zinc acetate dihydrate (5 mmol) in 25 ml n-propylamine, and a solution of 681 mg imidazole (10 mmol) in

---

[1] Results in this chapter have been published in Paper I.

25 ml DMF, were mixed together. Products were obtained after magnetic stirring (600 rpm), while synthesis time and temperature were controlled as listed in Table 3-1. The samples were dried before washed by dichloromethane for 3 times. A schematic process is demonstrated in Figure 3-1. The yields of all samples were calculated based on the input amount of zinc in Table 3-1, and the identities of the samples are discussed below.

Table 3-1 Synthesis conditions (time and temperature), topology, space group, and yield of the product of each process.

Sample No.	Time /hour	Temp /^{o}C	Topology	Space group	Yield /%
S1	0.083	23	amorphous	-	41
S2	18	10	coi+cag	$I\,4_1$+P bca	44
S3	24	10	zec	C 2/c	50
S4	48	10	nog	$P\,2_1$/n	48
S5	120	10	zni	$I\,4_1$ cd	66
S6	24	15	zec	C 2/c	47
S7	24	23	zec	C 2/c	50
S8	24	30	zec	C 2/c	90
S9	24	35	zec	C 2/c	58

3.1.1. SYNTHESIS TIME INFLUENCE

Figure 3-2 shows the PXRD patterns of samples S1-S5 which were synthesized at 10 °C with different durations. The PXRD pattern of S1 shows a broad hump at $2\theta \approx 15^{\circ}$, an indicative of its amorphous feature. In other words, a short synthesis time like 5 minutes is not enough for nucleation of ZIFs [Zn(Im)$_2$]. After comparing the PXRD pattern of S2 with the simulated ones from other polymorphs (60), sample S2 is assigned as mixed crystal phases of ZIF-4 in **cag** topology and one with **coi** topology, here denoted as ZIF-coi (CCDC code: EQOCOC) (Figure 3-2b) (63). With further increase of the synthesis time, pure crystalline phases of ZIFs [Zn(Im)$_2$] were obtained. Specifically, the crystal identities of S3-S5 are assigned as ZIF-zec (HICGEG), ZIF-nog (HIFWAV), and ZIF-zni, corresponding to the synthesis time of 18, 24, and 120 hours, respectively. The ^{1}H liquid-state NMR spectra of ZIF-zec and ZIF-nog crystals were also measured to verify the imidazolate ligand, as shown in Figure 3-12a. It is worth to note that ZIF-zni has been proved to process the most stable structure in thermodynamics in ZIF family (64).

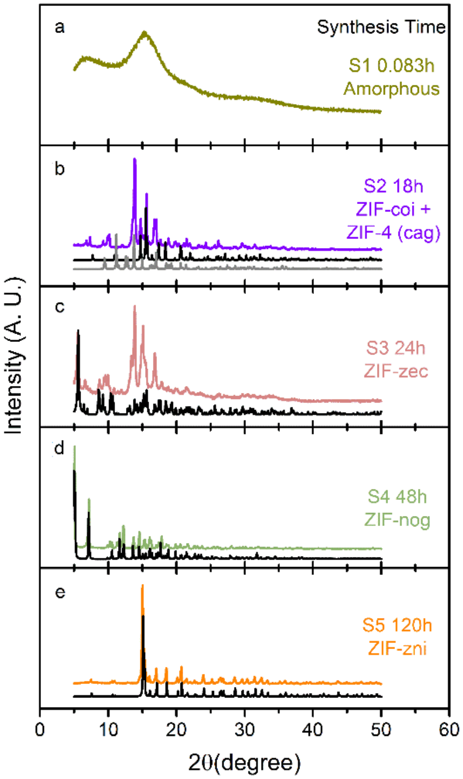

Figure 3-2 Experimental PXRD patterns of the samples S1-S5 obtained after different synthesis time, and the corresponding simulated spectra (black). Synthesis durations: (a) 0.083 h; (b) 18 h; (c) 24 h; (d) 48 h; and (e) 120 h.

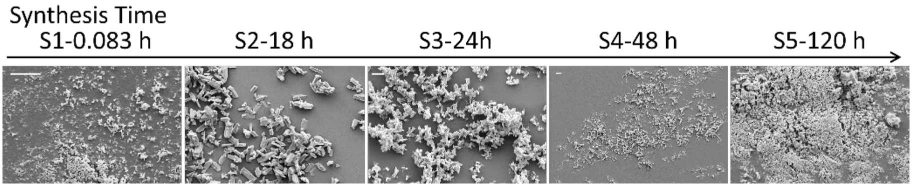

Figure 3-3 SEM micrographs of S1-S5 from left to right. Scale bar: 10 µm.

Crystal morphologies of S1-S5 were then characterized by SEM micrographs (Figure 3-3). Particles of S1 are ill defined, with an average size smaller than 1 µm. On the other hand, the micrographs of other samples show clear edges and planes, verifying their crystalline features. Specifically, S2 shows a rod-like morphology with particle size range of 5~20 µm. The morphology of S3 demonstrates an agglomerated feature with an ortahedral-like shape, and the particle size is around 2-5 µm. S4 presents a needle-like shape, which accords well with the simulated morphology from Mercury

3.9 package in terms of its cif file (63). When the synthesis time reaches to 120 hours, the ZIF-zni shows an aggregated morphology composed by granual-like particles, with the size of 5~10 μm.

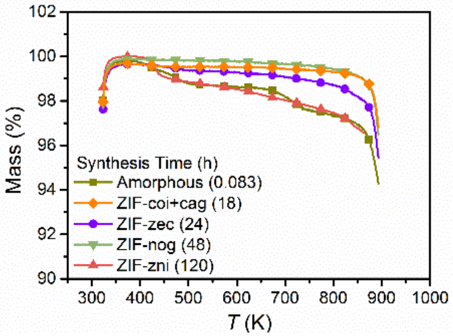

Figure 3-4 Thermogravimetric analysis of samples S1-S5.

Moreover, thermogravimetric measurements of samples S1-S5 were conducted (Figure 3-4). All samples show very small changes of mass (< 3 %) upon heating, before their decomposition temperature at $T_d \approx 863$ K (593 ˚C). This correlates well with the T_ds of other two $Zn(Im)_2$ polymorphs (ZIF-4 and ZIF-gis) in literature (10). Comparably, ZIFs obtained from solvothermal method normally show a ~10 % mass loss due to the loss of solvent from the framework voids (mostly DMF) when heating up to ~200 ˚C, even though the samples were evacuated in vacuum at 100 ˚C for 24 hours. This suggests that the ZIF-$Zn(Im)_2$ polymorphs synthesized via solution mixing method are easily activated for potential applications, such as gas absorption.

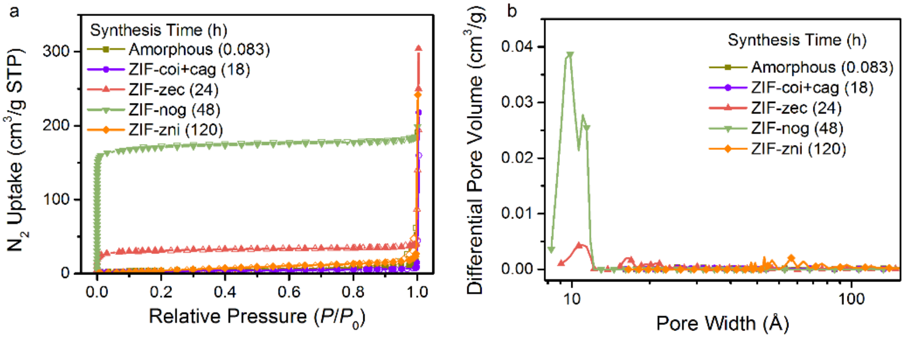

Figure 3-5 N_2 absorption-desorption isotherms of samples S1-S5 synthesized for different durations (a) Solid symbols: Absorption; Open symbols: Desorption. (b) Pore size distribution.

N_2 absorption-desorption isotherms were conducted on samples S1-S5 in Figure 3-5, Specific surface area (BET method) was obtained as illustrated in Table 3-2. N_2 update isotherms of all samples show a typical type-I behaviour. The pure crystalline phases of ZIF-zec and ZIF-nog have relatively high specific surface area, whereas the other three samples show quite low porosities in Figure 3-5a. Note that ZIF-4 has a BET surface area of 300 $m^2 g^{-1}$ (65). Pore distributions were also presented in Figure 3-5b. S1, S2, and S5 samples show low amount of pore volume. On the country, pore size of both ZIF-zec and ZIF-nog was mostly distributed to be around 1 nm, indicating the micro porous feature of both crystals. Density measurements of all samples were also carried out via a gas pycnometer using helium (Table 3-2). The densities of S1-S4 are similar, while the most densified ZIF-zni phase was confirmed with the highest density.

Table 3-2 Specific surface area (BET method), pore volume, N_2 uptakes (at $P/P_0=0.9$), and densities of samples S1-S5. The brackets give the standard error of the density from 10 cycle measurements.

Sample No.	Crystal phase	Surface area /$m^2 g^{-1}$	Micropore volume /$cm^3 g^{-1}$	N_2 uptake /$cm^3 g^{-1}$ (STP)	Density / $g cm^{-3}$
S1	Amorphous	16	0.012	9	1.648(8)
S2	ZIF-coi+ ZIF-cag	13	0.009	6	1.630(6)
S3	ZIF-zec	107	0.051	35	1.631(3)
S4	ZIF-nog	571	0.229	179	1.608(10)
S5	ZIF-zni	23	0.024	15	1.673(8)

Figure 3-2 to Figure 3-5 demonstrate that synthesis time has a significant influence on the crystal identity and formation of ZIFs with $Zn(Im)_2$ composition. The phase evolution of $Zn(Im)_2$ polymorphs with synthesis time can be explained by connecting the Ostwald's rule of stages (66): The least stable crystals form at the beginning, and then transform to metastable and stable polymorphs gradually with synthesis time.

3.1.2. SYNTHESIS TEMPERATURE INFLUENCE

Kinetic influence of the crystal formation of ZIF-$Zn(Im)_2$ has been investigated by changing the synthesis time. In contrast, thermodynamic effects on the polymorphs are explored via altering the synthesis temperature. ZIF-zec was considered to be kinetically stable since it is the first synthesized monocrystalline sample when prolonging the synthesis time. Here the temperature influence on the product of ZIFs $Zn(Im)_2$ was investigated with regard to the ZIF-zec formation.

By controlling the synthesis temperature from 15 to 35 °C for the same synthesis duration of 24 hours, samples S6-S9 were obtained (Table 3-1). Note that the boiling point of n-propylamine is 47.8 C, and the synthesis lasted for 24 hours, therefore the synthesis temperature was not raised above 35 °C for safety reasons. PXRD patterns of samples S6-S9 and S3 are presented in Figure 3-6, which are also associated with the simulated pattern of ZIF-zec. However, the relative intensities of the Bragg peaks of the experimental patterns show a small difference from the simulated PXRD pattern of the ZIF-zec phase. In specific, the relative intensity ratios of the strongest peak at $2\theta = 5.57^\circ$ associated with the (1 1 0) plane (*d-spacing* = 15.79 Å) to other Bragg peaks are lower than the expected value. This difference is ascribed to the preferred orientation during crystal nucleation under the solvent mixing synthesis, as well as the apparatus parameters during the data collections, such as Lorentz–polarization factor. Therefore structure refinements are required to study the differences of the crystalline structure of the samples obtained under different synthesis temperature.

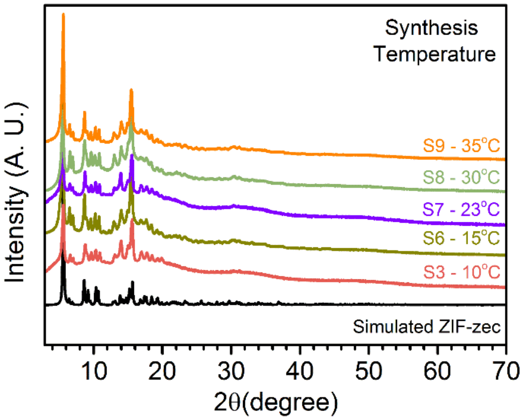

Figure 3-6 PXRD patterns of samples S3 and S6-S9 obtained at different temperature for 24 hours. Simulated XRD pattern of ZIF-zec is also shown in black.

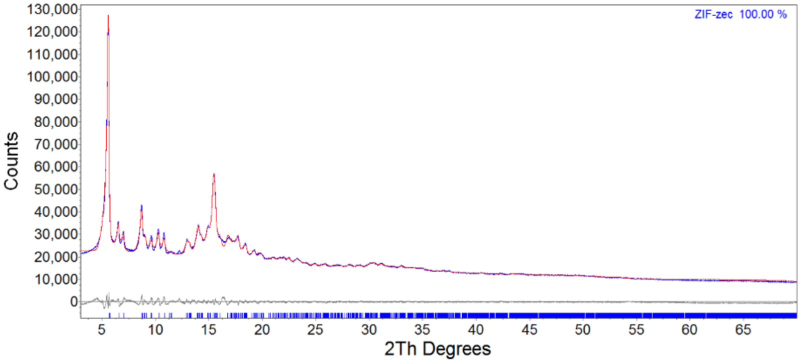

Figure 3-7 Rietveld refinement of the PXRD pattern of S6.

To reveal the crystalline structure difference of S3, S6-S9, Rietveld refinements were applied to the PXRD patterns with regard to the ZIF-zec phase. It has to be clarified that the relevant figures and results in Paper I were implemented in Pawley method.

Here the PXRD results in Figure 3-6 were collected specifically for Rietveld refinements in this section. The data were accumulated in the 2θ range of 3° to 70° using a step size of 0.013° with a dwell time of 360 s per step. With this condition, the intensity of the strongest peak was > 100000 counts (Figure 3-7). The refinement details are given in Section 2.2.2, and the refined parameters of the PXRD patterns are illustrated in Table 3-3. All R-factor values (weighted profile R-factor (R_{wp}), profile R-factor (R_{p}), Bragg R-factor (R_{Bragg}), and goodness of fit (χ^2) are small enough to show the good refinements of the PXRD patterns and their crystal identity of the ZIF-zec phase. The errors of the refined parameters (estimated standard deviations (ESD)) are also illustrated in Table 3-3, which are directly calculated from the program based on the inverted least-squares matrix.

Table 3-3 Refinement parameters of PXRD patterns of S3, S6-S9. Space group: C2/c. Values in brackets give the estimated standard deviations (ESDs) from the refinements.

Sample No.	3	6	7	8	9
a /Å	36.623 (46)	37.052 (67)	37.346 (57)	36.181 (55)	37.032 (75)
b /Å	19.829 (29)	19.523 (15)	19.422 (32)	19.436 (29)	19.517 (15)
c /Å	25.168 (27)	25.182 (11)	25.123 (16)	24.997 (31)	25.273 (10)
β /°	132.05 (16)	132.71 (11)	132.74 (12)	132.47 (5)	132.66 (15)
R_{wp} /%	4.20	5.75	6.12	6.66	5.68
R_{p} /%	3.28	3.90	4.36	5.06	3.90
R_{Bragg} /%	2.00	1.68	3.70	4.13	1.81
χ^2	2.77	3.72	4.04	4.24	3.76
Crystal size L_{vol} /nm	35(18)	30.2 (41)	47(18)	12.8(27)	46(17)
Cell volume/Å^3	13571 (54)	13385 (35)	13383 (41)	12966 (34)	13433 (43)
T/V /nm^{-3}	2.95	2.99	2.99	3.08	2.98

Moreover, peak shapes are assumed to be in both Lorentzian and Gaussian convolutions, and thus the peak profile were refined using the modified Thompson-Cox-Hastings Pseudo-Voigt model (PV_TCHZ peak type in TOPAS). Taken the pattern of sample S6 in Figure 3-7 as an example, a number of refinements are carried out with regard to the appropriate specimen broadening factors, including crystallite size broadening and microstrain broadening. The results indicate that, when only the size broadening factor is taken into account, the refinement yields the lowest R_{Bragg} factor, and the R_{p} factor shows weak dependence during these trials (3.87~4.04). Therefore the refinements here do not include the strain broadening factor but the size broadening one, and the crystallite sizes of the samples are obtained after refinements. Due to the anisotropic morphology of the ZIF-zec crystallite ($a \approx 1.9c$), the Scherrer approach would overestimate the crystallite size by applying the FWHM of the Bragg peaks. Alternatively, the crystallite sizes are thus determined by using the Stokes and Wilson method, i.e., the integral breadth based L_{vol} (volume weighted mean column heights). The crystallite sizes and the refined errors in Table 3-3 show that S8 has the smallest mean crystallite size.

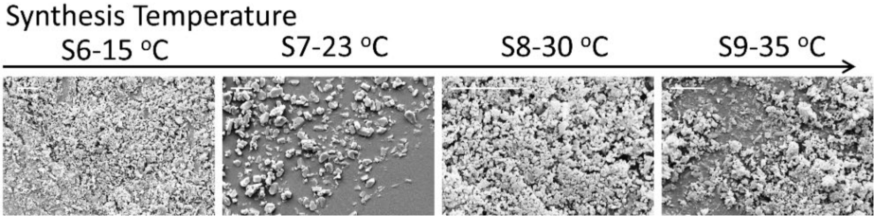

Figure 3-8 SEM micrographs of S6-S9 from left to right. Scale bar: 10 µm.

Crystal micrographs of S6-S9 are shown in Figure 3-8. Specifically, the micrographs of samples S6, S8, and S9, obtained at the synthesis temperature of 15, 30, and 35 ˚C respectively, exhibit aggregated phase composed by rice-like shaped particles, with the particle size of 2-5 µm. This morphology is similar to that of S3 synthesized at 10 ˚C (Figure 3-3). However, S7 (23 ˚C synthesis) demonstrates a brick-like morphology in a larger particle size (~5 µm) with no aggregation. It is worthy noting that the particle sizes observed from SEM micrographs are surely larger than the crystallite size determined from the refinements of the PXRD patterns. Although the correlation between characteristic size and synthesis temperature from either approach is slightly different, both results, however, indicates that the particle size and crystallite size of S7 are comparably larger. It shall be pointed out that although the mechanical stirring rate could significantly affect the crystal size, they normally show a positive correlation (67). As the stirring rates of all synthesis in the present work were controlled to be at 600 rpm, the crystal size dependence of stirring rate is not within our discussion.

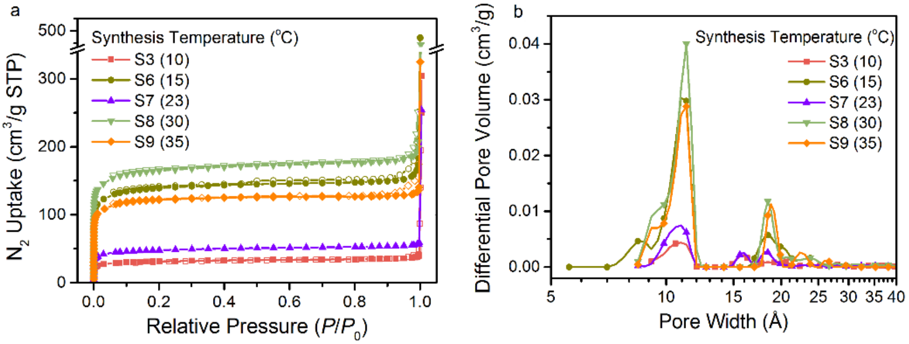

Figure 3-9 N_2 absorption-desorption isotherms of samples S3 and S6-S9 synthesized at different temperature. Solid and open symbols: Absorption and desorption, respectively. (b) Pore size distribution.

Porosities and pore size distributions of all ZIF-zec samples are studied by N_2 uptake measurements. Figure 3-9a shows that the N_2 uptake isotherms of all ZIF-zec samples demonstrate a type-I behaviour. Specific surface area from the BET method together with the micropore volume are derived (Table 3-4). All of the ZIF-zec samples have larger surface area compared to the S1, S2, and S5 samples. In all ZIF-zec samples, S8 obtained at 30 °C has the largest surface area (559 $m^2\ g^{-1}$), and S3 and S7 have relatively small surface area. Pore size distribution of the ZIF-zec samples are also derived from the N_2 absorption results (Figure 3-9b), where all samples have mesopores with the size of ~18 Å and micro pores at ~11 Å. However, S6, S8, and S9 samples have larger amount of the pore volume, compared to those of the other two samples. In addition, mesopores with the size of 16 Å are observed in S3 and S7 despite their low amount of the pore volume. Certainly, the distribution of the pore size and the amount of the pores in Figure 3-9b lead to the comparably small surface area of S3 and S7.

Table 3-4 Specific surface area (BET method), pore volume, N_2 uptakes (at P/P_0=0.9), and densities of all ZIF-zec samples.

Sample No.	Synthesis Temp/ °C	Surface area /$m^2\ g^{-1}$	Micropore volume /$cm^3\ g^{-1}$	N_2 uptake /$cm^3\ g^{-1}$ (STP)	Density / g cm^{-3}
S3	10	107	0.051	35	1.631(3)
S6	15	471	0.205	149	1.610(5)
S7	23	162	0.073	54	1.612(6)
S8	30	559	0.249	179	1.607(6)
S9	35	410	0.178	127	1.601(3)

Figures 3-5 and 3-9 show that ZIF-nog (S4) and a ZIF-zec sample (S8) have the surface area of > 500 $m^2\ g^{-1}$, larger than that of ZIF-4 (300 $m^2\ g^{-1}$) (65). Hence the ZIF-nog and ZIF-zec have potentials for gas absorption in ZIFs $Zn(Im)_2$, although the synthesis conditions need to be well controlled as presented in the current work.

Figure 3-10a summarizes the crystal phase of the $Zn(Im)_2$ products synthesized at different time and temperature in the present work. ZIF-zec and ZIF-nog were obtained after prolonging the synthesis time, meaning that both phases are more thermodynamically stable than ZIF-cag (ZIF-4). This can be related to the framework density (FD, T/V), which is the number of tetrahedral (T) per volume (V). As illustrated in Table 3-3, ZIF-zec has T/V values in range of 2.95~3.08 nm^{-3}, while ZIF-nog and ZIF-zni show the T/V values of 3.49 and 4.63 nm^{-3}, respectively (Figure 3-10b). The T/V results of each phase in the current work are also comparable to the ones from the corresponding cif files (see arrows in Figure 3-10b). The higher the FD is, the more stable the framework is in the thermodynamic viewpoint. Therefore the result of this phase evolution in Figure 3-10 is consistent with the Ostwald's rule of stages (66).s

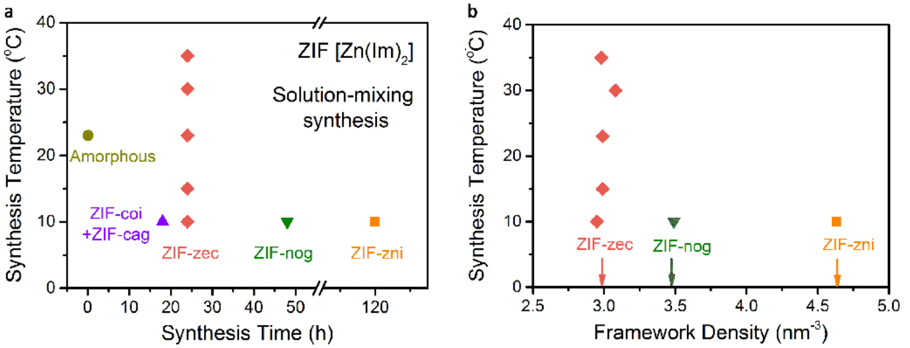

Figure 3-10 (a) Summary of crystal phases of synthesized for different time and at different temperature. (b) Framework densities (FD, T/V) of the polymorphic ZIFs from Table 3-3. The arrows give the FD of the corresponding crystals in literature (60).

3.2. GLASS FORMATION OF ZIF-ZEC AND ZIF-NOG

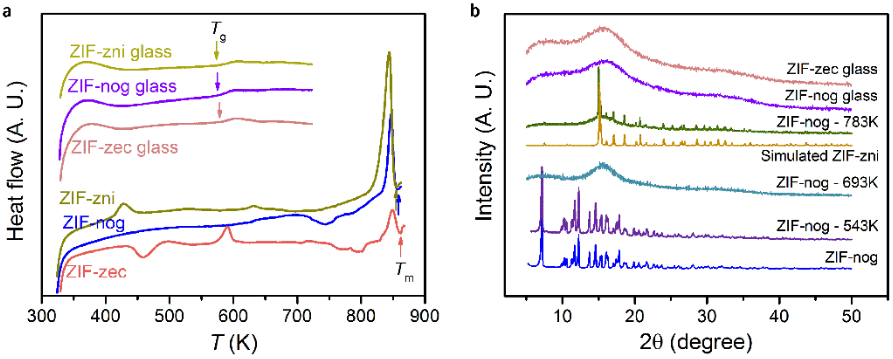

Figure 3-11 (a) Heat flow of the crystals and glasses of ZIF-nog, ZIF-zec (S8) and ZIF-zni; (b) PXRD patterns of ZIF-nog annealed at different temperature, ZIF-nog glass, ZIF-zec glass, and simulated XRD patterns of ZIF-nog and ZIF-zni.

Glass forming ability of the product with pure crystal phases, i.e., ZIF-zec, ZIF-nog, and ZIF-zni, was studied with various characterization methods. Figure 3-11 shows the DSC-TGA and PXRD results of the three crystals. All of them show a melting behaviour at ~855 K (~582 ℃) upon heating, indicated by the end-set points of the endothermic peaks on the DSC upscans. During heating, both ZIF-nog and ZIF-zec first become amorphous at 693 K, and recrystallize to ZIF-zni at 783 K. Hence the melting peaks on the DSC upscans result from the melting of ZIF-zni, the same as the cases in ZIF-4 and ZIF-gis (6,9). After melt-quenched from 863 K, MOF glasses of

$Zn(Im)_2$ were obtained, as verified by the broad hump without any Bragg diffraction peak on the PXRD patterns and by the glass transition peaks on the DSC upscans.

Table 3-5 Melting (T_m) and glass transition (T_g) temperature of the ZIF $Zn(Im)_2$ isomorphs, together with crystal porosity, the enthalpy of recrystallization (ΔH_{rc}) and the heat of fusion (ΔH_f) of the ZIF crystals.

Sample	Porosity /%	T_m /K	T_g /K	T_g/T_m	ΔH_{rc} / J g^{-1}	ΔH_f / J g^{-1}
ZIF-zec	35.8	858	578	0.674	12.88	12.16
ZIF-nog	24.6	853	575	0.674	21.26	21.91
ZIF-zni	8.8	851	575	0.676	-	65.27

Characteristic thermodynamic values derived from the DSC upscans are illustrated in Table 3-5. Since the melting peaks are actually attributed to the ZIF-zni phase, the three samples show similar melting temperature (T_m) and glass transition temperature (T_g). The exothermic area related to the recrystallization of ZIF-zec and ZIF-nog has been integrated to determine the enthalpy change during recrystallization (ΔH_{rc}), which is compared with the heat of fusion (ΔH_f) during melting. The ΔH_{rc} values of ZIF-zec and ZIF-nog are consistent well with the corresponding ΔH_f. Their small ΔH_f values compared to that of ZIF-zni suggest that ZIF-zec and ZIF-nog are not fully recrystallized to ZIF-zni upon heating, and hence less energy is required for melting.

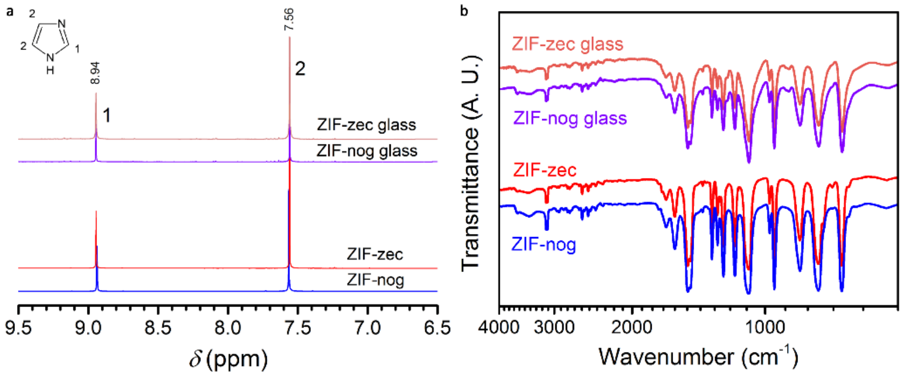

Figure 3-12 (a) Liquid-state ^1H NMR spectra and (b) FT-IR spectra of crystalline and glassy ZIF-nog and ZIF-zec.

Structural features of the amorphous ZIF-nog and ZIF-zec are investigated by comparing to the crystalline ones, as characterized by liquid-state ^{1}H NMR spectroscopy and FT-IR spectroscopy (Figure 3-12). As for the local environment around *H* from the imidazolate, the peak positions of the ZIF-zec and ZIF-nog glasses are the same as those of the crystals in the NMR spectra. Both samples show downfield resonance peaks at 8.94 and 7.56 ppm, corresponding to the *NC**H**N* and *NC**H**C**H*** on the aromatic ring, respectively. The integration of the peak area of Peak

1 and **2** gives the value in range of 1:(1.96~2.05), suggesting that the imidazolate ring remains intact after amorphization. Note that the solid-state NMR spectra are certainly better for characterizing the structure of the local environment of specific elements. It is however unpractical in the case of investigating glassy ZIFs, as the solid-state NMR measurements require a considerable amount of sample (500~1000 mg) to achieve a good collection. On the other hand, only 5~20 mg sample digested in solvent is enough for the liquid-state NMR measurements. Moreover, the liquid-state NMR spectra normally have a high resolution for quantification in a short time for measurements. It is thus commonly used for characterizing the local structure in MOFs or ZIFs in literature (9,45,52–55).

FT-IR spectra of the crystalline and glassy ZIF-nog and ZIF-zec show characteristic peaks in range of 1800~600 cm^{-1}, mostly coming from the change of dipole moment due to the vibration of the imidazolate ring. The peak positions are almost the same between the crystals and the glasses. The ratios between the peak intensities, however, show a small difference, which is attributed to the vibrational energy level changes from crystals to melt-quenched glasses, corresponding to vibrations of bending and stretching of the imidazole ring.

3.3. SUMMARY

In this Chapter, the influence of synthesis time and temperature on the crystal formation of ZIFs with the $Zn(Im)_2$ composition was systematically investigated using the solution mixing method. The results show that the crystal phases transform from a mixed phase to pure phases with more densed packing by prolonging the synthesis time. This phase evolution follows the Ostwald's rule of stages. ZIF-zec, ZIF-nog, and ZIF-zni are proved to be kinetically stable. Considering the thermodynamic effects on the crystal formation, synthesis at variable temperature was also conducted based on the process to obtain ZIF-zec phase. The characterization results demonstrate that the crystal identity (confirmed by Rietveld refinements) is not sensitive to the temperature, but the crystal morphologies and porosities are strongly affected. ZIF-zec and ZIF-nog shows a relatively high surface area compared to the ZIF-4 with **cag** topology.

Glass formation study on the ZIF-zec and ZIF-nog shows that both go through amorphization, recrystallization and melting upon heating, and they can be melt-quenched to MOF glasses as the case of ZIF-4. Structural features between the crystals and glasses are characterized by liquid-state ^1H NMR and FT-IR spectroscopy. The results indicate that the structures of both glasses heritage the crystalline ones, perhaps due to the remaining intact imidazolate ring after vitrification.

CHAPTER 4. ENTHALPY RELAXATION IN ZIF-62 GLASS

Thermodynamic and dynamic behaviours of amorphous materials are intrinsic physical properties and have connections with their structures and functionalities. As a new branch of glass, MOF glasses are rarely investigated in terms of structural relaxation, especially on the dynamic behaviour. Structural relaxation, as one of the universal dynamic features of amorphous materials, helps to physically understand glass transition and structural evolution, and the features can be connected to their macroscopic properties (68–70). Although it is easy to probe the relaxation behaviour in organic molecules and ionic liquid with dielectric spectroscopy, dynamic relaxations in other amorphous materials could be hard to detect in experiments. General approaches for studying relaxation, such as dielectric spectroscopy and dynamic mechanical spectroscopy, cannot be applied to the relaxation study on MOF glasses due to the limitation of their yield and detective temperature range. Alternatively, calorimetry for quantifying enthalpy relaxation in glasses does not require the materials to be a bulk size or a specific fluid state. In light of this, thermodynamic features of a MOF glass former were investigated regarding the theories of chemical thermodynamics, and deeply explored the enthalpy relaxation of a MOF glass. ZIF-62 [$Zn(Im)_{1.75}(bIm)_{0.25}$] (Im = imidazolate, $C_3H_3N_2^-$; bIm= benzimidazolate, $C_7H_5N_2^-$) was chosen due to its high glass forming ability (10,38) [2].

4.1. GLASS TRANSITION IN ZIF-62

Crystalline and glass ZIF-62 were characterized by PXRD and DSC as shown in Figure 4-1. The crystal structure of ZIF-62 was verified by matching the PXRD pattern with the simulated one (44). After quenching the melt from 753 K with a cooling rate of 10 K min^{-1}, ZIF-62 glass was obtained, which is denoted as a_gZIF-62 by following the nomenclature in literature (27). The PXRD pattern of the a_gZIF-62 shows a hump at a *d*-spacing of 5.9 Å ($2\theta \approx 15^\circ$), confirming its glassy nature.

DSC upscan of the crystalline ZIF-62 shows an endothermic peak at 540 K together with a mass decrease of ~13.1 %, which is ascribed to the DMF loss from the framework voids. A melting endothermic peak is observed with further heating, giving a melting point (T_m) at 711 K. The glass transition peak, with an onset temperature of T_g = 593 K (320 °C), is prominent on the upscan curve of the a_gZIF-62.

---

[2] Results in this chapter have been published in Paper II.

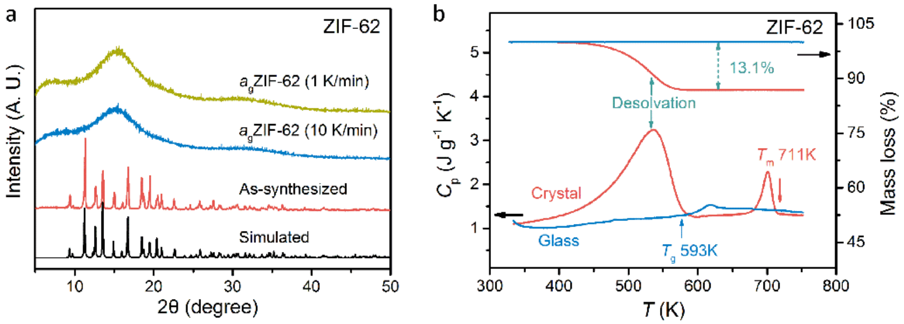

Figure 4-1 (a) PXRD of the simulated and as-synthesized crystalline ZIF-62, and a$_g$*ZIF-62 with different cooling rates. (b) Temperature dependence of* C_p *and mass loss of crystalline and glass ZIF-62 upon heating, shown as red and blue curves, respectively.*

Unlike metallic glasses with similar temperature range of T_g, in which exothermic peaks assigned as recrystallization are normally observed upon heating, a_gZIF-62 does not have a recrystallization process before its decomposition. To investigate its thermal stability against recrystallization, an a_gZIF-62 sample was heated to 658 K above its T_g and annealed for 12 hours, followed by a slow cooling rate (1 K min^{-1}) to room temperature. Bragg peak is not observed in the corresponding PXRD pattern (Figure 4-1a), confirming its high thermal stability. This high thermal stability is attributed to the high steric hindrance of its liquid structure (38). In particular, the liquid state of ZIFs has been proved to contain mostly interconnected $Zn(Im)_x$ (x = 3 or 4) species, leading to extremely sluggish diffusion kinetics given the size of the imidazolate ligand. The high steric hindrance is connected to a high energy barrier for nucleation, resulting in the enhancement of the glass stability against crystallization.

4.2. THERMODYNAMIC FEATURES OF ZIF-62

Classical thermodynamic theory was applied to study the thermodynamic feature of ZIF-62 crystal and melt. According to Kubaschewski (71), the temperature dependence of C_p of a supercooled liquid and that of the crystal can be described by the following power law:

$$C_p^{sl}(T) = 3R + a * T + b * T^{-2}, \qquad 4\text{-}1$$

$$C_p^{x}(T) = 3R + c * T + d * T^{2}, \qquad 4\text{-}2$$

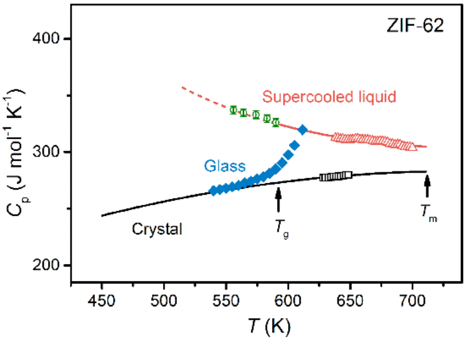

Figure 4-2 Temperature dependence of the heat capacity in supercooled liquid, glass and crystalline states of ZIF-62, shown as red line (Eq. 4-1), blue diamond points and black line (Eq. 4-2), respectively. The green circles are the heat capacity in supercooled liquid obtained from the enthalpy relaxation results.

Here a, b, c, and d are the fitting parameters, and R is the gas constant. After converting the unit of $C_p(T)$ to J mol^{-1} K^{-1} by using its molar mass (184.0 g mol^{-1}), the $C_p^{sl}(T)$ and $C_p^{x}(T)$ dependence on temperature are obtained by fitting to Eqs. 4-1 and 4-2, with the fitting parameters as follows: $a = 0.2396$ (± 0.0035) J mol^{-1} K^{-2}, $b = 5.531$ (± 0.105) $\times 10^7$ J K mol^{-1}, $c = 0.7000$ (± 0.0016) J mol^{-1} K^{-2} and $d = -4.744$ (± 0.025) $\times 10^{-4}$ J mol^{-1} K^{-3} (Figure 4-2). The difference in C_p between supercooled liquid and crystal of ZIF-62 at T_g, i.e., $C_{p_x}^{sl}\Big|_{T_g}$, is obtained as 51.5 J mol^{-1} K^{-1}. This value is smaller than those of most molecular and oxide glasses, but larger than those of alloys (72,73).

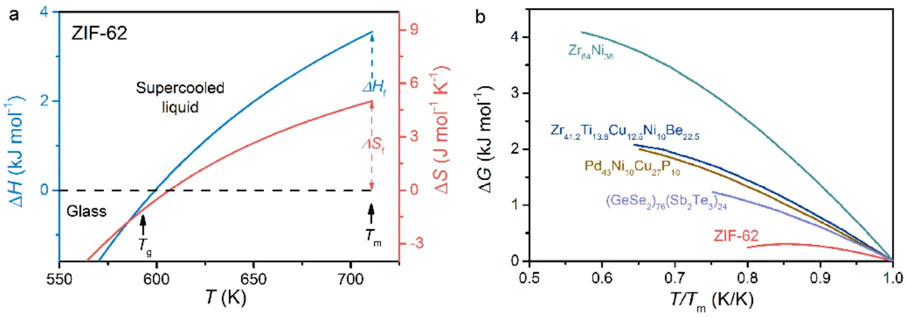

Figure 4-3 (a) $\Delta H^{sl-x}(T)$ and $\Delta S^{sl-x}(T)$ of ZIF-62. (b) $\Delta G^{sl-x}(T)$ of ZIF-62, together with the data of some alloys from literature (74–76).

By integrating the area of the melting peak, the enthalpy of fusion (ΔH_f) is determined as 3.566 kJ mol^{-1}, which is smaller than other zeolites and ZIFs (62,64,77). The entropy of fusion is also derived as $\Delta S_f = \Delta H_f / T_m = 5.015$ J mol^{-1} K^{-1}. Therefore, the differences in enthalpy (ΔH^{sl-x}) and entropy (ΔS^{sl-x}) between the supercooled liquid and crystal of ZIF-62 are obtained according to the following equations:

$$\Delta H^{sl-x}(T) = \Delta H_f - \int_T^{T_{liq}} \Delta C_p^{sl-x}(T')dT', \qquad 4\text{-}3$$

$$\Delta S^{sl-x}(T) = \Delta S_f - \int_T^{T_{liq}} \frac{\Delta C_p^{sl-x}(T')}{T'} dT'. \qquad 4\text{-}4$$

The fitted curves of ΔH^{sl-x} and ΔS^{sl-x} are shown in **Error! Reference source not found.**a. The Gibbs free energy difference between the supercooled liquid and crystals $\Delta G^{sl-x}(T)$ is hence determined by Eq. 4-5:

$$\Delta G^{sl-x}(T) = \Delta H^{sl-x}(T) - T * \Delta S^{sl-x}(T). \qquad 4\text{-}5$$

As shown in Figure 4-3b, the ΔG^{sl-x} increases with decreasing temperature below T_m, implying the recrystallization of a_gZIF-62 could spontaneously occur theoretically. Some $\Delta G^{sl-x}(T)$ data of other alloys from literature were also given for comparison in Figure 4-3b. Apparently the ΔG^{sl-x} of ZIF-62 liquid shows a quite weak dependence with temperature. This result explains that the recrystallization of a_gZIF-62 could be only achieved by an extremely low cooling rate from the ZIF-62 melt during cooling. The small $\Delta G^{sl-x}(T)$ values of ZIF-62 indicate the low driving force of nucleation in terms of thermodynamic factors and further confirm its high stability against crystallization.

In addition, Eqs. 4-1 ~ 4-5 can be discussed on a per atom basis. Each ZIF-62 molecule is regarded as 18.5 atoms based on its composition. The C_p value at T_g is ~15.6 J g-atom^{-1} K^{-1}, which is within the Dulong-Petit regime at high temperature (78,79). The obtained $\Delta G^{sl-x}(T)$ determined on a per atom basis shows very small values, as shown in Figure S2 in Paper II. However, this quantification is not appropriate in ZIF-62. The reason is that the aromatic rings in the organic linker in ZIF-62 are not destroyed after melting or vitrification, hence they cannot be treated as separate and harmonic atoms contributing to the heat capacity entirely. It is the same as the analysis on a per building unit basis as presented in Figure S3 in Paper II, where the three building units per molecule refer to the metallic node (Zn^{2+}) and the two organic ligands. After making these comparisons, the analysis in terms of thermodynamic mechanisms was rationally carried out on a per mol basis in this section.

4.3. ENTHALPY RELAXATION IN *A*GZIF-62

The enthalpy relaxation behaviour of a_gZIF-62 was studied by performing sub-T_g annealing in argon atmosphere at temperatures (T_a) between 553 and 587 K, i.e., 0.93 ~ 0.99 T_g. Figure 4-4 shows the C_p *vs.* T curves of ZIF-62 glass preheated at T_a = 559 K for various durations (t_a). With the increase of t_a, the overshoot of the glass transition peak becomes prominent, and the width of the peak broadens gradually. The onset T_g shows weak independence with t_a, indicating that only α relaxation was involved during annealing, whilst other relaxation processes, such as slow β relaxation, did not contribute to the difference in the thermal response during the subsequent DSC upscans after preheating with different t_a (80,81). In terms of the potential energy landscape (PEL), the configurational energy state of the annealed glass drops into a local minima with low configurational entropies (82). During reheating, an energy barrier needs to be overcome to return to the energy state corresponding to the standard glass (70), resulting in the overshoot of glass transition on the heat capacity curve. Moreover, the overshoot area increases with the annealing time t_a. This can be interpreted as a longer t_a leads to a lower energy minima during annealing, and also a larger energy recovered upon reheating, giving the larger overshoot area.

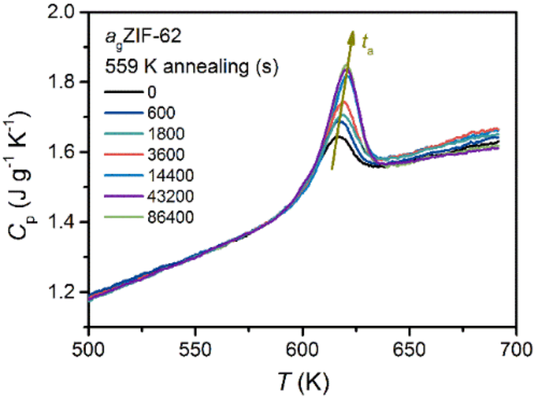

Figure 4-4 Temperature dependence of C_p of a_gZIF-62 annealed at 559 K for different durations t_a (in seconds).

The recovered enthalpy $\Delta H(T_a, t_a)$ is quantitatively determined by difference of the area of the glass transition peaks on C_p curves between the samples with a dwell time and the ones with no duration (t_a=0). At each annealing temperature, t_a has been increased up to 24 hours. The $\Delta H(T_a, t_a)$ values at each T_a are calculated as shown in Figure 4-5. The recovered enthalpy decreases with T_a for a certain t_a, and increases with t_a for a given T_a.

The enthalpy relaxation of glasses can be described by the non-exponential Kohlrausch-Williams-Watts (KWW) function according to the literature (83,84):

$$\varphi(t) = exp\left[-\left(\frac{t_a}{\tau_a}\right)^{\beta}\right] = \frac{\Delta H(T_a,\infty - t_a)}{\Delta H_{eq}(T_a,\infty)}, \qquad 4\text{-}6$$

where t_a is the annealing time, τ_a is the characteristic relaxation time at T_a, and β is the stretching exponent. Thus the $\Delta H(T_a, t_a)$ is described as:

$$\Delta H(T_a, t_a) = \Delta H_{eq}(T_a, \infty)\left\{1 - exp\left[-\left(\frac{t_a}{\tau_a}\right)^{\beta}\right]\right\}. \qquad 4\text{-}7$$

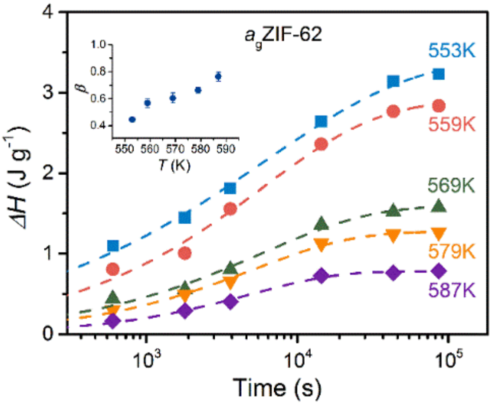

Figure 4-5 The recovered enthalpy (ΔH(T_a, t_a)) of a_gZIF-62 after annealing at different temperatures and time. Dashed lines: the fitted curves via Eq. 4-7. Inset: T_a dependence of β.

By inputting the $\Delta H(T_a, t_a)$ and t_a at each T_a to Eq. 4-7, the relaxation time τ_a, the stretching exponent β, and the $\Delta H_{eq}(T_a,\infty)$ can be derived (Table 4-1). The $\Delta H_{eq}(T_a,\infty)$ shows a negative trend with T_a as expected. This tendency demonstrates the glass gradually relaxed to the energy state of the standard glass with T_a in the vicinity of T_g (70,82). In addition, using the interpolation method, the C_p^{sl} at the $T = (T_{a1}+T_{a2})/2$ can be derived from the two $\Delta H_{eq}(T_a)$ values. The calculated $C_p^{sl}(T)$ values from the enthalpy relaxation are presented as green points in (Figure 4-2). All points agree well with the $C_p^{sl}(T)$ calculated from Eq. 4-1.

Table 4-1 Fitting parameters and standard errors from Eq. 4-7 in Figure 4-5.

T_a/K	$\Delta H_{eq}(T_a)$/J g^{-1}	τ_a /s	β
553	3.405 ± 0.121	6125 ± 393	0.444 ± 0.017
559	2.886 ± 0.108	5937 ± 378	0.567 ± 0.031
569	1.590 ± 0.061	5842 ± 379	0.604 ± 0.037
579	1.272 ± 0.024	5114 ± 160	0.662 ± 0.023
587	0.781 ± 0.017	4880 ± 170	0.763 ± 0.033

The relaxation time τ_a and the stretching exponent β are further discussed (Table 4-1). τ_a decreases with higher annealing temperature, which is attributed to the narrower energy barrier between the annealed glass a higher T_a and the standard glass (80). In contrast, according to the definition of glass transition, the relaxation time of T_g (593 K) is ~100 seconds. The results of Figure 4-1b derive this value to be 228 seconds from the width of the glass transition peak and the upscan rate (($T_{g,end}$-$T_{g,onset}$)/R_h). That is, the average relaxation time τ_a declines gradually with 5000 seconds in the sub-T_g temperature region, and drops dramatically to hundreds of seconds at T_g. It is not feasible to fit the τ_a vs. T_a via the Arrhenius equation for a_gZIF-62 because of its non-linear relationship, although this equation is commonly used to obtain the activation energy of the glass transition in literature. The long relaxation time τ_a in a_gZIF-62 can be ascribed to a high degree of dynamic heterogeneity as reported in (85). It is worth noting that some researchers explained the physical meaning of the fitted parameters (86,87). The τ_a shall be denoted as the characteristic relaxation time of the probability distribution τ^*, modified with a gamma function (fractional) function (87,88). With this modification, the relaxation time parameter τ at certain temperature could be much larger when β --> 0. However, as this parameter is constant and depends the β, it is difficult to add this modified parameter to fit the experimental data by the KWW equation. Hence, the τ^* is normally approximated as τ_a in literature (89–91,85,92).

Table 4-2 The glass transition temperature T_g, liquid fragility m, and the stretched exponent β from the KWW equation (Eq. 4-7) for different ranges of T_a/T_g.

Composition	T_g/K	Fragility	T_a/T_g range	β	Refs.
$La_{55}Al_{25}Ni_{10}Cu_{10}$	454	35	0.91-0.98	0.75-0.79	(93,94)
$Pd_{43}Ni_{10}Cu_{27}P_{20}$	576	65	0.97-0.99	0.68-0.75	(74)
ZIF-62	593	35	0.93-0.99	0.44-0.76	This work
$Zr_{58.5}Cu_{15.6}Ni_{12.8}$ $-Al_{10.3}Nb_{2.8}$	668	50	0.95-0.99	0.79-0.89	(95,96)
$Zr_{55}Cu_{30}Ni_5Al_{10}$	676	69	0.95-0.99	0.71-0.79	(97)
$Zr_{45}Cu_{39.3}Al_7Ag_{8.7}$	688	-	0.94-0.99	0.72-0.89	(83)
GeO_2	792	17-20	0.71-0.91	0.59-0.61	(80)

The stretching exponent β reflects the distribution width of the relaxation time, which normally ranges from 0 to 1. A smaller β corresponds to a wider distribution. Here the β value of a_gZIF-62 ranges from 0.44 to 0.76, corresponding to the annealing temperature T_a from 0.93T_g to 0.99T_g (Table 4-1). If extending the β to T_g in a linear relation, it would be almost at 1, which is an indicative of a strong liquid in terms of liquid fragility (Figure 4-5inset) (84,95,98). Table 4-2 summarizes the β values in the range of sub-T_g of a number of glass formers with similar T_g range to a_gZIF-62, which are also obtained from enthalpy relaxation. The fragility indices (m) and T_a ranges relative to T_g are also illustrated. The broad range of β of a_gZIF-62 suggests that this MOF glass is sensitive to T_a and exhibits strong dynamic heterogeneity. Based on an empirical correlation among β', m and the width of the typical glass transition peak from heat flow scan: $\Delta T_g/T_g = 2.20 \times (1/m + 0.0026) \times (1/\beta' - 0.59)$ (10,99), the β' of a_gZIF-62 is calculated to be 0.69. This value is comparable to that of a_TZIF-4 (β' = 0.71) (100). It is worth noting that this β' is derived from the non-liner Tool-Narayanaswamy-Moynihan-Hodge model but not from the currently used non-exponential KWW model. However, the consistency of the *β'* of a_TZIF-4 and a_gZIF-62 indicates a typical dynamic feature of MOF glasses.

4.4. STRUCTURAL FEATURES AFTER RELAXATION

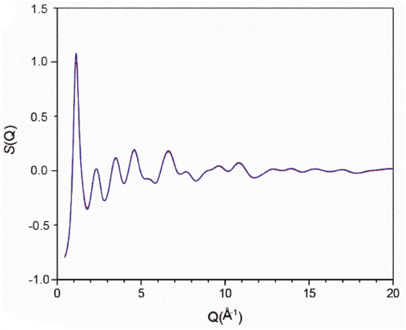

Figure 4-6 Structure factors S(Q) of a_g*ZIF-62 after melt quenching (red), annealing at 553 K with no duration (*t_a*=0) (purple), and annealing at 553 K for 72 hours (blue).*

To further reveal the structural changes during sub-T_g relaxation, X-ray total scattering measurements were conducted in Diamond Light Source, Didcot, UK. Three samples: an as-quenched a_gZIF-62 sample, an annealed sample with no duration a_gZIF-62 (553 K, 0 hour), and a fully-relaxed sample a_gZIF-62 (553 K, 72 hours) were selected for structural studies. Structural factors *S*(Q) of all three samples shows no Bragg peaks in Figure 4-6, verifying their amorphous features. The position of the first sharp diffraction peak at Q ~1.10 Å^{-1} remains invariant. Other than that, the spectra exhibit almost identical patterns giving us no more different information between the samples.

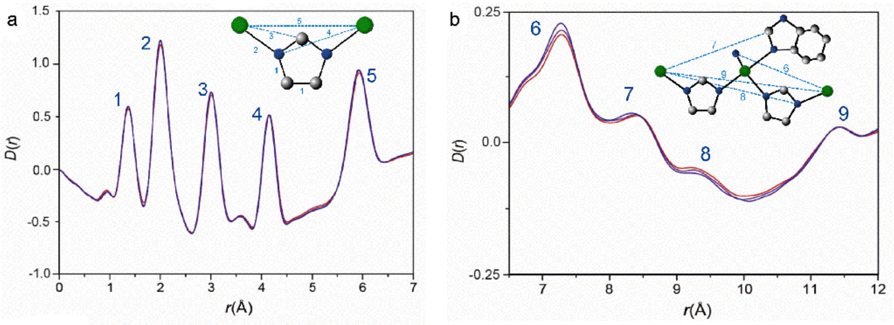

Figure 4-7 Corresponding pair distribution functions D(r) in the regions (a) 0 Å < r < 7 Å and (b) 6.5 Å < r < 12 Å.

Moreover, pair distribution functions (PDFs) *D*(r) of the samples are achieved by converting from total scattering data via Fourier transformation, as shown in Figure

4-7. In short range order 0-6 Å, the intra-organic and metal-linker-melt bonding does not show changes after annealing, consistent with the reported PDF results of crystalline ZIF-62 (10). In particular, the peaks at 1.3 Å and 2.0 Å, corresponding to C-C/C-N and Zn-N correlations, respectively, remain unchanged with sub-T_g annealing. As for the medium range order between 6-12 Å corresponding to the inter-linker bond connections, the PDFs are more featureless as general. Although the peaks 6-8 exhibit left shift, the tiny changes are attributed to the densification after annealing. Overall, no significant change of the glass structure is observed after sub-T_g annealing according to the PDF results of a_gZIF-62. This observation can be connected with its ultrahigh viscosity in liquid state and highly heterogeneous structure, which also coincides with the broad β range in Figure 4-5.

4.5. SUMMARY

In this Chapter, the enthalpy relaxation behavior of ZIF-62 glass was investigated. The small difference of the Gibbs free energy ΔG^{sl-x} indicates of a low driving force for nucleation in terms of thermodynamics. From the enthalpy relaxation measurements in T_a ranges of (0.93~0.99)T_g, the average relaxation time in the vicinity of T_g is ~5000 seconds, and the stretching exponent β ranges from 0.44 to 0.76, of which both suggest it a high degree of dynamic heterogeneity. Comparing the structures of as-quenched a_gZIF-62 with the ones after sub-T_g relaxation by PDF analysis, no significant change is detected.

CHAPTER 5. GLASS FORMING ABILITY OF MOFS

As melt-quenched MOF glasses are a new family of glassy materials, only tens of different kinds of MOF glasses have been reported until now. They were mostly discovered in ZIFs with the network structure analogous to silica (6,10). Exploring new amorphous and glassy MOFs would help to understand their physical properties, and further develop new frameworks and improve their functionalities. In light of the limited number of MOF glass formers, it is still difficult to describe the general mechanisms and glass forming ability of MOFs. An empirical rule to obtain MOF glasses via melt-quenching is to lower the melting point (T_m) than the decomposition temperature (T_d). For example, it has been achieved by inducing the secondary organic linker (10). This is attributed to the induced defects into MOFs to result in disorder structure. Other MOFs or coordination polymers (CPs) were also reported, including a series of CPs with phosphate anions and a number of ionic liquids (13,15). In literature, thermal stability of MOFs was mostly characterized only by thermogravimetric analysis. In other words, other phase transformations with no mass changes, such as melting behaviour, were not detected and considered. Hence, thermal stability and glass forming ability of most MOFs needs to be reconsidered.

Motivated by exploring more MOF glass formers and probing the relation between the amorphous structures and properties, glass forming ability of some candidates was investigated by calorimetric and thermogravimetric measurements in this Chapter. In particular, a melting process combined with an endothermic thermal response is highly expected prior to the decomposition upon heating. If so, an amorphous structure with a glass transition peak on its DSC upscan could verify a melt-quenched MOF. It shall be pointed out that with regard to the nomenclature of the MOF glasses, the names refer to the parent crystal structures from which the glasses originated [3].

5.1. GLASS FORMING ABILITY OF SOME MOFS

5.1.1. ZIF-11 & ZIF-12

ZIF-4 [Zn(Im)$_2$] and ZIF-62 [Zn(Im)$_{1.75}$(bIm)$_{0.25}$] (Im = imidazolate, $C_3H_3N_2^-$; bIm= benzimidazolate, $C_7H_5N_2^-$) have been manifested to have good glass forming ability, hence the contribution of bIm in the framework to the glass formation is considered. ZIF-7 [Zn(bIm)$_2$] in $R\overline{3}$ space group and **sod** (sodalite) topology has been investigated

---

[3] Results in 5.2 were included in Papers IV. The results in 5.3 were mostly measured and all analyzed independently by the author, and the manuscript regarding to this work will be submitted for publication in the near future.

by *in situ* PXRD measurements. It exhibited a reversible polymorphization at 500 ˚C in CO_2 or N_2 with no amorphization (101). Although ZIF-7 cannot form MOF glass via thermal activation and shows no melting, ZIF-11, with the same composition but in the $Pm\bar{3}m$ space group and **rho** topology, has a lower framework density (T/V=2.02) than ZIF-7 (T/V=2.49). That is, the metallic center Zn^{2+} and organic linker bIm is loosely packed in ZIF-11. It implies the susceptibility of having defects in the crystalline structure and thus higher possibility to become a disorder structure upon heating. Based on these reasons, ZIF-11 and ZIF-12 (the same structure but with Co^{2+} as the metal center) are synthesized and their thermodynamic properties are probed.

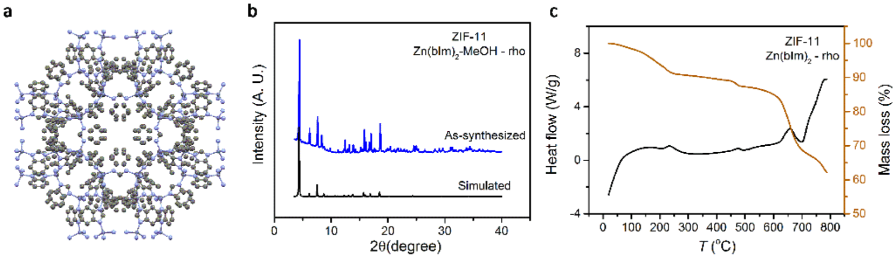

Figure 5-1 (a) Unit cell of ZIF-11 from the direction of b axis. Gray: C; Light blue: N; Dark blue: Zn. H atoms are omitted for clarity. (b) PXRD patterns of the as-synthesized and simulated ZIF-11. (c) DSC-TGA upscan curves of the as-synthesized ZIF-11.

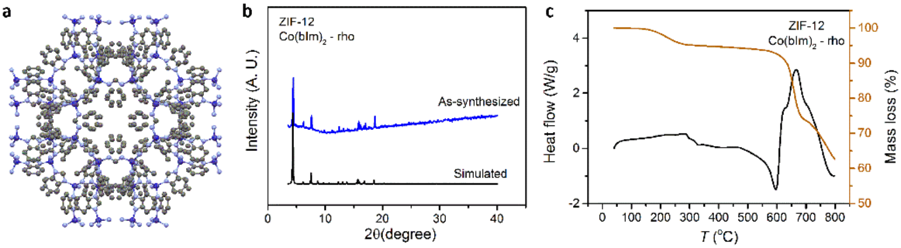

Figure 5-2 (a) Unit cell of ZIF-12 from the direction of b axis. Gray: C; Light blue: N; Dark blue: Co. H atoms are omitted for clarity. (b) PXRD patterns of the as-synthesized and simulated ZIF-12. (c) DSC-TGA upscan curves of the as-synthesized ZIF-12.

Figures 5-1 and 5-2 show the characterization results of ZIF-11 and ZIF-12, respectively. The PXRD patterns verify their structures by matching with the simulated ones. The simultaneous DSC-TGA results show that melting behaviour with noticeable exothermic peak and no mass change was not detected prior to their decomposition with significant mass loss at T_d~620 ˚C upon heating. It is worth noting that except for the desolvation peaks at ~220 ˚C, the bumps on the heat flow curve are attributed to the mass loss of the frameworks as the unit of heat flow is W g^{-1}.The T_ds of ZIF-11 and ZIF-12 are higher than most ZIFs. The high thermal stability of both structures is ascribed to the flexibility of both imidazolate and phenyl ring, and the rigid spatial hindrance of the organic linker. The results indicate that ZIF-11 and

ZIF-12 cannot be melted and thus cannot form MOF glasses, at least at ambient pressure in argon.

5.1.2. ZIF-71 & MCIF-1

A recent paper described the melting mechanism in ZIF-4 that in a short time scale, the Zn-N bond in the tetrahedral structure shows fluctuations, breakage, and reformation between the Zn center and N from other imidazolate rings (11). It is feasible to tune the electronic environment around the N atoms and thus affect the bonding energy of Zn-N, in order to detect the melting process. This can be obtained by controlling the structure of the aromatic ring with various kinds of chemical groups. Some groups such as $-CH_3$ on imidazole have studied in ZIF-8 (9). Here the effects of -CN and -Cl groups on melting are discussed in two frameworks, which are denoted as ZIF-71 and MCIF-1, respectively(40,102,103).

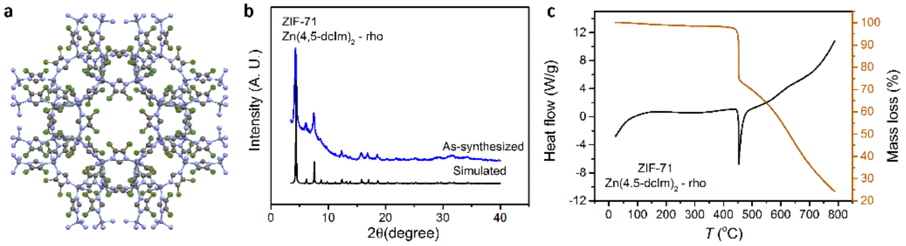

Figure 5-3 (a) Unit cell of ZIF-71 from the direction of b axis. Gray: C; Light blue: N; Green: Cl; Dark blue: Zn. H atoms are omitted for clarity. (b) PXRD patterns of the as-synthesized and simulated ZIF-71. (c) DSC-TGA upscan curves of the as-synthesized ZIF-71.

ZIF-71 $[Zn(dcIm)_2]$ shares the same topology and space group with ZIF-11. It was synthesized with a good yield (86 %), and the crystal phase was verified by PXRD pattern in Figure 5-3. DSC-TGA results show no mass loss or heat flow peaks during upscan before its decomposition at ~450 ˚C, suggesting its good thermal stability. No melting occurs in ZIF-71, ZIF-11 and ZIF-12 upon heating, implying that ZIFs with the **rho** topology could be difficult to be melted.

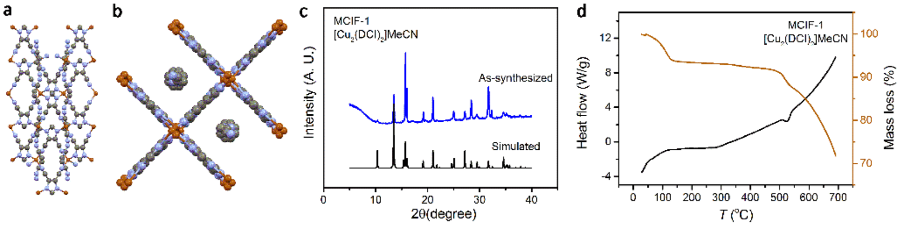

Figure 5-4 Unit cell of MCIF-1 from the direction of a axis (a) and c axis (b). Gray: C; Blue: N; Red: Cu. H atoms are omitted for clarity. (c) PXRD patterns of the as-synthesized and simulated MCIF-1. (d) DSC-TGA upscan curves of the as-synthesized MCIF-1.

MCIF-1 [$Cu_2(DCI)_2 \cdot MeCN$] (DCI: 4,5-dicyanoimidazolate), owing the structure in the $I4_122$ space group and simplified as (4, 4)-connected **pts** topology, was a recently reported metal cyanoimidazole framework (MCIF) by Zhao *et al.*, (103). This framework is successfully synthesized (Figure 5-4), yet the yield is quite low rather than a promising large scale as reported in literature. Thermodynamically speaking, a mass loss is detected at ~80 °C due to the desolvation of acetonitrile, and other signals related to possible phase transformations are not observed upon heating until the decomposition at ~500 °C. Although CN^- is a weak conjugate base and is expected to be less influential than Cl^- on the local electron environment, the N_{Im}-Cu-$N_{CN\text{-}group}$ bonds are coordinated in MCIF-1, which somehow stabilizes the framework. The results of MCIF-1 in Figure 5-4 suggest the -CN group may contribute more to the coordination of the topology than to the effects of the local environment of the N atoms on the imidazolate ring, leading to good thermal stability and no melting process.

5.1.3. TIF-5-CL & JUC-160

Different from the results of MOFs with mono ligand in Sections 5.1.1 and 5.1.2, in this section, MOFs with secondary ligands are discussed with regard to their glass forming ability. As a comparable study, inducing bIm into Im in the frameworks leads to the structure of from ZIF-4 to ZIF-62. This secondary ligand is regarded as defects in the frameworks which lowers the melting point to be detected (10). Although there are many ZIFs with two organic linkers (60), some of them have been proved to be easily decomposed, especially ones containing nitroimidazolate ligand. Here two ZIFs with diplo ligands are chosen to investigate \their glass forming ability.

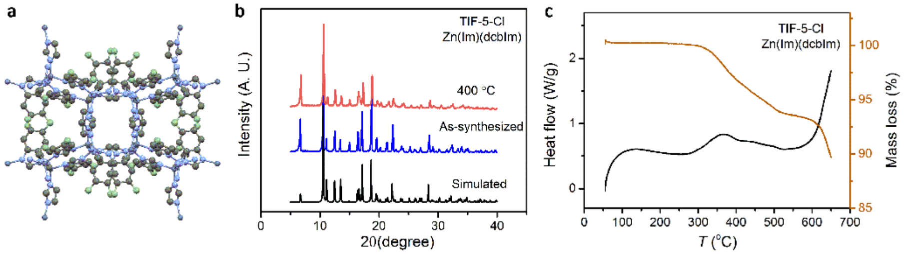

Figure 5-5 (a) Unit cell of TIF-5-Cl from the direction of b axis. Gray: C; Light blue: N; Green: Cl; Dark blue: Zn. H atoms are omitted for clarity. (b) PXRD patterns of the as-synthesized and simulated TIF-5-Cl, and one preheated at 400 °C. (c) DSC-TGA upscan curves of the as-synthesized TIF-5-Cl.

TIF-5-Cl [Zn(Im)(dcbIm)] was selected due to the similar composition of ZIF-62, with the dcbIm as the secondary organic linker to induce defects instead of bIm (63). Another reason is related to its structure in $I4_1/a$ space group and **gis** topology, the same as the glass former ZIF-gis (10). The structure was verified by the PXRD pattern Figure 5-5b. DSC-TGA measurements were conducted as shown in Figure 5-5c. The significant mass loss observed at ~620 °C results fom the decomposition. The reason of the gradual mass loss at 300 °C was not very clear. However, the PXRD pattern of a preheated sample to 400 °C exhibits no significant structural changes (Figure 5-5b), suggesting that the crystalline framework was intact after the mass loss. More experiments need to be carried out to investigate the structural changes during this temperature region, yet from the results in Figure 5-5, TIF-5-Cl can be confirmed as no melting behavior upon heating.

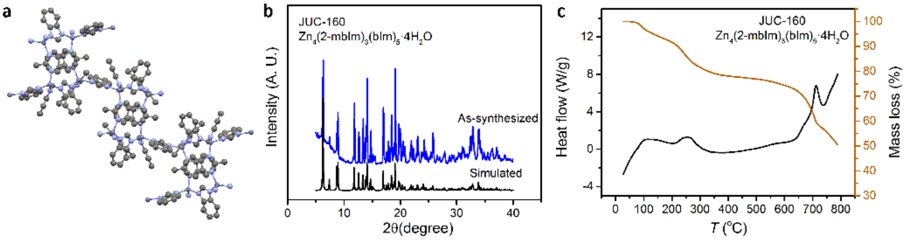

Figure 5-6 (a) Unit cell of JUC-160 from the direction of b axis. Gray: C; Light blue: N; Dark blue: Zn. H atoms are omitted for clarity. (b) PXRD patterns of the as-synthesized and simulated JUC-160. (c) DSC-TGA upscan curves of the as-synthesized JUC-160.

If the Im was considered as the secondary organic linker rather than bIm in ZIF-62, the Im can be replaced by other ligands, and thus the glass forming ability of the frameworks can be explored. JUC-160 $[Zn(2\text{-mbIm})_{0.75}(\text{bIm})_{1.25}]$, with 2-mbIm substitution of Im with regard to ZIF-62, was chosen as the candidate to study the glass forming ability (43). In addition, JUC-160 structurally shares the **gis** (gismondine) topology with ZIF-gis but it is in the *P*nma space group. The match of the PXRD pattern of JUC-160 with the simulated one confirms the crystalline structure. DSC-TGA results of JUC-160 show a mass loss owing to the release of solvents up to 280 °C. No more signal is detected upon heating before the decomposition at ~630 °C in argon. The results in Figures 5-5 and 5-6 indicate that the topology and secondary organic linkers as induced defects in MOFs might be not the critical aspect to dominate the melting behaviour. In contrast, compositions are suggested to be very influential on melting of MOFs.

5.1.4. ZTIF-1

Triazole or tetrazole is suggested to lower the melting point of MOFs as well (14). Therefore metal azolate frameworks (MAFs) and zeolitic tetrazolate-imidazolate frameworks (ZTIFs) are considered as good candidates to investigate their glass forming ability. Syntheses of several frameworks were tried including MAF-66 (or USTA-49), ZTIF-1, ZTIF-2, and ZTIF-6 based on the synthesis methods in literature (41,104–106). However, only ZTIF-1 crystals was obtained successfully after the second trial.

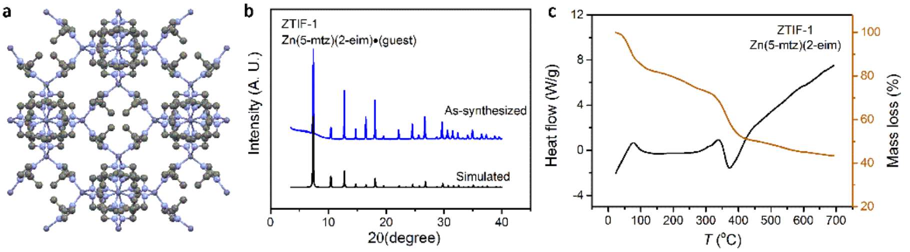

Figure 5-7 (a) Unit cell of ZTIF-1 from the direction of b axis. Gray: C; Light blue: N; Dark blue: Zn. H atoms are omitted for clarity. (b) PXRD patterns of the as-synthesized and simulated ZTIF-1. (c) DSC-TGA upscan curves of the as-synthesized ZTIF-1.

ZTIF-1 [Zn(5-mtz)(2-eIm)] is structurally in the $I\bar{4}3m$ space group and **sod** (sodalite) topology. The PXRD pattern verifies the crystalline structure (Figure 5-7). DSC-TGA upscans show a mass loss at 80 ˚C resulting from the removal of ethanol from the voids. The framework is stable with no visible decomposition feature when heating up to ~320 ˚C. Compared to other frameworks discussed in this Chapter, ZTIF-1 exhibits a weak thermal stability against decomposition. The bump of the DSC upscan curve at ~320 ˚C is ascribed to the significant effect of the mass loss rather than to a melting behaviour. Although the crystalline structure would change to mostly amorphous after preheated to 300 ˚C as suggested by PXRD results (41), the strongest diffraction peak at $2\theta \approx 7.39^\circ$ associated with the (1 1 0) plane remained there, manifesting its crystalline feature. Nevertheless, thermodynamic results on ZTIF-1 reveal no melting process upon heating at ambient pressure in argon.

5.2. GLASS FORMATION OF ZIF-76

5.2.1. GLASS FORMAITON OF ZIF-76

Inducing secondary ligand to increase the steric hindrance by congested bIm is suggested to lower the melting point in ZIF-62, while melting is not detected in TIF-5-Cl with 5,6-dcbIm and Im as ligands. Alternatively, an asymmetrical ligand - 5-chlorobenzimidazolate - is considered together with the parent Im ligand, and thus ZIF-76 [Zn(Im)(5-cbIm)] is developed for investigation of the glass forming ability. In addition, the crystalline structure of ZIF-76 has an **lta** (Linde Type A) topology with a very low framework density *T*/*V* of 1.03, implying the retention of the pores after amorphization.

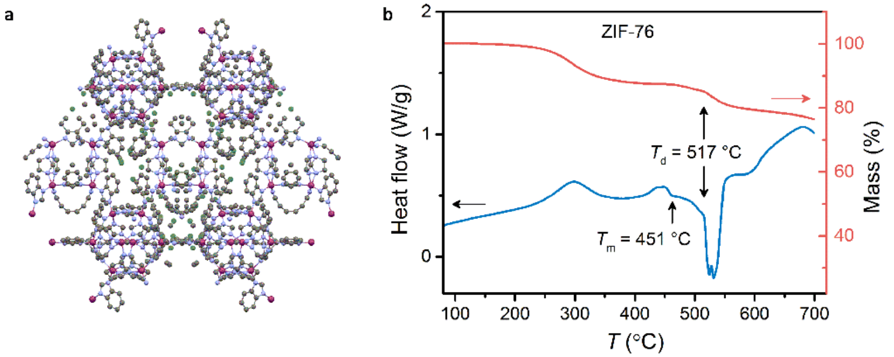

Figure 5-8 (a) Unit cell of ZIF-76 from the [1 0 1] orientation. Gray: C; Light blue: N; Green: Cl; Purple: Zn. H atoms are omitted for clarity. (b) DSC-TGA upscan curves of the as-synthesized ZIF-76.

The cystalline ZIF-76 was obtained as described in 2.1.9, and the structure is confirmed by PXRD results (Figure 5-9). The heat flow upscan of the crystalline ZIF-76 shows a melitng peak at 451 ˚C with the ΔH_f = 1.8 kJ mol^{-1} prior to the decomposition at 517 ˚C from the TGA trace (Figure 5-8). The PXRD pattern of the quenched ZIF-76 from the liquid state shows a hump at a *d*-spacing of 5.2 Å (2θ ≈ 17˚), confirming its amorphous nature (Figure 5-9a). The results manifest that ZIF-76 can be melt-quenched to a_gZIF-76. The DSC upscan of the glassy a_gZIF-76 shows a glass transition peak at T_g = 310 ˚C.

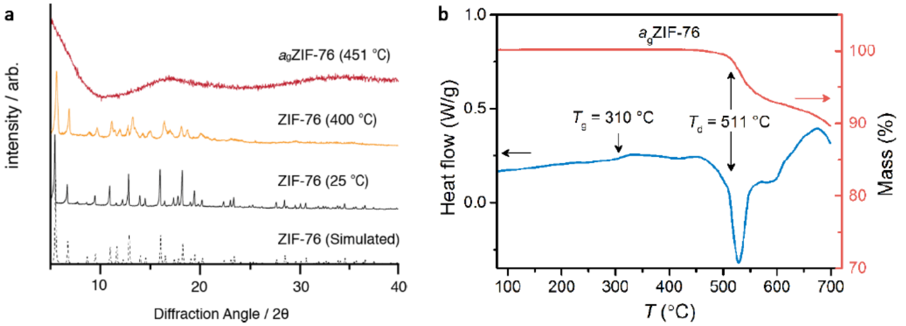

Figure 5-9 (a) PXRD patterns of the a_gZIF-76 and ones preheated at 400 ˚C and melting point (451 ˚C). (b) DSC-TGA upscan curves of the a_gZIF-76.

A ZIF-76 isomorph, ZIF-76-mbIm [Zn(Im)(5-mbIm)] (5-mbIm: 5-methylbenzimdazilate) was also investigated (45). The crystalline structure of ZIF-76-mbIm was confirmed, and DSC-TGA measurements were also carried out. Similar to the thermodynamic behaviour of ZIF-76, ZIF-76-mbIm also demonstrates a melting behaviour at T_m = 471 ˚C. DSC upscan curve of the melt-quenched a_gZIF-76-mbIm exhibits a glass transition peak at T_g = 317 ˚C.

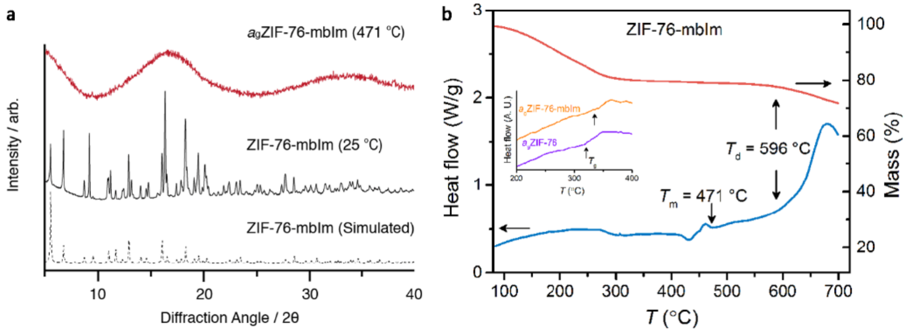

Figure 5-10 (a) PXRD patterns of the as-synthesized ZIF-76-mbIm and the one preheated at melting point (471 °C). (b) DSC-TGA upscan curves of the as-synthesized ZIF-76-mbIm. Inset: DSC upscans of a_gZIF-76 and a_gZIF-76-mbIm.

Table 5-1 Characteristic temperatures of crystalline and glassy ZIF-76 and ZIF-76-mbIm.

Sample	State	T_m /°C	T_d /°C	T_g /°C
ZIF-76	crystalline	451	517	-
a_gZIF-76	glass	-	511	310
ZIF-76-mbIm	crystalline	471	596	-
a_gZIF-76-mbIm	glass	-	590	317

The T_m, T_d and T_g of crystalline and glassy ZIF-76 and ZIF-76-mbIm are summarized in Table 5-1. The characteristic temperatures of ZIF-76-mbIm are all higher than those of the ZIF-76. It can be ascribed to the greater van der Waals radius of the methyl group than the -Cl which results in the stronger non-covalent interactions between the cbIm/mbIm and Im.

Structural features after vitrification of ZIF-76 and ZIF-76-mbIm were probed by ^{13}C magic angle spinning (MAS) NMR spectroscopy and synchrotron X-ray total scattering spectroscopy (Figures 2-3 in Paper IV and Figures S14-S18 in the SI). The signals from the ^{1}H and ^{13}C MAS NMR spectra in the crystalline samples match well with the positions expected from the chemical environments of their organic ligands. The spectra of the glassy samples are similar to those of their parent crystalline counterparts, indicating that the organic linkers remain intact after vitrification. 2D ^{1}H-^{13}C spin-diffusion NMR measurements in various mixing time were performed to detect the dynamic polarization transfer between protons in crystalline and glassy ZIF-76-mbIm. In brief, the rates of the polarization transfer through inter-linkers ($NC\boldsymbol{H}N_{\mathrm{Im}} \sim NCC\boldsymbol{H}_{3\ \mathrm{5\text{-}mbIm}}$) and intra-linker ($NC\boldsymbol{H}N_{\mathrm{5\text{-}mbIm}} \sim NCC\boldsymbol{H}_{3\ \mathrm{5\text{-}mbIm}}$) become faster after vitrification, demonstrating stronger chemical interactions between the different linkers and more prominent polarization between the 5-mbIm ligands. Moreover, the PDF results confirm the amorphous feature of a_gZIF-76 and a_gZIF-76-mbIm by showing featureless peaks in the range of $r > 6$ Å. The peak positions in the PDFs of the glasses in the range of $r = 0 \sim 6$ Å accord well with the ones from the corresponding crystals, indicating the consistent chemical composition before and after vitrification of ZIF-76 and ZIF-76-mbIm. More discussion can be referred to the context in Paper IV.

5.2.2. POROSITY

The porosities of the vitrified ZIF-76 and ZIF-76-mbIm are explored. Both crystals possess two cavities with the diameters of 5.7-5.8 Å and 15.6-15.7 Å, as detected by the positron annihilation lifetime spectroscopy (PALS) (Figure S19 in Paper IV) (31). After melt-quenched to glasses, the cavity of a_gZIF-76 only exhibits a single pore with the diameter of ~5 Å. Remarkably, the a_gZIF-76-mbIm retained two separate sizes of pores with the diameters of 4.8 Å and 7.2 Å (Figure S20 in Paper IV), respectively. This indicates that the a_gZIF-76-mbIm obtained directly from melt-quenching is more porous and could have the potential for gas absorption.

Table 5-2 Summary of the porous characteristics of ZIF-76, ZIF-76-mbIm and a_gZIF-76-mbIm. Surface area and pore volume are calculated from the NLDFT fitting of the CO_2 absorption isotherms.

	Temp/K	ZIF-76	ZIF-76-mbIm	a_gZIF-76-mbIm
H_2 uptake /cm^3 g^{-1}	77	187	130.5	-
N_2 uptake /cm^3 g^{-1}	77	338	339	-
CH_4 uptake /cm^3 g^{-1}	293	16.3	14.7	5.1
CO_2 uptake /cm^3 g^{-1}	273	59.9	54.4 (10 wt%)	(6.7 wt%)
Surface area /cm^2 g^{-1}	273	-	643	375
Pore volume /cm^3 g^{-1}	273	-	0.17	0.12

Diverse gas absorption isotherms on the crystals and glasses were carried out to analyse the porosities of the MOF glasses. The results are given in Figures 4 and S23-S34 in Paper IV, and some conclusive data are presented in Table 5-2. Both glasses show low uptakes of N_2, and a_gZIF-76-mbIm show a significant hysteresis uptake of H_2 (Figure S30 in Paper IV). Both phenomena indicate the restricted diffusion of the molecules, which is attributed to the constrictions of the dense framework after vitrification. However, both glasses, especially the a_gZIF-76-mbIm, yield good absorption of CO_2 (273 K) and CH_4 (293 K). a_gZIF-76 absorbed 4 wt% of CO_2 but with notable hysteresis upon desorption (Figure S29 in Paper IV). On the other hand, a_gZIF-76-mbIm reversibly absorbed 6.7 wt% CO_2 at 273 K and a pressure of 1 bar (Figure 4 in Paper IV). Although the surface area and CO_2 uptakes decline after vitrfication, it is rationally ascribed to the lower amount of pore volume in the glasses compared to the crystalline counterparts. Furthermore, the a_gZIF-76-mbIm also show a reversible absorption of CH_4 (Figure 4 in Paper IV). Regarding the large kinetic diameter of the CH_4 molecule (3.76 Å), the CO_2 and CH_4 absorption of the a_gZIF-76-

mbIm can be related to the retention of a number of pores in large sizes, as verified by the PALS results (7.2 Å, Figure S20 in Paper IV).

To sum up, ZIF-76 and the isomorph ZIF-76-mbIm are reported to be good MOF glass formers. The melt-quenched a_gZIF-76-mbIm shows permanently accessible porosity with reversible absorptions of guest molecules, such as CO_2 and CH_4. To clarify the contribution in Paper IV and this section, the author discovered the glass formation of ZIF-76 for the very first time. With this preliminary and crucial breakthrough, more observation, including the glass formation of ZIF-76-mbIm and the permanent accessible porosity in the glassy MOFs, are recognised. Except for the input of the manuscript of Paper IV, the author also joined in other experimental parts including the sample preparation for PDF measurements, data analysis of liquid ^{1}H NMR spectra, and nanoindentation measurements (not included in the manuscript).

5.3. PHASE TRANSFORMATION OF DUT-67

5.3.1. PHASE TRANSFORMATION OF DUT-67

Zirconium-based MOFs have attracted wide attentions due to their extraordinary properties for applications on catalysis, water absorption and electron conductivity (49,107,108). One of the well-studied Zr-based MOF is UiO-66 [$Zr_6O_4(OH)_4(bdc)_6$]. This framework can be easily synthesized with a high yield, possesses high porosity and thermal stability, and can be modified by other functional groups (109–112). A Zr-based MOF, DUT-67 [$Zr_6O_6(OH)_2(tdc)_4(Ac)_2$] (tdc: 2,5-thiophenedicarboxylate), showed high porosity and chemical resistance in acid, and catalytic capability after loading Pd (46,113,114). The building unit between Zr^{4+} and tdc^{2-} in DUT-67 exhibits an angle of 147.9°, which is reminiscent of the M-Im-M relationship with an angle of 145° in ZIFs and the Si-O-Si bond in silica. Moreover, the structure of DUT-67 is in $Fm\bar{3}m$ space group and a **reo** (ReO_3) topology, with a framework density of only T/V = 0.40, of which the value is distinctly smaller than ZIF-4 (3.68) and ZIF-76 (1.03). These features suggest this framework could be a good candidate of MOF glass former with accessible pores. In this section, structural and themodynamic features of DUT-67, together with the porosities, are investigated with the activation of temperature.

The framework was verified by the PXRD pattern Figure 5-11b. DSC-TGA measurements were performed, and the DUT-67 underwent solvent desolvation, an unknown phase transformation, and framework decomposition upon heating, corresponding to the Peak A, B, and C in Figure 5-11c, respectively. A mass loss of 2.5 %, associated with Peak A, is detected at ~200 °C due to the loss of water and DMF from the voids (113). The decomposition of the tdc linker as well as the framework is demonstrated at 350 °C (T_d), together with an increase of thermal response (Peak C).

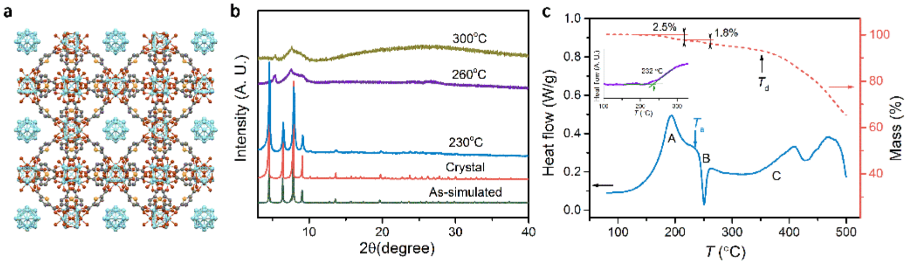

Figure 5-11 (a) Unit cell of DUT-67 from the direction of b axis. Gray: C; Yellow: S; Red: O; Light blue: Zr. H atoms are omitted for clarity. (b) PXRD patterns of the as-synthesized and simulated DUT-67, and ones heat-treated at 230 °C, 260 °C and 300 °C in argon. (c) DSC-TGA upscan curves of the as-synthesized DUT-67. Inset: DSC upscan after preheated at 260 °C.

Remarkably, the significant exothermic peak (Peak B) is observed between 230 and 260 °C on the DSC upscan curve. The slight mass loss at *ca*. 220 °C is attributed to the release of DMF and acetic acid according to the literature (46,113). Note that the hierarchical stages of mass loss can be normally observed in MOFs upon heating if more than two types of solvents are applied during MOF synthesis (10,105,106). PXRD measurements of preheated DUT-67 were carried out to reveal the structural changes during Peak B. The crystalline structure is retained at 230 °C. However, the Bragg peaks are mostly disappeared after pre-heated to 260 °C. At the same time, a number of notable Bragg peaks appear, which seem to be at the positions shifted to the higher angle side compared to the previous peak positions, together with a background of broad peak at $2\theta \approx 8°$. It is worthy noting that this PXRD pattern was repeated 5 times separately and the pattern is repeatable every time. Based on this PXRD pattern, the framework is expected to be mixed phases with (1) partially ordered structure (Bragg peaks) and (2) disordered amorphous structure. When the sample is preheated at 300 °C, the structure becomes more disordered and the sample starts decomposing (light-yellow color). The samples preheated at 230 and 260 °C are still in the form of white powder, similar to the as-synthesized crystals. Hereafter the sample preheated to 260 °C is referred to as DUT-67-HT, and the occurrence of the Peak B in Figure 5-11c was regarded as a phase transformation, which is further discussed in this section.

Refinements of PXRD patterns were carried out to discuss the structural changes further after the phase transformation. Rietveld refinement of the PXRD pattern of the as-synthesized crystal gives the lattice parameter a = 38.8953 (18) Å (R_{wp} = 4.48 %, R_{p} = 3.15 %, R_{Bragg} = 2.82 %, χ^2 = 3.72). This is associated with the a = 39.120 Å from the initial cif file. In light of the Bragg peaks of the DUT-67-HT, the PXRD pattern is refined using Le Bail method. The fit with the same space group ($Fm\bar{3}m$) as DUT-67 could yield a good fit (R_{wp} = 1.74 %, R_{p} = 1.38 %, χ^2 = 1.26) with a = 32.082 (17) Å. To be honest, as the $Fm\bar{3}m$ space group is highly symmetrical, the crystalline structure cannot be distinguishable from other Laue class such as $m\bar{3}$, especially in the cubic crystal system. More Le Bail refinements using structural models in lower symmetry crystal systems in the cubic class also give good fits with similar parameters (31.5~32.2 Å). Although other structural characterizations are required to fully understand the ordered structure of DUT-67-HT, the results of the structural refinements suggest the smaller domain size of the ordered structure after the phase transformation upon heating. On the other hand, a glass transition-like peak on DSC upscan trace of the DUT-67-HT was observed, with a characteristic temperature of 232 °C (Figure 5-11 inset). This result is comparable with the glass transition behaviour of other MOF glasses, verifying the disordered amorphous structure of the DUT-67-HT (10,115).

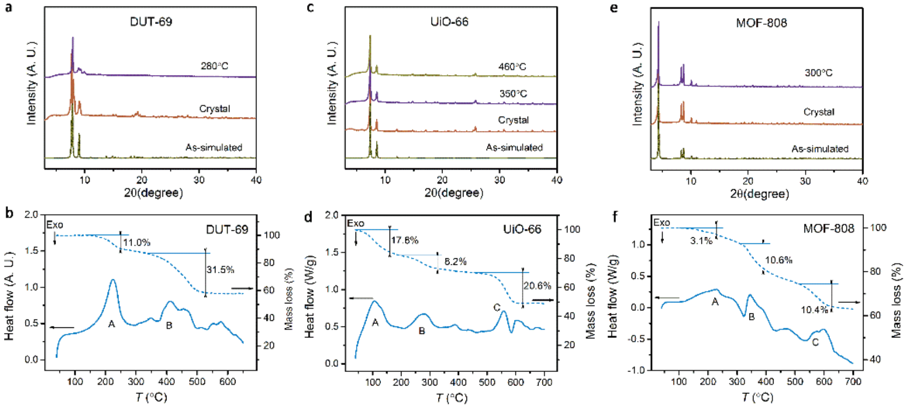

Figure 5-12 PXRD patterns of as-synthesized and simulated MOFs, and ones heat-treated at certain temperatures. (a) DUT-69, (c) UiO-66, and (e) MOF-808; DSC-TGA upscan curves of the as-synthesized (b) DUT-69, (d) UiO-66, and (f) MOF-808.

More syntheses and characterizations were conducted to discuss the universe of the phase transformation in DUT-67 in other Zr-based MOFs. Three more Zr-based MOFs were synthesized and characterized by PXRD and DSC-TGA (Figure 5-12). The synthesis details of DUT-69, UiO-66, and MOF-808 are given in 2.1.12~2.1.14. As a brief introduction, DUT-69 $[Zr_6O_4(OH)_4(tdc)_5(Ac)_2]$ has the same organic linker as DUT-67 (tdc), while this framework is in a orthorhombic crystal system (space group $P2_12_12_1$) with a **bct** topology (46). UiO-66 $[Zr_6O_4(OH)_4(bdc)_6]$ is one of the most investigated MOFs reported firstly in 2008 (107), of which the structure is in the $Fm\bar{3}m$ space group with a **fcu** topology. MOF-808 $[Zr_6O_4(OH)_4(btc)_2(Fa)_6]$ has a cubic structure in the $Fd\bar{3}m$ space group with a **spn** topology, and it possesses large pore sizes and high guest molecule uptakes in N_2 and water (49). The PXRD patterns in Figure 5-12 verify their crystal identity. Due to the thermal instability of the carboxyl group of the organic ligands (tdc, bdc, btc), all frameworks start to decompose at a lower temperature than ZIFs upon heating, as verified by the Peak B in Figure 5-12b, Peak C in Figure 5-12d, and Peaks B and C in Figure 5-12f on the DSC-TGA traces. All Peaks A are attributed to the solvent loss, as well as the Peak B in Figure 5-12d. To detect the structural changes after thermal-induced desolvation, each sample was preheated to a certain temperature before decomposition in argon, and afterwards PXRD patterns were collected to explore the structural changes. As shown in Figure 5-12, the crystalline structures are all preserved after pre-heated at >280 ˚C. That is, no thermal-driven phase transformation is observed before decomposition in the three Zr-based MOFs. It also manifests that the slight mass loss from the voids during heating does not prominently influence the structural identity in Zr-based MOFs. This comparable study indicates that the phase transformation observed in DUT-67 is a remarkable phenomenon, and it is not universal in other Zr-based MOFs.

5.3.2. STRUCTURAL FEATURES

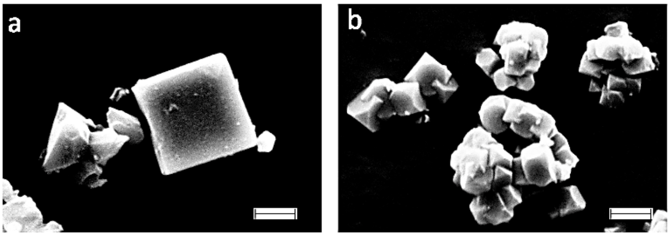

Figure 5-13 SEM micrographs of (a) DUT-67 and (b) DUT-67-HT. Scale bar: 2 µm.

Before presenting the the structural features of DUT-67 and DUT-67-HT, Figure 5-13 shows the morphology of both samples from the SEM measurements. The SEM image of DUT-67 shows clear edge and plane, which are associated with the crystalline morphology. As for the DUT-67-HT, most of the particles retain the clear planes, as an indicative of ordered or crystalline phase. The distinct feature of the DUT-67-HT morphology is that the small particles are keen to agglomerate together.

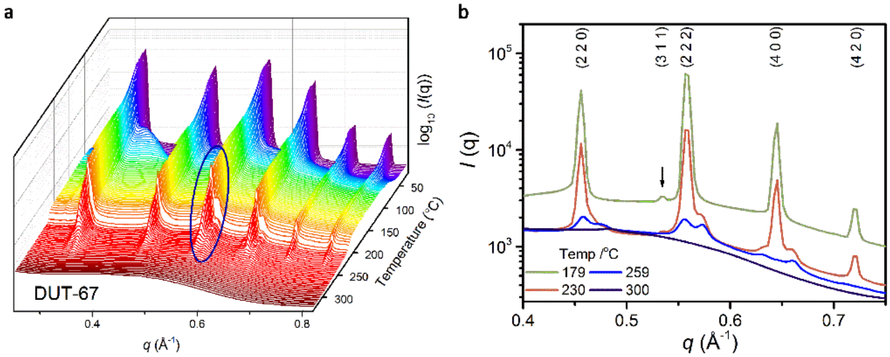

Figure 5-14 (a) In situ SAXS profile of DUT-67. (b) Some SAXS data at characteristic temperatures.

In situ small-angle X-ray scattering (SAXS) measurements were carried out to further study the structural evolution of DUT-67, and the (Figure 5-14). The structure is confirmed by the good refinement of the SAXS pattern at room temperature to the crystal structure of DUT-67. The miller indices of the diffraction peaks with strong intensities are assigned in Figure 5-14b. The peak intensity decreases gradually when heating up to 50 °C, which may result from the framework stabilization upon heating. The hump at $q \approx 0.4$ Å^{-1} gradually shifts to the right side upon heating, which can be related to the desolvation of water and DMF as the results in Figure 5-11b. The DUT-67 crystalline structure remains intact when heating up to ~220 °C. With further increasing the temperature from ~230 °C, the intensities of peaks corresponding to the original phase decrease significantly, whereas new Bragg peaks are notable next to the original peaks at a higher *q* side as an indicative of a ‘‘secondary’’ phase (Figure 5-14b). These peaks corresponding to the new phase are quite stable, such as the one with constant intensity at $q \approx 0.57$ Å^{-1} (Figure 5-14a). On the contrary, the gradual decrease of the peak intensities with temperature suggests the loss of the crystal symmetry of the preliminary DUT-67 phase. The structural changes with regard to the phase transformation are prominent at the peaks related to the planes of (2 2 0), (2 2 2), and (4 0 0) (Figure 5-14b). At 260 °C, both the preliminary phase and the new secondary phase exist. Continuous heating leads to the loss of the ordered structure of both phases. The sample at 325 °C shows no Bragg peaks, corresponding to the collapsed framework after decomposition. The SAXS results are conistent with the PXRD and DSC results in 5.3.1. According to the *in situ* SAXS results, the phase transformation from DUT-67 to DUT-67-HT can be related to the loss of the crystallinity of the preliminary DUT-67 phase and the formation of a secondary phase with smaller volume.

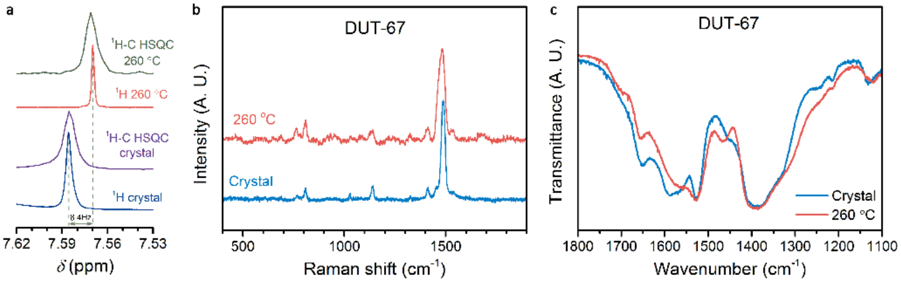

Figure 5-15 Comparison of the structure of DUT-67 and DUT-67-HT characterized by (a) ^{1}H *and* ^{1}H-^{13}C *HSQC liquid-state NMR, (b) Raman, and (c) FT-IR spectroscopy.*

Structural changes of the local chemical environment from DUT-67 to DUT-67-HT were investigated by NMR, Raman, and FT-IR spectroscopy (Figure 5-15). The ^{1}H liquid-state NMR spectrum of DUT-67 shows a strong signal at $\delta = 7.585$ ppm, which is assigned as the *SCC**H*** on the thiophene ring according to the literature (113). Except for signals from solvents (DMF and DCl), another signal at $\delta = 1.78$ ppm comes from the -$\boldsymbol{CH_3}$ in Ac. Both signal are also observed at the same position on the extracted ^{1}H

spectrum from the ^{1}H-^{13}C 2D HSQC NMR spectra. The data of DUT-67-HT shows that the peak related to the ***SCCH*** shifts to 7.57. This 8.4 Hz upfield shift indicates the weak deshielding effects of the thiophene ring on the protons in DUT-67-HT. Note that the ligands are intact after dissolving in the mixed solvent for NMR measurements; otherwise signals cannot be detected at this deshielding region.

Raman and FT-IR measurements of the two samples were also conducted, although the vibrational peaks from the same method are displayed more or less at same positions. The Raman shifts around 800 cm^{-1} are assigned as the vibration modes from the out-of-plane ring deformation, and the ones at 1150 and 1480 cm^{-1} are related to the C-C/C-S stretching and C-H bending (116). On the other hand, the broad peaks of FT-IR spectra in the range of 1700~1300 cm^{-1} are related to the vibrational modes of the stretches and bends in the thiophene ring (116). No significant difference of the peak positions on Raman and FT-IR spectra is observed after heating to 260 ˚C, while NMR results demonstrate weak deshielding effects of the tdc on the H atoms, indicating the alteration of the local electron environment of the thiophene ring.

5.3.3. THERMODYNAMICS

To further reveal this temperature-induced phase transformation in thermodynamic perspective, DSC upscans of DUT-67 annealed at different temperatures (T_as) were conducted (Figure 5-16a). The solvents of DMF and water are released after preheating to 195 ˚C. Annealing at 220 ˚C does not influence the exothermic response on the subsequent DSC upscan. A hump prior to the exothermic peak is noticed, probably due to the structural reformation prior to the phase transformation. With the T_as in the range of 230~260 ˚C, the exothermic peak area decreases gradually. The onset and peak temperatures also shift to lower temperatures with T_a. This indicates that the phase transformation happens at *ca.* 230 ˚C and completed at *ca.* 260 ˚C. Based on the structural results, the exothermic peak is attributed to the formation of both new secondary phase and the disordered structure from the preliminary DUT-67 phase. The heat flow response of the sample at T_a = 230 ˚C was almost symmetric, implying it a first-order transformation. DSC response is featureless with further annealing up to 300 ˚C. The results in Figure 5-16a also demonstrate that the thermal-induced phase transformation was irreversible.

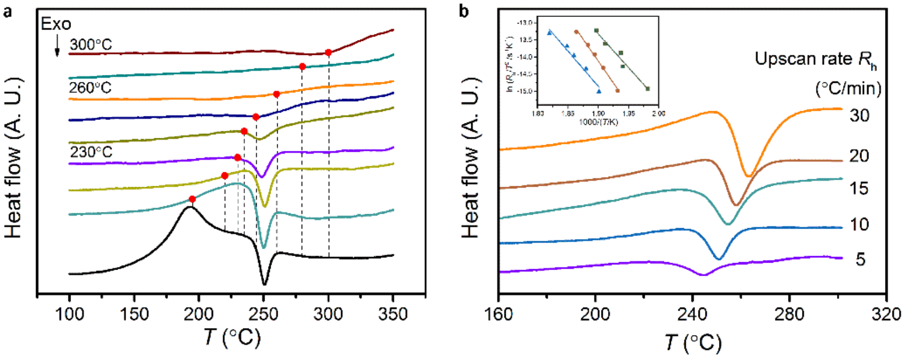

Figure 5-16 (a) DSC upscans of DUT-67 preheated at various temperatures. The red point on each scan indicates the preheated temperature. (b) DSC upscans at different heating rates R_h on the sample preheated to 220 °C. Inset: Linear fits of the characteristic onset, peak and end-set temperatures of the exothermic peak with heating rates.

The enthalpy release duing the phase transformation is determined as ΔH_{cryst}^{HT} = -20.15 kJ mol^{-1} (or -0.209 eV), from the DSC upscan preheated at 220 °C in a standard 10 K min^{-1} heating rate. According to the first law of thermodynamics, ΔH is contributed by the change of internal energy (ΔU) and the pressure-volume work $p\Delta V$. Based on the density changes measured from gas pycnometry (Table 5-3), the $p\Delta V_{cryst}^{HT}$ is calculated to be -1.63 kJ mol^{-1}. The ΔU is thus negative as well with respect to the phase transformation. The intrinsic energy of the DUT-67-HT is lower than that of its crystalline counterpart, indicting its higher thermal stability.

The activation energy to induce the transformation (E_a) is determined by performing DSC upscans at different heating rates on the sample preheated at 220 °C (Figure 5-16b). Although the widely used Kissinger's equation was derived for quantifying crystalline kinetics, it is still powerful and rational to analyse kinetic behaviour in complex processes from the physical viewpoint (117–120). As shown in Figure 5-16b-inset, the E_a values are determined to be 164.0 ± 19.0 kJ mol^{-1}, 213.4 ± 9.4 kJ mol^{-1}, and 171.5 ± 18.6 kJ mol^{-1}, from the onset, peak, and end-set shifts, respectively. Comparing with the small changes of the intrinsic energy ΔU, the energy barrier during phase transformation is considerably large in terms of the potential energy landscape (121,122). The results in Figure 5-16 demonstrate that the phase transformation of DUT-67 is a first-order and irreversible transformation, and the activation energy is determined to be on average 183 kJ mol^{-1} from different characteristic points.

5.3.4. POROSITY

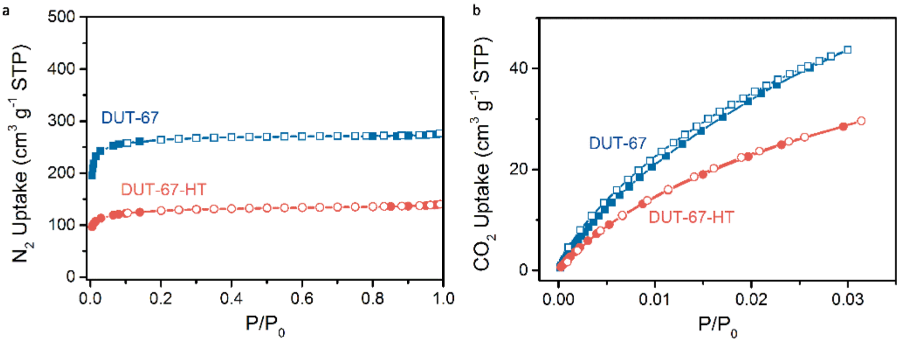

Figure 5-17 (a) N_2 and (b) CO_2 absorption-desorption isotherms of DUT-67 and DUT-67-HT. Solid points: Absorption; Open points: Desorption.

Table 5-3 Surface area (BET method from N_2 uptakes), pore volume, N_2 uptakes (P/P_0=0.9), CO_2 uptakes (P/P_0=0.03), and densities of DUT-67 and DUT-67-HT.

Sample	Surface area /m^2 g^{-1}	Micropore volume / cm^3 g^{-1}	N_2 uptake / cm^3 g^{-1} (STP)	CO_2 uptake / cm^3 g^{-1} (STP)	Density / g cm^{-3}
DUT-67	1038	0.428	276.4	40.7	2.074 (6)
DUT-67-HT	490	0.217	140.3	29.6	2.554 (8)

The porosities of DUT-67 and the sample after phase transformation were investigated by gas sorption using N_2 and CO_2 (Figure 5-17). Both N_2 absorption-desorption isotherms show type-I behavior. The surface area of DUT-67 from N_2 uptake is determined as 1038 m^2 g^{-1}, associated well with the reported 1064 m^2 g^{-1} in literature (46). The DUT-67-HT also shows a high surface area (490 m^2 g^{-1}), indicating the retention of the porosity after the phase transformation. This large surface area is contributed by the voids of the new secondary phase. Both samples demonstrate reversible CO_2 uptakes, showing their permanent porosities. The better accessibility of DUT-67 to CO_2 than most ZIFs could be ascribed to the beneficial -OH group in the framework, as manifested by the study of UiO-66 (112). The densities of both samples were also measured by helium pycnometry (Table 5-3). The considerable increase (23 %) of the density of DUT-67-HT accords with the dense framework with ordered secondary phase and disordered amorphous phase, as explained from other experimental results (PXRD, DSC, and SAXS).

5.4. SUMMARY

In this Chapter, the glass forming ability of selected MOFs are investigated from the thermodynamic viewpoint. Various factors, such as topologies, types of organic ligands, types of the secondary linkers, are investigated to probe MOFs with melting and glass forming properties. Several MOFs were hence chosen as candidates. DSC-TGA results verify that ZIF-11, ZIF-12, ZIF-71, MCIF-1, TIF-5-Cl, JUC-160, and ZTIF-1 do not show melting process prior to their decomposition upon heating. However, ZIF-76 and the isomorph ZIF-76-mbIm are discovered to be good MOF glass formers for the first time. Remarkably, the glassy a_gZIF-76-mbIm exhibits permanent accessible porosity with reversible CO_2 and CH_4 uptakes. The retention of the porosities is ascribed to the constricted framework with the pore size of 4-8 Å after glass formation of ZIF-76-mbIm.

Furthermore, a Zr-based MOF, DUT-67, is also investigated on the structure and thermodynamic response with temperature. An irreversible first-order phase transformation at 230~260 °C is revealed upon heating, with an activation energy of 183 kJ mol^{-1}. With regard to the structure, the DUT-67-HT after the phase transformation is suggested to be mixed phases of an ordered secondary phase and a disordered amorphous phase, according to the experimental results from various methods. The densified DUT-67-HT also possesses accessible porosities for guest molecules including N_2 and CO_2.

CHAPTER 6. ZIF-4 AND ZIF-62 LIQUID PHASE BLENDING IN THERMODYNAMIC ASPECTS

Liquid-state MOFs are investigation worthy because of their potentials of ion conduction and liquid-phase separation (15,16,123,124). It would be of great importance to control and develop MOFs with advanced properties, and most studies focus on controlling the functional group of MOFs during synthesis or with post-synthetic modification. As MOF glasses hold a temperature region of fluidity upon heating, it is feasible to modify the structure in the liquid state of MOFs. Since miscible polymers can be blended to study their physical properties (125–128), structure and properties of two MOFs quenched in the liquid and amorphous state were developed and studied. As discussed in Chapters 3 and 4, ZIF-4 and ZIF-62 phases were chosen as the candidates due to their good glass forming ability. The results of the blending of both phases were reported in Paper IV. Due to the contribution of each author, in this Chapter, only in the thermodynamic perspective of the blending results is presented [4].

6.1. ZIF-4-ZN & ZIF-62

ZIF-4-Zn and ZIF-62 crystals were synthesized as described in Section 2.1. The two ZIFs were mixed by equal weights (250 mg each) via ball-milling for 5 minutes, giving the mixture denoted here as ZIF-4-Zn/ZIF-62(50/50).

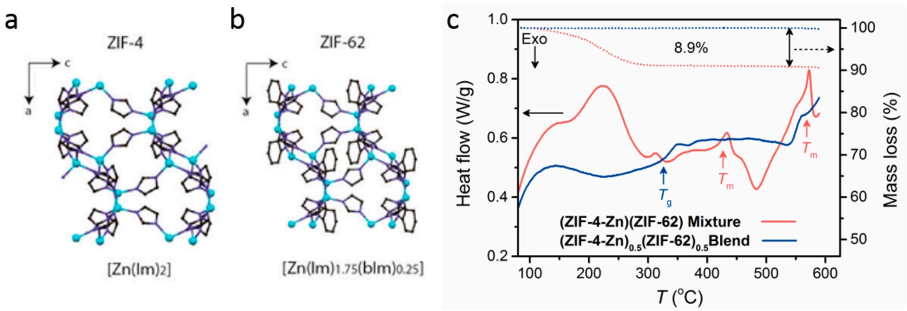

Figure 6-1 Unit cell of ZIF-4-Zn (a) and ZIF-62 (b) from the direction of b axis. Light blue: Zn; Dark blue: N; black: C; H atoms are omitted for clarity. (c) DSC and TGA results of ZIF-4-

---

[4] Results in this chapter have been published in Paper III.

Zn/ZIF-62(50/50) mixture (red line) and blended (ZIF-4-Zn)$_{0.5}$(ZIF-62)$_{0.5}$ (blue line). Upscan rate: 10 K min^{-1}.

Calorimetric study was conducted on the ZIF-4-Zn/ZIF-62(50/50), as shown in Figure 6-1c. The broad endothermic peak at ~200 ˚C is due to the desolvation of DMF from the voids of the framework, together with a mass loss of 8.9 %. Another two endothermic peaks with the end-set temperature at 445 ˚C and 580 ˚C are ascribed to the melting of ZIF-62 and ZIF-4-Zn, respectively. The enthalpy of ZIF-62 melting at 445 ˚C is integrated to be *ca.* 3 kJ mol^{-1}, consistent with the result in Section 4.2. In contrast, the exothermic peak at ~470 ˚C is contributed by the enthalpy release during the recrystallization of ZIF-4-Zn. The enthalpy corresponding to this peak is not determined by integration as it is difficult to find the end-set of the peak from Figure 6-1c.

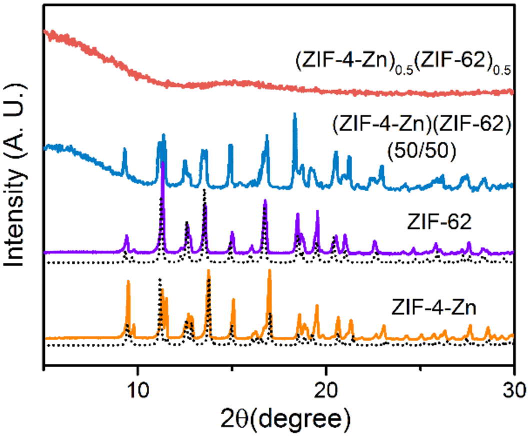

Figure 6-2 PXRD results. Purple and orange lines correspond to the patterns of ZIF-62 and ZIF-4-Zn, respectively, and the dashed lines are the simulated patterns, respectively. Blue and red lines represent the patterns of ZIF-4-Zn/ZIF-62(50/50) mixture and blended (ZIF-4-Zn)$_{0.5}$(ZIF-62)$_{0.5}$, respectively.

To blend the two ZIFs in liquid state, the mixture was heated to 590 ˚C where both frameworks were melted. The blended sample is thus referred to as (ZIF-4-Zn)$_{0.5}$(ZIF-62)$_{0.5}$. The PXRD result of (ZIF-4-Zn)$_{0.5}$(ZIF-62)$_{0.5}$ shows no Bragg peak, demonstrating its amorphous feature as expected (Figure 6-2). Calorimetric scan of the (ZIF-4-Zn)$_{0.5}$(ZIF-62)$_{0.5}$ was performed to investigate the glass transition of the blended sample. If the two phases are immiscible, then two glass transition peaks with T_gs at 293 ˚C and 320 ˚C would be observed which are attributed to the a_gZIF-4-Zn and a_gZIF-62, respectively. As shown in Figure 6-1c, however, (ZIF-4-Zn)$_{0.5}$(ZIF-62)$_{0.5}$ exhibits only one glass transition peak with T_g = 306 ˚C. This suggests the two phases were nicely blended in the liquid state, as reported in some miscible polymers, metallic glasses and oxide glass formers (126,129–133).

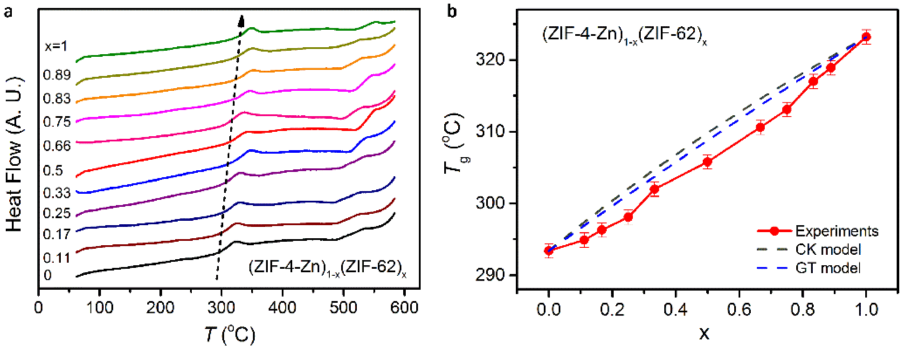

Figure 6-3 (a) DSC upscans of the blended (ZIF-4-Zn)$_{1-x}$(ZIF-62)$_x$. The dashed arrow represents the shift of T_g. (b) T_g shift with the wt% of ZIF-62 in the blended (ZIF-4-Zn)$_{1-x}$(ZIF-62)$_x$. Predicted T_g based on the properties of the two ZIFs are shown as the dashed lines in terms the CK and GT models.

Furthermore, a series of mixture between ZIF-4-Zn and ZIF-62 with different ratios was blended and the obtained (ZIF-4-Zn)$_{1-x}$(ZIF-62)$_x$ samples were characterized by DSC (Figure 6-3). All blended samples only show one glass transition peak upon heating. The T_g increases gradually with the amount of ZIF-62 in the series with a linear-like correlation (Figure 6-3b). Some models were proposed to describe and predict the composition dependence of T_g changes in a system with miscible polymer blends. Here two popular models are applied: the Couchman-Karasz (CK) model and the Gordon-Taylor (GT) model (134,135). The former one is based on the entropy continuity at the T_g, whilst the latter is based on the linear volume change with temperature. Both models share the equation of $T_g = (x_1 T_{g1} + k x_2 T_{g2})/(x_1 + k x_2)$, where in the CK model, $k_{CK} = \Delta C_{p1}/\Delta C_{p2}$ (ΔC_p is the jump of heat capacity at T_g), and in the GT model, $k_{GT} = \rho_2 T_{g2}/\rho_1 T_{g1}$ (ρ is the density of each composition) (136). The predicted T_gs of the blended (ZIF-4-Zn)$_{1-x}$(ZIF-62)$_x$ from the parameters of pure ZIF-4-Zn and ZIF-62 phases are presented in terms of the CK and GT model (Figure 6-3b). Both models slightly overestimate the T_gs compared to the experimental results, which suggests the mixture has positive mixing enthalpy ($\Delta H_{mix} > 0$), as the behaviour observed in the mixture of *o*- vs. *m*-methoxymethylbenzene (MBB) (136). Since the two models can only be applied to mixtures with relative weak intermolecular interactions, the derivations between the experimental results and the predictions suggest strong interactions between ZIF-4-Zn and ZIF-62 phases after blending.

6.2. ZIF-4-CO & ZIF-62

ZIF-4-Co has the same structure (space group: P_{bca}) as ZIF-4-Zn but the substitution of the metal center of Zn by Co. It is also applied to blend with ZIF-62 to further investigate the intermolecular interaction between two MOFs after blending in liquid state. The heat flow of the mixture ZIF-4-Co/ZIF-62(50/50) is shown in Figure 6-4c.

The characteristic thermal responses of the phase transformations of each phase during heating, such as thermal amorphization and melting, are pointed out on the DSC upscans by arrows in Figure 6-4c. As the atomic size of Co^{2+} is smaller than that of Zn^{2+}, giving weak Co-N bonds in ZIF-4-Co, the decomposing temperature of ZIF-4-Co is significantly lower than that of ZIF-4-Zn. To avoid the occurrence of the decomposition of ZIF-4-Co upon heating, the ZIF-4-Co/ZIF-62(50/50) was quenched after heating to 425 °C. In other word, this obtained $(\text{ZIF-4-Co})_{0.5}(\text{ZIF-62})_{0.5}$ was blended by amorphous ZIF-4-Co and ZIF-62 liquid rather than by two liquid phases in $(\text{ZIF-4-Zn})_{1-x}(\text{ZIF-62})_{x}$.

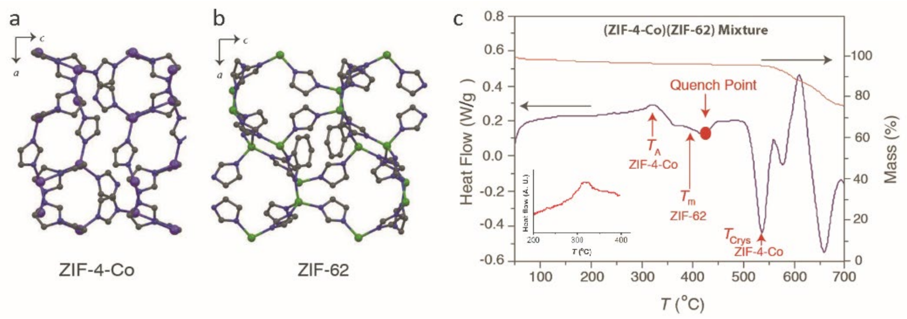

Figure 6-4 Unit cell of ZIF-4-Co (a) and ZIF-62 (b) from the direction of b axis. Green: Zn; Purple: Co; Dark blue: N; black: C; H atoms are omitted for clarity. (c) DSC and TGA results of ZIF-4-Co/ZIF-62(50/50) mixture (blue line) and blended $(\text{ZIF-4-Co})_{0.5}(\text{ZIF-62})_{0.5}$ (inset). The mixture was ball-milled for 5 minutes. Upscan rate: 10 K min^{-1}.

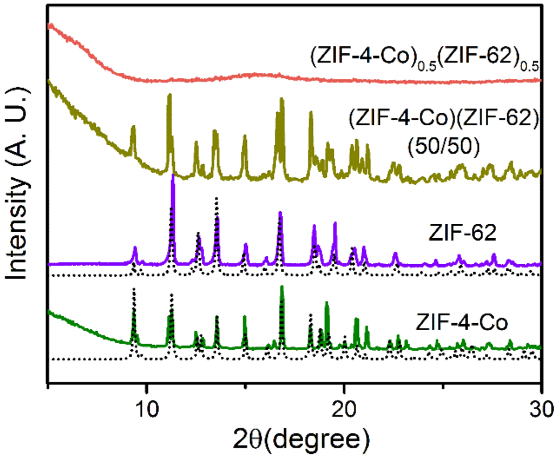

Figure 6-5 PXRD results. Purple and green lines correspond to the patterns of ZIF-62 and ZIF-4-Zn, respectively, and the dashed lines are the simulated patterns, respectively. Brown and red lines represent the patterns of ZIF-4-Co/ZIF-62(50/50) mixture and blended $(\text{ZIF-4-Co})_{0.5}(\text{ZIF-62})_{0.5}$, respectively.

Figure 6-5 shows the PXRD results in the case of ZIF-4-Co/ZIF-62. The blended (ZIF-4-Co)$_{0.5}$(ZIF-62)$_{0.5}$ also yields a glassy state, as verified by the red curve in Figure 6-5. The T_g of (ZIF-4-Co)$_{0.5}$(ZIF-62)$_{0.5}$ is determined by the DSC upscan to be ca. 300 °C. Similar to the thermodynamic behaviour of (ZIF-4-Zn)$_{0.5}$(ZIF-62)$_{0.5}$ in Figure 6-1c, only one glass transition peak is detected on the heat flow curve of (ZIF-4-Co)$_{0.5}$(ZIF-62)$_{0.5}$ (Figure 6-4c-inset). It indicates that amorphous ZIF-4-Co and ZIF-62 liquid have intermolecular interactions during blending.

Furthermore, X-ray energy dispersive spectroscopy (EDS) together with scanning transmission electron microscopy (STEM) were applied to investigate the interfacial bonding between each phase and the domain structure in (ZIF-4-Co)$_{0.5}$(ZIF-62)$_{0.5}$. As shown in Figures 4 and 5 in Paper III, the amorphous phases of ZIF-4-Co and ZIF-62 were blended with domain sizes of ~200 nm. The 3D image of (ZIF-4-Co)$_{0.5}$(ZIF-62)$_{0.5}$ from EDS tomography also confirms the heterogeneous mixing between both phases.

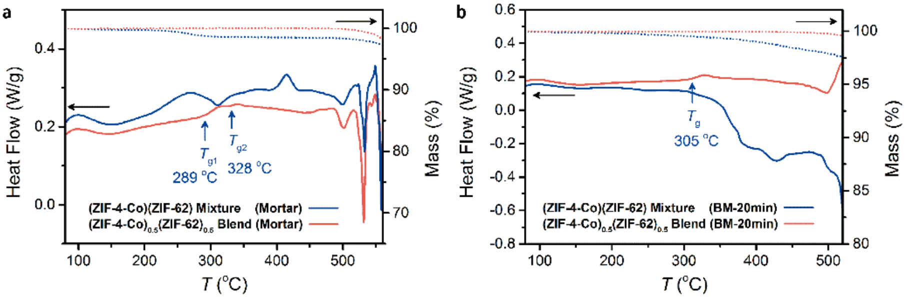

Figure 6-6 DSC and TGA results of ZIF-4-Co/ZIF-62(50/50) mixture (blue line) and blended (ZIF-4-Zn)$_{0.5}$(ZIF-62)$_{0.5}$ (red line) from different pre-treatments. (a) The mixture was light grinded in a mortar and pestle; (b) The mixture was ball-milled for 20 minutes. Upscan rate: 10 K min^{-1}.

For a comparable study of the domain size influence on the thermodynamic behaviour of (ZIF-4-Co)$_{0.5}$(ZIF-62)$_{0.5}$, a lightly grinded sample by mortar and pestle and a fully mixed sample after ball-milling for 20 minutes were prepared for blending. As seen in Figure S15 in the supplementary information of Paper III, the EDS-STEM images show that the Co and Zn phases interact after blending. With regard to the domain sizes of the blended samples, the light grinded one shows the domain sizes of > 500 nm, and 20 minutes ball-milled sample shows the size of only ~100 nm. Moreover, the domain sizes of both phases became larger after blending for the 5 and 20 minutes ball-milled samples, whereas the domain sizes of the light grinded sample show no significant change after blending. This could be ascribed to the liquid flow and diffusion in the liquid state during blending. It suggests that the two phases of the light grinded sample are physically heterogeneous and the other two samples are well mixed before blending.

Simultaneous DSC-TGA measurements were also carried out on these two samples (Figure 6-6). From the light grinded sample with larger domain sizes, the heat flow curve is the same as the one ball-milled for 5 minutes (Figure 6-4c): both samples show all thermal responses of ZIF-4-Co and ZIF-62 phases. The following upscan of the quenched mixture shows two T_gs, which are consistent with the T_g of a_TZIF-4-Co and a_gZIF-62, respectively. In contrast, the blended (ZIF-4-Co)$_{0.5}$(ZIF-62)$_{0.5}$ premixed for 20 minutes by ball-milling only exhibits one glass transition peak with T_g = 305 °C, which accords well with the results in Figure 6-4c. Considering the EDS-STEM results, it can be concluded that the glass transition behaviour after blending is strongly connected with the pre-treatment conditions. The one T_g peak after blending of two MOFs is attributed to the small domain sizes of each phases. The interfacial bonding concentration may somehow contribute to the glass transition behaviour, yet it is difficult to elucidate the connection between this factor to the heat flow signal based on the current results. It shall be pointed out that ZIF-4 (Zn or Co) and ZIF-62 are two compatible MOFs, hence the (ZIF-4-Zn)$_{1-x}$(ZIF-62)$_x$ and (ZIF-4-Co)$_{0.5}$(ZIF-62)$_{0.5}$ are miscible blends with strong interactions and could easily result in one T_g. Very recent results of a blended (ZIF-67)$_{0.2}$(ZIF-62)$_{0.8}$ with the flux melting method verify the feasibility to give rise to miscible blends from compatible MOFs (137). This practical approach could be extended for tailoring new structures and develop properties of amorphous MOFs.

6.3. SUMMARY

In this Chapter, the liquid phase blends between two MOF glass formers, ZIF-4 and ZIF-62, are revealed in thermodynamic aspects. The (ZIF-4-Zn)$_{1-x}$(ZIF-62)$_x$ glasses show one T_g on the DSC upscans, indicating the two amorphous phases are successfully blended with preliminarily ball-milling for 5 minutes. The T_gs shifts higher with the increasing amount of ZIF-62 in the mixture. By comparing the predicted T_gs with the experimental ones, the two frameworks are suggested to have strong intermolecular interactions in (ZIF-4-Zn)$_{1-x}$(ZIF-62)$_x$ glasses. Blended MOF glasses are also achieved with Co substitution of Zn in ZIF-4. Calorimetric results of the (ZIF-4-Co)$_{0.5}$(ZIF-62)$_{0.5}$ glasses demonstrate the strong connection between the glass transition behaviour and the preliminary domain sizes. One glass transition peak in a well-blended MOF glass can be observed (preliminarily ball-milled for 5 and 20 minutes), which is mostly ascribed to the small domain sizes of each phase before blending.

CHAPTER 7. POST-SYNTHETIC MODIFIED MOF WITH ENHANCED POROSITY AFTER AMORPHIZATION

As described in Chapter 1, the potential applications of MOF glasses somehow take advantages of their porosities although the voids in the framework are mostly vanished with the collapse of the structure after amorphization. It is thus crucial to improve the porosity of MOF glasses. An *in silico* study has shown that the possibility of melting and retention of porosity are strongly connected with the framework topology in ZIFs (12). This observation suggests a practical approach to retain the pores by modifying the framework. Post-synthetic modification (PSM) method has been applied to discover and obtain MOFs with desirable structures and functionalities that are incompatible with *de novo* synthesis. However, physical properties such as glass forming ability and thermodynamic properties of MOFs after PSM are far from investigation.

In this Chapter, a composite MOF obtained by PSM on ZIF-7 [$Zn(bIm)_2$] by imidazole was developed, which is denoted as ZIF-PSM. The chemical stability and glass forming ability of this composite are investigated, and this ZIF-PSM composite can be thermal-driven to amorphous MOF - a_TZIF-PSM. This amorphous MOF shows a higher surface area than the reported ones, as well as the ZIF-7 before modification. The structural features after amorphization are also studied [5].

7.1. CRYSTAL IDENTITY AFTER MODIFICATION

ZIF-7 [$Zn(bIm)_2$], with zinc and benzimidazolate (bIm) as tetrahedral node and organic linker, respectively, was modified by imidazole (Im) using mechanochemical method (138), as shown in **Error! Reference source not found.**a. A standard process to obtain the ZIF-PSM sample involves as-evacuated ZIF-7 crystal (150.9 mg, 0.5 mmol), imidazole (136.2 mg, 2 mmol) with 75 μL DMF as an assist solvent in a 10 ml stainless steel grinding jar. The mixture was ball-milled at 30 Hz for 60 minutes at room temperature. The obtained sample was dried and washed with distil water for the removal of unreacted imidazole and DMF. The ZIF-PSM sample was obtained after filtration and drying at 100 °C for four hours.

---

[5] Results in this chapter were mostly measured and all analyzed independently by the author, and the manuscript regarding to this work will be submitted for publication in the near future.

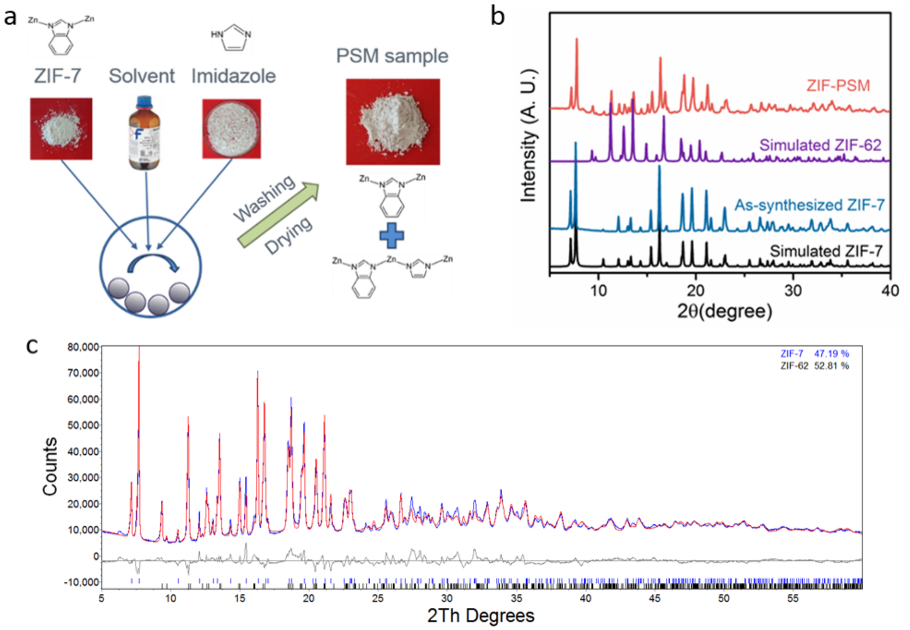

Figure 7-1 (a) Schematic modification process with mechanochemical method; (b) PXRD patterns of the ZIF-PSM crystal, together with the simulated ones of ZIF-7 and ZIF-62 phases; (c) Rietveld refinement of the PXRD pattern of the ZIF-PSM

To verify the crystal identity of the ZIF-PSM, the PXRD pattern of the ZIF-PSM sample was compared to all simulated patterns of the ZIFs with bIm and/or Im as organic linkers. The ZIF-PSM is hence verified as a composite with ZIF-7 and ZIF-62 phases (Figure 7-1b) (38,44). Rietveld refinement of the PXRD pattern of the ZIF-PSM was carried out to quantify the amount of each phase (R_{wp} = 6.99 %, R_{p} = 5.44 %, χ^2 = 1.97), and the refinement parameters with ESDs are given in Table 7-1. FWHM based PV_TCHZ model was applied to refine the peak profile regarding the crystallite size broadening. March-Dollase preferred orientation corrections were used on both phases to yield a good refinement (Table 7-1). Atomic coordinate was imported from cif files without further refinements. Only isotropic atomic displacement parameters (ADPs, B_{iso}) of Zn atoms in each phase (occupancy = 1) were refined with other elements occupying the same crystallographic site from cif files. After the careful Rietveld refinement of the PXRD pattern of the ZIF-PSM, the composition of the ZIF-PSM is determined as (ZIF-7)$_{47.2}$(ZIF-62)$_{52.8}$, almost half of each phase after modification (Figure 7-1c). Although the simulated patterns of ZIF-62 and ZIF-4 are similar, a unique Bragg peak at $2\theta = 11.56^{\circ}$ associated with (2 0 0) plane in ZIF-4 is not observed in the PXRD pattern of ZIF-PSM. This indicates that ZIF-4 phase is not formed after modification.

Table 7-1 Refinement parameters of the PXRD pattern in Figure 7-1c. Values in brackets are ESDs from refinements.

Phase	ZIF-7	ZIF-62
Space group	$R\bar{3}$	$Pbca$
Rietveld wt%	47.19(31)	52.81(31)
Preferred Orientation		
hkl	(1 -3 -2)	(2 1 1)
	0.76 (12)	0.71 (28)
a /Å	22.9204(13)	15.5061(16)
b /Å	-	15.6716(16)
c /Å	15.7491(14)	18.1892(18)
R_{Bragg} /%	5.44	4.55
B_{iso} /Å^2		
Zn1	1.66(27)	1.51(56)
Zn2	-	1.52(50)

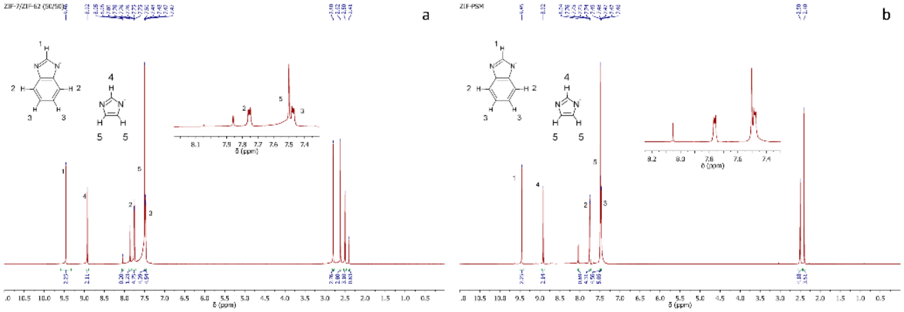

*Figure 7-2 Liquid-state ^{1}H NMR spectrum of the mixture of ZIF-7/ZIF-62(50/50) (a) and the ZIF-PSM (b) digested in DCl/D$_2$O/DMSO-d$_6$. Peak assignments of ZIF-7/ZIF-62(50/50): 9.46 (s, 1H): NC**H**N (bIm); 8.92 (s, 1H): NC**H**N (Im); 7.75 (dd, J = 6.1, 3.1 Hz, 2H): NCC**H** (bIm); 7.50 (s, 2H): NC**H**C**H** (Im); 7.47 (dd, J = 6.1, 3.1 Hz, 2H): NCCHC**H** (bIm). Peak assignments of ZIF-PSM: 9.45 (s, 1H): NC**H**N (bIm); 8.92 (s, 1H): NC**H**N (Im); 7.75 (dd, J = 6.1, 3.0 Hz, 2H): NCC**H** (bIm); 7.49 (s, 2H): NC**H**C**H** (Im); 7.47 (dd, J = 6.0, 3.1 Hz, 2H): NCCHC**H** (bIm).*

Liquid-state ^{1}H NMR spectrum of the ZIF-PSM confirms the existence of the imidazolate in the ZIF-PSM. The ratio of the peak area between the peak assigned to the *NC**H**N* from the bIm ring and that from Im one in the NMR spectra is quantitatively determined. This value derived from the ZIF-PSM spectrum is comparable to the one calculated from the spectrum of the physical mixed ZIF-7/ZIF-62(50/50). This consistency manifests the composition of the ZIF-PSM (Figure 7-2). A systematic study from Gustafsson *et al.* showed that by varying concertation of

Zn^{2+}, bIm, and Im in the solvent during solvothermal synthesis, only single phase of ZIFs, i.e., either ZIF-7 or ZIF-62, could be obtained, whereas a composite of both phases can be hardly achieved directly (139). Figure 7-1 demonstrates that using the mechanochemical PSM approach the composite with ZIF-7 and ZIF-62 phases could be obtained which is difficult to be *de novo* obtained.

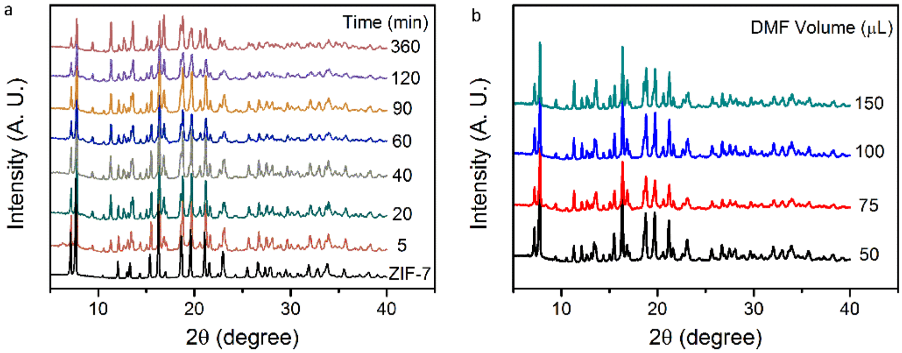

Figure 7-3 (a) PXRD patterns of modified ZIF-7 by imidazole and 75 μL DMF for different durations. (b) PXRD patterns of modified ZIF-7 by imidazole for 60 minutes with different volume of DMF. Note that the ZIF-PSM sample refers to the one specifically modified for 60 minutes with 75 μL DMF.

Kinetic and chemical influences during modification with the mechanochemical method are further investigated. A series of PSM samples were obtained by altering the modification time from 5 to 360 minutes. Figure 7-3a shows that the PXRD spectra accord well with the spectrum of ZIF-PSM, the one with a modification time of 60 minutes. This congruity demonstrates that the PSM samples modified with different durations are also composed by ZIF-7 and ZIF-62 phases. The relative intensities between the Bragg peaks are almost consistent, suggesting that the percentage of each phase does not change significantly. Moreover, changing the amount of the assisted solvent (DMF) from 50 to 150 μL yields the modified products with similar PXRD patterns, as an indicative of the same composition by ZIF-7 and ZIF-62 (Figure 7-3b).

Although aspects such as the induced stress during ball-milling are not considered, the results in Figure 7-3 suggest the phases and composition of the PSM samples of ZIF-7 modified by imidazole are not driven by kinetic reasons, including the modification time and volume of assisted solvent.

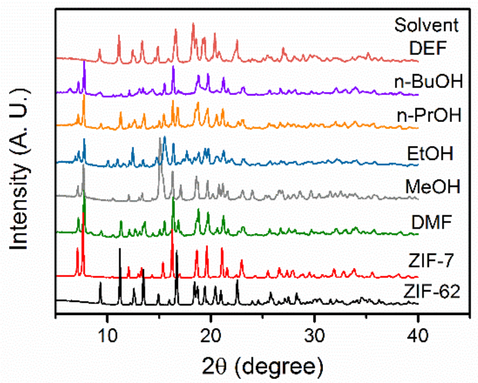

Figure 7-4 PXRD patterns of modified ZIF-7 by imidazole for 60 minutes with 75 µL of different types of solvent.

As guest solvents also play an important role during modification (140), the influence of six different types of assisted solvent on the PSM products is investigated. The PXRD patterns of the obtained samples after modification are collected (Figure 7-4). To resolve the compositions of the phases of these PSM samples, the PXRD patterns are also refined using the Rietveld method, and some refinement parameters are presented in Table 7-2. Only the one with n-PrOH has a similar structure to the ZIF-PSM sample with DMF. Interestingly, ZIF-7 can be totally modified to ZIF-62 in DEF, whereas ZIF-zni, the most dense phase of [Zn(Im)$_2$] composition as mentioned in Chapter 3, was formed together with the initial ZIF-7 phase with the assisted solvent of MeOH.

Table 7-2 Compositions of the PSM samples with different types of solvents, quantified by Rietveld refinements of the PXRD patterns in Figure 7-4.

Solvent	Composition/%			R_{wp} /%	χ^2	R_p /%	R_{Bragg} /%	
	ZIF-7	ZIF-62	ZIF-zni				ZIF-7	ZIF-62
DMF	47.19	52.81	-	6.99	1.97	5.44	5.44	4.55
MeOH	46.22	-	53.78	10.77	2.71	8.09	8.55	4.64
EtOH	67.70	32.30	-	17.75	4.65	9.88	6.17	8.83
n-PrOH	53.50	46.50	-	8.84	2.40	6.68	3.84	3.80
n-BuOH	85.20	14.80	-	12.31	3.14	9.63	6.49	7.02
DEF	1.01	98.99	-	18.38	4.69	7.79	5.64	7.16

Alternatively, solvothermal post-synthetic modification of ZIF-7 by imidazole was also performed in DMF and n-BuOH (Figure 7-5) The experimental process is: As-evacuated ZIF-7 crystal (90.5 mg, 0.3 mmol) and imidazole (81.7 mg, 1.2 mmol) were dissolved in 10 ml DMF or n-BuOH in a glass vial, which was later heated to 130 °C for 48 hours for ligand exchanges. According to the PXRD patterns of the modified sample in DMF, the product is verified as (ZIF-7)$_{24.7}$(ZIF-62)$_{75.3}$ (R_{wp} = 11.45 %,

R_p = 9.04 %, $R_{\text{Bragg-ZIF-7}}$ = 5.84 %, $R_{\text{Bragg-ZIF-62}}$ = 7.10 %, χ^2 = 1.92). This composition has a larger amount of the new phase (ZIF-62) than the ZIF-PSM sample via mechanochemical approach. However, the solvothermal modified sample in n-BuOH only shows the parent ZIF-7 phase, demonstrating no linker exchange after modification. The results in Figures 7-4 and 7-5 show the significant influence of the types of assisted solvents on the products after modification. Solvents such as DMF, DEF, n-PrOH, and MeOH are suggested to be good structure-directing templates with regard to the modification in ZIFs.

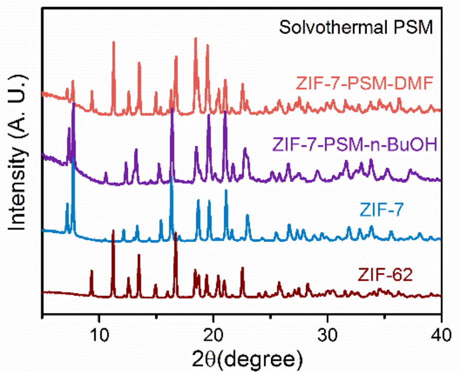

Figure 7-5 PXRD patterns of modified ZIF-7 by imidazole with DMF and n-BuOH using solvothermal method.

The rule of mechanochemical modification has been demonstrated that only ligands with lower basicity can be readily substituted by ones with higher basicity (141). Since the pK_a value of imidazolate ($C_3H_3N_2^-$) is also larger than that of 2-methylimidazolate (2-mIm) and 2-ethylimidazolate (2-eIm), the mIm and eIm ligands in ZIFs should be exchanged by Im. As a comparable study, mechanochemical modifications on ZIF-8 [Zn(mIm)$_2$] and ZIF-14 [Zn(eIm)$_2$] by imidazole were also conducted (Figure 7-6). As a result, both modified samples are assigned as the ZIF-zni phase. That is, the organic ligands in ZIF-8 and ZIF-14 were fully substituted by imidazole during modification. This phenomenon is not observed in the case of the PSM on ZIF-7, in which the composite does not show the formation of ZIF-zni. The difference of the PSM products on ZIF-7 and ZIF-8/ZIF-14 could be connected to the spatial topologies (phenyl group in ZIF-7) and/or the potential energy barriers between the preliminary and modified frameworks. The ZIF-zni from PSM of ZIF-8 and ZIF-14 is not further characterized in the present work, as this phase has been well investigated in literature (5,19,31,57,142).

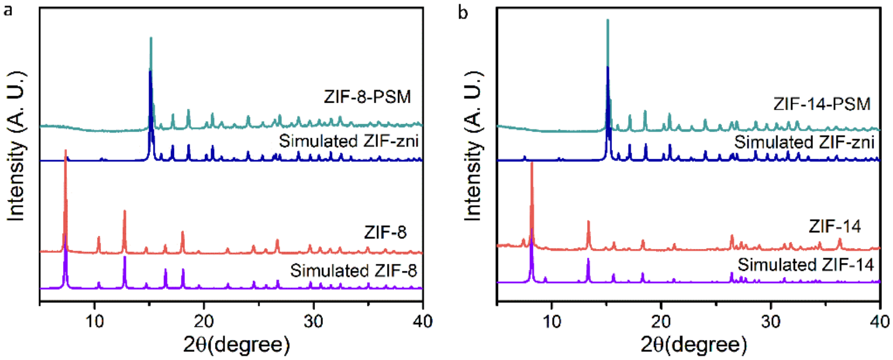

Figure 7-6 PXRD patterns of as-synthesized and modified ZIF-8 (a) and ZIF-14 (b) by imidazole for 60 minutes with 75 µL DMF.

7.2. GLASS FORMATION AND STRUCTURAL EVOLUTION

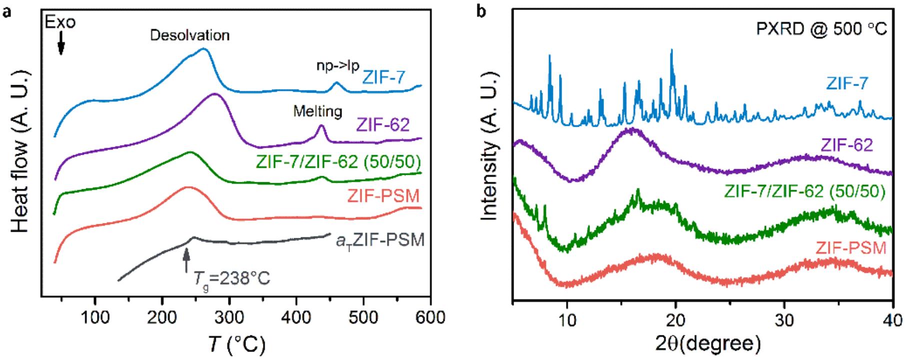

Figure 7-7 (a) Heat flow of ZIF-7, ZIF-62, mixture (ZIF-7)(ZIF-62)(50/50), ZIF-PSM crystal and a$_T$ZIF-PSM. Upscan rate: 20 K min^{-1}; (b) PXRD patterns of ZIF-7, ZIF-62, (ZIF-7)(ZIF-62)(50/50) and ZIF-PSM samples after preheated at 500 °C.

Thermodynamic response of the ZIF-PSM sample, pure phase of ZIF-7 and ZIF-62, and the physical mixture of ZIF-7 and ZIF-62 (50/50) (by mortar and pestle), was probed by DSC and TGA (Figure 7-7a). Broad endothermic peaks at ~250 °C on all DSC upscans of the crystals are ascribed to the desolvation of DMF. Crystalline ZIF-7 shows an endothermic peak at 460 °C, corresponding to the polymorphic transition from narrow-pore (np) phase to large-pore (lp) phase (101,143), and ZIF-62 undergoes a melting process at 440 °C with the enthalpy of fusion (ΔH_f) of 9.0 J g^{-1} upon heating. The heat flow curve of the mixture ZIF-7/ZIF-62 (50/50) shows the thermodynamic features of both phases. An endothermic peak at 440 °C is noticed with the enthalpy absorption of 4.4 J g^{-1}, almost half of ΔH_f of ZIF-62. This peak is assigned as the melting of ZIF-62, and hence the heat response of polymorphic transition of ZIF-7 in the mixture is not detected. The DSC upscan of the ZIF-PSM crystal, however, shows no thermal response in the temperature range of 300-500 ˚C. This different thermodynamic response suggests the structural differences of the ZIF-PSM sample and the physical mixture of ZIF-7 and ZIF-62. It implies that the two phases in ZIF-PSM are chemically bonded around their interfaces.

To explore structure changes after heat treatments, PXRD patterns of the samples after heating to 500 ˚C were measured (Figure 7-7b). The structures of ZIF-7 and ZIF-62 at 500 ˚C are assigned as crystalline lp-ZIF-7 and ZIF-62 glass (a_gZIF-62), respectively (10,143). The preheated mixture turns into mixed phases of ZIF-62 glass and lp-ZIF-7 crystal as expected. However, the PXRD pattern of the ZIF-PSM sample shows no Bragg peak but only a broad hump at $2\theta \approx 18^{\circ}$, revealing its amorphous feature. The composite ZIF-PSM is hence regarded as a glass former, and this amorphous sample cooled from 500 ˚C is denoted as a_TZIF-PSM hereafter.

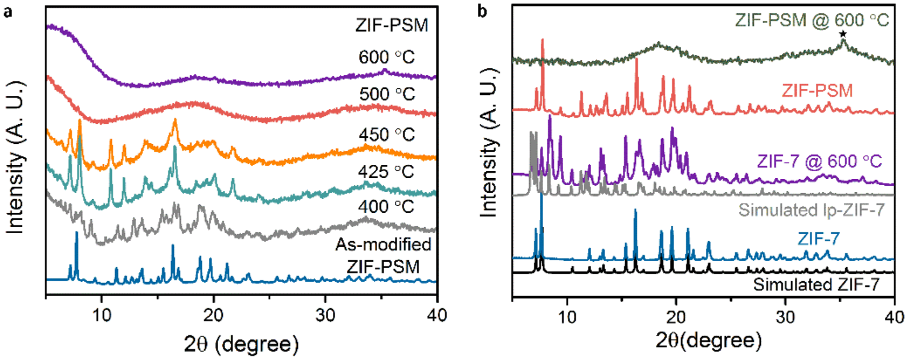

Figure 7-8 (a) Ex-situ PXRD measurements of the ZIF-PSM sample preheated at different temperature. (b) A comparison of the PXRD patterns of ZIF-7 and ZIF-PSM at room temperature and preheated at 600 ˚C. The star indicates the ZnO phase.

Ex situ variable-temperature PXRD results of the ZIF-PSM (Figure 7-8a) show that the ZIF-PSM gradually becomes amorphous after preheated at 400 ˚C, which is probably attributed to the vitrification of the ZIF-62 phase. The thermal stability of a_TZIF-PSM up to *ca.* 600 ˚C, with the appearance of the ZnO phase. With regard to the high thermal stability of the parent ZIF-7 phases, ZIF-7 was preheated to 600 ˚C, and the initial phase becomes crystalline lp-ZIF-7 phase without amorphization or decomposition (Figure 7-8b).

DSC upscan of a_TZIF-PSM exhibits a glass transition peak with the characteristic temperature (T_g) of 253 ˚C (Figure 7-7a). This T_g is far below the one (T_g=320 ˚C) of the a_gZIF-62 (Figure 4-1b), indicating that the a_TZIF-PSM is thermodynamically different from the a_gZIF-62 due to the ZIF-7 phase. Elemental analysis (Table 7-3) and ^{1}H liquid-state NMR results (Figure 7-9) show few differences between the crystalline ZIF-PSM and the amorphous a_TZIF-PSM. That is, the aromatic rings in the framework remains intact after amorphization.

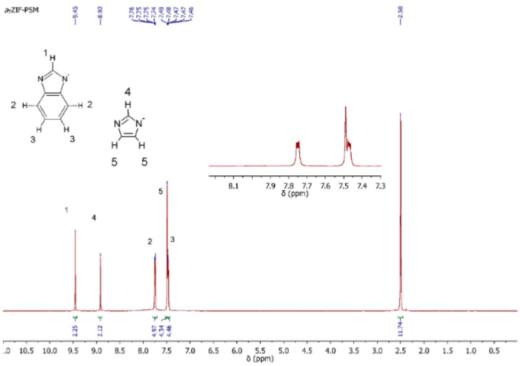

*Figure 7-9 Liquid-state ^1H NMR spectrum of the a_TZIF-PSM digested in DCl/D$_2$O/DMSO-d_6. Peak assignments: 9.45 (s, 1H): NC**H**N (bIm); 8.92 (s, 1H): NC**H**N (Im); 7.75 (dd, J = 6.1, 3.1 Hz, 2H): NCC**H** (bIm); 7.49 (s, 2H): NC**HCH** (Im); 7.47 (dd, J = 6.1, 3.1 Hz, 2H): NCCHC**H** (bIm).*

Table 7-3 Elemental analysis of the ZIF-PSM and a_TZIF-PSM (based on the composition of (ZIF-7)$_{47.2}$(ZIF-62)$_{52.8}$, ZIF-7: $ZnC_{14}H_{10}N_4$; ZIF-62: $ZnC_7H_{6.5}N_4$)

	C /%	H /%	N /%
ZIF-PSM			
Calculated	48.16	3.72	22.67
Found	50.62	3.25	21.15
a_TZIF-PSM			
Calculated	47.42	3.22	22.78
Found	50.67	2.62	21.22

7.3. MORPHOLOGY AND MECHANICAL PROPERTIES

The morphology and the mechanical properties of the modified framework is discussed in this section. SEM measurements were performed to probe the morphology before and after PSM (Figure 7-10). The morphology of crystalline ZIF-7 is consistent with the simulated one. The ZIF-7 and ZIF-62 phases in the physical mixture are well separated (not shown here), whereas the morphology of the ZIF-PSM only shows smooth edges among planes (Figure 7-10b). The particle shapes of the ZIF-PSM heritage the ZIF-7 crystals before modification, though they are keen to agglomerate together. The partical sizes (~300 nm) become smaller after mechanochemical PSM. By preheating the ZIF-PSM at 500 °C, the a_TZIF-PSM shows smooth and round-like morphology, as an indicative of the flowing surface (Figure 7-10c). It would be mostly ascribed to melted ZIF-62.

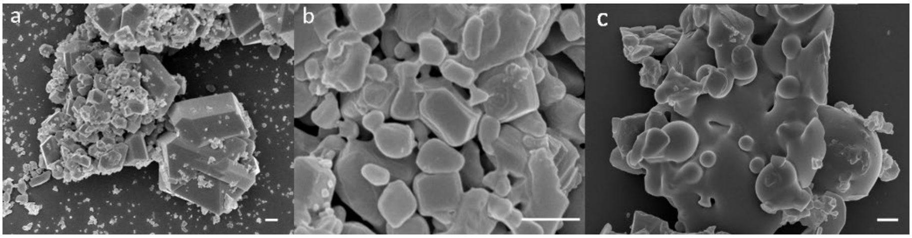

Figure 7-10 SEM micrographs of (a) ZIF-7, (b) ZIF-PSM, and (c) a_TZIF-PSM. Scale bar: 500 nm.

Before the experiments, the two phases of the ZIF-PSM is anticipated to be connected in one of the following modes: (1) it is a core-shell structure with the parent ZIF-7 phase inside covered by the ZIF-62 shell; (2) the parent ZIF-7 nanoclusters as droplets are surrounded by ZIF-62 phase as a matric, like a chocolate cookie; (3) the two phase are randomly allocated and chemically interconnected around the interface. Although core-shell and droplet-matric structures are normally verified by SEM and TEM images in literature (144–148), the two phases with obvious interfaces cannot be observed in the present work. It could be ascribed to: (1) There is only one type of metallic elements (Zn) before and after modification, therefore EDS or BSE mode cannot tell the two different phases from microscopic images; (2) The morphology of the ZIF-PSM is hardly well-shaped after the collisions by ball-milling. It is unfortunately hard to draw a conclusion which one of the three assumptions is the mode in ZIF-PSM based on Figure 7-10. Nevertheless, the morphological changes from ZIF-PSM to a_TZIF-PSM suggest the interaction of the two phases among the particles, and it is consistent with its amorphous feature from the PXRD results in Figure 7-7b.

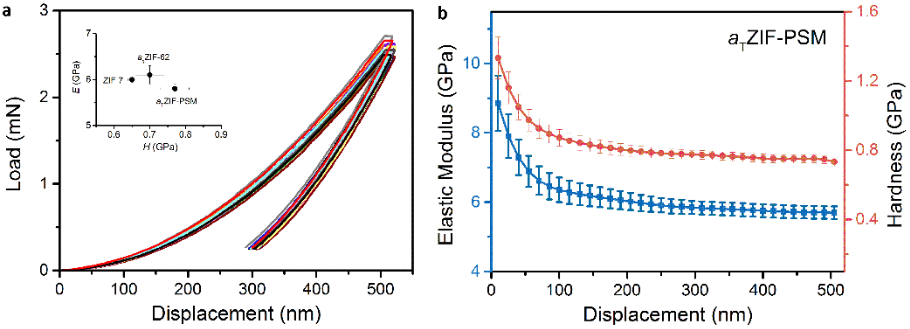

Figure 7-11 (a) Load-displacement curve from nanoindentation measurement of the a_TZIF-PSM. Inset: E-H relationship of ZIF-7, a_gZIF-62 and a_TZIF-PSM (10,57). (b) Elastic modulus (E) and hardness (H) as a function of indentation depth of a_TZIF-PSM. Error bars come from the standard deviation of 26 measurements.

Nanoindentation measurements were performed to probe the mechanical properties of the a_TZIF-PSM (Figure 7-11). The hardness of a_TZIF-PSM (0.70 GPa) is slightly larger than the values of ZIF-7 crystal and ZIF-62 glass (Figure 7-11a inset). Comparing the hardness with that of the a_{g}ZIF-62, ZIF-7 phase increases the resistance of plastic deformation, leading to the increase of the hardness of the a_{T}ZIF-PSM. However, the elastic modulus value of the a_{T}ZIF-PSM is more or less the same as the ones of ZIF-7 crystal and ZIF-62 glass. It is noteworthy that due to the very limited size, it is not possible to measure the mechanical properties of the ZIF-PSM via nanoindentation method.

In addition, the densities of the ZIF-PSM and the a_{T}ZIF-PSM determined from helium pycnometry are 1.520 (5) g cm^{-3} and 1.558 (2) g cm^{-3}, respectively. Both values lies in between the densities of ZIF-7 (1.467 g cm^{-3}, this work) and a_{g}ZIF-62 (1.566 g cm^{-3}, from (10)). On the other hand, the density of ZIF-7/ZIF-62(50/50) mixture is measured as 1.484 g cm^{-3}, smaller than that of ZIF-PSM. In addition, the density of a_{T}ZIF-PSM is more closer to the value of a_{g}ZIF-62. Both comparisons suggest that the two phases in the composite are densely packed in both crystalline and amorphous state.

7.4. POROSITY OF A_{T}ZIF-PSM

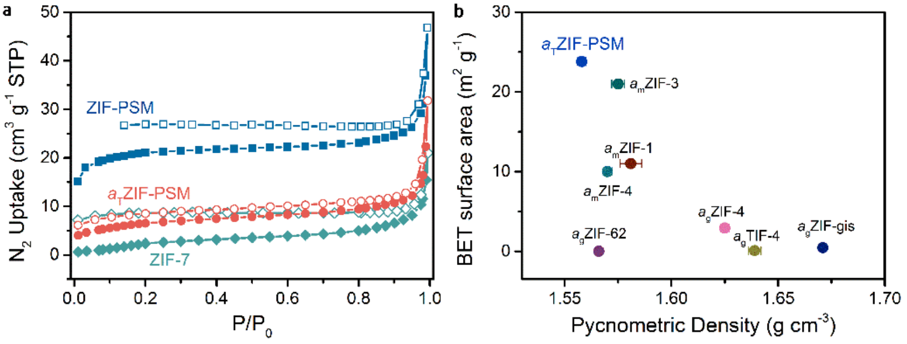

Figure 7-12 (a) N_2 absorption-desorption isotherms of ZIF-7 crystal, ZIF-PSM, and a_{T}ZIF-PSM at 77 K. Solid points: Absorption; Open points: Desorption. (b) Relations between BET surface area from N_2 uptake measurements and pycnometric density of some amorphous MOFs (10,19).

One of the crucial motivations of the present work is to improve the porosity of MOF glasses. N_2 uptake isotherms were carried out on ZIF-7 crystal, ZIF-PSM, and a_{T}ZIF-PSM at 77 K, all of which show type-I behaviour with permanent accessible porosities (Figure 7-12a). The low N_2 uptakes of ZIF-7 are ascribed to its narrow pore which is only favourable of guest molecules with small kinetic diameters. This has been manifested in literature that ZIF-7 could demonstrate large amount of CO_2 uptakes rather than N_2, because of the smaller molecule size of CO_2 (3.3 Å) than N_2 (3.64 Å) (149–151). After modified by imidazole, ZIF-PSM exhibits a surface area as 71.8 m^2 g^{-1} based on N_2 absorption using the BET method. This surface area is higher than the value of ZIF-7. Considering that crystalline ZIF-62 has almost no porosity (152), this large surface area of ZIF-PSM can be only attributed to the pores of ZIF-7. The ZIF-7 framework in ZIF-PSM is presumably constricted by the ZIF-62 phase, leading to opening the gates for the access to large molecules such as N_2. The surface area of the a_TZIF-PSM derived from N_2 absorption isotherms decreases to 23.8 m^2 g^{-1}. In the light of no porosity in a_gZIF-62 (10), the pore and surface area in a_TZIF-PSM are benefited from the gate-opening ZIF-7 phase. Although the surface area decreases due to the collapse of the framework during vitrification, this value is still larger than most of the reported amorphous MOFs, especially those activated by temperature (Figure 7-12b). The relatively high porosity of the a_TZIF-PSM is also connected with its low pycnometric density when comparing with other amorphous ZIFs. To sum up, this thermal-induced amorphous MOF obtained via PSM possesses a larger porosity than the reported ones, which is ascribed to the retention of the stable parent phase (ZIF-7) after modification. The results in Figure 7-12 demonstrate that modified MOFs can facilitate the retention of the porosity even after amorphization.

7.5. STRUCTURAL FEATURES OF *A*$_T$ZIF-PSM

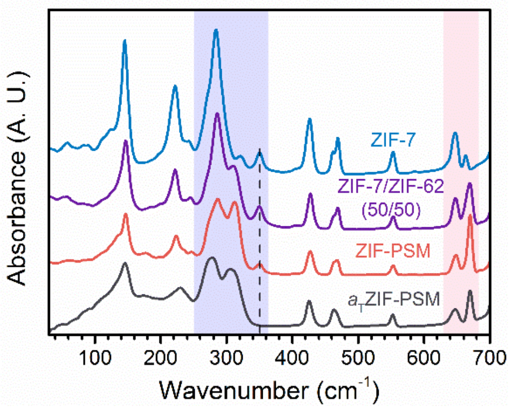

Figure 7-13 Synchrotron radiation far-infrared (SR-FIR) spectra of ZIF-7 crystal, ZIF-7/ZIF-62 (50/50) mixture, ZIF-PSM and a_TZIF-PSM.

Structure features of the composite ZIF-PSM and the amorphized a_TZIF-PSM were probed by using synchrotron radiation far-infrared (SR-FIR) spectroscopy, which has proved to identify the structural instability of crystalline and amorphous ZIFs (30,153). Note that this is the only experimental result with the assist of collaborators in this Chapter, while other results and all analysis are carried out by the author independently. As shown in Figure 7-13, the characteristic two peaks in the range of 260-330 cm^{-1} are assigned as the vibration modes of tetrahedral N-Zn-N bond stretching (153). The spectra of composite ZIF-PSM and the ZIF-7/ZIF-62 (50/50) mixture are compared and discussed. Although the positions of the two vibrational modes in the purple region in Figure 7-13 do not shift significantly, the intensity of the two peaks is almost equivalent in the ZIF-PSM spectrum. However, these observations show differently in the spectrum of the mixture. This difference again verifies that the ZIF-7 and ZIF-62 phases in ZIF-PSM are chemically coordinated rather than physically mixed. Taken the peak at 430 cm^{-1} as a reference, the intensity of the peaks in the range of 630-680 cm^{-1} in the ZIF-PSM pattern is stronger than the mixed one, an indicative of a stronger response of aromatic ring deformation in the composite ZIF-PSM (30,153). Few differences are observed on the a_TZIF-PSM spectrum compared to the ZIF-PSM one, except the loss of the peak at 350 cm^{-1}, which corresponds to the vibrational motions of organic linker twisting. Remarkably, the vibrational motions related to the ring bending and pore breathing giving the peaks at 145 cm^{-1} and 225 cm^{-1} can still be detected in a_TZIF-PSM (153). The SR-FIR results structurally confirm the porosity in a_TZIF-PSM with regard to the discussion of Figure 7-12.

7.6. SUMMARY

In this Chapter, post-synthetic modification (PSM) of ZIF-7 by imidazole is systematically investigated. The modified product is verified to be composed by the initial ZIF-7 phase and modified ZIF-62 phase. The constituent of this ZIF-PSM composite shows weak dependence on the modification time and the amount of assisted solvent (DMF). However, the types of solvents strongly influence the phases of the modified products. The ZIF-PSM can be thermally driven to the amorphous counterpart a_TZIF-PSM at 500 °C, of which the calorimetric behaviour differs from the ZIF-7/ZIF-62 (50/50) mixture. As the motivation in enhancing the porosity of amorphous MOFs, this obtained a_TZIF-PSM comparably shows accessible porosity, and relatively large surface area with a low pycnometric density. SR-FIR results of a_TZIF-PSM demonstrate the vibrational modes associated with ring bending and pore breathing, verifying the retention of the pores in ZIF-PSM after amorphization.

CHAPTER 8. CONCLUSIONS AND PERSPECTIVE

8.1. CONCLUSIONS

Although metal-organic frameworks (MOFs) have been extensively investigated, amorphization and glass formation of MOFs are discovered very recently. This new cutting field connects the scientific fields of materials chemistry including materials design for new structures and functionalities, and the amorphous physics such as applicability of the classic condensed matter theories. In this thesis, the following three aspects of the research related to amorphization and glass-forming MOFs are facilitated and developed: (1) Probing crystalline MOF synthesis influence on MOF amorphization (Chapter 3); (2) Understanding the physical properties of amorphous MOF with regard to dynamic relaxation, melting, glass transition, and phase transformation (Chapters 4 and 5); (3) Exploring and promoting the practical applications of MOF glasses (Chapters 6 and 7). Highlights are summarized as follows:

As ZIF-4 [Zn(Im)$_2$] with **cag** topology was the first reported MOF glass, the influence of synthesis time and temperature on the crystal formation of ZIF [Zn(Im)$_2$] isomorphs was systematically investigated via solution mixing method (Chapter 3). The synthesis time significantly affects the crystal identity of ZIF [Zn(Im)$_2$], whereas the varying synthesis temperature only influences the morphologies and porosities but not the crystal identity. The large surface area (>500 m^2 g^{-1}) of ZIF-zec and ZIF-nog is revealed. Both phases can be melt-quenched to MOF glasses before amorphized and recrystallized to ZIF-zni upon heating, as the case of ZIF-4.

With the aim of understanding the physical properties of MOF glasses, sub-T_g enthalpy relaxation of ZIF-62 glass is investigated (Chapter 4). The long relaxation time in the vicinity of T_g and the wide range of the stretching exponent indicate the high degree of structural heterogeneity in a_gZIF-62. Glass forming ability of a number of MOF candidates is also studied (Chapter 5). Most candidates decompose directly with no melting process upon heating. Fortunately, ZIF-76 and the isomorph ZIF-76-mbIm show the melting behavior, with the T_gs of a_gZIF-76 and a_gZIF-76-mbIm at 310 ˚C and 317 ˚C, respectively. Both phases are first discovered to be good MOF glass formers. Moreover, the glassy a_gZIF-76-mbIm exhibits permanent accessible porosity with reversible CO_2 and CH_4 uptakes, which opens a new category of porous glass materials. In addition, a Zr-based MOF, DUT-67, shows an irreversible first-order phase transformation at 230~260 ˚C upon heating, with an average activation energy of 183 kJ mol^{-1}. During the phase transformation, the preliminary network gradually becomes disordered, resulting in the enthalpy release.

Simultaneously, the new crystalline phase formed after desolvation is preserved, contributing to the retention of the pores for N_2 and CO_2 absorption.

Motivated by facilitating the application of MOF glasses, two areas of studies a conducted as discussed in Chapters 6 and 7. First, ZIF-4 and ZIF-62 phases are revealed to be well blended in liquid or amorphous state (Chapter 6), which develops the approach to tune the functionalities of MOF glasses by blending with another phase. Another mission is to improve the porosity of amorphous MOFs, especially the thermally induced ones. In Chapter 7, post-synthetic modification method was applied on ZIF-7 modified by linker exchange of imidazole. A composite ZIF-PSM composed by half of ZIF-7 and half of ZIF-62 is obtained, which is difficult to be *de novo* synthesized. The ZIF-PSM is kinetically stable as verified by a series of products, and can be thermally amorphized to a_TZIF-PSM at 500 ˚C. The surface area of the a_TZIF-PSM is larger than the reported values of thermal-driven amorphous MOFs. The retention of the pores in the a_TZIF-PSM is manifested by the SR-FIR results.

8.2. PERSPECTIVE

The outcomes of this thesis suggest the following research projects for future investigations.

With regard to the amorphous features, some theories for glasses, such as the constraint theory and thermodynamic and relaxation models, can be applied to MOF glass formers to understand the disordered structure. MOF glasses and ultrastable glasses may share structural similarities due to their high thermal stability. A recent study manifested that thermal-driven, ball-milling, and melt-quenching amorphous ZIF-4 samples showed no significant difference in structures by PDF and simulation results (22). We reckon that statistical approaches such as calorimetry or dynamical mechanical analysis could shed lights on the differences of the amorphous MOFs obtained from different routes. Certainly, glass forming ability of most MOFs is still under exploration. With the studies of more glass formers, mechanisms for melting and glass formation of MOFs would be facilitated.

To develop MOF glasses with enhanced properties, liquid blends of various types of MOF are worthy investigating. Blends in ZIF-62/UiO-66 and ZIF-62/MIL-53 have been studied, and the related results will be submitted to relevant journal soon. As a_gZIF-76-mbIm and a_TZIF-PSM show accessible porosities, MOFs with complex structures, such as ones with three types of organic ligands, could be perhaps vitrified with the retention of pores. In addition, for the purpose to facilitate applications of MOF glasses on membranes or in liquid, it is essential to investigate the chemical durability of MOF glasses in acidic and alkaline environment.

BIBLIOGRAPHY

1. Chae HK, Siberio-Pérez DY, Kim J, Go Y, Eddaoudi M, Matzger AJ, et al. A route to high surface area, porosity and inclusion of large molecules in crystals. Nature. 2004;427:523–7.

2. Cheetham AK, Rao CNR, Feller RK. Structural diversity and chemical trends in hybrid inorganic–organic framework materials. Chem Commun. 2006;0:4780–95.

3. Stock N, Biswas S. Synthesis of Metal-Organic Frameworks (MOFs): Routes to Various MOF Topologies, Morphologies, and Composites. Chem Rev. 2012;112:933–69.

4. Furukawa H, Cordova KE, O'Keeffe M, Yaghi OM. The Chemistry and Applications of Metal-Organic Frameworks. Science. 2013;341:1230444.

5. Bennett TD, Goodwin AL, Dove MT, Keen DA, Tucker MG, Barney ER, et al. Structure and Properties of an Amorphous Metal-Organic Framework. Phys Rev Lett. 2010;104:115503.

6. Bennett TD, Keen DA, Tan J-C, Barney ER, Goodwin AL, Cheetham AK. Thermal Amorphization of Zeolitic Imidazolate Frameworks. Angew Chem Int Ed. 2011;50:3067–71.

7. Bennett TD, Horike S. Liquid, glass and amorphous solid states of coordination polymers and metal–organic frameworks. Nat Rev Mater. 2018;1.

8. Tao H, Bennett TD, Yue Y. Melt-Quenched Hybrid Glasses from Metal–Organic Frameworks. Adv Mater. 2017;29:1601705.

9. Bennett TD, Tan J-C, Yue Y, Baxter E, Ducati C, Terrill NJ, et al. Hybrid glasses from strong and fragile metal-organic framework liquids. Nat Commun. 2015;6:8079.

10. Bennett TD, Yue Y, Li P, Qiao A, Tao H, Greaves NG, et al. Melt-Quenched Glasses of Metal–Organic Frameworks. J Am Chem Soc. 2016;138:3484–92.

11. Gaillac R, Pullumbi P, Beyer KA, Chapman KW, Keen DA, Bennett TD, et al. Liquid metal–organic frameworks. Nat Mater. 2017;16:nmat4998.

12. Gaillac R, Pullumbi P, Coudert F-X. Melting of Zeolitic Imidazolate Frameworks with Different Topologies: Insight from First-Principles Molecular Dynamics. J Phys Chem C. 2018;122:6730–6.

13. Umeyama D, Horike S, Inukai M, Itakura T, Kitagawa S. Reversible Solid-to-Liquid Phase Transition of Coordination Polymer Crystals. J Am Chem Soc. 2015;137:864–70.

14. Chen W, Horike S, Umeyama D, Ogiwara N, Itakura T, Tassel C, et al. Glass Formation of a Coordination Polymer Crystal for Enhanced Proton Conductivity and Material Flexibility. Angew Chem. 2016;128:5281–6.

15. Spielberg ET, Edengeiser E, Mallick B, Havenith M, Mudring A-V. (1-Butyl-4-methyl-pyridinium)[Cu(SCN)$_2$]: A Coordination Polymer and Ionic Liquid. Chem – Eur J. 2014;20:5338–45.

16. Depuydt D, Brooks NR, Schaltin S, Van Meervelt L, Fransaer J, Binnemans K. Silver-Containing Ionic Liquids with Alkylamine Ligands. ChemPlusChem. 2013;78:578–88.

17. Hirai Y, Nakanishi T, Kitagawa Y, Fushimi K, Seki T, Ito H, et al. Luminescent Coordination Glass: Remarkable Morphological Strategy for Assembled Eu(III) Complexes. Inorg Chem. 2015;54:4364–70.

18. Moriya M, Kato D, Sakamoto W, Yogo T. Structural Design of Ionic Conduction Paths in Molecular Crystals for Selective and Enhanced Lithium Ion Conduction. Chem – Eur J. 2013;19:13554–60.

19. Bennett TD, Cao S, Tan JC, Keen DA, Bithell EG, Beldon PJ, et al. Facile Mechanosynthesis of Amorphous Zeolitic Imidazolate Frameworks. J Am Chem Soc. 2011;133:14546–9.

20. Cao S, Bennett TD, Keen DA, Goodwin AL, Cheetham AK. Amorphization of the prototypical zeolitic imidazolate framework ZIF-8 by ball-milling. Chem Commun. 2012;48:7805–7.

21. Baxter EF, Bennett TD, Mellot-Draznieks C, Gervais C, Blanc F, Cheetham AK. Combined experimental and computational NMR study of crystalline and amorphous zeolitic imidazolate frameworks. Phys Chem Chem Phys. 2015;17:25191–6.

22. Keen DA, Bennett TD. Structural investigations of amorphous metal–organic frameworks formed via different routes. Phys Chem Chem Phys. 2018;20:7857–61.

23. Chapman KW, Halder GJ, Chupas PJ. Pressure-Induced Amorphization and Porosity Modification in a Metal−Organic Framework. J Am Chem Soc. 2009;131:17546–7.

24. Bennett TD, Todorova TK, Baxter EF, Reid DG, Gervais C, Bueken B, et al. Connecting defects and amorphization in UiO-66 and MIL-140 metal–organic frameworks: a combined experimental and computational study. Phys Chem Chem Phys. 2016;18:2192–201.

25. Ohtsu H, Bennett TD, Kojima T, Keen DA, Niwa Y, Kawano M. Amorphous–amorphous transition in a porous coordination polymer. Chem Commun. 2017;53:7060–3.

26. Yang F, Li W, Tang B. Facile synthesis of amorphous UiO-66 (Zr-MOF) for supercapacitor application. J Alloys Compd. 2018;733:8–14.

27. Bennett TD, Cheetham AK. Amorphous Metal–Organic Frameworks. Acc Chem Res. 2014;47:1555–62.

28. Cravillon J, Schröder CA, Nayuk R, Gummel J, Huber K, Wiebcke M. Fast Nucleation and Growth of ZIF-8 Nanocrystals Monitored by Time-Resolved In Situ Small-Angle and Wide-Angle X-Ray Scattering. Angew Chem Int Ed. 2011;50:8067–71.

29. Tsao C-S, Yu M-S, Chung T-Y, Wu H-C, Wang C-Y, Chang K-S, et al. Characterization of Pore Structure in Metal−Organic Framework by Small-Angle X-ray Scattering. J Am Chem Soc. 2007;129:15997–6004.

30. R. Ryder M, D. Bennett T, S. Kelley C, D. Frogley M, Cinque G, Tan J-C. Tracking thermal-induced amorphization of a zeolitic imidazolate framework via synchrotron in situ far-infrared spectroscopy. Chem Commun. 2017;53:7041–4.

31. W. Thornton A, E. Jelfs K, Konstas K, M. Doherty C, J. Hill A, K. Cheetham A, et al. Porosity in metal–organic framework glasses. Chem Commun. 2016;52:3750–3.

32. Park KS, Ni Z, Côté AP, Choi JY, Huang R, Uribe-Romo FJ, et al. Exceptional chemical and thermal stability of zeolitic imidazolate frameworks. Proc Natl Acad Sci. 2006;103:10186–91.

33. Kim H, Yang S, Rao SR, Narayanan S, Kapustin EA, Furukawa H, et al. Water harvesting from air with metal-organic frameworks powered by natural sunlight. Science. 2017;eaam8743.

34. Sava DF, Rodriguez MA, Chapman KW, Chupas PJ, Greathouse JA, Crozier PS, et al. Capture of Volatile Iodine, a Gaseous Fission Product, by Zeolitic Imidazolate Framework-8. J Am Chem Soc. 2011;133:12398–401.

35. Bennett TD, Saines PJ, Keen DA, Tan J-C, Cheetham AK. Ball-Milling-Induced Amorphization of Zeolitic Imidazolate Frameworks (ZIFs) for the Irreversible Trapping of Iodine. Chem - Eur J. 2013;19:7049–55.

36. Orellana-Tavra C, Baxter EF, Tian T, Bennett TD, Slater NKH, Cheetham AK, et al. Amorphous metal–organic frameworks for drug delivery. Chem Commun. 2015;51:13878–81.

37. Zhang C, Koros WJ. Zeolitic Imidazolate Framework-Enabled Membranes: Challenges and Opportunities. J Phys Chem Lett. 2015;6:3841–9.

38. Qiao A, Bennett TD, Tao H, Krajnc A, Mali G, Doherty CM, et al. A metal-organic framework with ultrahigh glass-forming ability. Sci Adv. 2018;4:eaao6827.

39. He M, Yao J, Liu Q, Zhong Z, Wang H. Toluene-assisted synthesis of RHO-type zeolitic imidazolate frameworks: synthesis and formation mechanism of ZIF-11 and ZIF-12. Dalton Trans. 2013;42:16608–13.

40. Lively RP, Dose ME, Thompson JA, McCool BA, Chance RR, Koros WJ. Ethanol and water adsorption in methanol-derived ZIF-71. Chem Commun. 2011;47:8667–9.

41. Wang F, Fu H-R, Kang Y, Zhang J. A new approach towards zeolitic tetrazolate-imidazolate frameworks (ZTIFs) with uncoordinated N-heteroatom sites for high CO_2 uptake. Chem Commun. 2014;50:12065–8.

42. Wu T, Bu X, Zhang J, Feng P. New Zeolitic Imidazolate Frameworks: From Unprecedented Assembly of Cubic Clusters to Ordered Cooperative Organization of Complementary Ligands. Chem Mater. 2008;20:7377–82.

43. Huang L, Xue M, Song Q, Chen S, Pan Y, Qiu S. Carbon dioxide selective adsorption within a highly stable mixed-ligand Zeolitic Imidazolate Framework. Inorg Chem Commun. 2014;46:9–12.

44. Banerjee R, Phan A, Wang B, Knobler C, Furukawa H, O’Keeffe M, et al. High-Throughput Synthesis of Zeolitic Imidazolate Frameworks and Application to CO_2 Capture. Science. 2008;319:939–43.

45. Peralta D, Chaplais G, Simon-Masseron A, Barthelet K, Pirngruber GD. Synthesis and adsorption properties of ZIF-76 isomorphs. Microporous Mesoporous Mater. 2012;153:1–7.

46. Bon V, Senkovska I, Baburin IA, Kaskel S. Zr- and Hf-Based Metal–Organic Frameworks: Tracking Down the Polymorphism. Cryst Growth Des. 2013;13:1231–7.

47. Drache F, Bon V, Senkovska I, Getzschmann J, Kaskel S. The modulator driven polymorphism of Zr(IV) based metal–organic frameworks. Phil Trans R Soc A. 2017;375:20160027.

48. Voorde BV de, Stassen I, Bueken B, Vermoortele F, Vos DD, Ameloot R, et al. Improving the mechanical stability of zirconium-based metal–organic frameworks by incorporation of acidic modulators. J Mater Chem A. 2014;3:1737–42.

49. Furukawa H, Gándara F, Zhang Y-B, Jiang J, Queen WL, Hudson MR, et al. Water Adsorption in Porous Metal–Organic Frameworks and Related Materials. J Am Chem Soc. 2014;136:4369–81.

50. Cheary RW, Coelho A. A fundamental parameters approach to X-ray line-profile fitting. J Appl Crystallogr. 1992;25:109–21.

51. McCusker LB, Von Dreele RB, Cox DE, Louër D, Scardi P. Rietveld refinement guidelines. J Appl Crystallogr. 1999;32:36–50.

52. Peralta D, Chaplais G, Simon-Masseron A, Barthelet K, Chizallet C, Quoineaud A-A, et al. Comparison of the Behavior of Metal–Organic Frameworks and Zeolites for Hydrocarbon Separations. J Am Chem Soc. 2012;134:8115–26.

53. Schweinefuß ME, Springer S, Baburin IA, Hikov T, Huber K, Leoni S, et al. Zeolitic imidazolate framework-71 nanocrystals and a novel SOD-type polymorph: solution mediated phase transformations, phase selection via coordination modulation and a density functional theory derived energy landscape. Dalton Trans. 2014;43:3528–36.

54. Ezugwu CI, Mousavi B, Asraf MA, Luo Z, Verpoort F. Post-synthetic modified MOF for Sonogashira cross-coupling and Knoevenagel condensation reactions. J Catal. 2016;344:445–54.

55. Lalonde MB, Mondloch JE, Deria P, Sarjeant AA, Al-Juaid SS, Osman OI, et al. Selective Solvent-Assisted Linker Exchange (SALE) in a Series of Zeolitic Imidazolate Frameworks. Inorg Chem. 2015;54:7142–4.

56. Oliver WC, Pharr GM. Measurement of hardness and elastic modulus by instrumented indentation: Advances in understanding and refinements to methodology. J Mater Res. 2004;19:3–20.

57. Tan JC, Bennett TD, Cheetham AK. Chemical structure, network topology, and porosity effects on the mechanical properties of Zeolitic Imidazolate Frameworks. Proc Natl Acad Sci. 2010;107:9938–43.

58. Soper AK. GudrunN and GudrunX: Programs for Correcting Raw Neutron and X-ray Diffraction Data to Differential Scattering Cross Section. Tech Rep. 2011;RAL-TR-2011-013.

59. Soper AK, Barney ER. Extracting the pair distribution function from white-beam X-ray total scattering data. J Appl Crystallogr. 2011;44:714–26.

60. Phan A, Doonan CJ, Uribe-Romo FJ, Knobler CB, O’Keeffe M, Yaghi OM. Synthesis, Structure, and Carbon Dioxide Capture Properties of Zeolitic Imidazolate Frameworks. Acc Chem Res. 2010;43:58–67.

61. Puškarić A, Katsenis AD, Mottillo C, Halasz I, Užarević K, Pham M-H, et al. *In situ* X-ray diffraction monitoring of a mechanochemical reaction reveals a unique topology metal-organic framework. Nat Commun. 2015;6:6662.

62. Hughes JT, Bennett TD, Cheetham AK, Navrotsky A. Thermochemistry of Zeolitic Imidazolate Frameworks of Varying Porosity. J Am Chem Soc. 2013;135:598–601.

63. Tian Y-Q, Zhao Y-M, Chen Z-X, Zhang G-N, Weng L-H, Zhao D-Y. Design and Generation of Extended Zeolitic Metal–Organic Frameworks (ZMOFs): Synthesis and Crystal Structures of Zinc(II) Imidazolate Polymers with Zeolitic Topologies. Chem - Eur J. 2007;13:4146–54.

64. Lewis DW, Ruiz-Salvador AR, Gómez A, Rodriguez-Albelo LM, Coudert F-X, Slater B, et al. Zeolitic imidazole frameworks: structural and energetics trends compared with their zeolite analogues. CrystEngComm. 2009;11:2272–6.

65. Miura H, Bon V, Senkovska I, Ehrling S, Watanabe S, Ohba M, et al. Tuning the gate-opening pressure and particle size distribution of the switchable

metal–organic framework DUT-8(Ni) by controlled nucleation in a micromixer. Dalton Trans. 2017;46:14002–11.

66. Burley JC, Duer MJ, Stein RS, Vrcelj RM. Enforcing Ostwald's rule of stages: Isolation of paracetamol forms III and II. Eur J Pharm Sci. 2007;31:271–6.

67. Akrap M, Kuzmanić N, Prlić-Kardum J. Effect of mixing on the crystal size distribution of borax decahydrate in a batch cooling crystallizer. J Cryst Growth. 2010;312:3603–8.

68. Ngai KL. Relaxation and Diffusion in Complex Systems. New York, NY: Springer New York; 2011. 853 p.

69. Shelby JE. Introduction to Glass Science and Technology. Royal Society of Chemistry; 2005. 316 p.

70. Yue YZ. Characteristic temperatures of enthalpy relaxation in glass. J Non-Cryst Solids. 2008;354:1112–8.

71. Kubaschewski O, Alcock CB, Spencer PJ. Materials thermochemistry. Pergamon Press; 1993. 384 p.

72. Wang L-M, Angell CA, Richert R. Fragility and thermodynamics in nonpolymeric glass-forming liquids. J Chem Phys. 2006;125:074505.

73. Gallino I, Schroers J, Busch R. Kinetic and thermodynamic studies of the fragility of bulk metallic glass forming liquids. J Appl Phys. 2010;108:063501.

74. Fan GJ, Löffler JF, Wunderlich RK, Fecht H-J. Thermodynamics, enthalpy relaxation and fragility of the bulk metallic glass-forming liquid Pd43Ni10Cu27P20. Acta Mater. 2004;52:667–74.

75. Wunderlich RK, Fecht H-J. Thermophysical Properties of Bulk Metallic Glass Forming Alloys in the Stable and Undercooled Liquid - A Microgravity Investigation. Mater Trans. 2001;42:565–78.

76. Suriñach S, Baro MD, Clavaguera-Mora MT, Clavaguera N. Thermodynamic and kinetic characterization of vitreous eutectic GeSe2-Sb2Te3 alloy. Thermochim Acta. 1985;85:175–8.

77. Wu D, Navrotsky A. Thermodynamics of metal-organic frameworks. J Solid State Chem. 2015;223:53–8.

78. Kittel C. Introduction to Solid State Physics. Wiley; 2004. 704 p.

79. Oliveira MJ de. Equilibrium Thermodynamics. 2nd ed. Berlin Heidelberg: Springer-Verlag; 2017.

80. Hu LN, Yue YZ. Secondary Relaxation Behavior in a Strong Glass. J Phys Chem B. 2008;112:9053–7.

81. Zhu F, Nguyen HK, Song SX, Aji DPB, Hirata A, Wang H, et al. Intrinsic correlation between β-relaxation and spatial heterogeneity in a metallic glass. Nat Commun. 2016;7:11516.

82. Debenedetti PG, Stillinger FH. Supercooled liquids and the glass transition. Nature. 2001;410:259–67.

83. Zhang Y, Hahn H. Study of the kinetics of free volume in $Zr_{45.0}Cu_{39.3}Al_{7.0}Ag_{8.7}$ bulk metallic glasses during isothermal relaxation by enthalpy relaxation experiments. J Non-Cryst Solids. 2009;355:2616–21.

84. Böhmer R, Ngai KL, Angell CA, Plazek DJ. Nonexponential relaxations in strong and fragile glass formers. J Chem Phys. 1993;99:4201–9.

85. Zhang YF, Hu LN, Liu SJ, Zhu CF, Yue YZ. Sub-T_g enthalpy relaxation in an extremely unstable oxide glass and its implication for structural heterogeneity. J Non-Cryst Solids. 2013;381:23–8.

86. Berberan-Santos M. A relaxation function encompassing the stretched exponential and the compressed hyperbola. 2008; Available from: https://arxiv.org/abs/0804.2702

87. Johnston DC. Stretched exponential relaxation arising from a continuous sum of exponential decays. Phys Rev B. 2006;74:184430.

88. Johnston DC, Baek S-H, Zong X, Borsa F, Schmalian J, Kondo S. Dynamics of Magnetic Defects in Heavy Fermion LiV_2O_4 from Stretched Exponential ^7Li NMR Relaxation. Phys Rev Lett. 2005;95:176408.

89. Kakalios J, Street RA, Jackson WB. Stretched-exponential relaxation arising from dispersive diffusion of hydrogen in amorphous silicon. Phys Rev Lett. 1987;59:1037–40.

90. Phillips JC. Stretched exponential relaxation in molecular and electronic glasses. Rep Prog Phys. 1996;59:1133.

91. Lupascu DC, Fedosov S, Verdier C, Rödel J, von Seggern H. Stretched exponential relaxation in perovskite ferroelectrics after cyclic loading. J Appl Phys. 2004;95:1386–90.

92. Qiao A, Tao H, Yue Y. Sub-T_g enthalpy relaxation in a milling-derived chalcogenide glass. J Am Ceram Soc. 2017;100:968–74.

93. Lu ZP, Li Y, Liu CT. Glass-forming tendency of bulk La–Al–Ni–Cu–(Co) metallic glass-forming liquids. J Appl Phys. 2003;93:286–90.

94. Zhang T, Ye F, Wang YL, Lin JP. Structural Relaxation of $La_{55}Al_{25}Ni_{10}Cu_{10}$ Bulk Metallic Glass. Metall Mater Trans A. 2008;39:1953–7.

95. Gallino I, Shah MB, Busch R. Enthalpy relaxation and its relation to the thermodynamics and crystallization of the $Zr_{58.5}Cu_{15.6}Ni_{12.8}Al_{10.3}Nb_{2.8}$ bulk metallic glass-forming alloy. Acta Mater. 2007;55:1367–76.

96. Sun QJ, Zhou C, Yue YZ, Hu LN. A Direct Link between the Fragile-to-Strong Transition and Relaxation in Supercooled Liquids. J Phys Chem Lett. 2014;5:1170–4.

97. Qiao JC, Pelletier JM. Enthalpy relaxation in $Cu_{46}Zr_{45}Al_7Y_2$ and $Zr_{55}Cu_{30}Ni_5Al_{10}$ bulk metallic glasses by differential scanning calorimetry (DSC). Intermetallics. 2011;19:9–18.

98. Angell CA. Relaxation in liquids, polymers and plastic crystals - strong/fragile patterns and problems. J Non-Cryst Solids. 1991;131–133, Part 1:13–31.

99. Chen Z, Zhao L, Tu W, Li Z, Gao Y, Wang L-M. Dependence of calorimetric glass transition profiles on relaxation dynamics in non-polymeric glass formers. J Non-Cryst Solids. 2016;433:20–7.

100. Xu D, Liu Y, Tian Y, Wang L-M. Communication: Enthalpy relaxation in a metal-organic zeolite imidazole framework (ZIF-4) glass-former. J Chem Phys. 2017;146:121101.

101. Du Y, Wooler B, Nines M, Kortunov P, Paur CS, Zengel J, et al. New High- and Low-Temperature Phase Changes of ZIF-7: Elucidation and Prediction of the Thermodynamics of Transitions. J Am Chem Soc. 2015;137:13603–11.

102. Saha S, Springer S, Schweinefuß ME, Pontoni D, Wiebcke M, Huber K. Insight into Fast Nucleation and Growth of Zeolitic Imidazolate Framework-71 by In Situ Time-Resolved Light and X-ray Scattering Experiments. Cryst Growth Des. 2016;16:2002–10.

103. Zhao N, Li P, Mu X, Liu C, Sun F, Zhu G. Facile synthesis of an ultra-stable metal-organic framework with excellent acid and base resistance. Faraday Discuss. 2017;201:63–70.

104. Lin R-B, Chen D, Lin Y-Y, Zhang J-P, Chen X-M. A Zeolite-Like Zinc Triazolate Framework with High Gas Adsorption and Separation Performance. Inorg Chem. 2012;51:9950–5.

105. Xiong S, Gong Y, Wang H, Wang H, Liu Q, Gu M, et al. A new tetrazolate zeolite-like framework for highly selective CO_2/CH_4 and CO_2/N_2 separation. Chem Commun. 2014;50:12101–4.

106. Li M-Y, Wang F, Zhang J. Zeolitic Tetrazolate-Imidazolate Frameworks with High Chemical Stability for Selective Separation of Small Hydrocarbons. Cryst Growth Des. 2016;16:3063–6.

107. Cavka JH, Jakobsen S, Olsbye U, Guillou N, Lamberti C, Bordiga S, et al. A New Zirconium Inorganic Building Brick Forming Metal Organic Frameworks with Exceptional Stability. J Am Chem Soc. 2008;130:13850–1.

108. Guillerm V., Ragon F., Dan-Hardi M., Devic T., Vishnuvarthan M., Campo B., et al. A Series of Isoreticular, Highly Stable, Porous Zirconium Oxide Based Metal–Organic Frameworks. Angew Chem Int Ed. 2012;51:9267–71.

109. Zhu X, Gu J, Wang Y, Li B, Li Y, Zhao W, et al. Inherent anchorages in UiO-66 nanoparticles for efficient capture of alendronate and its mediated release. Chem Commun. 2014;50:8779–82.

110. Vermoortele F, Bueken B, Le Bars G, Van de Voorde B, Vandichel M, Houthoofd K, et al. Synthesis modulation as a tool to increase the catalytic activity of metal-organic frameworks: the unique case of UiO-66(Zr). J Am Chem Soc. 2013;135:11465–8.

111. Bai Y, Dou Y, Xie L-H, Rutledge W, Li J-R, Zhou H-C. Zr-based metal–organic frameworks: design, synthesis, structure, and applications. Chem Soc Rev. 2016;45:2327–67.

112. Wu H, Chua YS, Krungleviciute V, Tyagi M, Chen P, Yildirim T, et al. Unusual and Highly Tunable Missing-Linker Defects in Zirconium Metal–Organic Framework UiO-66 and Their Important Effects on Gas Adsorption. J Am Chem Soc. 2013;135:10525–32.

113. Drache F, Bon V, Senkovska I, Marschelke C, Synytska A, Kaskel S. Postsynthetic Inner-Surface Functionalization of the Highly Stable

Zirconium-Based Metal–Organic Framework DUT-67. Inorg Chem. 2016;55:7206–13.

114. Zhuang G, Bai J, Tan L, Huang H, Gao Y, Zhong X, et al. Preparation and catalytic properties of Pd nanoparticles supported on micro-crystal DUT-67 MOFs. RSC Adv. 2015;5:32714–9.

115. Longley L, Collins SM, Zhou C, Smales GJ, Norman SE, Brownbill NJ, et al. Liquid phase blending of metal-organic frameworks. Nat Commun. 2018;9:2135.

116. Ryder MR, Van de Voorde B, Civalleri B, Bennett TD, Mukhopadhyay S, Cinque G, et al. Detecting Molecular Rotational Dynamics Complementing the Low-Frequency Terahertz Vibrations in a Zirconium-Based Metal-Organic Framework. Phys Rev Lett. 2017;118:255502.

117. Kissinger HE. Reaction Kinetics in Differential Thermal Analysis. Anal Chem. 1957;29:1702–6.

118. Svoboda R, Málek J. Is the original Kissinger equation obsolete today? J Therm Anal Calorim. 2013;115:1961–7.

119. Ruitenberg G. Applying Kissinger analysis to the glass transition peak in amorphous metals. Thermochim Acta. 2003;404:207–11.

120. Zhou C, Yue Y, Hu L. Revealing the connection between the slow β relaxation and sub-T_g enthalpy relaxation in metallic glasses. J Appl Phys. 2016;120:225110.

121. Angell CA. Formation of Glasses from Liquids and Biopolymers. Science. 1995;267:1924–35.

122. Frauenfelder H, Bishop AR, Garcia A, Perelson A, Schuster P, Sherrington D, et al. Landscape paradigms in physics and biology. Phys Nonlinear Phenom. 1997;107:117–439.

123. Horike S, Umeyama D, Kitagawa S. Ion Conductivity and Transport by Porous Coordination Polymers and Metal–Organic Frameworks. Acc Chem Res. 2013;46:2376–84.

124. Voorde BV de, Bueken B, Denayer J, Vos DD. Adsorptive separation on metal–organic frameworks in the liquid phase. Chem Soc Rev. 2014;43:5766–88.

125. Wang L-M, Tian Y, Liu R, Richert R. Structural Relaxation Dynamics in Binary Glass-Forming Molecular Liquids with Ideal and Complex Mixing Behavior. J Phys Chem B. 2010;114:3618–22.

126. Gao P, Tu W, Li P, Wang L-M. Variation in entropies of fusion driven by mixing in binary glass forming eutectics. J Alloys Compd. 2018;736:12–6.

127. Mayhew EJ, Neal CH, Lee S-Y, Schmidt SJ. Glass transition prediction strategies based on the Couchman-Karasz equation in model confectionary systems. J Food Eng. 2017;214:287–302.

128. Kalogeras IM, Brostow W. Glass transition temperatures in binary polymer blends. J Polym Sci Part B Polym Phys. 2009;47:80–95.

129. Wang WH. The elastic properties, elastic models and elastic perspectives of metallic glasses. Prog Mater Sci. 2012;57:487–656.

130. Mattern N, Schöps A, Kühn U, Acker J, Khvostikova O, Eckert J. Structural behavior of Cu_xZr_{100-x} metallic glass (x=35−70). J Non-Cryst Solids. 2008;354:1054–60.

131. Zheng Q, Potuzak M, Mauro JC, Smedskjaer MM, Youngman RE, Yue Y. Composition–structure–property relationships in boroaluminosilicate glasses. J Non-Cryst Solids. 2012;358:993–1002.

132. Liu H, M. Smedskjaer M, Tao H, R. Jensen L, Zhao X, Yue Y. A medium range order structural connection to the configurational heat capacity of borate–silicate mixed glasses. Phys Chem Chem Phys. 2016;18:10887–95.

133. Zheng Q, Smedskjaer MM, Youngman RE, Potuzak M, Mauro JC, Yue Y. Influence of aluminum speciation on the stability of aluminosilicate glasses against crystallization. Appl Phys Lett. 2012;101:041906.

134. Couchman PR, Karasz FE. A Classical Thermodynamic Discussion of the Effect of Composition on Glass-Transition Temperatures. Macromolecules. 1978;11:117–9.

135. Gordon M, Taylor JS. Ideal copolymers and the second-order transitions of synthetic rubbers. i. non-crystalline copolymers. J Appl Chem. 1952;2:493–500.

136. Tu W, Wang Y, Li X, Zhang P, Tian Y, Jin S, et al. Unveiling the Dependence of Glass Transitions on Mixing Thermodynamics in Miscible Systems. Sci Rep. 2015;5:8500.

137. Longley L, Collins SM, Smales GJ, Erucar I, Qiao A, Hou J, et al. Flux Melting of Metal-Organic Frameworks. 2018; Available from: http://europepmc.org/abstract/ppr/ppr55319

138. Beldon PJ, Fábián L, Stein RS, Thirumurugan A, Cheetham AK, Friščić T. Rapid Room-Temperature Synthesis of Zeolitic Imidazolate Frameworks by Using Mechanochemistry. Angew Chem Int Ed. 2010;49:9640–3.

139. Gustafsson M, Zou X. Crystal formation and size control of zeolitic imidazolate frameworks with mixed imidazolate linkers. J Porous Mater. 2012;20:55–63.

140. Yuan W, Friščić T, Apperley D, James SL. High Reactivity of Metal–Organic Frameworks under Grinding Conditions: Parallels with Organic Molecular Materials. Angew Chem Int Ed. 2010;49:3916–9.

141. Islamoglu T, Goswami S, Li Z, Howarth AJ, Farha OK, Hupp JT. Postsynthetic Tuning of Metal–Organic Frameworks for Targeted Applications. Acc Chem Res. 2017;50:805–13.

142. Spencer EC, Angel RJ, Ross NL, Hanson BE, Howard JAK. Pressure-Induced Cooperative Bond Rearrangement in a Zinc Imidazolate Framework: A High-Pressure Single-Crystal X-Ray Diffraction Study. J Am Chem Soc. 2009;131:4022–6.

143. Zhao P, Lampronti GI, Lloyd GO, Wharmby MT, Facq S, Cheetham AK, et al. Phase Transitions in Zeolitic Imidazolate Framework 7: The Importance of Framework Flexibility and Guest-Induced Instability. Chem Mater. 2014;26:1767–9.

144. Zeng M, Chai Z, Deng X, Li Q, Feng S, Wang J, et al. Core–shell CdS@ZIF-8 structures for improved selectivity in photocatalytic H_2 generation from formic acid. Nano Res. 2016;9:2729–34.

145. He X, Yang C, Wang D, Iii SEG, Chen D-R, Wang W-N. Facile synthesis of ZnO@ZIF core–shell nanofibers: crystal growth and gas adsorption. CrystEngComm. 2017;19:2445–50.

146. Wu X, Xiong S, Mao Z, Hu S, Long X. A Designed ZnO@ZIF-8 Core–Shell Nanorod Film as a Gas Sensor with Excellent Selectivity for H2 over CO. Chem - Eur J. 2017;23:7969–75.

147. Yang Xinyu, Yuan Shuai, Zou Lanfang, Drake Hannah, Zhang Yingmu, Qin Junsheng, et al. One-Step Synthesis of Hybrid Core–Shell Metal–Organic Frameworks. Angew Chem Int Ed. 2018;57:3927–32.

148. Liu H, Youngman RE, Kapoor S, Jensen LR, Smedskjaer MM, Yue Y. Nanophase separation and structural ordering in silica-rich mixed network former glasses. Phys Chem Chem Phys. 2018;20:15707–17.

149. Thompson JA, Blad CR, Brunelli NA, Lydon ME, Lively RP, Jones CW, et al. Hybrid Zeolitic Imidazolate Frameworks: Controlling Framework Porosity and Functionality by Mixed-Linker Synthesis. Chem Mater. 2012;24:1930–6.

150. van den Bergh J, Gücüyener C, Pidko EA, Hensen EJM, Gascon J, Kapteijn F. Understanding the Anomalous Alkane Selectivity of ZIF-7 in the Separation of Light Alkane/Alkene Mixtures. Chem - Eur J. 2011;17:8832–40.

151. Şahin F, Topuz B, Kalıpçılar H. Synthesis of ZIF-7, ZIF-8, ZIF-67 and ZIF-L from recycled mother liquors. Microporous Mesoporous Mater. 2018;261:259–67.

152. Widmer RN, Lampronti GI, Anzellini S, Gaillac R, Farsang S, Zhou C, et al. Pressure Promoted Low-Temperature Melting of Metal-Organic Frameworks. 2018; Available from: doi:10.26434/chemrxiv.6541190.v3

153. Ryder MR, Civalleri B, Bennett TD, Henke S, Rudić S, Cinque G, et al. Identifying the Role of Terahertz Vibrations in Metal-Organic Frameworks: From Gate-Opening Phenomenon to Shear-Driven Structural Destabilization. Phys Rev Lett. 2014;113:215502.

LIST OF PUBLICATIONS

PUBLICATIONS IN PEER-REVIEW JOURNALS

1) **Zhou C.** Stepniewska M., Sørensen J. M., Scarpa L., Magnacca G., Boffa V., Bennett T. D., Yue Y. Z., Polymorph formation for a zeolitic imidazolate framework composition - $Zn(Im)_2$. *Microporous and Mesoporous Materials*, 265, 57-62 (2018).
2) **Zhou C.**, Stepniewska M., Longley L., Ashling C. W., Chater P. A., Keen D. A., Bennett T. D., Yue Y. Z., Thermodynamic Features and Enthalpy Relaxation in a Metal-Organic Framework Glass. *Physical Chemistry Chemical Physics*, 20, 18291-18296 (2018).
3) Longley L., Collins S. M., **Zhou C.**, Smales G. J., Norman S. E., Brownbill N. J., Ashling C. W., Chater P. A., Tovey R., Schönlieb C., Headen T. F., Terrill N. J., Yue Y., Smith A. J., Blanc F., Keen D. A., Midgley P. A., Bennett T. D., Liquid Phase Blending of Metal-Organic Frameworks. *Nature Communications*, 9, 2153 (2018).
4) **Zhou C.**, Longley L., Krajnc A., Smales G. J., Qiao A., Erucar I., Doherty C. M., Thornton A. W., Hill A. J., Ashling C. W., Qazvini O. T., Lee S. J., Chater P. A., Terrill N. J., Smith A. J., Yue Y., Mali G., Keen D. A., Telfer S. G., Bennett T. D., Metal-Organic Framework Glasses with Permanent Accessible Porosity. *Nature Communications, in press.*
5) Widmer R. N., Lampronti G. I., Anzellini S., Gaillac R., Farsang S., **Zhou C.**, Belenguer A. M., Palmer H., Kleppe A. K., Wharmby M. T., Redfern S. A., Coudert F. -X., MacLeod S. G., Bennett T. D., Pressure Promoted Low-Temperature Melting of Metal-Organic Frameworks. *10.26434/chemrxiv.6541190.v3*, *Nature Materials, under review.*
6) Hou J., Ashling C. W., Collins S. M., Krajnc A., **Zhou C.**, Longley L., Johnstone D. N., Chater P. A., Li S., Coudert F. -X., Keen D. A., Midgley P. A., Mali G., Chen V., Bennett T. D., Metal-Organic Framework Crystal-Glass Composites, *10.26434/chemrxiv.7093862.v1*, *Science, under review.*
7) Hou J., Sutrisna P. D., Wang T., Gao S., Li Q., **Zhou C.**, Sun S., Yang H. C., Wei. F., Ruggiero M. T., Zeitler J. A., Cheetham A. K., Liang K., Chen V., Unraveling the interfacial structure-performance correlation of flexible metal-organic framework membranes on polymeric substrates, *Chemistry of Science, under review.*
8) **Zhou C.**, Yue Y. Z., Hu L. N., Revealing the connection between the slow β relaxation and sub-T_g enthalpy relaxation in metallic glasses. *Journal of Applied Physics,* 120, 225110 (2016).

ORAL AND POSTER PRESENTATIONS AT CONFERENCES

1) 67th Lindau Nobel Laureate Meeting - Chemistry, Lindau, Germany (2017).
2) **Zhou C.**, Hou J. W., Yue. Y. Z., Bennett T. D., Metal-Organic Framework Glass after Post-Synthetic Modification. **Oral**: *the 15th International Conference on the Physics of Non-Crystalline Solids (PNCS) and the 14th European Society of Glass Conference (ESG)*, St. Malo, France (2018).
3) **Zhou C.**, Bennett T. D., Yue Y. Z., Enthalpy Relaxation and Theromdynamic Features in a Metal-organic Framework Glass. **Poster**: *Dynamics of Glass-Forming Liquids: Will theory and experiment ever meet?* Copenhagen, Denmark (2017).
4) Yue Y. Z., Qiao A., **Zhou C.**, Bennett T. D., Tao H. Z., Greaves N., Glass-Forming Metal-Organic Frameworks. **Oral**; **Zhou C.**, Bennett T. D., Yue Y. Z., Glass transition in Metal-Organic Framework Glasses. **Poster**: *8th International Discussion Meeting on Relaxations in Complex Systems (8 IDMRCS)*, Wisla, Poland (2017).
5) **Zhou C.**, Stepniewska M., Bennett T. D., Yue Y. Z., Crystal Formation and Glass transition of Zeolitic Imidazolate Frameworks. **Poster**: *2nd European Conference on Metal Organic Frameworks and Porous Polymers (2nd EuroMOF)*, Delft, Netherlands (2017).
6) **Zhou C.**, Hu L. N., Yue Y. Z., A Hyperquenching-calorimetric Method to Determine the Activation energy of Slow β Relaxation in Metallic Glasses. **Oral**: *24th International Congress on Glass (24 ICG)*, Shanghai, China (2016).

AWARD

1) Elite Research Travel Scholarship (EliteForsk-rejsestipendier) from Danish Ministry of Science (Uddannelses- og Forskningsministeriet) (2017)

PAPER I

Microporous and Mesoporous Materials 265 (2018) 57–62

Contents lists available at ScienceDirect

Microporous and Mesoporous Materials

journal homepage: www.elsevier.com/locate/micromeso

Polymorph formation for a zeolitic imidazolate framework composition - Zn(Im)$_2$

Chao Zhou[a], Malwina Stepniewska[a], Jens Martin Sørensen[a], Luca Scarpa[a], Giuliana Magnacca[b], Vittorio Boffa[a], Thomas D. Bennett[c], Yuanzheng Yue[a,]*

[a] Department of Chemistry and Bioscience, Aalborg University, DK-9220 Aalborg, Denmark
[b] Department of Chemistry and NIS Centre, University of Turin, 10125 Turin, Italy
[c] Department of Materials Science and Metallurgy, University of Cambridge, CB3 0FS, UK

ARTICLE INFO

Keywords:
Zeolitic imidazolate framework
Synthesis conditions
Morphology
Porosity
MOF glass

ABSTRACT

We study the effect of synthesis time and temperature on the crystal formation, morphology and size of zeolitic imidazolate frameworks (ZIFs) with the Zn(Im)$_2$ composition by using the solution mixing method. The crystal structure, morphology and thermodynamic properties of the ZIFs were characterized by powder X-ray diffraction, scanning electron microscopy and nitrogen sorption isotherms. Our results indicate that the synthesis time significantly influences the structure and topology of crystal products. The crystal structure transforms from ZIF-coi to the progressively denser polymorphs (ZIF-zec, ZIF-nog and ZIF-zni) upon increasing synthesis time from 18 to 120 hours at 10 °C, in accordance with Ostwald's step rule. Increasing synthesis temperature does not change the formation of the ZIF-zec crystals but affects their morphologies and porosities. Both ZIF-nog and ZIF-zec exhibit relatively large surface areas ($> 500\,m^2/g$). Furthermore, heating ZIF-nog and ZIF-zec causes recrystallization to ZIF-zni and subsequent melting. Quenching the MOF-liquid results in Zn(Im)$_2$ glass. This work helps to understand and control the crystal formation of ZIFs, and reveals two new MOF glass formers.

1. Introduction

Zeolite imidazolate frameworks (ZIFs), a subset of metal-organic frameworks (MOFs), have attracted attention owing to their high thermal stability, chemical stability and surface area compared to many of other MOFs [1,2]. Such characteristics have led to potential applications in gas storage [3–6], separation [7–9], catalysis [10,11] and chemical sensing [12–14]. ZIFs have extended three-dimensional structures with tetrahedral topologies, which are built up by metallic nodes (M = e.g. Zn^{2+}, Co^{2+}, Cu^{2+}, Cd^{2+}) connected by imidazolate (Im, $C_3H_3N_2^-$) linkers [1,15]. Polymorphism in the family has been extensively observed [16], and, like across the MOF family [17], synthetic conditions such as synthesis time, temperature, concentration and pressure are used to control the precise nature of the formed polymorphs [18–20].

For example, it has been observed that the mechanochemical synthesis of ZIF-8 causes amorphization [21], before subsequent recrystallization to dense polymorphs with the **dia** or **kat** topologies [22]. A second *in-situ* study shows that Im or 2-ethylimidazole based ZIFs also undergo polymorphic transitions, and the solvent amount influences the dynamics of the formation of the ZIFs [23]. The crystal size and morphology of the polymorphs formed are also of great importance, with respect to their proposed applications. For instance, the gate opening pressure in a porous and flexible framework, DUT-8, is significantly influenced by the crystal size [24].

The effect of synthesis conditions on the ZIF structure, however, has not been fully understood. ZIF-4 [Zn(Im)$_2$], which possesses the same **cag** topology as the mineral variscite CaGa$_2$O$_4$, is of current interest due to its structural collapse [25]. In particular, it has been observed to undergo polyamorphization, recrystallization and melting before decomposition upon heating. The glass formed by quenching the ZIF-4 liquid is the first-reported hybrid glass in contrast to the conventional melt-quenched glass families (inorganic, metallic, organic systems) [26,27]. Other [Zn(Im)$_2$] polymorphs possess different network topologies, such as **cag**, **coi**, **crb**, **dft**, **gis**, **mer**, **nog**, **zec** and **zni** [16], and have been found to display an array of different behaviours on heating [28,29]. Calorimetric and computational studies have ordered these polymorphs in terms of density and enthalpy relative to the **zni** ground state [30–32], though a synthetic study of their formation conditions has, to the best of our knowledge, not yet been attempted.

Accordingly, here we study the influence of the synthesis conditions (time and temperature) on the crystal formation of ZIFs with the Zn

---

* Corresponding author.
E-mail address: yy@bio.aau.dk (Y. Yue).

https://doi.org/10.1016/j.micromeso.2018.01.038
Received 8 December 2017; Received in revised form 5 January 2018; Accepted 31 January 2018

$(Im)_2$ composition, by using a solution mixing method. Specifically, we found that at the synthesis temperature of 10 °C, different synthesis times lead to products with different topologies, whereas altering the synthesis temperature from 10 to 35 °C only affects the crystal morphologies and porosities of the products but does not change the crystal identity (ZIF-zec). As part of the study, we obtained two types of ZIFs, namely, ZIF-zec and ZIF-nog, and their glass-forming ability has not been reported. Powder X-ray diffraction and calorimetric results demonstrate that both undergo amorphization and recrystallization to ZIF-zni upon heating, and vitrification upon quenching as in the case of ZIF-4.

2. Experimental procedure

2.1. Synthesis

A solution mixing method was used to synthesize ZIFs with the $Zn(Im)_2$ composition in the present work [33]. In all synthetic procedures, 1.097 g of zinc(II) acetate dihydrate ($Zn(Ac)_2$•$2H_2O$, 5 mmol) was dissolved in 25 mL of n-propylamine, and 681 mg of imidazole (10 mmol) was dissolved in 25 mL of N,N-diethylformamide. The zinc acetate and imidazole solutions were then mixed together with magnetic stirrer (~600 rpm). Details of the synthesis time and temperature of each samples are given in Table 1. Colourless products were washed three times with dichloromethane and then the samples were filtered in vacuum with ceramic filters. The obtained products were dried in fume hood at room temperature (~23 °C) overnight. The yields of product from each synthesis process were calculated according to the molar ratio of zinc, as given in Table 1.

2.2. Characterization

Powder X-ray diffraction (PXRD) measurements of the samples were performed on a PANalytical empyrean X-ray diffractometer with Cu $K\alpha$ (λ = 1.5406 Å) radiation. The PXRD patterns were collected in the 2θ range of 5-50° with a step size of 0.013°. Thermodynamic properties were determined by differential scanning calorimetry (DSC) and thermogravimetry (TGA) using Netzsch STA 404 C upon heating in argon atmosphere. The upscan rate for all DSC and TGA measurements was 10 K/min. Scanning electron microscopy (SEM) measurements were conducted using Zeiss EVO 60 SEM. For observations, samples were coated with a ~15 nm thick gold layer. Surface area and nitrogen absorption-desorption isotherm measurements were performed using a Micrometrics gas-volumetric apparatus (ASAP 2020) at liquid nitrogen temperature (77 K). Samples were degassed for 4 h at 30 °C and then under vacuum for 12 h at 100 °C before starting the absorption measurements up to a maximum pressure of 1 bar. Densities were determined by using a Micromeritics AccuPyc 1340 helium pycnometer. Liquid-state ^{1}H nuclear magnetic resonance (NMR) spectra of digested ZIF-nog and ZIF-zec crystals and glasses ($DCl/D_2O/DMSO$-d_6) were recorded on a Bruker DPX600 Advance spectrometer operating at a frequency of 600 MHz. Fourier transform-infrared (FTIR) spectra of the ZIF-nog and ZIF-zec samples were performed on a Varian 640 IR spectrophotometer in transmittance mode with the KBr technique (KBr:sample = 100:1).

Table 1
Synthesis conditions, topology, space group, and yield of the product of each process.

Sample No.	Time/hour	Temp/°C	Topology	Space group	Yield/%
S1	0.083	23	amorphous	–	41
S2	18	10	coi + cag	$I\ 4_1 + P$ bca	44
S3	24	10	zec	$C\ 2/c$	50
S4	48	10	nog	$P\ 2_1/n$	48
S5	120	10	zni	$I\ 4_1$ cd	66
S6	24	15	zec	$C\ 2/c$	47
S7	24	23	zec	$C\ 2/c$	50
S8	24	30	zec	$C\ 2/c$	90
S9	24	35	zec	$C\ 2/c$	58

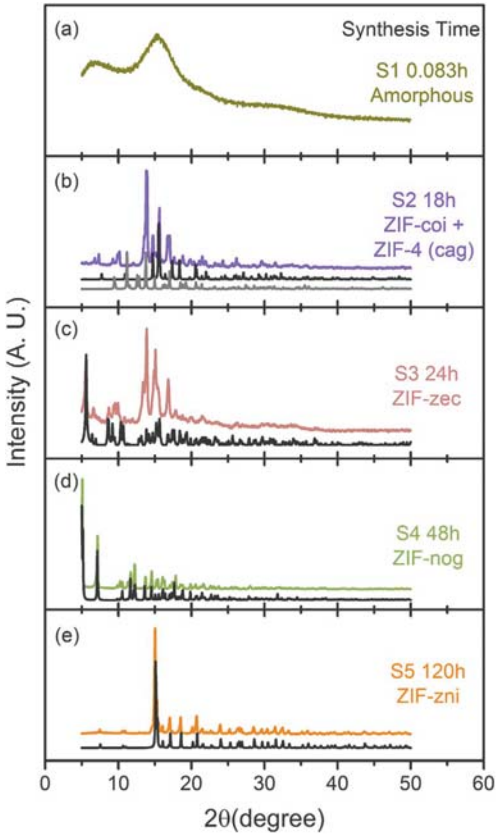

Fig. 1. Experimental and simulated (black) PXRD patterns of the samples S1–S5 obtained after different synthesis time and simulated spectra. Synthesis durations: (a) 0.083 h; (b) 18 h; (c) 24 h; (d) 48 h; and (e) 120 h.

3. Results and discussion

3.1. Influence of the synthesis time on the crystal formation

The synthesis of ZIFs [$Zn(Im)_2$] was conducted by employing synthesis durations from 0.083 to 120 h at 10 °C. The powder X-ray diffraction patterns are presented in Fig. 1, from which the different identities of the products were elucidated. Fig. 1(a) shows a broad hump at ca. 15° on the PXRD pattern, indicating the amorphous feature of S1. This suggests that a synthesis time of 0.083 h is not enough for the nucleation of a crystalline region. In Fig. 1(b)–(e) clear Bragg peaks are observed, demonstrating that the S2–S5 samples have crystalline structures. The crystal identity of each sample is assigned by comparing the experimental spectra with the simulated ones. S2 synthesized for 18 h is therefore assigned as mixed phases of ZIF-4 (cag topology) and ZIF-[$Zn(Im)_2$]-coi (CCDC code: EQOCOC) [1,33]. With an increase of the synthesis time, the crystal topology transforms to ZIF-[$Zn(Im)_2$]-zec (HICGEG) and to ZIF-[$Zn(Im)_2$]-nog (HIFWAV), corresponding to the synthesis durations of 24 and 48 h, respectively [33]. Additionally, liquid-state ^{1}H NMR spectra also confirm the presence of the imidazole

Fig. 2. SEM micrographs of S1–S5 from left to right. Each scale bar corresponds to 10 μm.

ligand in the two frameworks (See Figs. S1-S2). To make their crystal names convenient, we omit their composition ([Zn(Im)$_2$]) hereafter, and name the crystals according to their topologies, e.g ZIF-zec and ZIF-nog [16]. Furthermore, the 120-h synthesis was performed and S5 was obtained. The PXRD pattern of S5 signifies its crystalline structure as ZIF-zni, the most thermodynamically stable of the ZIFs family [32].

Crystal morphologies were characterized by SEM, and micrographs of representative particles of S1–S5 are shown in Fig. 2. Particles of S1 are ill defined, and their average size is smaller than 1 μm. The SEM micrographs of S2–S5 present clear edges and planes, indicating the crystalline features of these samples. In details, the micrograph of S2 shows that the morphology of S2 has a rod-like shape with a particle size range of 5–20 μm. The S3 sample presents agglomerated crystals with an octahedral-like shape of 2–5 μm. The morphology of S4 demonstrates that ZIF-nog crystal has a needle-like shape, associated with its simulated morphology from its crystallographic information [33]. Upon 120 h synthesis, the ZIF-zni has a morphology aggregated by granual-like particles with a size of 5–10 μm. The phase transformation with synthesis time can be related to the Ostwald's rule of stages, in which the least stable crystals form first, and then subsequently transform to metastable and stable polymorphs [34]. Figs. 1–2 indicate that synthesis time has a great influence on the crystal formation of ZIFs [Zn(Im)$_2$].

3.2. Influence of the synthesis temperature on the crystal formation

Compared to the kinetic influence on the crystal formation by altering the synthesis time, thermodynamic factors for ZIF synthesis can be studied by changing the synthesis temperature. Since ZIF-zec is the first monocrystalline product we obtained by prolonging the synthesis time from 18 to 24 h at 10 °C, it is regarded as a kinetically stable topology. Taken ZIF-zec as an example, we explore the effects of synthesis temperature on the crystal formation of ZIFs [Zn(Im)$_2$].

Samples S6–S9 were obtained by increasing the synthesis temperature from 15 to 35 °C for the synthesis time of 24 h. The PXRD patterns for those samples and S3 synthesized at 10 °C are shown in Fig. 3. Rietveld refinements of the PXRD data in Fig. 3 confirm the identity of all as ZIF-zec (Fig. S5). The PXRD patterns of S3 and S6 suggest that they are slightly less crystalline considering the lower intensity of their Bragg peak at 2θ = 5.64° associated with the (1 1 0) plane. Fig. 4 shows that ZIF-zec is thermodynamically stable and the crystal phase is not sensitive to the synthesis temperature.

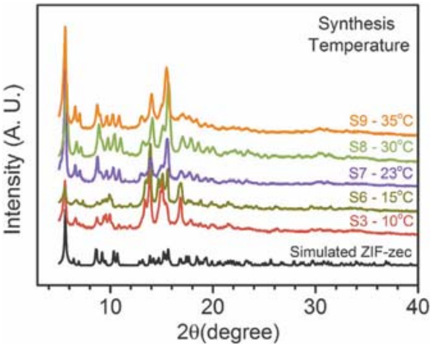

Fig. 3. Experimental PXRD data of samples S3 and S6–S9 synthesized at different temperature for 24 h. Simulated XRD pattern of ZIF-zec is shown in black.

SEM micrographs of samples S6–S9 are presented in Fig. 4. The micrographs of S6, S8, and S9, corresponding to the synthesis temperature of 15, 30, and 35 °C, respectively, show rice-like shapes in aggregated particles with about 2–5 μm. Their morphologies are also similar to that of S3 obtained at the synthesis temperature of 10 °C (Fig. 2). The S7 sample, however, shows a brick-like morphology and has a relatively large particle size without aggregation (~5 μm). To compare their morphology, cell volume and crystal size of each sample are calculated through the Rietveld refinements and the Scherrer equation, respectively (Table S1). It is seen that S7 has the largest average crystal size of 261.6 nm, whereas other samples only have the average crystal sizes of 65–115 nm, in accordance with the SEM results. That is, both the SEM morphologies and the calculated crystal size demonstrate that S7 synthesized at 23 °C has a relatively larger particle size compared to other ZIF-zec samples.

3.3. Porosity of samples

Nitrogen absorption measurements on all samples were carried out to study the porosity and pore size of the samples. Fig. 5 shows the nitrogen absorption-desorption and pore size distribution results of S1–S9. Nitrogen absorption isotherms of all samples show a typical type-I behaviour. Brunauer–Emmett–Teller (BET) surface area, Langmuir model surface area, and micropore volume were determined from the nitrogen absorption isotherms (Table 2). Densities of all samples measured by a helium pycnometer are also given in Table 2. Only ZIF-nog and ZIF-zec have a higher surface area (the pore size of ~1 nm) than the samples obtained for other synthesis time. Other samples show almost no porosity according to the surface area and pore size distribution as shown in Fig. 5 (a) and (c).

The nitrogen absorption-desorption isotherms and pore size distributions of all ZIF-zec samples obtained at different synthesis temperatures are plotted in Fig. 5 (b) and (d). All ZIF-zec samples have relatively large surface area than samples S1, S2 and S5. However, the surface area of the ZIF-zec samples varies with the synthesis temperature. S8 synthesized at 30 °C has the largest BET surface area (559 m^2/g) among all ZIF-zec samples. The BET values of S6 and S9 are also relatively large, whereas S3 and S7 have comparably small surface area. Fig. 5(d) shows that the amount of the pores with a size of ~1.1 nm in S3 and S7 is less than that of other ZIF-zec samples. Furthermore, the meso-pore sizes of S3 and S7 are around 1.6 and 1.8 nm, whereas the other ones only have meso-pores with the size larger than ~1.8 nm. Both the pore sizes and their distribution give rise to the small surface area of S3 and S7. Fig. 5 demonstrates that the ZIF-zec samples synthesized at different temperatures show a great difference in porosities (pore size distribution and surface area). It has been reported that ZIF-4 with the cag topology has a BET surface area of ~300 m^2/g [24]. Compared to ZIF-4, ZIF-nog (S4) and ZIF-zec (S8) possess larger surface area and may have a potential to be used for gas absorption in ZIFs with the Zn(Im)$_2$ composition.

Fig. 6(a) shows the synthesis temperature ~ time matrix for obtaining the polymorphs with various topologies. ZIF-zec and ZIF-nog are obtained by prolonging the synthesis time, indicating that both crystalline structures are more thermodynamically stable than ZIF-cag. This is rationalized by considering the framework densities (T/V) of the

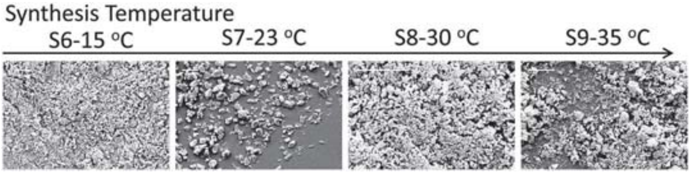

Fig. 4. SEM micrographs of S6–S9 from left to right. Each scale bar corresponds to 10 μm.

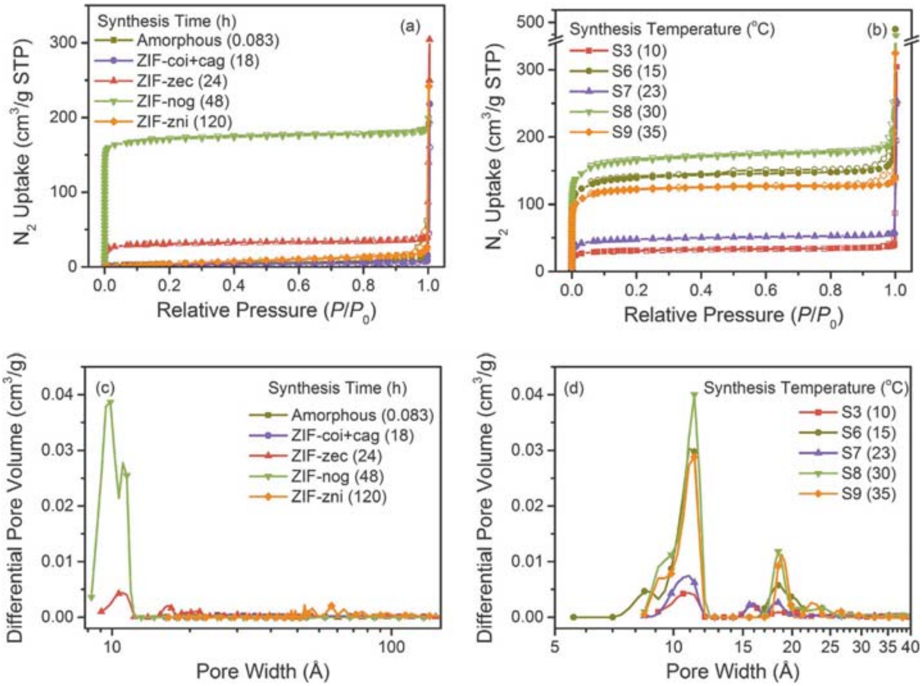

Fig. 5. N_2 absorption-desorption isotherms of samples S1–S9 synthesized for different durations (a) and at different temperature; (b) Solid symbols: Absorption; Open symbols: Desorption. (c) and (d): Pore size distribution.

Table 2
Specific surface area (BET and Langmuir methods), pore volume, N_2 uptakes (at $P/P_0 = 0.9$), and densities of samples S1–S9.

Sample No.	Crystal Phases	BET/m^2 g^{-1}	Langmuir/m^2 g^{-1}	Micropore volume/cm^3 g^{-1}	N_2 uptake/cm^3 g^{-1} (STP)	Density/cm^3 g^{-1}
1	Amorphous	16	23	0.012	9	1.648(8)
2	ZIF-coi + cag	13	19	0.009	6	1.630(6)
3	ZIF-zec	107	143	0.051	35	1.631(3)
4	ZIF-nog	571	754	0.229	179	1.608(10)
5	ZIF-zni	23	50	0.024	15	1.673(8)
6	ZIF-zec	471	625	0.205	149	1.610(5)
7	ZIF-zec	162	216	0.073	54	1.612(6)
8	ZIF-zec	559	738	0.249	179	1.607(6)
9	ZIF-zec	410	545	0.178	127	1.601(3)

ZIFs, i.e., the number of tetrahedral (*T*) per volume (*V*). As shown in Fig. 6(b), the T/V value of 3.57 nm^{-3} places ZIF-nog between ZIF-zec (T/V = 2.59–2.95 nm^{-3}) and ZIF-zni (T/V = 4.64 nm^{-3}), indicating that the phase transformations of ZIFs with the increase of synthesis time are consistent with the Ostwald's rule of stages [34].

3.4. *Glass forming of ZIF-zec and ZIF-nog*

The thermodynamic behaviour of the ZIF-nog, ZIF-zec and ZIF-zni samples were characterized by DSC and TGA, and the structures at high temperature were characterized by PXRD (Fig. 7, S6 and S7). The structure of ZIF-nog was retained after heating to 543 K, after which an exothermic peak followed by a broad endothermic peak around 600 K indicates thermal amorphization, consistent with X-ray diffraction on a sample cooled from 693 K and results on other polymorphs [27,28]. A broad exothermic peak observed at the temperature range of 700–800 K on the DSC upscan curve corresponds to recrystallization from the amorphous ZIF to ZIF-zni, consistent with the PXRD pattern of the

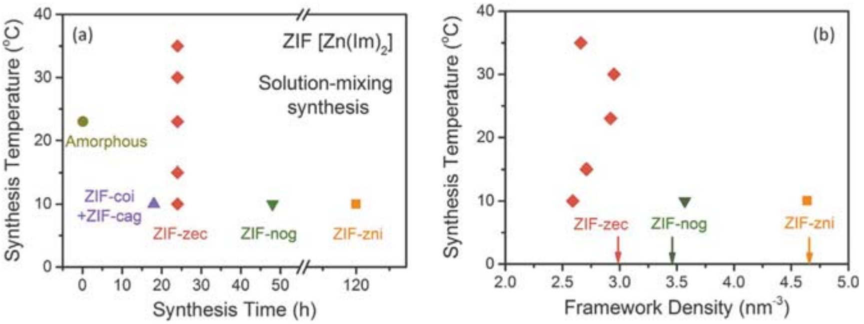

Fig. 6. (a) An outline of the topologies of the products synthesized for different time and at different temperature; (b) Framework densities (FD, *T/V*) of the polymorphic ZIFs. FD data are given in Table S1. The arrows represent the FD of the corresponding crystals in literature [16].

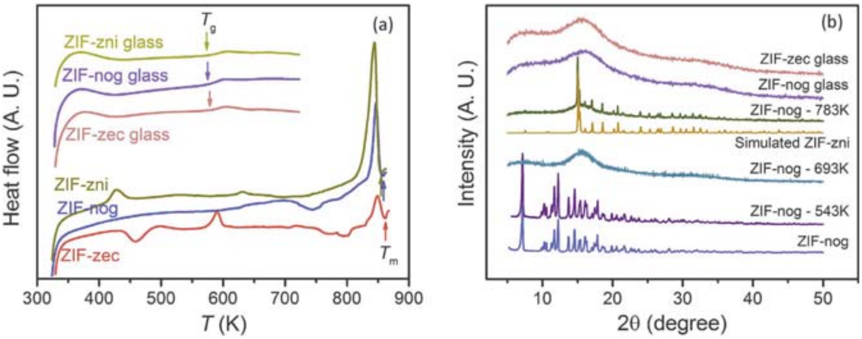

Fig. 7. (a) Heat flow of the crystals and glasses of ZIF-nog, ZIF-zec (S8) and ZIF-zni; (b) PXRD patterns of ZIF-nog annealed at different temperature, ZIF-nog glass, ZIF-zec glass, and simulated XRD patterns of ZIF-nog and ZIF-zni.

Table 3
Melting (T_m) and glass transition (T_g) temperatures of the ZIF glasses, crystal porosity, and the enthalpy of recrystallization (ΔH_{rc}) and the heat of fusion (ΔH_f) of the ZIF crystals.

Sample	Porosity/%	T_m/K	T_g/K	T_g/T_m	ΔH_{rc}/J g^{-1}	ΔH_f/J g^{-1}
ZIF-zec	35.8	858	578	0.674	12.88	12.16
ZIF-nog	24.6	853	575	0.674	21.26	21.91
ZIF-zni	8.8	851	575	0.676	–	65.27

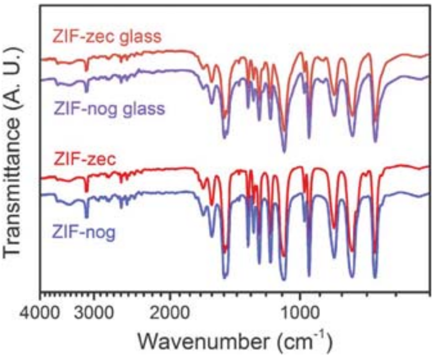

Fig. 8. FT-IR spectra of ZIF-nog, ZIF-zec, ZIF-nog glass, and ZIF-zec glass.

sampled annealed at 783 K. A subsequent sharp endotherm at 858 K is assigned to the melting of the zni phase, with an amorphous product formed upon melt quenching. The glass transition upon reheating is observed at 575 K, similar to the thermodynamic behaviour of ZIF-4 [29]. Another polymorph, ZIF-zec, displays almost the identical thermodynamic behaviour as ZIF-nog upon heating, given in Fig. 7(a) and Fig. S6. DSC results of ZIF-zni and the glassy ZIF-zni also show the similar melting and glass transition behaviours as ZIF-nog and ZIF-zec in Fig. 7(a). Note that the thermodynamic behaviour of the amorphous ZIF (S1) is shown by the DSC curve, where a glass-transition like peak appears, but no melting process is detected (Fig. S8).

Table 3 shows the glass transition and melting and temperatures (T_g and T_m), crystallization enthalpy (ΔH_{rc}) and fusion enthalpy (ΔH_f) of ZIF-nog, -zec and -zni. The melting peaks on the DSC upscan curves (Fig. 7(a)) are attributed to melting of ZIF-zni, therefore the T_m and T_g values of the three samples are similar. The ΔH_{rc} of ZIF-nog and ZIF-zec is identical to their ΔH_f. The ΔH_f of ZIF-zni is rather different among the three samples. The smaller ΔH_f of ZIF-nog and ZIF-zec implies that their amorphous phases are not fully transformed into ZIF-zni, and hence, less energy is needed during the melting stage.

Liquid-state ^{1}H NMR and FT-IR measurements were performed to compare the structures of ZIF-nog and ZIF-zec crystals and their glasses (Figs. S1-S4 and Fig. 8). The ^{1}H NMR spectra of the two glasses are comparable to those of the crystals, indicating that the imidazolate ligand remains largely intact after vitrification in both samples. The peak positions from FT-IR spectra of the glasses are also in good agreement with those of the crystals. There is only a slight difference in the ratios between the transmittance peaks in the range of 1500-600 cm^{-1} on the FT-IR spectra, suggesting a small change of the stretching and bending of the imidazole ring after glass forming.

4. Conclusions

Synthesis time and temperature have pronounced effects on the crystal formation, morphology and porosity of ZIFs with $Zn(Im)_2$ composition obtained by the liquid mixing method. Longer synthetic time leads to denser polymorphs, which is consistent with Ostwald's rule of stages. Nitrogen absorption-desorption results indicate that ZIF-zec synthesized at 30 °C (S8) and ZIF-nog (S4) have larger surface area ($> 500\,m^2/g$) than ZIF-4. Furthermore, the thermodynamic behaviour of the ZIF-nog and the ZIF-zec are studied. Both crystals undergo amorphization, recrystallization to ZIF-zni and melting upon heating, comparable to the phase transitions in ZIF-4. The structures between the crystals and glasses are characterized by liquid-state ^{1}H NMR and FT-IR spectra.

Acknowledgements

The authors acknowledge Usuma Naknikham and Deyong Wang for the help of experiments, and we also thank Jingwei Hou for valuable discussions. Chao Zhou is grateful for the financial support from China Scholarship Council. Thomas D. Bennett would like to thank the Royal Society for a University Research Fellowship, and for their support.

Appendix A. Supplementary data

Supplementary data related to this article can be found at http://dx.doi.org/10.1016/j.micromeso.2018.01.038.

References

[1] K.S. Park, Z. Ni, A.P. Côté, J.Y. Choi, R. Huang, F.J. Uribe-Romo, H.K. Chae, M. O'Keeffe, O.M. Yaghi, Proc. Natl. Acad. Sci. 103 (2006) 10186–10191.
[2] B. Chen, Z. Yang, Y. Zhu, Y. Xia, J. Mater. Chem. A 2 (2014) 16811–16831.
[3] R. Banerjee, A. Phan, B. Wang, C. Knobler, H. Furukawa, M. O'Keeffe, O.M. Yaghi, Science 319 (2008) 939–943.
[4] A.W. Thornton, S.A. Furman, K.M. Nairn, A.J. Hill, J.M. Hill, M.R. Hill, Microporous Mesoporous Mater. 167 (2013) 188–197.
[5] S. Bhattacharyya, S.H. Pang, M.R. Dutzer, R.P. Lively, K.S. Walton, D.S. Sholl, S. Nair, J. Phys. Chem. C 120 (2016) 27221–27229.
[6] G. Kaur, R.K. Rai, D. Tyagi, X. Yao, P.-Z. Li, X.-C. Yang, Y. Zhao, Q. Xu, S.K. Singh, J. Mater. Chem. A 4 (2016) 14932–14938.
[7] K. Jayaramulu, K.K.R. Datta, C. Rösler, M. Petr, M. Otyepka, R. Zboril, R.A. Fischer, Angew. Chem. Int. Ed. 55 (2016) 1178–1182.
[8] Y. Ban, Y. Li, Y. Peng, H. Jin, W. Jiao, X. Liu, W. Yang, Chem. Eur J. 20 (2014) 11402–11409.
[9] P.D. Sutrisna, J. Hou, H. Li, Y. Zhang, V. Chen, J. Membr. Sci. 524 (2017) 266–279.
[10] V. Armel, J. Hannauer, F. Jaouen, Catalysts 5 (2015) 1333–1351.
[11] Y. Deng, Y. Dong, G. Wang, K. Sun, X. Shi, L. Zheng, X. Li, S. Liao, ACS Appl. Mater. Interfaces 9 (2017) 9699–9709.
[12] Y. Hwang, H. Sohn, A. Phan, O.M. Yaghi, R.N. Candler, Nano Lett. 13 (2013) 5271–5276.
[13] I. Stassen, N. Burtch, A. Talin, P. Falcaro, M. Allendorf, R. Ameloot, Chem. Soc. Rev. 46 (2017) 3185–3241.
[14] X. Wu, S. Xiong, Z. Mao, S. Hu, X. Long, Chem. Eur J. 23 (2017) 7969–7975.
[15] M. Eddaoudi, D.F. Sava, J.F. Eubank, K. Adil, V. Guillerm, Chem. Soc. Rev. 44 (2014) 228–249.
[16] A. Phan, C.J. Doonan, F.J. Uribe-Romo, C.B. Knobler, M. O'Keeffe, O.M. Yaghi, Acc. Chem. Res. 43 (2010) 58–67.
[17] A.K. Cheetham, C.N.R. Rao, R.K. Feller, Chem. Commun. 0 (2006) 4780–4795.
[18] N. Stock, S. Biswas, Chem. Rev. 112 (2012) 933–969.
[19] Y.-R. Lee, J. Kim, W.-S. Ahn, Korean J. Chem. Eng 30 (2013) 1667–1680.
[20] M. Gustafsson, X. Zou, J. Porous Mater. 20 (2012) 55–63.
[21] S. Cao, T.D. Bennett, D.A. Keen, A.L. Goodwin, A.K. Cheetham, Chem. Commun. 48 (2012) 7805–7807.
[22] A. Puškarić, A.D. Katsenis, C. Mottillo, I. Halasz, K. Užarević, M.-H. Pham, O. Magdysyuk, P.A. Julien, P. Lazić, R.E. Dinnebier, S.A.J. Kimber, T. Friščić, T.-O. Do, V. Štrukil, Nat. Commun. 6 (2015) 6662.
[23] A.M. Belenguer, F. Adams, I. Halasz, P.J. Beldon, R.E. Dinnebier, S.A.J. Kimber, T. Friščić, V. Honkimäki, Nat. Chem. 5 (2013) 66.
[24] H. Miura, V. Bon, I. Senkovska, S. Ehrling, S. Watanabe, M. Ohba, S. Kaskel, Dalton Trans. 46 (2017) 14002–14011.
[25] T.D. Bennett, A.K. Cheetham, Acc. Chem. Res. 47 (2014) 1555–1562.
[26] R. Gaillac, P. Pullumbi, K.A. Beyer, K.W. Chapman, D.A. Keen, T.D. Bennett, F.-X. Coudert, Nat. Mater. 16 (2017) nmat4998.
[27] T.D. Bennett, J.-C. Tan, Y.Z. Yue, E. Baxter, C. Ducati, N.J. Terrill, H.H.-M. Yeung, Z. Zhou, W. Chen, S. Henke, A.K. Cheetham, G.N. Greaves, Nat. Commun. 6 (2015) 8079.
[28] T.D. Bennett, D.A. Keen, J.-C. Tan, E.R. Barney, A.L. Goodwin, A.K. Cheetham, Angew. Chem. Int. Ed. 50 (2011) 3067–3071.
[29] T.D. Bennett, Y.Z. Yue, P. Li, A. Qiao, H. Tao, N.G. Greaves, T. Richards, G.I. Lampronti, S.A.T. Redfern, F. Blanc, O.K. Farha, J.T. Hupp, A.K. Cheetham, D.A. Keen, J. Am. Chem. Soc. 138 (2016) 3484–3492.
[30] J.T. Hughes, T.D. Bennett, A.K. Cheetham, A. Navrotsky, J. Am. Chem. Soc. 135 (2013) 598–601.
[31] D. Wu, A. Navrotsky, J. Solid State Chem. 223 (2015) 53–58.
[32] D.W. Lewis, A.R. Ruiz-Salvador, A. Gómez, L.M. Rodriguez-Albelo, F.-X. Coudert, B. Slater, A.K. Cheetham, C. Mellot-Draznieks, CrystEngComm 11 (2009) 2272–2276.
[33] Y.-Q. Tian, Y.-M. Zhao, Z.-X. Chen, G.-N. Zhang, L.-H. Weng, D.-Y. Zhao, Chem. Eur J. 13 (2007) 4146–4154.
[34] J.C. Burley, M.J. Duer, R.S. Stein, R.M. Vrcelj, Eur. J. Pharm. Sci. 31 (2007) 271–276.

Supporting Information

Polymorph Formation for a Zeolitic Imidazolate Framework composition - $Zn(Im)_2$

Chao Zhou,[1] Malwina Stepniewska,[1] Jens Martin Sørensen,[1] Luca Scarpa,[1] Giuliana Magnacca,[2]
Vittorio Buffa,[1] Thomas D. Bennett,[3] Yuanzheng Yue[1,*]

[1]*Department of Chemistry and Bioscience, Aalborg University, DK-9220 Aalborg, Denmark*
[2]*Department of Chemistry and NIS Centre, University of Turin, 10125 Turin, Italy*
[3]*Department of Materials Science and Metallurgy, University of Cambridge, CB3 0FS, UK*

^{1}H liquid-state NMR spectra (Figs. S1-S4)

Rietveld refinements and parameters (Fig. S5, Table S1)

PXRD patterns of S8 (Fig. S6)

TGA spectra of S1-S5 (Fig. S7)

DSC-TGA of S1 (Fig. S8)

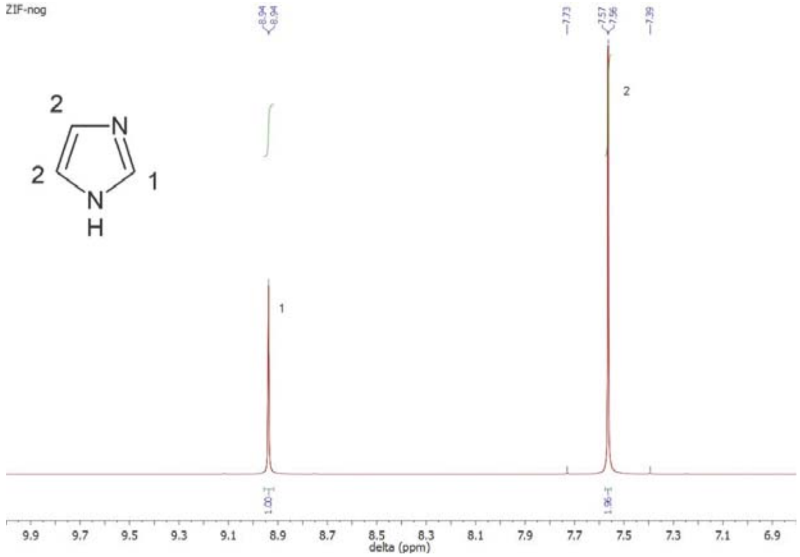

Fig. S1 ^{1}H NMR spectrum of ZIF-nog (S4). A digested sample of evacuated ZIF-nog in DCl/D2O/DMSO-d_6.

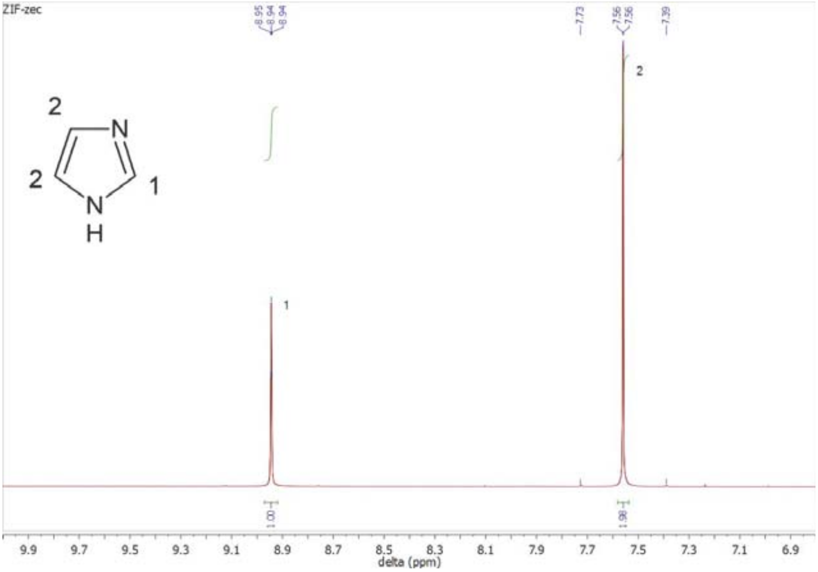

Fig. S2 ^{1}H NMR spectrum of ZIF-zec (S3).

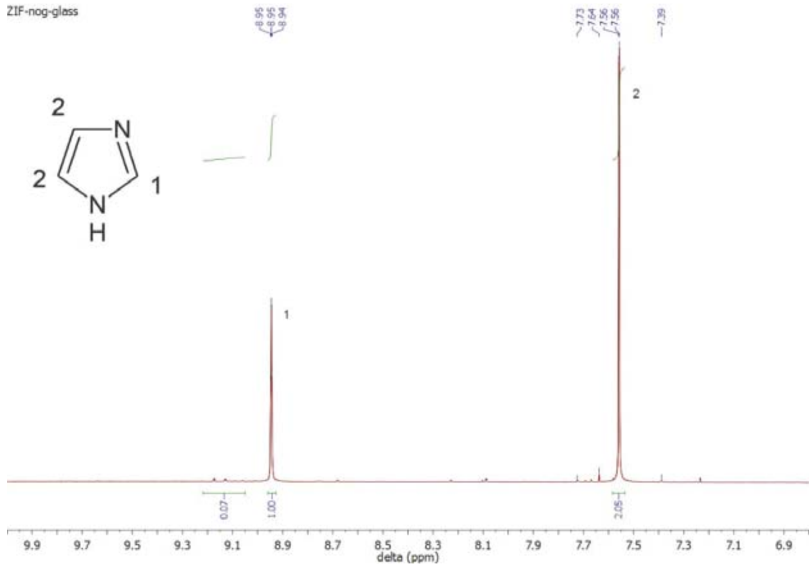

Fig. S3 ^{1}H NMR spectrum of ZIF-nog glass.

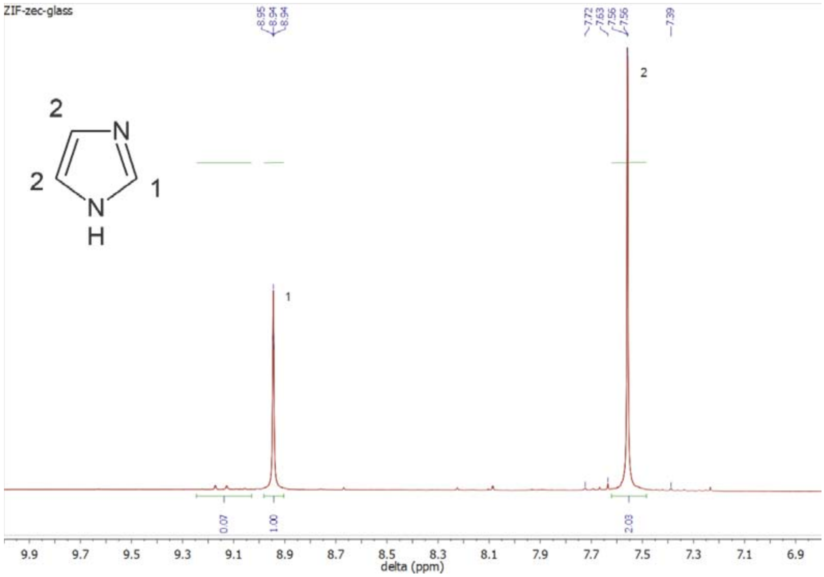

Fig. S4 ^{1}H NMR spectrum of ZIF-zec glass.

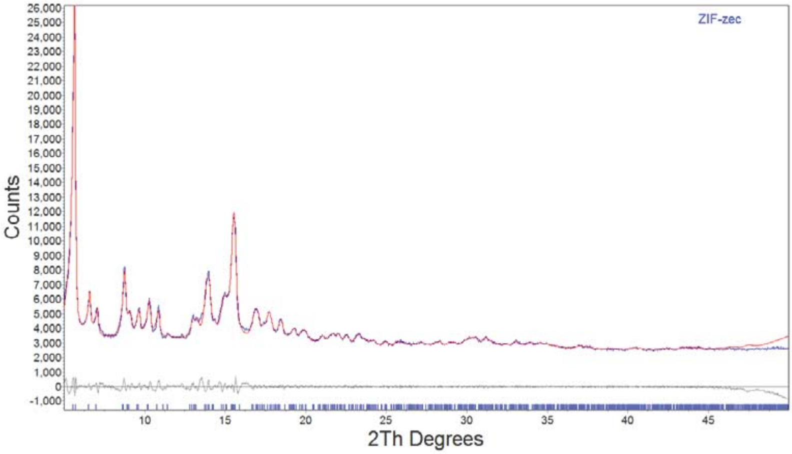

Fig. S5 Rietveld refinement of the PXRD pattern of S7.

Table S1 Refinement parameters of PXRD patterns of S3-S9.

Sample No.	3	4	5	6	7	8	9
Rwp	2.45	5.227	5.281	3.155	2.836	2.508	3.607
Rp	1.74	2.93	3.45	1.94	1.94	1.70	2.01
gof	3.24	4.94	3.23	3.75	3.18	2.59	4.72
Rexp	0.76	1.06	1.63	0.84	0.89	0.97	0.76
R-Bragg	0.065	0.247	0.476	0.065	0.15	0.083	0.090
Crystal size /nm	93.7	185.4	69.2	66.4	261.6	70.9	113.5
Cell Volume/Å^3	15436.3	5597.5	6903.1	14774.2	13692.8	13553.5	15065.0
T/V /nm^{-3}	2.59	3.57	4.64	2.71	2.92	2.95	2.66

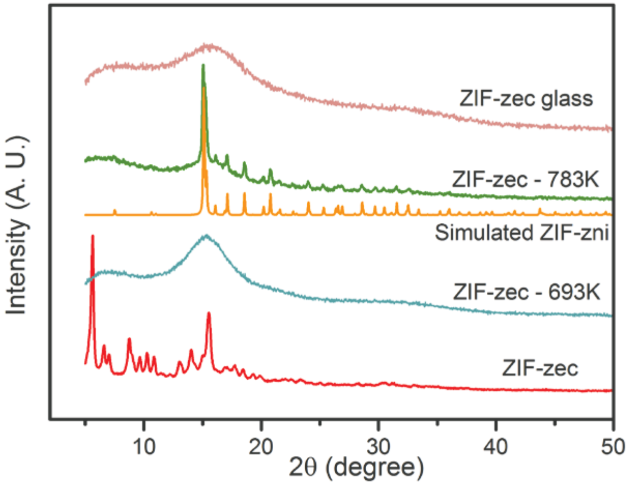

Fig. S6 PXRD patterns of ZIF-zec annealed at 693 and 783 K, and ZIF-zec glass, and simulated XRD pattern of ZIF-zni.

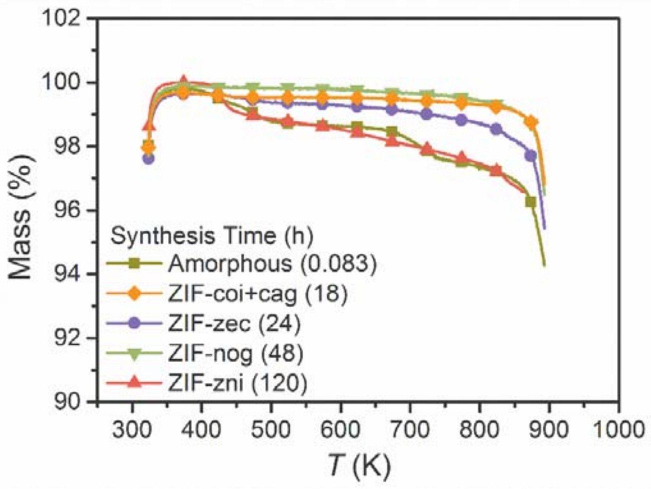

Fig. S7 Thermogravimetric analysis of samples S1-S5.

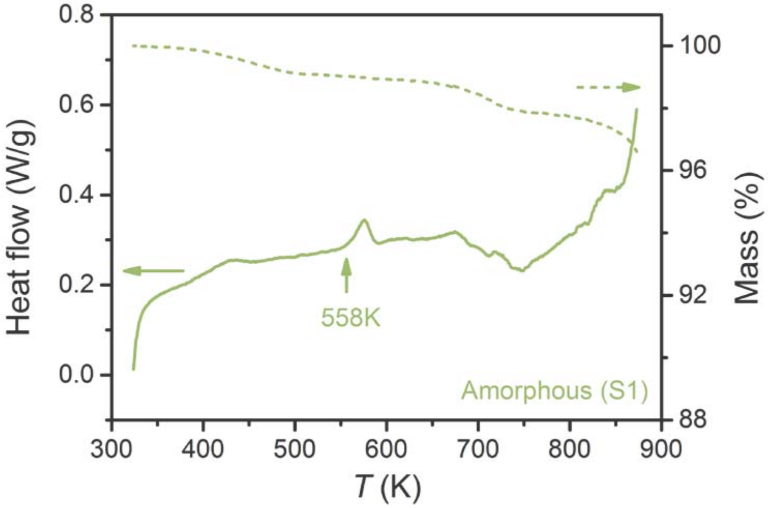

Fig. S8 DSC and TGA curves of S1.

PAPER II

PCCP

PAPER

Cite this: *Phys. Chem. Chem. Phys.*, 2018, **20**, 18291

Thermodynamic features and enthalpy relaxation in a metal–organic framework glass†

Chao Zhou,[a] Malwina Stepniewska,[a] Louis Longley,[b] Christopher W. Ashling,[b] Philip A. Chater,[c] David A. Keen,[d] Thomas D. Bennett*[b] and Yuanzheng Yue*[ae]

Received 12th April 2018,
Accepted 23rd June 2018

DOI: 10.1039/c8cp02340a

rsc.li/pccp

In this work, we explore the thermodynamic evolution in a melt-quenched metal–organic framework glass, formed from ZIF-62 upon heating to the melting point (T_m), and subsequent enthalpy relaxation. The temperature dependence of the difference in Gibbs free energy between the liquid and crystal states of ZIF-62 in the temperature range from the glass transition temperature (T_g) to T_m is found to be weaker than those of other types of glasses, *e.g.*, metallic glasses. Additionally, we find that the stretched exponent of the enthalpy relaxation function in the glass varies significantly (β = 0.44–0.76) upon changing the extent of sub-T_g annealing, compared to metallic and oxide glasses with similar T_gs, suggesting a high degree of structural heterogeneity. Pair distribution function results suggest no significant structural changes during the sub-T_g relaxation in ZIF-62 glass.

Introduction

Metal–organic frameworks (MOFs), or coordination polymers, have been intensively investigated in recent decades owing to their multiple functionalities and potential for applications such as in gas absorption, catalysis and sensing.[1–3] Recently, several members of the zeolitic imidazolate framework (ZIF) family, a subset of MOFs, have been discovered to melt prior to decomposition, and can be vitrified upon quenching.[4–8] These 'MOF-glasses' are novel in the glass family and present a new opportunity to explore one of the most complex problems in condensed matter science, *i.e.*, the mechanism of melting and glass formation. A previous study demonstrated that the melting temperature (T_m) and the interval between T_m and decomposition temperature depends on the identity of the framework forming organic ligands.[6] However, further links between MOF-glasses and classical glass theory, including the effect of defects, disorder and flexibility upon T_m and T_g, have thus far not been made.[9]

A study of the dynamic behavior of MOF-glasses is important for understanding glass formation upon quenching in the supercooled MOF liquid temperature region, and also for exploring the time dependence of the properties of MOF-glasses. Relaxation, a universal dynamic feature of amorphous materials specific to different glass-forming systems and linked to cohesive force and bonding identity, is strongly connected with structural evolution and macroscopic properties.[10–13] For example, glass enthalpy and stress generally decrease during isothermal relaxation below the glass transition temperature (T_g), resulting in the enhancement of plasticity and hardness of glasses after annealing.[14–16] Chen *et al.* have shown that, together with the liquid fragility index (m), the stretching exponent β plays a key role in determining the relaxation dynamics in various types of glasses.[17] The β value, alongside the dependence of the Gibbs free energy on temperature, is therefore a useful quantity in evaluating the relaxation behavior of MOF-glasses. Additionally, structural evolution during relaxation in glasses is generally difficult to detect and observe directly in experiments due to the disordered nature of amorphous matter.

In this work, we explore the thermodynamic features of the glass formed from ZIF-62 [$Zn(Im)_{1.75}(bIm)_{0.25}$] (Im = imidazolate, $C_3H_3N_2^-$; bIm = benzimidazolate, $C_7H_5N_2^-$) (*i.e.* a_gZIF-62), and the extent of enthalpy relaxation in the supercooled regime. The origin of the high thermal stability against crystallization is discussed in terms of the thermodynamic driving force (Gibbs free energy) of nucleation in the glass state. The enthalpy relaxation of the glass was investigated by determining the stretching exponent of the Kohrausch function during sub-T_g annealing at various temperatures. Structural changes induced by sub-T_g relaxation were characterized by synchrotron X-ray total scattering.

---

[a] *Department of Chemistry and Bioscience, Aalborg University, Aalborg DK-9220, Denmark. E-mail: yy@bio.aau.dk*
[b] *Department of Materials Science and Metallurgy, University of Cambridge, Cambridge CB3 0FS, UK. E-mail: tdb35@cam.ac.uk*
[c] *Diamond Light Source Ltd, Diamond House, Harwell Science and Innovation Campus, Didcot OX11 0DE, UK*
[d] *ISIS Facility, Rutherford Appleton Laboratory, Harwell Campus, Didcot, Oxon OX11 0QX, UK*
[e] *State Key Laboratory of Silicate Materials for Architectures, Wuhan University of Technology, Wuhan 430070, China*

† Electronic supplementary information (ESI) available: Fig. S1–S4. See DOI: 10.1039/c8cp02340a

Experimental

Sample preparation

ZIF-62 was synthesized by a solvothermal method,[6,18] in which 1.515 g $Zn(NO_3)_2 \cdot 6H_2O$ (8 mmol), 7.35 g imidazole (108 mmol), and 1.418 g benzimidazole (12 mmol) were dissolved in 75 ml of dimethylformamide (DMF) and transferred into a 100 ml glass jar. The jar was sealed tightly and heated to 403 K for 48 h in an oven. After cooling to room temperature, colourless prism-shaped ZIF-62 crystals were collected from the mother liquid and washed with ~30 ml DMF three times and ~30 ml of dichloromethane. The crystalline sample was characterized before drying at 373 K under vacuum for 10 h. a_gZIF-62 was obtained by heating crystalline ZIF-62 to 753 K at a heating rate of 10 K min^{-1}, and then melt-quenching to room temperature at 10 K min^{-1} under an argon atmosphere. Annealed glasses were prepared by heating the as-quenched glass to various temperatures for various durations.

Characterization

Powder X-ray diffraction (PXRD) measurements were conducted on both ZIF-62 crystalline and glass samples with a PANalytical empyrean XRD using Cu $K\alpha_1$ radiation (λ = 1.54098 Å). The structural identity of the crystalline phase was confirmed by comparing the experimental PXRD pattern to the simulated one (Fig. 1a).[19] The amorphous nature of the ZIF-62 glass was verified by the absence of Bragg peaks in the collected diffraction pattern (Fig. 1a). All thermodynamic measurements were performed in a differential scanning calorimeter (DSC) (STA 449 F1 Jupiter, Netzsch GmbH). The crucibles for sample and reference were both made of Pt/Rh. A baseline was used to correct the DSC output of all measurements. The isobaric heat capacity (C_p) curves (*i.e.* $C_p \sim T$ curve) of the samples were determined by comparing their DSC output with that of a reference sapphire at the upscan rate of 10 K min^{-1}. The sample mass of ZIF-62 glasses for DSC measurements was of the order of 15 mg. The mass changes were recorded simultaneously during the DSC scans.

X-ray total scattering data were collected at the I15-1 beamline at the Diamond Light Source, UK, at a wavelength of λ = 0.161669 Å. Data were collected in the region of $\sim 0.4 < Q < \sim 26$ Å^{-1}. Finely powdered samples of the melt quenched and annealed glasses were loaded into 1.17 mm (inner diameter) borosilicate capillaries, and data from an empty instrument and capillary were also collected for use in background subtraction. Corrections for background, multiple, container and Compton scattering, along with absorption were performed using the GudrunX program.[20,21] The normalized reciprocal space data were then converted to the pair distribution functions (PDFs) *via* Fourier transform.

Results and discussion

Glass stability of ZIF-62

Crystalline and glass ZIF-62 samples were characterized using PXRD and DSC (Fig. 1). A broad hump, *i.e.* diffuse scattering, in the PXRD pattern of the glass at a *d*-spacing of 5.9 Å ($2\theta \approx 15°$) confirmed the glassy nature of a_gZIF-62. Fig. 1(b) shows the temperature dependence of C_p and mass loss for both ZIF-62 and a_gZIF-62 during upscans. A pronounced endothermic peak around 540 K on the C_p curve of the crystal, coincident with a gradual mass loss of 13.1%, confirms this is due to removal of DMF from the framework voids. The second endothermic peak with an offset temperature of 711 K (defined as T_m) is assigned to the melting event.[6]

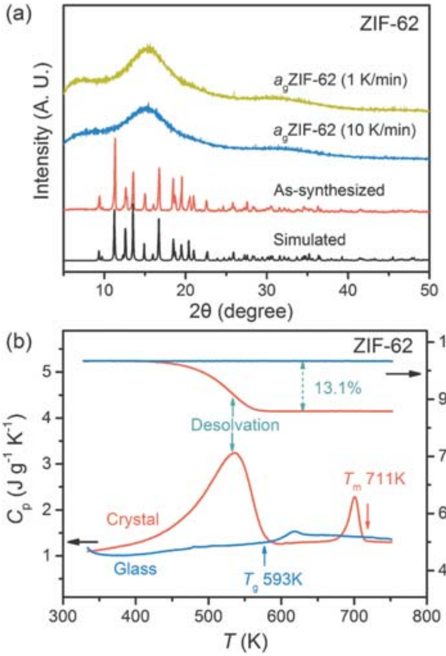

Fig. 1 (a) PXRD of the predicted[19] and as-synthesized crystalline ZIF-62, melt-quenched ZIF-62 glass and a glass sample cooled at 1 K min^{-1} after annealing at 658 K, shown in black, red, blue and green, respectively. (b) The C_p and mass loss curves of crystalline and glassy ZIF-62 upon heating, shown as red and blue, respectively. Both upscan rates were 10 K min^{-1}.

The liquid formed from ZIF-62 has a large range of stability (up to 100 K above T_m) compared with other glass-forming ZIFs, where decomposition temperatures are close to T_m.[6,22] A typical glass transition feature is observed upon reheating a_gZIF-62. The onset temperature (593 K) of the peak is defined as the calorimetric glass transition temperature (T_g).[6,13] However, no crystallization peak is observed on the second upscan curve. Furthermore, annealing the sample at 658 K below T_m for 12 hours, followed by slow cooling to room temperature at 1 K min^{-1}, does not result in the appearance of any Bragg peaks in the XRD pattern (Fig. 1a), implying a high stability of a_gZIF-62 against crystallization. This is attributed to the high steric hindrance of the liquid structure.[5,22] Specifically, the liquid state has been shown to contain mainly interconnected $Zn(Im)_x$ (x = 3 or 4) species, which, given the size of the imidazolate ligand, have extremely sluggish diffusion kinetics. The high steric hindrance increases the energy barrier for nucleation and thereby enhances the glass stability against crystallization.

Thermodynamic features of ZIF-62 glass

Fig. 2(a) shows the isobaric heat capacity (C_p) as a function of temperature for the liquid, glassy and crystalline ZIF-62. According to Kubaschewski,[26] the temperature dependence of C_p of a supercooled liquid $C_p^{sl}(T)$ and that of the corresponding crystal $C_p^x(T)$ can be described by the power law:

$$C_p^{sl}(T) = 3R + a \times T + b \times T^{-2}, \quad (1)$$

$$C_p^{x}(T) = 3R + c \times T + d \times T^{2}, \quad (2)$$

where R is the gas constant, and a, b, c and d are fitting parameters. Here, we change the units of C_p from J g^{-1} K^{-1} to J mol^{-1} K^{-1}.[19] The C_p data of the supercooled liquid and the crystal are fitted to eqn (1) and (2), respectively, and thus the following fitting parameters are obtained: a = 0.2396 (±0.0035) J mol^{-1} K^{-2}, b = 5.531 (±0.105) × 10^{7} J K mol^{-1}, c = 0.7000 (±0.0016) J mol^{-1} K^{-2} and d = −4.744 (±0.025) × 10^{-4} J mol^{-1} K^{-3}. The difference in C_p between supercooled liquid and crystal of ZIF-62 at T_g is found to be 51.5 J mol^{-1} K^{-1}, which is smaller than those of most molecular and oxide glasses but larger than those of metallic glasses.[27,28]

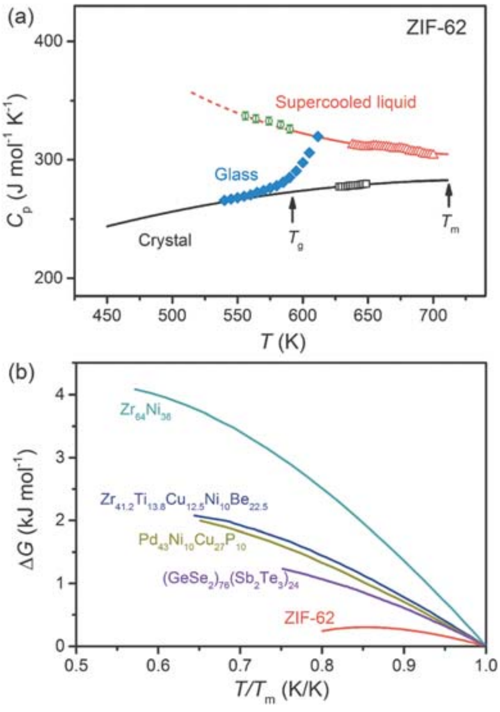

Fig. 2 (a) The heat capacity dependence on temperature in supercooled liquid, glass and crystalline states of ZIF-62, shown as red line (eqn (1)), blue diamond points and black line (eqn (2)), respectively. The green points are the heat capacity in supercooled liquid obtained from the enthalpy relaxation results. (b) The variation of the Gibbs free energy difference $\Delta G^{sl-x}(T)$ between the supercooled liquid and the crystal of ZIF-62. The $\Delta G^{sl-x}(T)$ of some alloys are also given as comparisons from literature.[23–25] Note that one atom is taken as per mol for metallic glasses and the chalcogenide glass, whilst 18.5 atoms are used as per mol for ZIF-62 according to the formula.

The temperature dependence of the differences in C_p between liquid and crystal $\Delta C_p^{sl-x}(T)$ was also determined. The enthalpy of fusion (ΔH_f) is obtained from the melting peak in Fig. 1(b) to be 3.566 kJ mol^{-1}. This value is much smaller than the formation enthalpy of other ZIFs and zeolites.[29–31] The differences in enthalpy (ΔH^{sl-x}) and entropy (ΔS^{sl-x}) between the supercooled liquid and crystal are calculated by the following equations, respectively (Fig. S1, ESI†):

$$\Delta H^{sl-x}(T) = \Delta H_f - \int_T^{T_{liq}} \Delta C_p^{sl-x}\left(T'\right) dT' \quad (3)$$

$$\Delta S^{sl-x}(T) = \Delta S_f - \int_T^{T_{liq}} \frac{\Delta C_p^{sl-x}\left(T'\right)}{T'} dT'. \quad (4)$$

The entropy of fusion is determined to be $\Delta S_f = \Delta H_f/T_m$ = 5.015 J mol^{-1} K^{-1}. The Gibbs free energy difference between the liquid and crystalline forms $\Delta G^{sl-x}(T)$ in the supercooled liquid region is determined by the equation:

$$\Delta G^{sl-x}(T) = \Delta H^{sl-x}(T) - T \times \Delta S^{sl-x}(T). \quad (5)$$

As shown in Fig. 2(b), the Gibbs free energy difference between the liquid and crystalline forms of ZIF-62 increases with decreasing temperature below T_m. This suggests that the recrystallization of liquid ZIF-62 during cooling could be theoretically achieved if the cooling rate is low enough for nucleation. However, compared to the $\Delta G^{sl-x}(T)$ of some typical metallic glasses and a chalcogenide glass, the $\Delta G^{sl-x}(T)$ dependence on temperature below T_m in ZIF-62 is weak. A comparison of $\Delta G^{sl-x}(T)$ on a per atom basis is shown in Fig. S2 (ESI†), which yields smaller values of ΔG. These are however not suitable as a comparison, as atoms within each organic ligand of the central metal ion (Zn^{2+}) remain bonded to one another throughout the melting and vitrification process, and are thus not independent in terms of mobility. Additionally, $\Delta G^{sl-x}(T)$ is expressed on a per building unit basis (referring to one metal center unit and two organic linker units) as shown in Fig. S3 (ESI†), which thus has smaller values of ΔG. Using analogies to SiO_2 of this ZIF family, we thus plot $\Delta G^{sl-x}(T)$ on a per mol basis (Fig. 2b). The small $\Delta G^{sl-x}(T)$ value of ZIF-62 indicates the low thermodynamic driving force of nucleation, supporting the high resistance against crystallization.[22]

Enthalpy relaxation in ZIF-62 glass

The enthalpy relaxation behavior of a_gZIF-62 was studied by performing annealing treatments at sub-T_g temperatures (T_a) between 553 and 587 K, *i.e.*, 0.93–0.99T_g, in argon. Fig. 3 shows the C_p *vs.* T curves of ZIF-62 glass annealed at T_a = 559 K for various durations (t_a). The overshoot of the glass transition peak becomes prominent and the width of the peak broadens gradually with t_a. Fig. 3 shows that annealing time does not influence the onset temperature of the glass transition, indicating that only α relaxation is involved during annealing rather than other relaxation processes during the subsequent DSC upscans.[14,32] In terms of the potential energy landscape

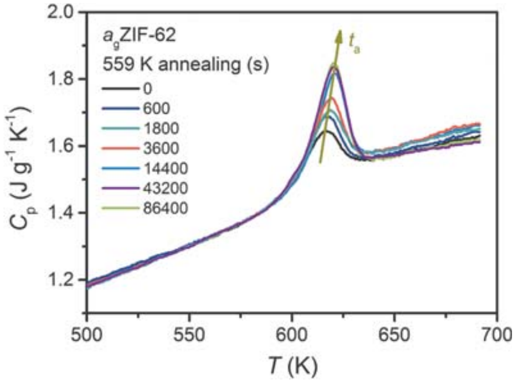

Fig. 3 Temperature dependence of the isobaric heat capacity (C_p) of a_gZIF-62 after annealing at 559 K for different durations (in seconds). The upscan rates of all measurements were 10 K min^{-1}.

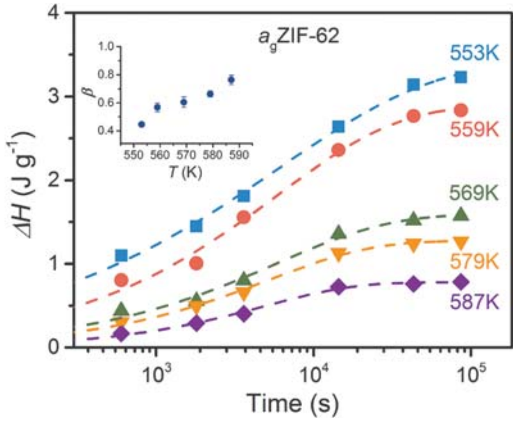

Fig. 4 The recovered enthalpy ($\Delta H(T_a, t_a)$) of a_gZIF-62 after annealing at different temperatures and time. Dashed lines: the fitted curves *via* eqn (7). Inset: T_a dependence of β.

(PEL), the configurational state of the glass enters a local minima with low configurational entropies during sub-T_g annealing.[33] An energy barrier between such local minima therefore needs to be overcome in order for the glass to return to the potential energy of the standard glass (cooled at 10 K min^{-1}) during upscanning,[13] leading to the observed glass transition overshoot. In addition, the overshoot area of glass transition peak becomes larger with t_a. The longer t_a is, the lower potential energies the glasses can reach upon annealing, and the greater the observed enthalpy recovery is upon reheating.

The enthalpy $\Delta H(T_a, t_a)$ recovered during annealing is determined by integrating the C_p differences of the glass transition peaks between the samples with $t_a > 0$ and the one with no duration ($t_a = 0$). Fig. 4 shows the ΔH of the glass after annealing for different t_a up to 24 hours at five different T_a. The ΔH increases with t_a for a given T_a, and decreases with T_a for a given t_a.

The enthalpy relaxation in the ZIF-62 glass is described by the Kohlrausch–Williams–Watts (KWW) function:[34,35]

$$\varphi(t) = \exp\left[-\left(\frac{t_a}{\tau_a}\right)^{\beta}\right], \quad (6)$$

where t_a is the annealing time, τ_a is the characteristic relaxation time at a certain temperature, and β is the stretching exponent. The $\Delta H(T_a, t_a)$ can be hence expressed as:

$$\Delta H(T_a, t_a) = \Delta H_{eq}(T_a)\left\{1 - \exp\left[-\left(\frac{t_a}{\tau_a}\right)^{\beta}\right]\right\}, \quad (7)$$

where $\Delta H_{eq}(T_a)$ is the recovered enthalpy at T_a for an infinite annealing time. The t_a dependence of the recovered enthalpy at each T_a is fitted to eqn (7) to obtain the parameters of τ_a and β.

Fig. 4 shows that the ΔH_{eq} decreases with T_a, indicating that the glass system gradually relaxes toward the potential energy level of the standard glass.[13,33] The heat capacity of the supercooled liquid (C_p^{sl}) below T_g cannot be directly determined, but the heat capacity difference $\Delta C_p^{sl-g}(T')$ between the supercooled liquid and the glass can be calculated through the relation $\Delta C_p^{sl-g}(T') = (\Delta H_{eq}(T_{a1}) - \Delta H_{eq}(T_{a2}))/(T_{a2} - T_{a1})$, where T' is the average value of two adjacent annealing temperatures $(T_{a1} + T_{a2})/2$. Note that the interval between T_{a1} and T_{a2} should be an infinitesimally small value. The calculated C_p^{sl} data from the enthalpy relaxation agree well with the eqn (1) fit (see green circles and red dashed line in Fig. 2a).

The τ_a and β values, which were obtained from the fit of eqn (7) to the t_a dependence of the recovered enthalpy at various T_a are given in Table 1. A higher sub-T_g annealing temperature corresponds to a shorter average relaxation time τ_a, which is ascribed to the narrower energy gap between the energy state of the annealed glass at higher T_a and that of the standard glass.[14] The τ_a value decreases slightly with increased T_a, but it decreases drastically to ~100 seconds when the temperature approaches T_g (593 K) based on its definition. The Arrhenius equation is often used to fit the τ_a *vs.* T_a relation to obtain the activation energy of the glass transition. However, in the present work, the τ_a at T_a = 587 K is still found to be around 5000 seconds, whereas the τ_a at T_g, determined by dividing the width of the glass transition region by the upscan rate (Fig. 1b), is just 228 seconds. Hence, it is not reasonable to fit the τ_a *vs.* T_a relation to the Arrhenius equation due to the non-linear nature. According to a previous study,[41] a large τ_a value determined from sub-T_g relaxation experiments can be related to a higher degree of structural heterogeneity. Therefore, the long τ_a at T_a = 587 K suggests that the structure of the ZIF-62 glass is highly heterogeneous.

Table 1 Fitting parameters and standard errors from eqn (7) in Fig. 4

T_a/K	$\Delta H_{eq}(T_a)$/J g^{-1}	τ_a/s	β
553	3.405 ± 0.121	6125 ± 393	0.444 ± 0.017
559	2.886 ± 0.108	5937 ± 378	0.567 ± 0.031
569	1.590 ± 0.061	5842 ± 379	0.604 ± 0.037
579	1.272 ± 0.024	5114 ± 160	0.662 ± 0.023
587	0.781 ± 0.017	4880 ± 170	0.763 ± 0.033

The stretching exponent β is a measure of the distribution width of the relaxation time, which normally ranges from 0 to 1. The β value of a_gZIF-62 increases from 0.44 to 0.76 when T_a increases from 0.93 to 0.99T_g (Table 1). The β values increase with T_a and approaches unity at T_g, which is a typical feature of a strong liquid (Fig. 4 inset).[34,38,42] The ranges of β values in other types of glass formers with similar T_g to a_gZIF-62 are summarized in Table 2, along with their fragility indices (m) and annealing temperatures. a_gZIF-62 exhibits a broad range of β for the sub-T_g annealing, indicating its sensitivity of β to T_a and its high degree of structural heterogeneity. According to an empirical relationship between the width of the glass transition peak, liquid fragility index and the stretching exponent β' ($\Delta T_g/T_g = 2.20 \times (1/m + 0.0026) \times (1/\beta' - 0.59)$),[6,17] the β' of a_gZIF-62 here is determined to be 0.69. In addition, another study reported that the stretching exponent β' of the related glass a_TZIF-4 (Zn(Im)$_2$) is 0.71.[43] However, both β' values are derived from the non-linear Tool–Narayanaswamy–Moynihan–Hodge equation and not from the current non-exponential KWW model.

The structural evolution of a_gZIF-62 during sub-T_g relaxation was also characterized by synchrotron X-ray total scattering (Fig. 5). Data were collected on the as-quenched glass, alongside those annealed at 553 K for t_a = 0 and 72 hours. The structural factors $S(Q)$ showed no signs of Bragg peaks (Fig. 5a) confirming that all the samples were fully amorphous. The position of the first sharp diffraction peak remained invariant at $Q \sim 1.10$ Å^{-1}. Both short range (0–6 Å, Fig. 5b) and medium range (0–12 Å, Fig. 5c) atom-atom correlations were obtained after conversion of the total scattering data to the corresponding pair distribution functions (PDFs). Consistent with previous PDF data collected on ZIF-62,[6] intra-organic and metal-linker-metal bonding up to 6 Å is maintained upon glass formation and annealing. This short range order is near identical between annealed samples. Peaks at ∼1.3 Å and 2.0 Å, belonging to C–C/C–N, and Zn–N correlations, remain unchanged as expected (Fig. 5b). Few differences exist in the medium range order (Fig. 5c) and the PDFs are featureless and identical above 12 Å (Fig. S4, ESI†), as expected for amorphous ZIF samples. The lack of significant changes in glass structure upon annealing is consistent with the high viscosity, whereas the substantial heterogeneity of the glass is reflected by the broad range of β values obtained in the narrow sub-T_g temperature range.

Table 2 The glass transition temperature T_g, liquid fragility m, and the stretched exponent β from the KWW equation (eqn (7)) for different ranges of T_a/T_g

Composition	T_g/K	Fragility	T_a/T_g range	β	Ref.
$La_{55}Al_{25}Ni_{10}Cu_{10}$	454	35	0.91–0.98	0.75–0.79	36 and 37
$Pd_{43}Ni_{10}Cu_{27}P_{20}$	576	65	0.97–0.99	0.68–0.75	23
ZIF-62	593	35	0.93–0.99	0.44–0.76	This work
$Zr_{58.5}Cu_{15.6}Ni_{12.8}$-$Al_{10.3}Nb_{2.8}$	668	50	0.95–0.99	0.79–0.89	38 and 39
$Zr_{55}Cu_{30}Ni_5Al_{10}$	676	69	0.95–0.99	0.71–0.79	40
$Zr_{45}Cu_{39.3}Al_7Ag_{8.7}$	688	—	0.94–0.99	0.72–0.89	35
GeO_2	792	17–20	0.71–0.91	0.59–0.61	14

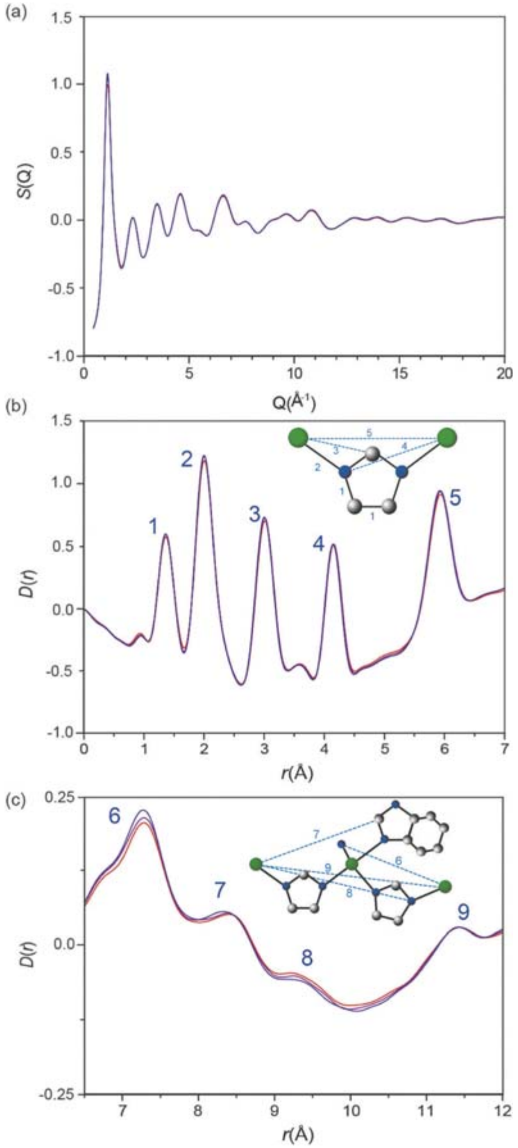

Fig. 5 (a) $S(Q)$ of a_gZIF-62 after melt quenching (red), annealing at 553 K with no duration (t_a = 0) (purple), and annealing at 553 K for 72 hours (blue). Corresponding pair distribution functions $D(r)$ in the regions (b) 0 Å < r < 7 Å and (c) 6.5 Å < r < 12 Å.

Conclusions

We have investigated the thermodynamic features and the enthalpy relaxation of a_gZIF-62. The small difference in the Gibbs free energy between crystal and supercooled liquid for ZIF-62 indicates a low thermodynamic driving force of nucleation in the temperature region between T_g and T_m. The enthalpy relaxation study demonstrates a wide range of the stretched exponent (β = 0.44–0.76) for a_gZIF-62, suggesting a substantial degree of structural heterogeneity. Pair distribution function measurements of the annealed glasses suggest no significant structural changes during sub-T_g relaxation.

Conflicts of interest

There are no conflicts to declare.

Acknowledgements

The authors are grateful to Ang Qiao for valuable discussions. CZ would like to thank the financial support from China Scholarship Council and the Elite Research Travel Scholarship from the Danish Ministry of Higher Education and Science (6161-00069B). We acknowledge the provision of synchrotron access to Beamline I15-1 (EE171151) at the Diamond Light Source, Rutherford Appleton Laboratory UK. TDB would like to thank the Royal Society for a University Research Fellowship. LL would like to thank the EPSRC for an allocated studentship. CWA thanks the Royal Society for a PhD studentship (RG160498), and the Commonwealth Scientific and Industrial Research Council for additional support (C2017/3108).

Notes and references

1 O. M. Yaghi, M. O'Keeffe, N. W. Ockwig, H. K. Chae, M. Eddaoudi and J. Kim, *Nature*, 2003, **423**, 705–714.
2 H. Furukawa, K. E. Cordova, M. O'Keeffe and O. M. Yaghi, *Science*, 2013, **341**, 1230444.
3 R. Ricco, C. Pfeiffer, K. Sumida, C. J. Sumby, P. Falcaro, S. Furukawa, N. R. Champness and C. J. Doonan, *CrystEngComm*, 2016, **18**, 6532–6542.
4 H. Tao, T. D. Bennett and Y. Yue, *Adv. Mater.*, 2017, **29**, 1601705.
5 T. D. Bennett, J.-C. Tan, Y. Yue, E. Baxter, C. Ducati, N. J. Terrill, H. H.-M. Yeung, Z. Zhou, W. Chen, S. Henke, A. K. Cheetham and G. N. Greaves, *Nat. Commun.*, 2015, **6**, 8079.
6 T. D. Bennett, Y. Yue, P. Li, A. Qiao, H. Tao, N. G. Greaves, T. Richards, G. I. Lampronti, S. A. T. Redfern, F. Blanc, O. K. Farha, J. T. Hupp, A. K. Cheetham and D. A. Keen, *J. Am. Chem. Soc.*, 2016, **138**, 3484–3492.
7 D. Umeyama, S. Horike, M. Inukai, T. Itakura and S. Kitagawa, *J. Am. Chem. Soc.*, 2015, **137**, 864–870.
8 L. Longley, S. M. Collins, C. Zhou, G. J. Smales, S. E. Norman, N. J. Brownbill, C. W. Ashling, P. A. Chater, R. Tovey, C.-B. Schönlieb, T. F. Headen, N. J. Terrill, Y. Yue, A. J. Smith, F. Blanc, D. A. Keen, P. A. Midgley and T. D. Bennett, *Nat. Commun.*, 2018, **9**, 2135.
9 T. D. Bennett, A. K. Cheetham, A. H. Fuchs and F.-X. Coudert, *Nat. Chem.*, 2017, **9**, 11–16.
10 K. L. Ngai, *Relaxation and Diffusion in Complex Systems*, Springer New York, New York, NY, 2011.
11 J. E. Shelby, *Introduction to Glass Science and Technology*, Royal Society of Chemistry, 2005.
12 Y. Z. Yue and C. A. Angell, *Nature*, 2004, **427**, 717–720.
13 Y. Z. Yue, *J. Non-Cryst. Solids*, 2008, **354**, 1112–1118.
14 L. N. Hu and Y. Z. Yue, *J. Phys. Chem. B*, 2008, **112**, 9053–9057.
15 Z. Wang, B. A. Sun, H. Y. Bai and W. H. Wang, *Nat. Commun.*, 2014, **5**, 5823.
16 J. C. Qiao, J. M. Pelletier, C. Esnouf, Y. Liu and H. Kato, *J. Alloys Compd.*, 2014, **607**, 139–149.
17 Z. Chen, L. Zhao, W. Tu, Z. Li, Y. Gao and L.-M. Wang, *J. Non-Cryst. Solids*, 2016, **433**, 20–27.
18 M. Gustafsson and X. Zou, *J. Porous Mater.*, 2012, **20**, 55–63.
19 R. Banerjee, A. Phan, B. Wang, C. Knobler, H. Furukawa, M. O'Keeffe and O. M. Yaghi, *Science*, 2008, **319**, 939–943.
20 A. K. Soper, Rutherford Appleton Laboratory, Technical Report, RAL-TR-2011-013, Didcot, UK, 2011.
21 A. K. Soper and E. R. Barney, *J. Appl. Crystallogr.*, 2011, **44**, 714–726.
22 A. Qiao, T. D. Bennett, H. Tao, A. Krajnc, G. Mali, C. M. Doherty, A. W. Thornton, J. C. Mauro, G. N. Greaves and Y. Yue, *Sci. Adv.*, 2018, **4**, eaao6827.
23 G. J. Fan, J. F. Löffler, R. K. Wunderlich and H.-J. Fecht, *Acta Mater.*, 2004, **52**, 667–674.
24 R. K. Wunderlich and H.-J. Fecht, *Mater. Trans.*, 2001, **42**, 565–578.
25 S. Suriñach, M. D. Baro, M. T. Clavaguera-Mora and N. Clavaguera, *Thermochim. Acta*, 1985, **85**, 175–178.
26 O. Kubaschewski, C. B. Alcock and P. J. Spencer, *Materials thermochemistry*, Pergamon Press, 1993.
27 L.-M. Wang, C. A. Angell and R. Richert, *J. Chem. Phys.*, 2006, **125**, 074505.
28 I. Gallino, J. Schroers and R. Busch, *J. Appl. Phys.*, 2010, **108**, 063501.
29 D. W. Lewis, A. R. Ruiz-Salvador, A. Gómez, L. M. Rodriguez-Albelo, F.-X. Coudert, B. Slater, A. K. Cheetham and C. Mellot-Draznieks, *CrystEngComm*, 2009, **11**, 2272–2276.
30 D. Wu and A. Navrotsky, *J. Solid State Chem.*, 2015, **223**, 53–58.
31 J. T. Hughes, T. D. Bennett, A. K. Cheetham and A. Navrotsky, *J. Am. Chem. Soc.*, 2013, **135**, 598–601.
32 F. Zhu, H. K. Nguyen, S. X. Song, D. P. B. Aji, A. Hirata, H. Wang, K. Nakajima and M. W. Chen, *Nat. Commun.*, 2016, **7**, 11516.
33 P. G. Debenedetti and F. H. Stillinger, *Nature*, 2001, **410**, 259–267.
34 R. Böhmer, K. L. Ngai, C. A. Angell and D. J. Plazek, *J. Chem. Phys.*, 1993, **99**, 4201–4209.
35 Y. Zhang and H. Hahn, *J. Non-Cryst. Solids*, 2009, **355**, 2616–2621.
36 Z. P. Lu, Y. Li and C. T. Liu, *J. Appl. Phys.*, 2003, **93**, 286–290.
37 T. Zhang, F. Ye, Y. L. Wang and J. P. Lin, *Metall. Mater. Trans. A*, 2008, **39**, 1953–1957.
38 I. Gallino, M. B. Shah and R. Busch, *Acta Mater.*, 2007, **55**, 1367–1376.
39 Q. J. Sun, C. Zhou, Y. Z. Yue and L. N. Hu, *J. Phys. Chem. Lett.*, 2014, **5**, 1170–1174.
40 J. C. Qiao and J. M. Pelletier, *Intermetallics*, 2011, **19**, 9–18.
41 Y. F. Zhang, L. N. Hu, S. J. Liu, C. F. Zhu and Y. Z. Yue, *J. Non-Cryst. Solids*, 2013, **381**, 23–28.
42 C. A. Angell, *J. Non-Cryst. Solids*, 1991, **131–133**(Part 1), 13–31.
43 D. Xu, Y. Liu, Y. Tian and L.-M. Wang, *J. Chem. Phys.*, 2017, **146**, 121101.

Electronic Supplementary Material (ESI) for Physical Chemistry Chemical Physics.

Thermodynamic features and enthalpy relaxation in a metal-organic framework glass

Chao Zhou,[a] Malwina Stepniewska,[a] Louis Longley,[b] Christopher W. Ashling,[b] Philip A. Chater,[c] David A. Keen,[d] Thomas D. Bennett*[b] and Yuanzheng Yue*[a,e]

ESI: Figures S1-S4.

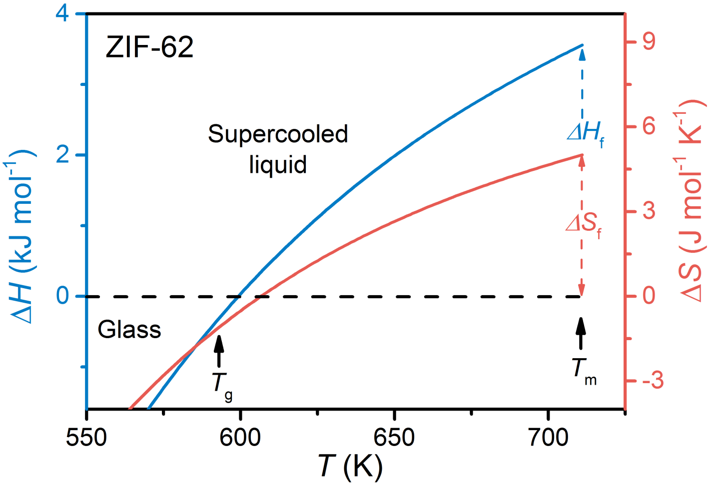

Fig. S1 Differences in enthalpy $\Delta H^{sl-x}(T)$ and entropy $\Delta S^{sl-x}(T)$ between the supercooled liquid and crystal in ZIF-62.

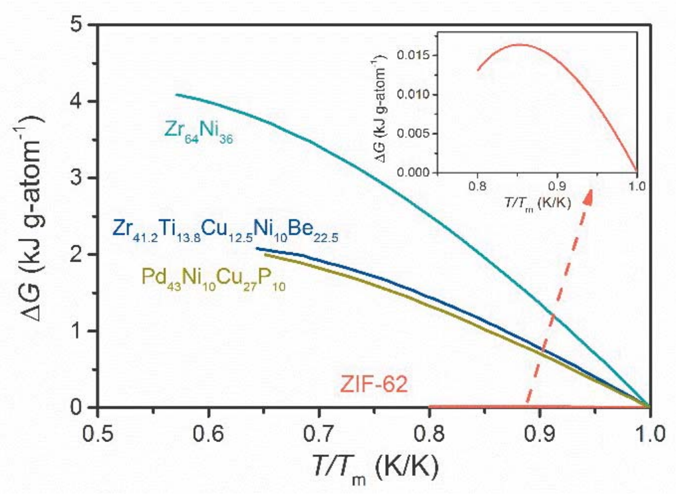

Fig. S2 Differences in the Gibbs free energy difference $\Delta G^{sl-x}(T)$ between the supercooled liquid and the crystal of ZIF-62, using a kJ g-atom^{-1} basis (18.5 atoms per ZIF-62 molecule according to the formula). The $\Delta G^{sl-x}(T)$ of some alloys are also given as comparisons from literature, in which one atom is taken as per mol.

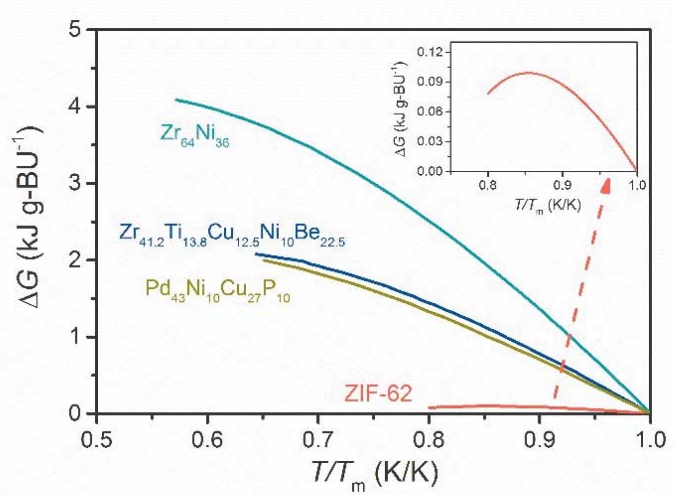

Fig. S3 Differences in the Gibbs free energy difference $\Delta G^{sl-x}(T)$ between the supercooled liquid and the crystal of ZIF-62, using a kJ g-BU^{-1} basis (BU: building unit, referring to Imidazolate, benzimidazolate and Zn^{2+}. Each ZIF-62 [Zn(Im)$_{1.75}$(bIm)$_{0.25}$] molecule has three BUs.) The $\Delta G^{sl-x}(T)$ of some alloys are also given as comparisons from literature, in which one BU is taken as per mol.

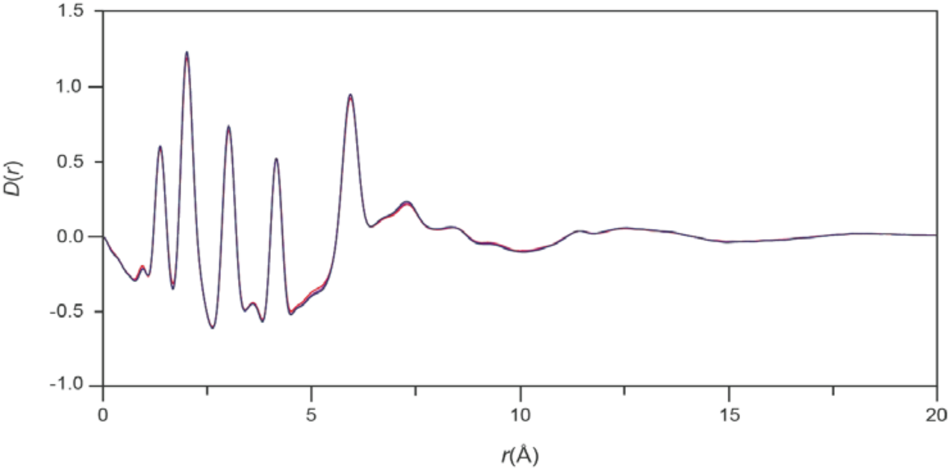

Fig. S4 Pair distribution function, $D(r)$ of a_gZIF-62 after melt quenching (red), annealed at 553 K with no duration (t_a=0) (purple), and annealed at 553 K for 72 hours (blue) in the region of 0~20 Å.

PAPER III

nature COMMUNICATIONS

ARTICLE

DOI: 10.1038/s41467-018-04553-6 OPEN

Liquid phase blending of metal-organic frameworks

Louis Longley[1], Sean M. Collins[1], Chao Zhou[2], Glen J. Smales[3,4], Sarah E. Norman[5], Nick J. Brownbill[6], Christopher W. Ashling[1], Philip A. Chater[4], Robert Tovey[7], Carola-Bibiane Schönlieb[7], Thomas F. Headen[5], Nicholas J. Terrill[4], Yuanzheng Yue[2,8,9], Andrew J. Smith[4], Frédéric Blanc[6,10], David A. Keen[5], Paul A. Midgley[1] & Thomas D. Bennett[1]

The liquid and glass states of metal–organic frameworks (MOFs) have recently become of interest due to the potential for liquid-phase separations and ion transport, alongside the fundamental nature of the latter as a new, fourth category of melt-quenched glass. Here we show that the MOF liquid state can be blended with another MOF component, resulting in a domain structured MOF glass with a single, tailorable glass transition. Intra-domain connectivity and short range order is confirmed by nuclear magnetic resonance spectroscopy and pair distribution function measurements. The interfacial binding between MOF domains in the glass state is evidenced by electron tomography, and the relationship between domain size and T_g investigated. Nanoindentation experiments are also performed to place this new class of MOF materials into context with organic blends and inorganic alloys.

---

[1] Department of Materials Science and Metallurgy, University of Cambridge, Charles Babbage Road, Cambridge CB3 0FS, UK. [2] Department of Chemistry and Bioscience, Aalborg University, DK-9220 Aalborg, Denmark. [3] Department of Chemistry, University College London, Gordon Street, London WC1H 0AJ, UK. [4] Diamond Light Source Ltd, Diamond House, Harwell Science and Innovation Campus, Didcot OX11 0DE, UK. [5] ISIS Facility, Rutherford Appleton Laboratory, Harwell Campus, Didcot OX11 0QX, UK. [6] Department of Chemistry, University of Liverpool, Crown Street, Liverpool L69 7ZD, UK. [7] Department of Applied Mathematics and Theoretical Physics, Centre for Mathematical Sciences, Wilberforce Road, Cambridge CB3 0WA, UK. [8] State Key Laboratory of Silicate Materials for Architectures, Wuhan University of Technology, 430070 Wuhan, China. [9] School of Materials Science and Engineering, Qilu University of Technology, 250353 Jinan, China. [10] Stephenson Institute for Renewable Energy, University of Liverpool, Crown Street, Liverpool L69 7ZD, UK. Correspondence and requests for materials should be addressed to T.D.B. (email: Tdb35@cam.ac.uk)

Metal–organic frameworks (MOFs), or networked structures of inorganic nodes connected by organic ligands, are flexible materials[1, 2] that can be broadly separated into two classes according to their porosity. Those that contain high internal surface areas are of intense interest for gas separations and catalysis[3–6], while dense MOF materials are investigated for their potential in other applications, e.g., conduction and magnetism[7–9].

The zeolitic imidazolate framework (ZIF) family of MOFs contains structures of tetrahedral M^{n+} nodes, (M = e.g., Zn, Co, Li, B, Ni, Mg) linked through the N atoms of imidazolate ligands[10–12]. Several members, e.g. ZIF-4-Zn, have been observed to possess accessible melting temperatures (T_m) between 400 and 600 °C[13]. The melting process proceeds via a dissociation–association mechanism of Zn-N coordination bonding and associated ligand switching between Zn^{2+} centres[14]. This becomes sub-nanosecond at T_m, in a manner analogous to the switching between hydrogen bonds in liquid water.

Such liquid states will be of particular intrigue in the development of alternatives to solid-state compounds for industrial-scale gas sorption and separations, due to the better handling and ease of installation compared to their classical solid-state counterparts[15]. Additionally, the intrinsic instabilities of microcrystalline MOF structures often preclude processing into the physical forms and bodies required by industry[16, 17]. Solution casting techniques combine the processability of organic polymers with selective MOF additives[18], though drop-casting, fibre drawing or melt spinning of single-component MOF liquid states would circumvent chemical compatibility concerns.

Cooling of (strongly associated) MOF liquids from above T_m results in a family of melt-quenched glasses chemically different from the inorganic, organic and metallic glass categories known at present. Accordingly, the formation of the liquid and glass phases of MOFs has recently emerged as a new area in an ever-expanding field[13, 14, 19–22]. The reactivity of these 'MOF liquids' has not yet been studied. Possibilities also exist in the production of novel MOF glasses, given the potential to incorporate multiple, designed chemical functionalities within a single glass, or in the creation of hybrid equivalents of alloys, blends and ceramics. Progress in the preparation of crystalline materials containing multiple inorganic or/and organic functionalities within a single framework structure has already been made[23, 24]. These multivariate MOFs[25, 26] arise from the interaction of several chemical components during solvothermal or mechanochemical synthesis, though not in the liquid state.

Here we are interested in how a MOF liquid behaves when combined with a secondary MOF component and the fundamental possibilities that this may afford in new materials' discovery. Specifically, we hypothesize that this may result in the formation of a glass containing interlocking MOF domains. Motivated by the concept of forming this type of material, which we term 'MOF blends', we investigated the high temperature reactions within mixtures of ZIF-4 [$M(Im)_2$] and ZIF-62 [$Zn(Im)_{1.75}(bIm)_{0.25}$] ($M = Co^{2+}$, Zn^{2+}, Im: $C_3H_3N_2^-$, bIm: $C_7H_5N_2^-$). Previously, it has been observed that, upon heating, both ZIF-4-Zn and ZIF-4-Co undergo a transition to a high-density amorphous phase and a dense crystal on heating to 300 °C and 450 °C, respectively. The zinc framework melts at 550 °C, unlike the dense cobalt crystal, which remains intact until thermal decomposition at ca. 570 °C. ZIF-62 remains in the room temperature crystalline state until liquid formation at 410 °C[13, 27].

Results

Differential scanning calorimetry. Samples of ZIF-4-Zn and ZIF-62 were synthesized and evacuated according to previously reported solvothermal procedures (Fig. 1a)[27–29]. A physical mixture of the two frameworks in equal weight portions, hereby referred to as (ZIF-4-Zn)(ZIF-62)(50/50), was prepared by ball-milling to ensure sample homogeneity (see Methods). Differential scanning calorimetric (DSC) experiments were then performed up to 590 °C in an argon atmosphere, beyond which thermal decomposition of the liquid state occurred. The first endothermic feature at 225 °C is coincident with a mass loss of ca. 9% and ascribed to desolvation. As expected, two endothermic features belonging to the respective melting points of ZIF-62 and ZIF-4-Zn (445 °C and 580 °C, respectively) were noted, identical to those recorded from pure samples (Fig. 1b)[13]. The melting enthalpy of ZIF-62 was recorded as ca. 3 kJ mol^{-1}. Quenching after isothermal treatment for 2 min at 590 °C yielded a glassy, amorphous product (Supplementary Figure 1).

Re-heating of this amorphous sample revealed a single glass transition, glass transition temperature (T_g) = 306 °C (Fig. 1b, blue solid line), whereas two separate features at 292 °C (ZIF-4-Zn) and 318 °C (ZIF-62) would have been anticipated[13]. A physical mixture of the two glasses formed separately yielded the expected two T_gs (Supplementary Figures 2 and 3). Such a markedly different, single value is indicative of liquid phase mixing, as is also the case in e.g. metallic glasses[30], inorganic oxides and phosphates[31], or miscible polymer blending in organics[32]. We name the blend produced $(ZIF\text{-}4\text{-}Zn)_{0.5}(ZIF\text{-}62)_{0.5}$. The ability to tailor T_g was explored through analysis of a further set of $(ZIF\text{-}4\text{-}Zn)_{1-x}(ZIF\text{-}62)_x$ mixtures. The results from DSC experiments on the glasses formed upon quenching the liquids from 590 °C (Supplementary Figure 4) show a composition-dependent shift in T_g (Fig. 1c). The increase in T_g with increasing ZIF-62 content follows a linear relation, analogous to the trends observed in binary organic mixtures exhibiting mass additivity behaviour ($\Delta T_g = 0$) e.g. poly(1,3-trimethylene adipate) and poly(vinyl methyl ether)[32].

In order to facilitate the use of electron microscopy as a characterization technique for the blended glass, a physical mixture of ZIF-4-Co and ZIF-62, hereby referred to as (ZIF-4-Co)(ZIF-62)(50/50), was analysed. A pure sample of ZIF-4-Co was synthesized by following prior literature[33]. As expected[27], it possesses a stable amorphous region from 325 to 500 °C (Supplementary Figure 5), before the expected recrystallization to a dense ZIF at ca. 510 °C. No melting above this temperature is observed. DSC experiments on (ZIF-4-Co)(ZIF-62)(50/50) confirmed these transitions, along with the expected T_m of ZIF-62 (Fig. 1d). Quenching of the sample from 425 °C, i.e. a region containing amorphous ZIF-4-Co and liquid ZIF-62, yielded a glass (Supplementary Figure 6). A subsequent DSC of the quenched glass again demonstrated a single T_g, at ca. 300 °C (Supplementary Figure 7), despite the fact that it was formed from an interaction between an amorphous solid and a liquid. A second measurement using a slower heating rate again yielded only one T_g (Supplementary Figure 1). Differences between $(ZIF\text{-}4\text{-}Co)_{0.5}(ZIF\text{-}62)_{0.5}$ and $(ZIF\text{-}4\text{-}Zn)_{0.5}(ZIF\text{-}62)_{0.5}$ are perhaps expected to be small, given the very high viscosities for both ZIF-4-Zn and ZIF-62 reported previously[14, 34].

Structural characterization. Small-angle X-ray scattering (SAXS) has previously been used to reveal information on the pore surface and characteristics of MOF-5[35], HKUST-1[36] and monitor particle evolution and growth in situ[37, 38]. Combined with wide-angle X-ray scattering (WAXS), it provides a powerful tool that has also been used to study the collapse of some MOFs to amorphous states[21].

The temperature-resolved WAXS profile of ZIF-62 (Fig. 2a) shows consistent Bragg diffraction from the sample, which

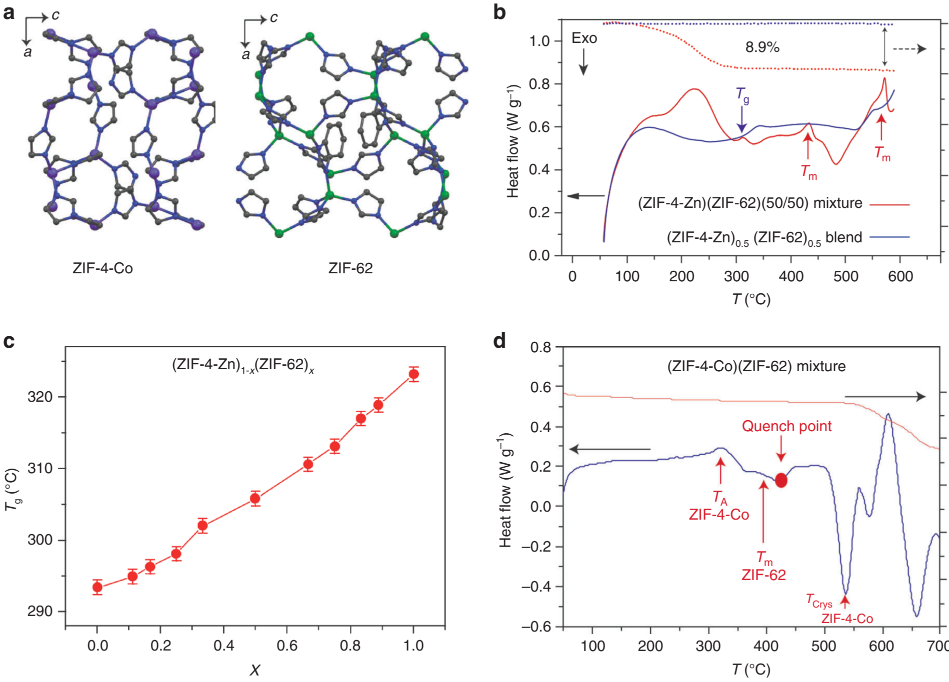

Fig. 1 MOF liquid dynamics and tailoring glass transition temperature. **a** View down the *b* axis of the unit cells of ZIF-4-Co and ZIF-62. N—dark blue, C—grey, Zn—green, Co—purple, H atoms omitted for clarity. **b** Enthalpy response (red curve) and mass change (dotted curve) in the physical mixture (ZIF-4-Zn)(ZIF-62)(50/50) during heating at 10 °C/min. Blue curve: reheating curve representing the enthalpy response of the corresponding glass that forms upon quenching, i.e., (ZIF-4-Zn)$_{0.5}$(ZIF-62)$_{0.5}$ during prior cooling at 10 °C min^{-1}. **c** Evolving glass transition of the sample series (ZIF-4-Zn)$_{1-x}$(ZIF-62)$_x$. **d** Enthalpy response (blue curve) and mass change (orange curve) of the physical mixture (ZIF-4-Co)(ZIF-62)(50/50) during heating at 10 °C min^{-1}

reduces in intensity and then disappears at ca. 340 °C upon gradual formation of the liquid state. Decomposition of this MOF liquid is then evidenced at ca. 550 °C by the emergence of several Bragg features at relatively large q values. The temperature-resolved WAXS profile of (ZIF-4-Co)$_{0.5}$(ZIF-62)$_{0.5}$ (Fig. 2b) contains a region in which amorphous ZIF-4-Co and the ZIF-62 liquid are co-existent, between ca. 340 °C and ca. 400 °C. Recrystallization of amorphous ZIF-4-Co to a dense phase is then observed. These observations are broadly consistent with the DSC results presented in Fig. 1, though these differ because of the dissimilar temperature–time profiles of the two experiments.

The decay in SAXS signal at room temperature was extracted from the three-dimensional, variable temperature plot of the SAXS intensity I_{SAXS} for ZIF-62 and follows power law behaviour of the form $q^{-\alpha}$, where $\alpha = 3.9$ (Supplementary Figure 9). At ca. 440 °C, a decrease to $\alpha = 3.4$ is observed, consistent with the formation of rougher internal surfaces upon melting. Computation of the volume-weighted fraction of the particles (Supplementary Figure 9) shows an initial expansion in particle radii from 5 nm at the point of melting, which is consistent with interfacial particle coalescence. The radii then drop drastically and the volume fraction tends to zero, as homogeneous melting of the sample occurs. The increase in particle size at ca. 460 °C then marks the onset of gradual thermal decomposition.

The variable temperature plot of the SAXS intensity I_{SAXS} for (ZIF-4-Co)(ZIF-62)(50/50) (Fig. 2c) was also fitted and displays a lower initial value of $\alpha = 3.66$, consistent with the presence of different internal pore structures and particle sizes within the ball-milled mixture of MOFs. This value increases to 4 on heating to 340 °C when ZIF-4-Co amorphizes, before decreasing to 3.1 due to both recrystallization of ZIF-4-Co and melting of ZIF-62. The volume-weighted fraction of the particles also reveals that the distribution of particle scatterers is much broader in the initial instance, consistent with the inhomogeneity in sample composition. Like ZIF-62, the particles disappear rapidly upon liquid formation at 340 °C. The broad distribution of particles that starts to appear at ca. 450 °C is ascribed to the known formation of crystallites of a dense ZIF from ZIF-4-Co at these higher temperatures (Fig. 2d).

Liquid-state ^{1}H nuclear magnetic resonance (NMR) was carried out by digesting samples of (ZIF-4-Co)(ZIF-62)(50/50) and (ZIF-4-Co)$_{0.5}$(ZIF-62)$_{0.5}$ (produced by quenching from 445 °C) in a mixture of deuterium chloride (DCl; 35%)/deuterium oxide (D_2O; 100 µL) and DMSO-d$_6$ (500 µL) (Supplementary Figure 10). Resonances in both spectra are fairly broad, arising from the substantial paramagnetic broadening induced by the presence of Co^{2+}, predominantly in an octahedral complex coordinated by either H_2O or dimethyl sulphoxide (DMSO)[39] giving the metal centre a likely electronic arrangement of $t_{2g}^{5}e_g^{2}$ and three unpaired electrons[40]. This prevents the integration of most of the aromatic signals of the imidazolate ligands. Both NC***H***N$_{\mathrm{Im}}$ and NC***H***N$_{\mathrm{bIm}}$ peaks are, however, well resolved in the 9–9.7 ppm high-field region and are used to determine the Im:bIm ligand concentration ratios; values of 1:0.076 ± 0.010 and 1:0.054 ± 0.015 are obtained for (ZIF-4-Co)(ZIF-62)(50/50) and (ZIF-4-Co)$_{0.5}$(ZIF-62)$_{0.5}$, respectively (Supplementary Figure 10). Within error, these values are both in agreement with the expected 1:0.066 stoichiometric ratio. Additionally, in the glass

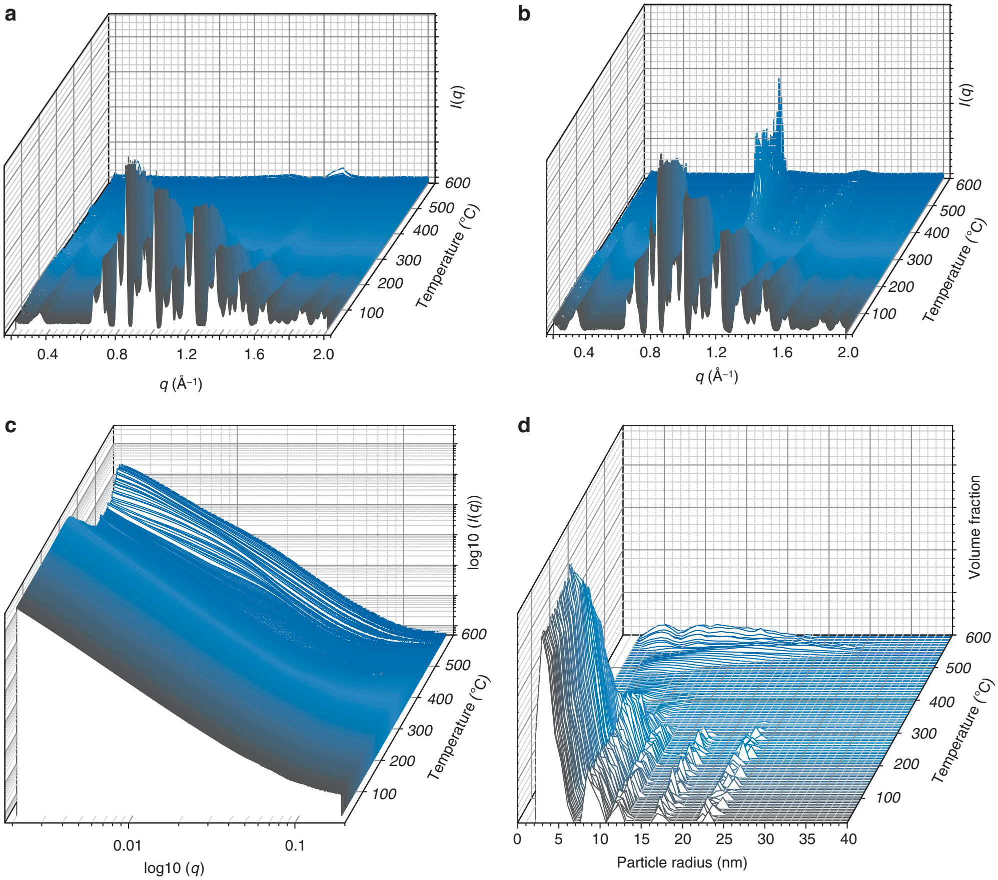

Fig. 2 Temperature-resolved diffraction. **a** Temperature-resolved WAXS profile of ZIF-62 upon heating from 25 °C to 600 °C. **b** The corresponding data for (ZIF-4-Co)(ZIF-62)(50/50). **c** Temperature-resolved SAXS profile for (ZIF-4-Co)(ZIF-62)(50/50). **d** Temperature-resolved volume fraction distributions of (ZIF-4-Co)(ZIF-62)(50/50)

sample, a second resolved peak of the bIm ligand (C***H***CN$_{\mathrm{bIm}}$) can be integrated relative to NC***H***N in Im, giving a 1:0.12 ± 0.01 ratio (expected integration from stoichiometry is 1:0.13), confirming that any loss of ligand in the amorphization process is negligible and/or below the detection limit of NMR. The absence of impurity peaks in the 7–9 ppm region indicates minimal decomposition of imidazolates during digestion/amorphization.

The chemical structure of the blend was probed through synchrotron neutron and X-ray total scattering. Whereas the X-ray structure factor $S(Q)$ of (ZIF-4-Co)(ZIF-62)(50/50) contained Bragg diffraction, that of (ZIF-4-Co)$_{0.5}$(ZIF-62)$_{0.5}$, as expected, did not. This rules out small regions of crystallinity in the latter (Fig. 3a). After appropriate data corrections (see Methods section), the data were converted to the corresponding pair distribution functions (PDFs) (Fig. 3b), which are weighted histograms of the atom pair distances present in both samples. Interatomic distances at 1.3, 2, 3, 4 and 6 Å were common between both crystal and blend samples, consistent with previous conclusions on near-identical short-range order between crystal and glass ZIFs[14].

Above this distance, oscillations at high r were present from the crystalline mixture (ZIF-4-Co)(ZIF-62)(50/50), though the PDF of (ZIF-4-Co)$_{0.5}$(ZIF-62)$_{0.5}$ was relatively featureless. A dual-phase refinement in PDFGUI[41] of the PDF for (ZIF-4-Co)(ZIF-62)(50/50) was performed in the range 1–15 Å, confirming the presence of both crystalline phases (Fig. 3b inset). Neutron total scattering was also carried out on a deuterated sample of (ZIF-4-Co)$_{0.5}$(ZIF-62)$_{0.5}$ (Supplementary Figures 11 and 12). The expected C-D peak below 1 Å was not visible in the PDF, due to the sample containing a higher hydrogen content than expected. Above this distance and below 6 Å, the PDF was similar to those previously reported for deuterated Zn(Im)$_2$ polymorphs[42].

To probe the evolution in domain structure or size upon heating, synchrotron X-ray diffraction data were collected on a sample of (ZIF-4-Co)$_{0.5}$(ZIF-62)$_{0.5}$ heated from room temperature to 460 °C (Fig. 3c). The first sharp diffraction peak in the $S(Q)$ varied little in intensity or position. While the second and third peaks also remained approximately invariant on heating, some 'flattening' of features at high Q values occurred upon heating above 300 °C. This temperature corresponds to the T_g of (ZIF-4-Co)$_{0.5}$(ZIF-62)$_{0.5}$, and the flattening is consistent with formation of a more liquid-like state. The peak in the $D(r)$ at r = 1.3 Å, which only contains contributions from C-C and C-N pairs

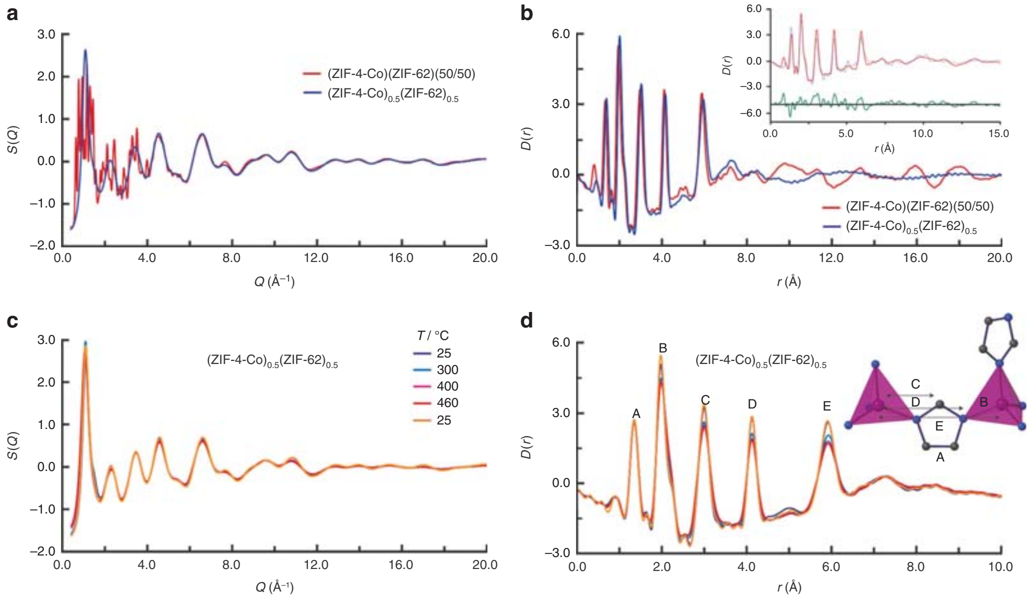

Fig. 3 Intra-domain structure. **a** X-ray structure factors $S_x(Q)$ of (ZIF-4-Co)(ZIF-62)(50/50) and (ZIF-4-Co)$_{0.5}$(ZIF-62)$_{0.5}$. **b** Corresponding X-ray pair distribution functions, $D(r)$. Inset: refinement of (ZIF-4-Co)(ZIF-62)(50/50) against the published structure files for ZIF-62 and ZIF-4-Co. Fit—broken blue line. **c** X-ray structure factors of (ZIF-4-Co)$_{0.5}$(ZIF-62)$_{0.5}$ upon heating. **d** Pair distribution functions $D(r)$ of (ZIF-4-Co)$_{0.5}$(ZIF-62)$_{0.5}$ upon heating, with the atom pairs that contribute most of the intensity in the labelled peaks indicated in the structural fragment (A–E)

and no contributions from pairs involving Co or Zn, remained constant in intensity and position (Fig. 3d). Those peaks arising mainly from M-N$_1$ ('B'~2 Å), M-C ('C'~3 Å), M-N$_2$ ('D'~4 Å) and M-M ('E'~6 Å) correlations, however, were observed to undergo a reduction in intensity upon heating. The intensity recovered upon cooling back to ambient temperature, showing that no permanent change in short-range order had taken place.

To investigate the suitability of transmission electron microscopy as a characterization technique for MOF glasses, pure samples of crystalline ZIF-62, (ZIF-4-Co)(ZIF-62)(50/50) and (ZIF-4-Co)$_{0.5}$(ZIF-62)$_{0.5}$ were investigated by electron energy loss spectroscopy (EELS, Fig. 4a, Supplementary Figures 13 and 14). The K (1s) ionization edges for C and N atoms exhibited high-intensity π^* peak features, which are a signature of conjugated heterocycles and consistent with the π^* signature previously reported for EELS of molecular imidazole[43]. These observations demonstrated that the ligands were not damaged under the selected electron beam conditions used. A sample of (ZIF-4-Co)$_{0.5}$(ZIF-62)$_{0.5}$ was subsequently investigated using annular dark field (ADF) scanning transmission electron microscopy (STEM) exhibiting thickness and atomic number contrast and EELS and X-ray energy dispersive spectroscopy (EDS) for chemical mapping at similar or lower electron beam exposures.

EELS performed on a single shard of the glass (Fig. 4a) clearly showed the presence of Co and Zn (Fig. 4b) along with an interfacial region. EDS was performed to yield more insight into the domain structure and interfacial bonding present in the glass particles too thick for EELS analysis (Fig. 4b, c). These revealed a more extended network exhibiting relatively sharp interfaces between Co and Zn domains. Domain sizes were observed ranging from 200 nm to >1 μm in width. This is markedly different to (ZIF-4-Co)(ZIF-62)(50/50), where separate particles of each framework, without domain mixing, were located (Supplementary Figure 15). In STEM analyses, the electron probe is transmitted through the sample, resulting in EELS and EDS signals that arise from the entire volume through the three-dimensional sample. As a result, these two-dimensional analyses alone were not sufficient to fully characterize the interfaces between the lamellar domains of Co and Zn MOFs. Two-dimensional interface regions with mixed signal composition are not distinguishable from single-phase compositional domains overlapping along the electron beam direction.

EDS tomography was performed in order to address this uncertainty and to characterize the sharpness of the interface between the Co- and Zn-containing regions (Fig. 5). A single-piece shard of (ZIF-4-Co)$_{0.5}$(ZIF-62)$_{0.5}$ was located that contained two large domains of predominantly Co and Zn, respectively. At the interface, there were two regions (labelled 1 and 2 in Fig. 5) characteristic of heterogeneous mixing between the Co and Zn phases and exhibiting a similar interlocked microstructure as those observed in Fig. 4b, c. Inspection of the tomographic reconstruction volumes at these features revealed that, at feature 1, the Co protrusion is present in a region with negligible Zn content. At feature 2, both Co and Zn were found in the same three-dimensional region, suggesting some minor homogeneous mixing. While some regions of the three-dimensional interface exhibited micro-scale mixing of Co and Zn, the majority were segregated into single-metal domains within an interlocked network microstructure.

Mechanical properties. Nanoindentation has previously been used to probe the Young's moduli, E, of crystalline and amorphous MOFs[44], though it often results in significant differences between the identified values and those gained from computational studies. The Young's moduli provides a descriptor of the stiffness of a structure under strain and is highly dependent on

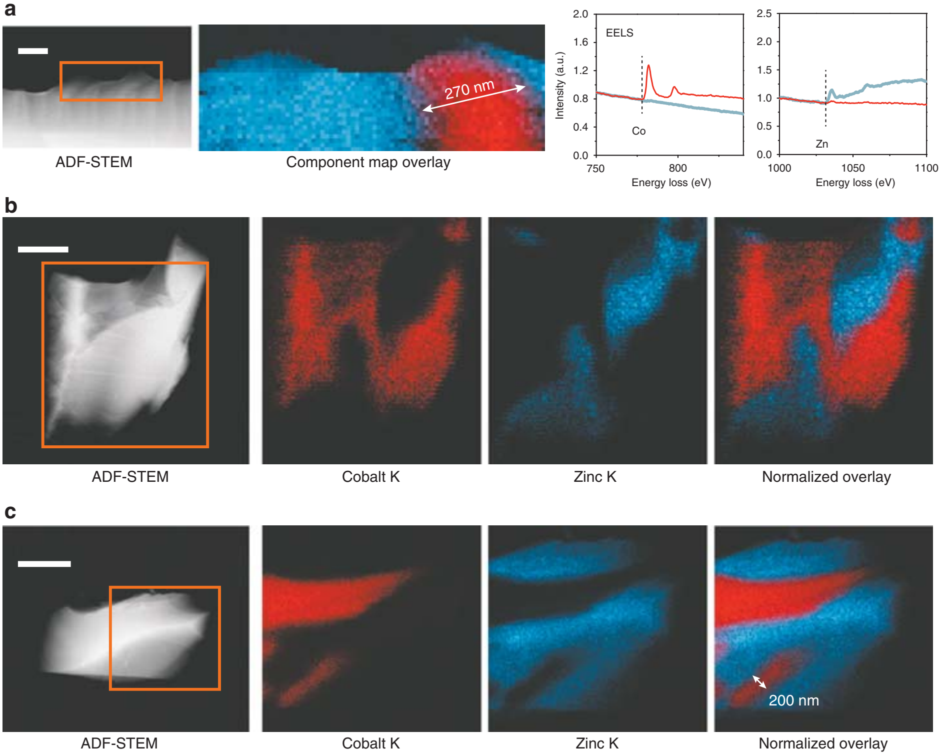

Fig. 4 Chemical mapping of domain structures in (ZIF-4-Co)$_{0.5}$(ZIF-62)$_{0.5}$. **a** ADF-STEM image and corresponding EELS analysis. Independent component analysis was carried out to separate Co and Zn signals and plotted as a component map overlay (the spectral signals are shown on the right). Scale bar is 250 nm. **b** ADF-STEM image and corresponding X-ray EDS mapping for a second glass particle. Scale bar is 1 µm. **c** ADF-STEM image and corresponding X-ray EDS mapping for a third glass particle. The orange boxes highlight the regions analysed for chemical mapping. Scale bar is 1 µm

the molecular structure. Nanoindentation experiments were thus performed on two independent samples of (ZIF-4-Co)$_{0.5}$(ZIF-62)$_{0.5}$. The existence of both constituent phases in a single glass monolith, in domain sizes smaller than the indenter tip, was confirmed by the consistency across measurements of E. Average values of E (7.5 ± 0.5 GPa and 7.1 ± 0.4 GPa, Fig. 6a) were recorded from the load–displacement data (Fig. 6b) of indentations on polished glass monoliths (Fig. 6a inset) between 100 nm and 500 nm. These values lie roughly intermediate between the upper bound of that expected for organic polymers and the lower bound for inorganic glasses (Fig. 6c).

The blend is of comparable pycnometric density to single-phase samples of *a*ZIF-4-Co and the ZIF-62 glass[13, 27], though it exhibits less compliant behaviour under the indenter tip. The increase in E relative to the pure samples (*a*ZIF-4-Co, $E = 6.6$ GPa and ZIF-62 glass, $E = 6.1$ GPa) is ascribed to the isothermal treatment of 2 min above T_m, which is necessary for blend formation. This is similar to the increase in E from quenching a ZIF-62 liquid from T_m ($E = 6.6$ GPa) and 572 °C ($E = 8.8$ GPa)[13]. It should also be noted that the relatively poor agreement between calculated and experimental values of E for MOFs has been ascribed to various factors including the large surface effects from small single crystals or monoliths, structural defects and macroscale sample cracking[45]. The prior values of E reported for *a*ZIF-4-Co were gained from non-coalesced single-crystal samples, and the extent of defects in all three systems has not been the subject of investigation.

Discussion

We have demonstrated that the two MOF liquids derived from ZIF-4-Zn and ZIF-62 can be blended or alloyed together. The resultant melt-quenched glass shows a single T_g, the position of which can be controlled according to the sample composition. The resultant glass structure was probed through electron microscopic measurements on a glass derived from ZIF-4-Co and ZIF-62, finding heterogeneous domain formation. Binding between the domains was investigated using electron tomography, showing regions of homogeneous Co and Zn concentration—indicative of liquid–liquid reactivity. The absence of complete homogeneous mixing is in this instance ascribed to the high viscosity of both molten phases. The interfacial binding of the separate MOF domains to one another is entirely consistent with the observed mechanism of MOF melting, which proceeds via imidazolate dissociation from a M^{2+} centre, and subsequent association of a different imidazolate ligand. We therefore ascribe the domain interlocking mechanism to ligand 'swapping' between the liquid MOF phase and amorphous solid, resulting in the heterometallic MOF glasses shown[14]. Similar heterogeneous structures are also found in SiO_2-Al_2O_3 glasses, where SiO_2-rich domains are embedded within Al_2O_3-rich phases[46].

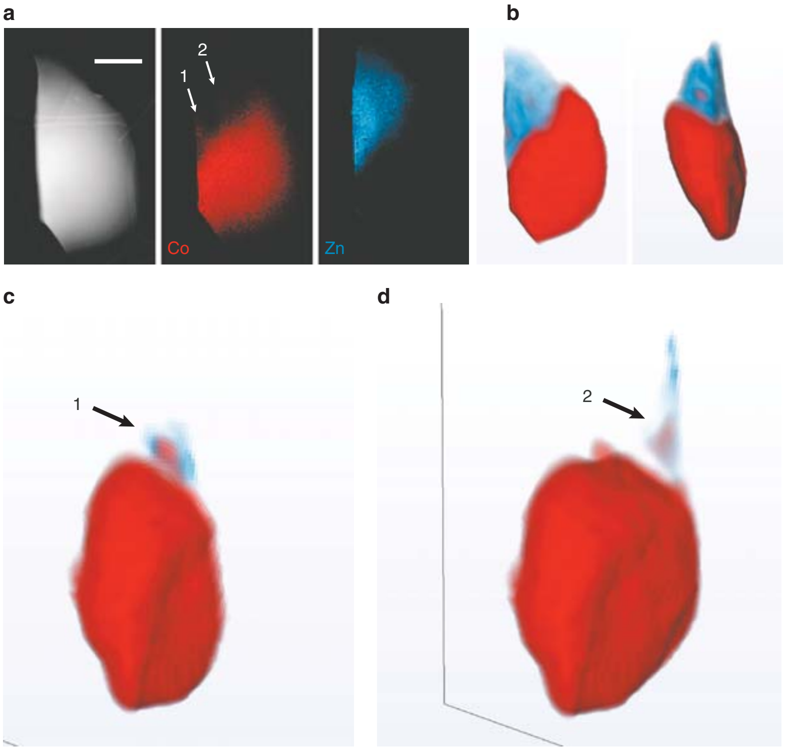

Fig. 5 EDS tomography of a (ZIF-4-Co)$_{0.5}$(ZIF-62)$_{0.5}$ glass particle. **a** Two-dimensional analyses by ADF-STEM showing the particle morphology and EDS chemical maps of Co and Zn. Scale bar is 500 nm. **b** A volume rendering of the tomographic reconstructions for the Co and Zn signals (two orthogonal viewing directions). **c**, **d** Discrete two-dimensional slices from the three-dimensional volume reconstruction for Zn plotted with the transected volume rendering of the Co reconstruction. Two protrusions from the principal Co domain are highlighted with the numbers 1 and 2. These highlight the extent of three-dimensional spatial overlap in Co and Zn in **c**, **d**

The relationship between domain size and T_g was investigated through the synthesis of two further (ZIF-4-Co)(ZIF-62)(50/50) samples with both larger and smaller initial particle sizes. The first sample was formed through light grinding of ZIF-62 and ZIF-4-Co in a mortar and pestle and compared to a second sample, where the two crystalline frameworks were ball-milled for 20 min together (as opposed to the 5 min used initially). EDS experiments provided qualitative support for the differences in domain sizes of each component using these three different methods of sample preparation (Supplementary Figure 15). Furthermore, DSC experiments confirmed that the sample formed through light grinding contained two distinct T_gs (Supplementary Figures 16 and 17), while that formed by ball-milling for a longer time (Supplementary Figure 18) possesses only one, in a near identical position to the original blend sample (ca. 300 ° C).

The binary MOF blend formed and characterized here belongs to the compatible polymer blend category, due to the chemically compatible interactions between the two components and the observation of a single glass transition[47]. A mixture of two chemically incompatible MOF liquids would therefore be expected give rise to an immiscible blend with two or more T_gs. The results will prove important in understanding the possibilities afforded by the glass and liquid states of MOFs, demonstrating that blended materials containing two or more MOFs can be produced. We have also shown that the reactivity of the liquid MOF state may be utilized in binding to other MOF components and that the T_g of MOF glasses may be tailored according to blend composition.

Methods

Synthesis. All crystalline samples studied here crystallize in the *Pbca* space group, with cell volumes of 4342 Å^3, 4280 Å^3 and 4466 Å^3 for ZIF-4-Zn, ZIF-4-Co and ZIF-62, respectively. The preparation of mixed samples was done in 0.5 g quantities. For example, for a 50/50 ratio mixture, 0.25 g of each MOF was placed in a 10 ml stainless steel jar, along with 2 × 7 mm diameter stainless steel balls. The mixture was then milled for 5 min (or, to produce a finer particle size for one control sample, for 20 min) in a Retsch MM400 grinder mill operating at 25 Hz. Powder X-ray diffraction patterns of both ball-milled mixtures are shown in Supplementary Information, demonstrating the lack of amorphization.

Differential scanning calorimetry. DSC characterizations were conducted using a Netzsch STA 449 F1 instrument in platinum crucibles at a 10 °C min^{-1} heating rate. The simultaneous DSC–thermogravimetric analysis in Supplementary Figure 5 was performed using a TA instruments Q-600 series differential scanning calorimeter, with the sample (~7 mg) held on an aluminium pan under a continuous flow of dry Ar gas. The data were obtained using a heating rate of 10 °C min^{-1}. T_gs were determined by the method described elsewhere[48].

X-ray powder diffraction. Data were collected with a Bruker-AXS D8 diffractometer using Cu Kα ($\lambda = 1.540598$ Å) radiation and a LynxEye position sensitive detector in Bragg–Brentano parafocussing geometry.

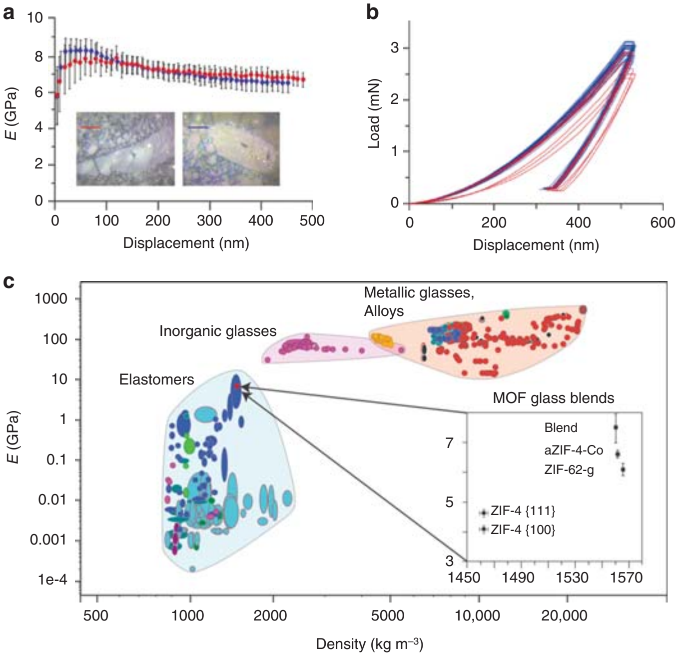

Fig. 6 Mechanical properties. **a** The Young's modulus, *E*, as a function of indentation depth for two samples of (ZIF-4-Co)$_{0.5}$(ZIF-62)$_{0.5}$. Error bars represent the standard deviation of 26 measurements for sample 1 (blue) and 8 for sample 2 (red). Inset—optical images of the two samples. Scale bars are 20 μm. **b** Load-displacement curves for both samples and **c** Ashby-style plot of existing alloys, blends and glasses, with the materials here placed into context. Data for ZIF-4 was taken from previous work[27]. Different shadings represent broad material classes

Combined SAXS and WAXS. X-ray data were collected at the I22 beamline at the Diamond Light Source, UK ($\lambda = 0.9998$ Å, 12.401 keV). The SAXS detector was positioned at a distance of 9.23634 m from the sample as calibrated using a 100 nm period Si_3N_4 grating (Silson, UK), giving a usable *Q* range of 0.0018–0.18 Å^{-1}. The WAXS detector was positioned at a distance of 0.16474 m from the sample as calibrated using a standard CeO_2 sample (NIST SRM 674b, Gaithersburg, USA), giving a usable *Q* range of 0.17–4.9 Å^{-1}. Samples were loaded into 1.5 mm diameter borosilicate capillaries under argon inside a glovebox and sealed with Blu-tac and Para-film to prevent the ingress of air. Samples were heated using a Linkam THMS600 capillary stage (Linkam Scientific, UK) from room temperature to 600 °C at 10 °C min^{-1}. Simultaneous SAXS/WAXS data were collected every 1 °C. Data were reduced to one dimensional using the DAWN package[49, 50] and standard reduction pipelines[51]. Values for the power law behaviour of the samples were found using the power law model of SASView 4.1.1[52]. Data were fitted over the range $0.003 \le q \le 0.005$ Å^{-1}. Particle size distributions were calculated using the McSAS package[53, 54], a minimal assumption Monte Carlo method for extracting size distributions from small-angle scattering data. Data were fitted over the range $0.002 \le q \le 0.18$ Å^{-1} with a sphere model.

NMR spectroscopy. NMR samples were prepared by digesting ~8 mg of sample in 100 μL of 35 wt% DCl in D_2O (purchased from Sigma Aldrich, 99% deuterated) then dissolved in 500 μL of DMSO-d_6 (purchased from Sigma Aldrich, 99.9% deuterated). All ^{1}H NMR spectra were recorded on a Bruker Avance III 400 MHz spectrometer.

Total scattering measurements. X-ray data were collected at the I15-1 beamline at the Diamond Light Source, UK ($\lambda = 0.161669$ Å, 76.7 keV). A sample of (ZIF-4-Co)(ZIF-62)(50/50), and a small amount of the (ZIF-4-Co)$_{0.5}$(ZIF-62)$_{0.5}$ sample used in the neutron total scattering experiment were loaded into borosilicate glass capillaries of 1.17 mm (inner) diameter. Data on the samples, empty instrument and capillary were collected in the region of $\sim 0.4 < Q < \sim 26$ Å^{-1}. Corrections for background, multiple scattering, container scattering, Compton scattering and absorption were performed using the GudrunX program[55, 56]. Variable temperature measurements were performed using an identical set-up, though the capillaries were sealed with araldite. Data were taken upon heating at 25 °C, 100 °C, 200 °C, 280 °C and then in 10 °C steps to 340 °C. Further data were collected in 20 °C intervals to 460 °C, before cooling and a final data set taken at room temperature. Data were corrected using equivalent measurements taken from an empty capillary heated to identical temperatures. Published structures for ZIF-4-Co and ZIF-62 were used to refine data in PDFGUI[10, 33]. The values U_{11}, U_{22} and U_{33} were set to 0.003 Å^2 and constrained to be isotropic. Cross-diagonal terms were set to 0, and data beyond 15 Å were not fitted because of the lack of intensity. The final R_w value was 0.34, due to some disordering in the initial mixture introduced by ball-milling.

Deuterated samples of ZIF-4-Co and ZIF-62 were prepared by equimolar replacement of the hydrogenated benzimidazole and imidazole in their respective syntheses, by the deuterated equivalents, supplied by the ISIS Deuteration Facility. A glass sample of (ZIF-4-Co)$_{0.5}$(ZIF-62)$_{0.5}$ was then produced as reported in the manuscript. Data were measured at room temperature using the NIMROD diffractometer at ISIS[57]. A sample was placed into an 8-mm diameter thin-walled vanadium can, and data from an empty vanadium can, empty instrument, 8 mm V-5.14% Nb rod was used to correct the data in the Gudrun software[55].

Gas pycnometry. Pycnometric measurements were carried out using a Micromeritics Accupyc 1340 helium pycnometer. The typical mass used was 200 mg; the values quoted are the mean and standard deviation from a cycle of 10 measurements.

Electron microscopy and spectroscopy. STEM data were acquired using an FEI Osiris microscope equipped with a high-brightness X-FEG electron source and operated at 80 kV. The beam convergence was set to 11.0 mrad. EELS was acquired using a post-column Gatan Enfinium spectrometer. A 2.5 mm entrance aperture was selected, defining a collection semiangle of 19.4 mrad. Spectra were acquired in dual EELS mode: electrons undergoing no inelastic scattering (the zero loss peak) and those undergoing low energy losses were recorded with a fast acquisition time (0.0001 s) and nearly simultaneously electrons undergoing inelastic scattering at element-specific core loss ionization edges were recorded at longer exposures times (100 ms exposure at C and N *K* edges and 500 ms at Co and Zn L_{23} edges). Probe currents in this electron optical configuration were typically <150 pA. X-ray EDS was acquired using a 'Super-X' EDS detector system with four detectors mounted symmetrically about the optic axis of the microscope (200 ms per pixel). For all spectroscopic data, images were also simultaneously recorded on ADF detectors. These images contain atomic number and thickness contrast, giving structural information in parallel with the chemical mapping obtained in the EELS and EDS data. For EDS tilt-series tomography, EDS spectrum images were acquired from −70° to 70° in 10° increments.

Data were processed using Hyperspy[58], an open-source software coded in Python. For EELS data, the spectra were first aligned to the ZLP, initially by shifting the maximum intensity channel to zero followed by cross-correlation-based sub-pixel alignment. Spikes due to X-rays striking the charge-coupled device detector were removed using a routine that automatically identified outlying high-intensity pixels and performed interpolation in the spectral region after removal of the spike. Independent component analysis was likewise performed in Hyperspy. For tilt-series tomography, Zn and Co chemical maps were initially combined for alignment of the tilt-series image-stack. In order to correct for detector shadowing as a function of tilt angle, the chemical maps were re-normalized to maintain constant integrated intensities at all tilts. This procedure was based on the constant total quantity of Zn and Co in the particle recorded within the field of view at all tilt angles. The combined Zn and Co image-stack was aligned using Scikit-Image, an open-source image processing software coded in Python, first using cross-correlation, and then the tilt axis was subsequently aligned by applying shifts and rotations to minimize artefacts in back projection reconstructions. The alignments were then applied to each of the Zn and Co tilt series. A compressed sensing reconstruction algorithm coded in MATLAB (Mathworks) was then used to perform the final independent reconstructions of the Zn and Co tilt series. Broadly, compressed sensing tomography approaches make use of prior knowledge of the sparsity of the signal undergoing reconstruction in a particular transform domain (the sparsity is given as the number of non-zero intensities) in order to recover high-fidelity tomographic reconstructions from highly undersampled tilt-series data[59, 60]. This compressed sensing tomography implementation used three-dimensional total generalized variation[61] regularization for the sparsity constraint in conjunction with a real-space projection operator from the Astra toolbox[62] and using the primal-dual hybrid gradient method[63] to solve the reconstruction problem. Reconstructions were further processed in ImageJ and FEI Avizo software for visualization. The total particle shape recovered in the tomographic reconstruction was used to threshold the volume to remove spurious signals due to noise in the reconstruction volume outside the particle sub-volume. No further processing was applied to the intensities within the particle.

Nanoindentation. The Young's modulus (*E*) of the samples was measured using an MTS Nanoindenter XP at ambient conditions. Samples were mounted in an epoxy resin and polished using increasingly fine diamond suspensions. Indentation experiments were performed under the dynamic displacement controlled mode, at a constant strain rate of $0.05\,s^{-1}$. All tests were conducted using a three-sided pyramidal (Berkovich) diamond indenter tip, to a maximum surface penetration depth of 500 nm. The load–displacement data collected were analysed using the Oliver and Pharr method[64]. A Poisson's ratio of 0.2 was used, in accordance with prior studies on ZIF materials[65].

Data availability. The data that support the findings of this study are available from the corresponding author upon request.

Received: 11 December 2017 Accepted: 10 May 2018

References

1. Carrington, E. J. et al. Solvent-switchable continuous-breathing behaviour in a diamondoid metal–organic framework and its influence on CO_2 versus CH4 selectivity. *Nat. Chem.* **9**, 882–889 (2017).
2. Schneemann, A. et al. Flexible metal-organic frameworks. *Chem. Soc. Rev.* **43**, 6062–6096 (2014).
3. Furukawa, H., Cordova, K. E., O'Keeffe, M. & Yaghi, O. M. The chemistry and applications of metal-organic frameworks. *Science* **341**, 974–986 (2013).
4. Banerjee, D. et al. Metal-organic framework with optimally selective xenon adsorption and separation. *Nat. Commun.* **7**, 11831 (2016).
5. Mason, J. A. et al. Methane storage in flexible metal-organic frameworks with intrinsic thermal management. *Nature* **527**, 357–361 (2015).
6. Yoon, J. W. et al. Selective nitrogen capture by porous hybrid materials containing accessible transition metal ion sites. *Nat. Mater.* **16**, 526–531 (2017).
7. Tominaka, S. et al. Topochemical conversion of a dense metal-organic framework from a crystalline insulator to an amorphous semiconductor. *Chem. Sci.* **6**, 1465–1473 (2015).
8. Lorusso, G. et al. A dense metal-organic framework for enhanced magnetic refrigeration. *Adv. Mater.* **25**, 4653–4656 (2013).
9. Sun, L., Campbell, M. G. & Dinca, M. Electrically conductive porous metal-organic frameworks. *Angew. Chem. Int. Ed. Engl.* **55**, 3566–3579 (2016).
10. Banerjee, R. et al. High-throughput synthesis of zeolitic imidazolate frameworks and application to CO_2 capture. *Science* **319**, 939–943 (2008).
11. Zhang, J. P., Zhang, Y. B., Lin, J. B. & Chen, X. M. Metal azolate frameworks: from crystal engineering to functional materials. *Chem. Rev.* **112**, 1001–1033 (2012).
12. Horike, S., Kadota, K., Itakura, T., Inukai, M. & Kitagawa, S. Synthesis of magnesium ZIF-8 from Mg(BH(4))(2). *Dalton. Trans.* **44**, 15107–15110 (2015).
13. Bennett, T. D. et al. Melt-quenched glasses of metal-organic frameworks. *J. Am. Chem. Soc.* **138**, 3484–3492 (2016).
14. Gaillac, R. et al. Liquid metal-organic frameworks. *Nat. Mater.* **16**, 1149–1154 (2017).
15. Giri, N. et al. Liquids with permanent porosity. *Nature* **527**, 216–220 (2015).
16. Chen, Y. et al. Shaping of metal–organic frameworks: from fluid to shaped bodies and robust foams. *J. Am. Chem. Soc.* **138**, 10810–10813 (2016).
17. Sumida, K. et al. Sol–gel processing of metal–organic frameworks. *Chem. Mater.* **29**, 2626–2645 (2017).
18. Seoane, B. et al. Metal-organic framework based mixed matrix membranes: a solution for highly efficient CO_2 capture? *Chem. Soc. Rev.* **44**, 2421–2454 (2015).
19. Umeyama, D., Horike, S., Inukai, M., Itakura, T. & Kitagawa, S. Reversible solid-to-liquid phase transition of coordination polymer crystals. *J. Am. Chem. Soc.* **137**, 864–870 (2015).
20. Chen, W. Q. et al. Glass formation of a coordination polymer crystal for enhanced proton conductivity and material flexibility. *Angew. Chem. Int. Ed. Engl.* **55**, 5195–5200 (2016).
21. Bennett, T. D. et al. Hybrid glasses from strong and fragile metal-organic framework liquids. *Nat. Commun.* **6**, 8079 (2015).
22. Zhao, Y., Lee, S.-Y., Becknell, N., Yaghi, O. M. & Angell, C. A. Nanoporous transparent MOF glasses with accessible internal surface. *J. Am. Chem. Soc.* **138**, 10818–10821 (2016).
23. Fukushima, T. et al. Solid solutions of soft porous coordination polymers: fine-tuning of gas adsorption properties. *Angew. Chem. Int. Ed. Engl.* **49**, 4820–4824 (2010).
24. Panda, T. et al. Mechanical alloying of metal-organic frameworks. *Angew. Chem. Int. Ed. Engl.* **56**, 2413–2417 (2017).
25. Cadman, L. K. et al. Compositional control of pore geometry in multivariate metal-organic frameworks: an experimental and computational study. *Dalton Trans.* **45**, 4316–4326 (2016).
26. Zhang, Y. B. et al. Introduction of functionality, selection of topology, and enhancement of gas adsorption in multivariate metal organic framework-177. *J. Am. Chem. Soc.* **137**, 2641–2650 (2015).
27. Bennett, T. D. et al. Thermal amorphization of zeolitic imidazolate frameworks. *Angew. Chem. Int. Ed. Engl.* **50**, 3067–3071 (2011).
28. Wharmby, M. T. et al. Extreme flexibility in a zeolitic imidazolate framework: porous to dense phase transition in desolvated ZIF-4. *Angew. Chem. Int. Ed. Engl.* **54**, 6447–6451 (2015).
29. Gustafsson, M. & Zou, X. D. Crystal formation and size control of zeolitic imidazolate frameworks with mixed imidazolate linkers. *J. Porous Mater.* **20**, 55–63 (2013).
30. Mattern, N. et al. Structural behavior of CuxZr100-x metallic glass (x=35-70). *J. Non Cryst. Solids* **354**, 1054–1060 (2008).
31. Fulchiron, R., Belyamani, I., Otaigbe, J. U. & Bounor-Legare, V. A simple method for tuning the glass transition process in inorganic phosphate glasses. *Sci. Rep.* **5**, 8369 (2015).
32. Kalogeras, I. M. & Brostow, W. Glass transition temperatures in binary polymer blends. *J. Polym. Sci. Pol. Phys.* **47**, 80–95 (2009).
33. Tian, Y. Q. et al. Two polymorphs of cobalt(II) imidazolate polymers synthesized solvothermally by using one organic template *N,N*-dimethylacetamide. *Inorg. Chem.* **43**, 4631–4635 (2004).
34. Qiao, A. et al. A metal-organic framework with ultrahigh glass-forming ability. *Sci. Adv.* **4**, eaao6827 (2018).
35. Tsao, C. S. et al. Characterization of pore structure in metal-organic framework by small-angle X-ray scattering. *J. Am. Chem. Soc.* **129**, 15997–16004 (2007).
36. Klimakow, M., Klobes, P., Thünemann, A. F., Rademann, K. & Emmerling, F. Mechanochemical synthesis of metal-organic frameworks: a fast and facile approach toward quantitative yields and high specific surface areas. *Chem. Mater.* **22**, 5216–5221 (2010).
37. Cravillon, J. et al. Fast nucleation and growth of ZIF-8 nanocrystals monitored by time-resolved in situ small-angle and wide-angle X-ray scattering. *Angew. Chem. Int. Ed. Engl.* **50**, 8067–8071 (2011).
38. Goesten, M. G. et al. Small-angle X-ray scattering documents the growth of metal-organic frameworks. *Catal. Today* **205**, 120–127 (2013).
39. Magnell, K. R. & Reynolds, W. L. Complexes of cobalt(II) with chloride and thiocyanate ions in dimethyl sulfoxide. *Inorg. Chim. Acta* **6**, 571–574 (1972).
40. Housecroft, C. E. & Sharpe, A. G. *Inorganic Chemistry* 3rd edn (Pearson Education Limited, UK, 2008).

41. Farrow, C. L. et al. PDFfit2 and PDFgui: computer programs for studying nanostructure in crystals. *J. Phys. Condens. Matter* **19**, 335219 (2007).
42. Bennett, T. D. et al. Structure and properties of an amorphous metal-organic framework. *Phys. Rev. Lett.* **104**, 115503 (2010).
43. Apen, E., Hitchcock, A. P. & Gland, J. L. Experimental studies of the core excitation of imidazole, 4,5-dicyanoimidazole, and S-triazine. *J. Phys. Chem.* **97**, 6859–6866 (1993).
44. Tan, J. C. & Cheetham, A. K. Mechanical properties of hybrid inorganic-organic framework materials: establishing fundamental structure-property relationships. *Chem. Soc. Rev.* **40**, 1059–1080 (2011).
45. Hobday, C. L. et al. A computational and experimental approach linking disorder, high-pressure behavior, and mechanical properties in UiO frameworks. *Angew. Chem. Int. Ed. Engl.* **55**, 2401–2405 (2016).
46. Zhang, Y. F., Hu, L. N., Liu, S. J., Zhu, C. F. & Yue, Y. Z. Sub-T-g enthalpy relaxation in an extremely unstable oxide glass and its implication for structural heterogeneity. *J. Non Cryst. Solids* **381**, 23–28 (2013).
47. Alemán, J. V. et al. Definitions of terms relating to the structure and processing of sols, gels, networks, and inorganic-organic hybrid materials (IUPAC Recommendations 2007). *Pure Appl. Chem.* **79**, 1801–1829 (2007).
48. Yue, Y. Z. Characteristic temperatures of enthalpy relaxation in glass. *J. Non Cryst. Solids* **354**, 1112–1118 (2008).
49. Basham, M. et al. Data Analysis WorkbeNch (DAWN). *J. Synchrotron Radiat.* **22**, 853–858 (2015).
50. Filik, J. et al. Processing two-dimensional X-ray diffraction and small-angle scattering data in DAWN 2. *J. Appl. Crystallogr.* **50**, 959–966 (2017).
51. Pauw, B. R., Smith, A. J., Snow, T., Terrill, N. J. & Thünemann, A. F. The modular small-angle X-ray scattering data correction sequence. *J. Appl. Crystallogr.* **50**, 1800–1811 (2017).
52. SasView v4.1 (The SasView Project, 2017).
53. Pauw, B. R., Pedersen, J. S., Tardif, S., Takata, M. & Iversen, B. B. Improvements and considerations for size distribution retrieval from small-angle scattering data by Monte Carlo methods. *J. Appl. Crystallogr.* **46**, 365–371 (2013).
54. Bressler, I., Pauw, B. R. & Thünemann, A. F. McSAS: software for the retrieval of model parameter distributions from scattering patterns. *J. Appl. Crystallogr.* **48**, 962–969 (2015).
55. Soper, A. K. *GudrunN and GudrunX: Programs for Correcting Raw Neutron and X-Ray Diffraction Data to Differential Scattering Cross Section.* Technical Report RAL-TR-2011-2013 (Rutherford Appleton Laboratory, Didcot, UK, 2011).
56. Soper, A. K. & Barney, E. R. Extracting the pair distribution function from white-beam X-ray total scattering data. *J. Appl. Crystallogr.* **44**, 714–726 (2011).
57. Bowron, D. T. et al. NIMROD: the Near and InterMediate Range Order Diffractometer of the ISIS second target station. *Rev. Sci. Instrum.* **81**, 033905 (2010).
58. de la Peña, F. et al. hyperspy: HyperSpy v.1.0.1 (2016).
59. Saghi, Z. et al. Three-dimensional morphology of iron oxide nanoparticles with reactive concave surfaces. a compressed sensing-electron tomography (CS-ET) approach. *Nano Lett.* **11**, 4666–4673 (2011).
60. Leary, R., Saghi, Z., Midgley, P. A. & Holland, D. J. Compressed sensing electron tomography. *Ultramicroscopy* **131**, 70–91 (2013).
61. Bredies, K., Kunisch, K. & Pock, T. Total generalized variation. *Siam J. Imaging Sci.* **3**, 492–526 (2010).
62. van Aarle, W. et al. The ASTRA toolbox: a platform for advanced algorithm development in electron tomography. *Ultramicroscopy* **157**, 35–47 (2015).
63. Chambolle, A. & Pock, T. A first-order primal-dual algorithm for convex problems with applications to imaging. *J. Math. Imaging Vis.* **40**, 120–145 (2011).
64. Oliver, W. C. & Pharr, G. M. Measurement of hardness and elastic modulus by instrumented indentation: advances in understanding and refinements to methodology. *J. Mater. Res.* **19**, 3–20 (2004).
65. Tan, J. C., Bennett, T. D. & Cheetham, A. K. Chemical structure, network topology, and porosity effects on the mechanical properties of Zeolitic Imidazolate Frameworks. *Proc. Natl. Acad. Sci. USA* **107**, 9938–9943 (2010).

Acknowledgements

T.D.B. would like to thank the Royal Society for a University Research Fellowship, and L. L. and N.J.B. acknowledge EPSRC studentships. C.W.A. acknowledges the Royal Society for funding. C.Z. acknowledges the financial support from China Scholarship Council and the Elite Research Travel Scholarship from the Danish Ministry of Higher Education and Science. We acknowledge the provision of synchrotron access to beamlines I15-1 (EE171151) and I22 (NT18236-1) at the Diamond Light Source, Rutherford Appleton Laboratory UK. The authors thank Jiayan Zhang for assistance for a DSC measurement. This work benefited from the use of the SasView application, originally developed under NSF Award DMR-0520547. SasView also contains code developed with funding from the EU Horizon 2020 programme under the SINE2020 project Grant No. 654000. Experiments at the ISIS Pulsed Neutron and Muon Source (on the NIMROD instrument) were supported by a beam-time allocation from the Science and Technology Facilities Council, on proposal RB1720006. S.M.C. acknowledges the Henslow Research Fellowship and Girton College, Cambridge. S.M.C. and P.A.M. acknowledge funding from the European Research Council under the European Union’s Seventh Framework Program (No. FP7/2007-2013)/ERC Grant Agreement No. 291522-3DIMAGE. C.-B.S. acknowledges support from the Leverhulme Trust project Breaking the non-convexity barrier, EPSRC grant EP/M00483X/1, EPSRC centre EP/N014588/1 and from CHiPS (Horizon 2020 RISE project grant). R.T. acknowledges funding from EPSRC grant EP/L016516/1 for the Cambridge Centre for Analysis. R.T. and C.-B.S. also acknowledge the Cantab Capital Institute for the Mathematics of Information.

Author contributions

T.D.B. designed the project and wrote the manuscript with L.L. and S.M.C., with input from all authors. Electron microscopy was performed by P.A.M. and S.M.C. SAXS/WAXS experiments were performed by T.D.B., A.J.S., N.T. and G.J.S., with analysis performed by A.J.S. and G.J.S. DSC measurements and sample preparation were carried out by L.L. and C.Z., facilitated by Y.Y. Deuterated organic ligands were provided by S.E. N., and PDF measurements carried out and analysed by T.D.B., D.A.K., C.W.A., C.Z., L. L., T.F.H. and P.A.C. NMR measurements were carried out and analysed by F.B. and N.J. B. R.T. and C.-B.S. developed the tomography reconstruction code.

Additional information

Supplementary Information accompanies this paper at https://doi.org/10.1038/s41467-018-04553-6.

Competing interests: The authors declare no competing interests.

Supplementary Information

Liquid Phase Blending of Metal-Organic Frameworks

Louis Longley et al,

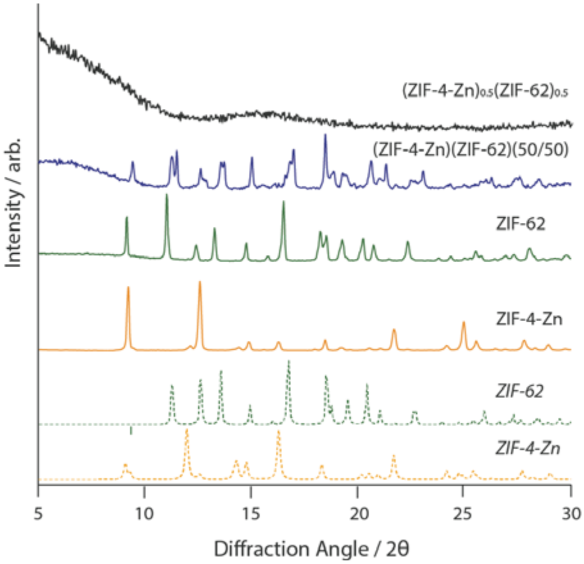

Supplementary Figure 1. X-ray powder diffraction patterns of crystalline and blended samples, along with the simulated structures (solid and broken traces respectively). The tick mark on the simulated trace of ZIF-62 indicates the presence of a Bragg peak of low intensity.

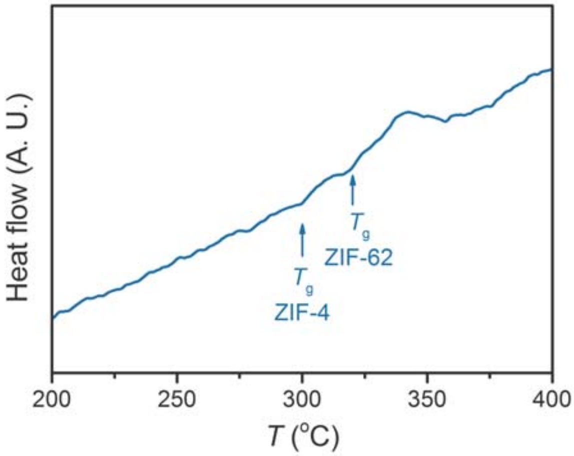

Supplementary Figure 2. DSC trace of a physical mixture formed by mixing equal weights of ZIF-62 and ZIF-4 glasses (pre-formed).

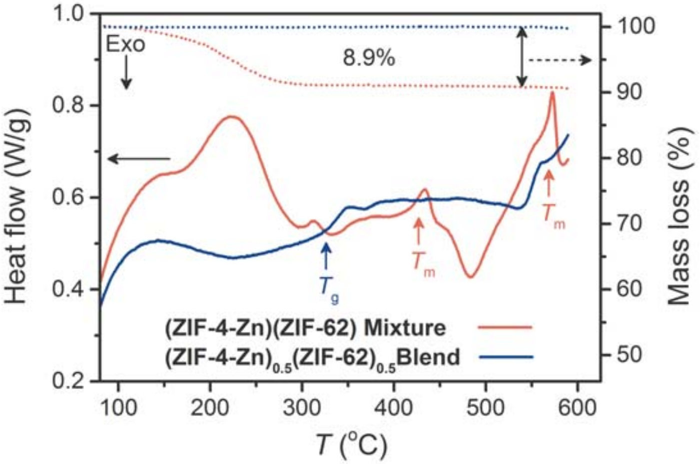

Supplementary Figure 3. Enthalpy response (red curve) and mass change (dotted curve) in the physical mixture (ZIF-4-Zn)(ZIF-62)(50/50) during heating at 10 °C min^{-1}. Blue curve: reheating curve representing the enthalpy response of the corresponding glass that forms upon quenching, i.e. (ZIF-4-Zn)$_{0.5}$(ZIF-62)$_{0.5}$ during prior cooling at 10 °C min^{-1}. This is the same data as presented in Fig. 1b, but with a higher magnification for comparison with Supplementary Figure 3.

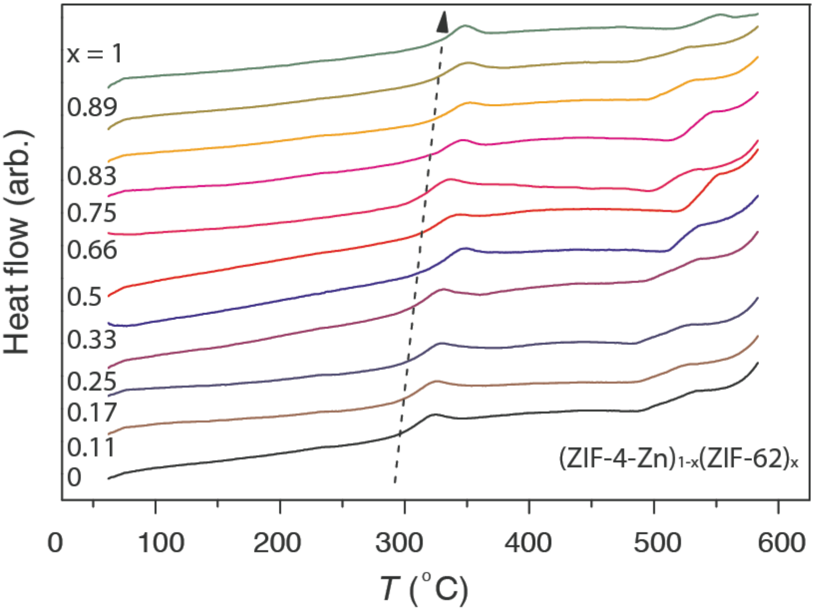

Supplementary Figure 4. DSC upscans of glasses of the sample series (ZIF-4-Zn)$_{1-x}$(ZIF-62)$_x$. Heating rate 10 °C min^{-1}.

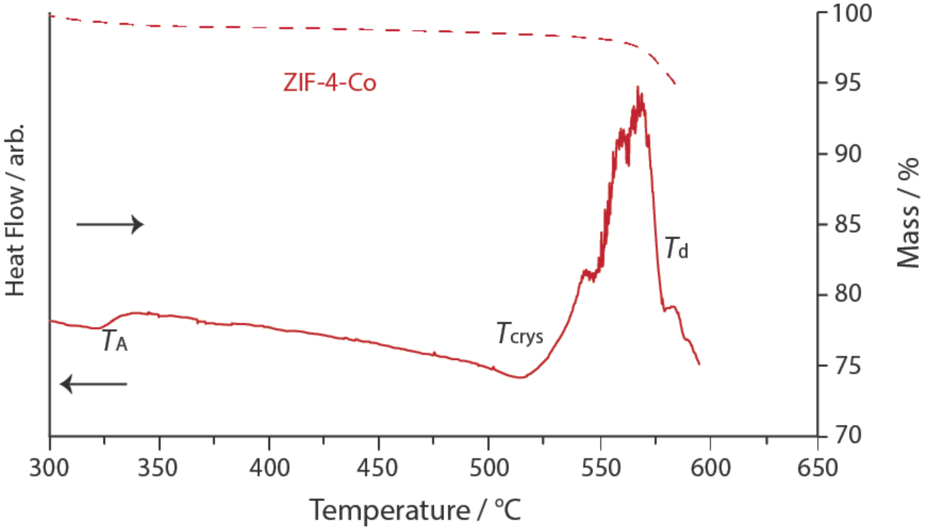

Supplementary Figure 5. Simultaneous DSC/TGA of ZIF-4-Co. Heating rate 10 °C min^{-1}.

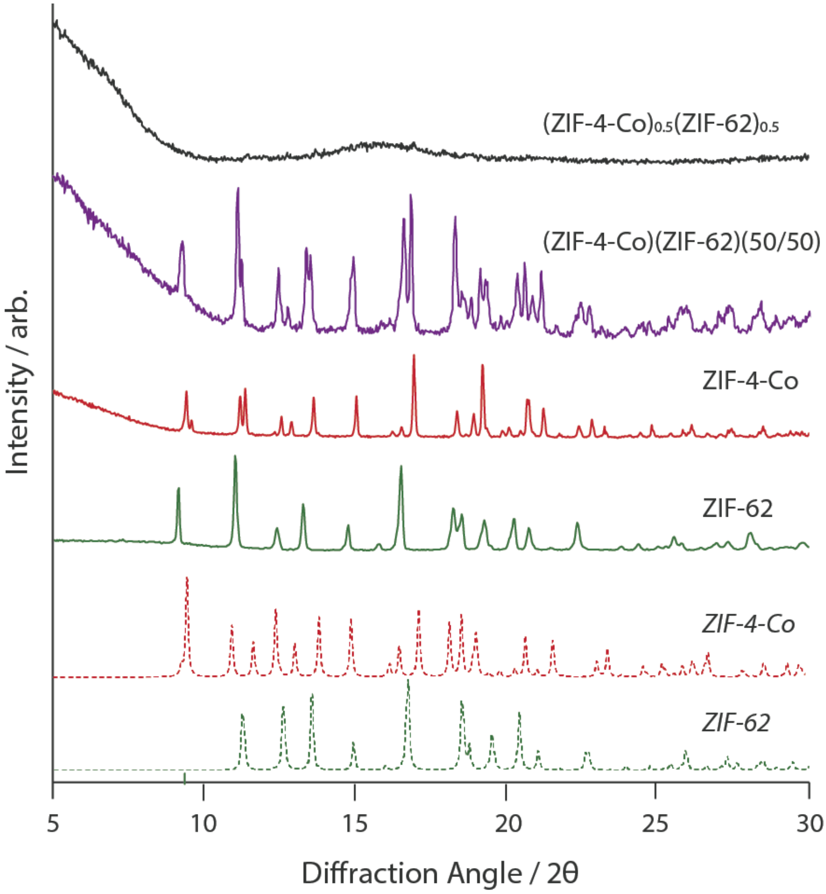

Supplementary Figure 6. X-ray powder diffraction patterns of ZIF-62 (green), ZIF-4-Co (red), (ZIF-4-Co)(ZIF-62)(50/50) (purple) and (ZIF-4-Co)$_{0.5}$(ZIF-62)$_{0.5}$ (black). Extremely small Bragg peaks can be seen in the diffraction pattern, though the impact of them cannot be seen in the PDF.

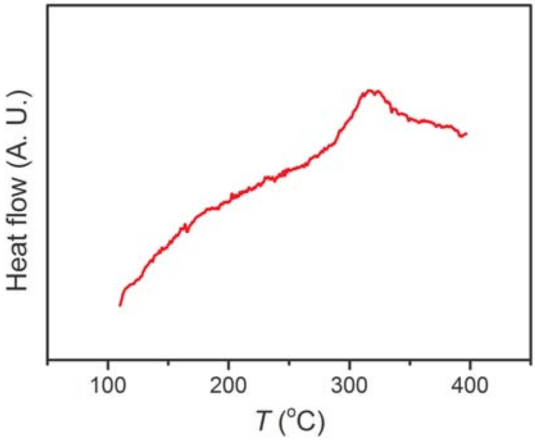

Supplementary Figure 7.. DSC trace of (ZIF-4-Co)$_{0.5}$(ZIF-62)$_{0.5}$, conducted at a heating rate 10 °C min^{-1} heating rate.

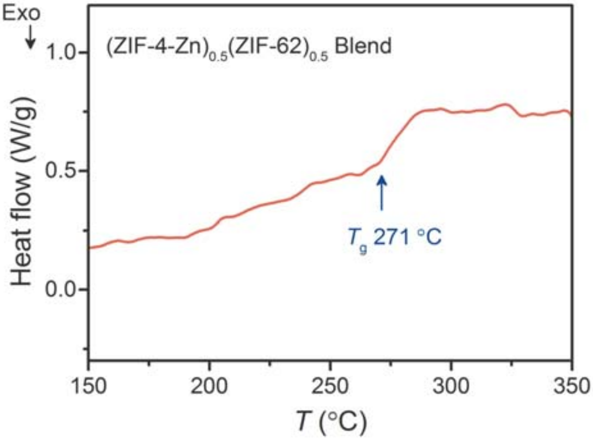

Supplementary Figure 8. DSC trace of (ZIF-4-Co)$_{0.5}$(ZIF-62)$_{0.5}$, conducted at 5 °C min^{-1} heating rate.

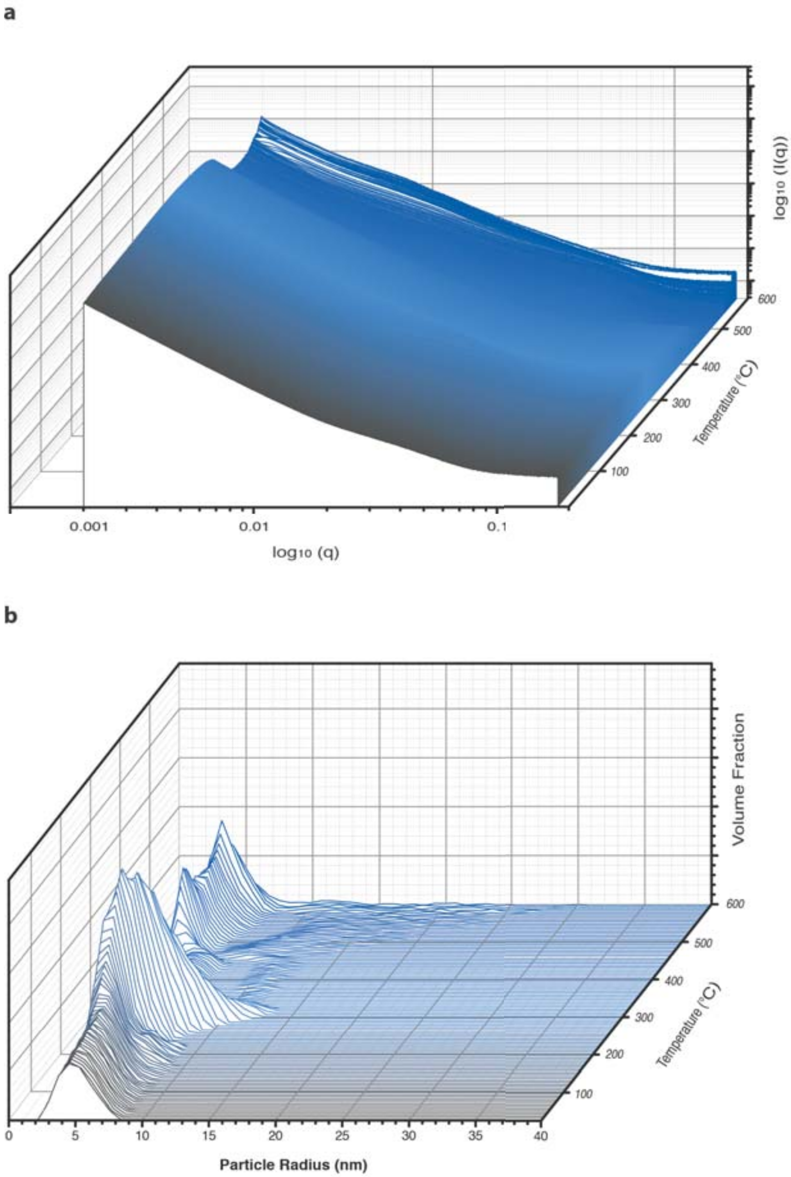

Supplementary Figure 9. Temperature resolved (a) SAXS profile and (b) volume fraction distributions of ZIF-62.

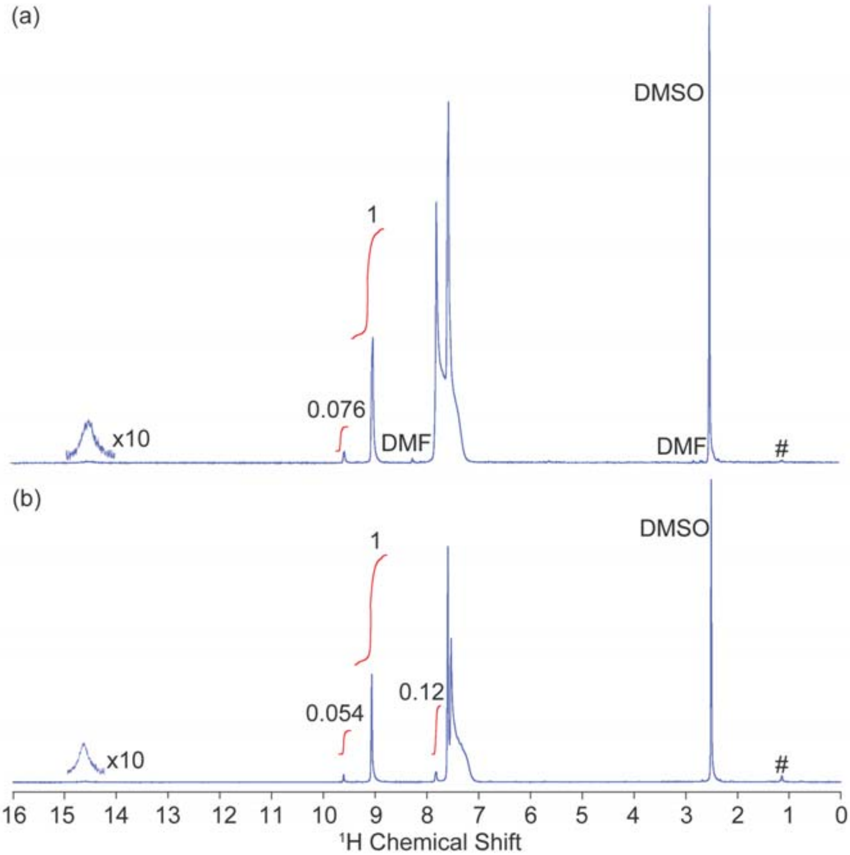

Supplementary Figure 10. Liquid-state ^{1}H NMR spectra of (a) (ZIF-4-Co)(ZIF-62)(50/50) and (b) (ZIF-4-Co)$_{0.5}$(ZIF-62)$_{0.5}$, (see below for complete spectral assignment). Integrations of individual ^{1}H shown in red only when resolution allowed. Solvent peaks are labelled, and # denote resonances from small amount of grease.

(ZIF-4-Co)(ZIF-62)(50/50): ^{1}H NMR (400 MHz, DMSO-d_6): δ (ppm) 1.14 (grease), 2.51 (DMSO), 2.63, 2.81 (DMF), 7.39 (C***H***CHCN$_{\mathrm{bIm}}$), 7.52 (HCl/H$_2$O), 7.57 (C***H***C***H***N$_{\mathrm{Im}}$), 7.78 (C***H***CN$_{\mathrm{bIm}}$), 8.23 (DMF), 9.02 (NC***H***N$_{\mathrm{Im}}$), 9.57 (NC***H***N$_{\mathrm{bIm}}$), 14.49 (N***H***$_{\mathrm{Im/bIm}}$).
(ZIF-4-Co)$_{0.5}$(ZIF-62)$_{0.5}$: ^{1}H NMR (400 MHz, DMSO-d_6): δ (ppm) 1.14 (grease), 2.51 (DMSO), 7.39 (C***H***CHCN$_{\mathrm{bIm}}$), 7.52 (HCl/H$_2$O), 7.59 (C***H***C***H***N$_{\mathrm{Im}}$), 7.82 (C***H***CN$_{\mathrm{bIm}}$), 9.07 (NC***H***N$_{\mathrm{Im}}$), 9.61 (NC***H***N$_{\mathrm{bIm}}$), 14.59 (N***H***$_{\mathrm{Im/bIm}}$).

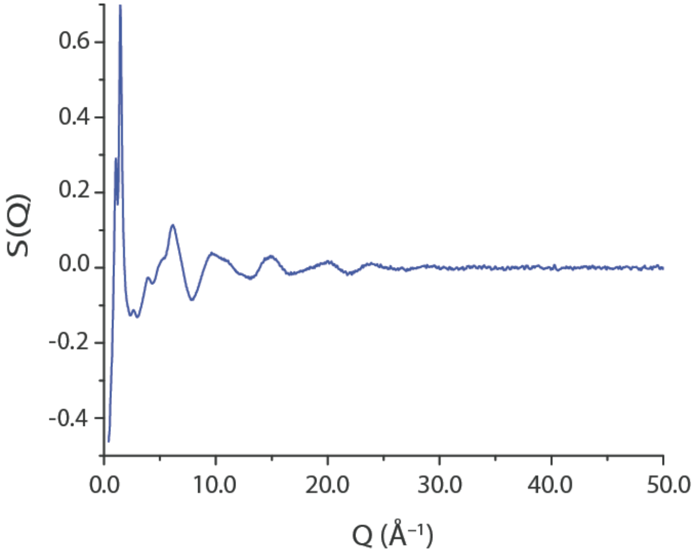

Supplementary Figure 11. Neutron total scattering structure factor *S*(*Q*) of (ZIF-4-Co)$_{0.5}$(ZIF-62)$_{0.5}$.

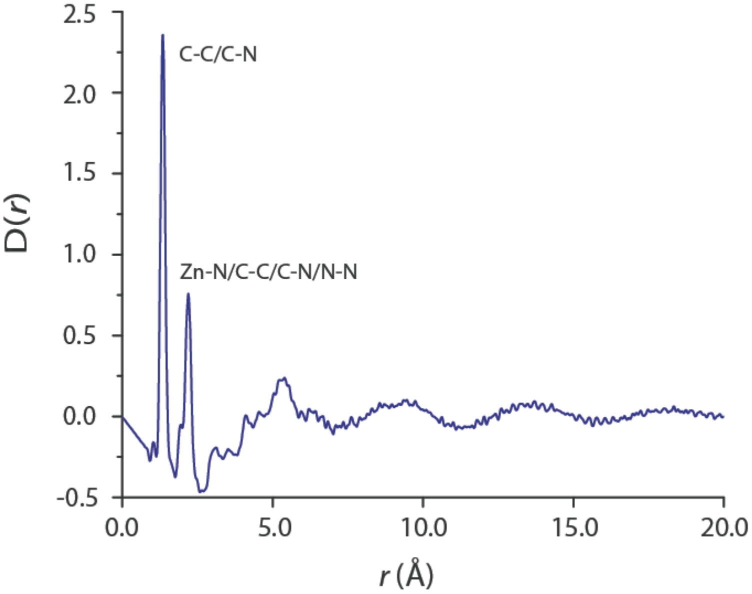

Supplementary Figure 12. Neutron pair distribution function *D*(*r*) of (ZIF-4-Co)$_{0.5}$(ZIF-62)$_{0.5}$.

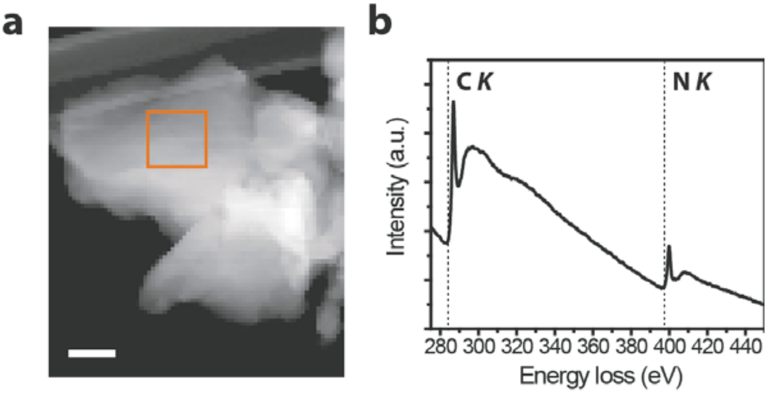

Supplementary Figure 13. **Electron Microscopy on Pure ZIF-62 Crystal and Glass Samples**. (a) ADF-STEM and (b) EELS characterization of a crystalline ZIF-62 particle supported on lacey carbon. The spectrum in (b) is from the boxed region in (a) with no contribution from the lacey carbon support. The scale bar is 100 nm.

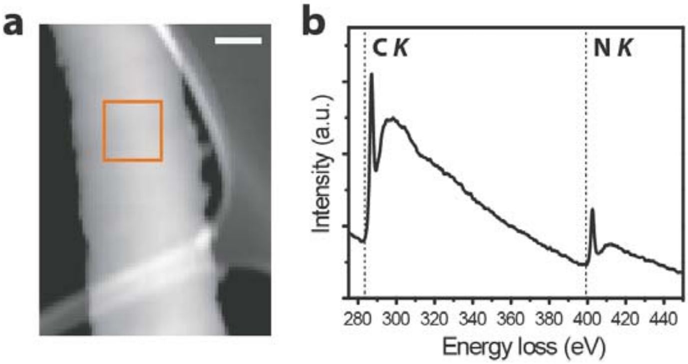

Supplementary Figure 14. (a) ADF-STEM and (b) EELS of a ZIF-62 glass particle supported on lacey carbon. The spectrum in (b) is from the boxed region in (a) with no contribution from the lacey carbon support. The scale bar is 100 nm.

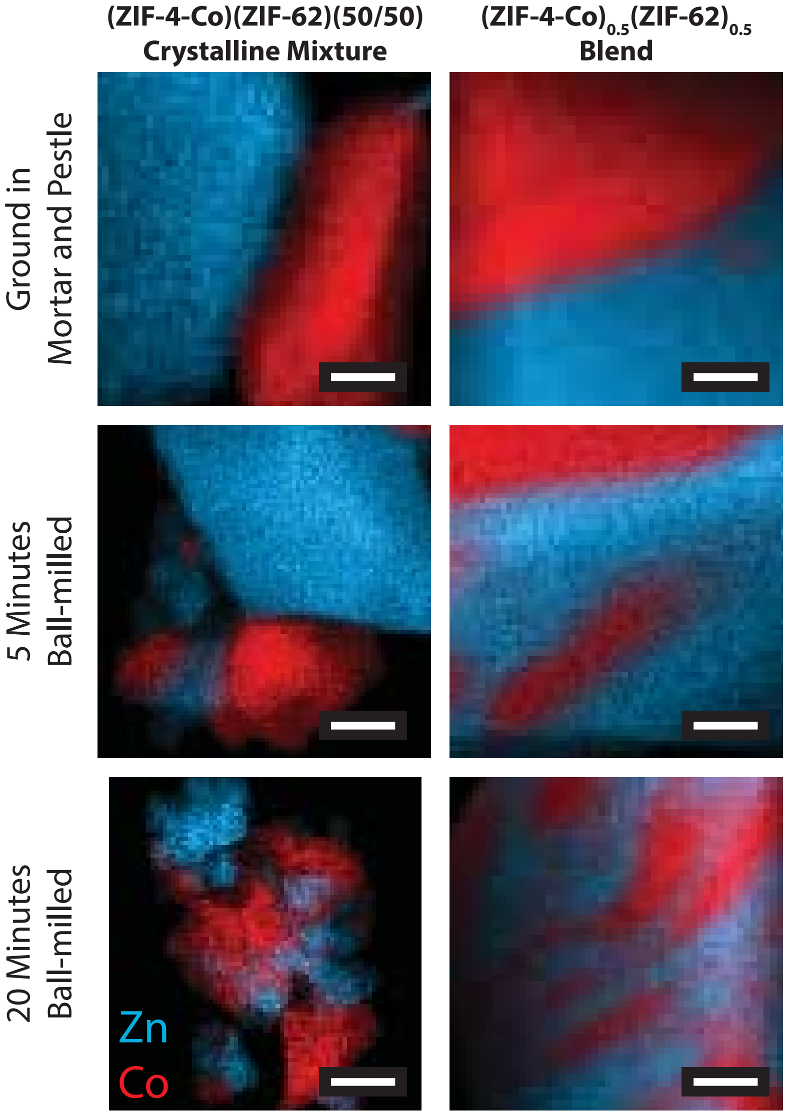

Supplementary Figure 15. ADF-STEM image of samples of (ZIF-4-Co)(ZIF-62)(50/50) formed by (top) lightly grinding crystalline ZIF-4-Co and ZIF-62 in a mortar and pestle, (middle) ball-milling together for 5 minutes and (bottom) ball-milling together for 20 minutes. Maps were generated by peak integration at the K_{α} X-ray lines for Co and Zn, shown as an overlay. The right hand column contains identical analysis of the glass samples. Scale bars correspond to 200 nm.

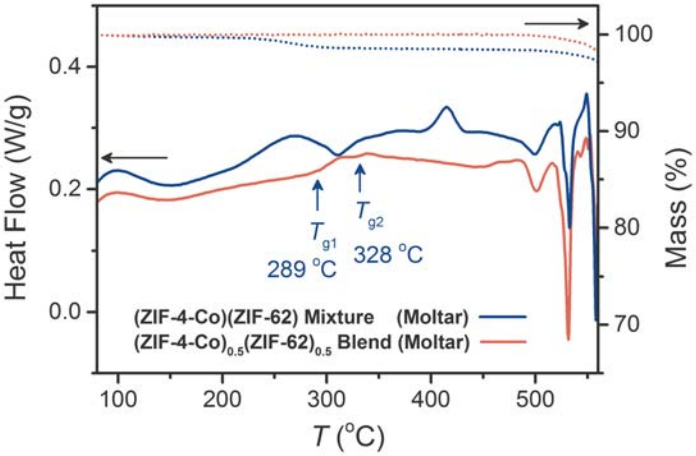

Supplementary Figure 16. DSC scan on a sample of **(**ZIF-4-Co)(ZIF-62)(50/50) formed by hand grinding, and the resultant glass, conducted at 10 °C min^{-1} heating rate. The second glass transition temperature T_{g2} is defined as the intersection point between lines constructed from the (constant) heatflow after T_{g1} and before the next increase in heat flow, and a line drawn at a tangent to the point at which the heat flow increase is ½ of the total (see Supplementary Figure 17 below).

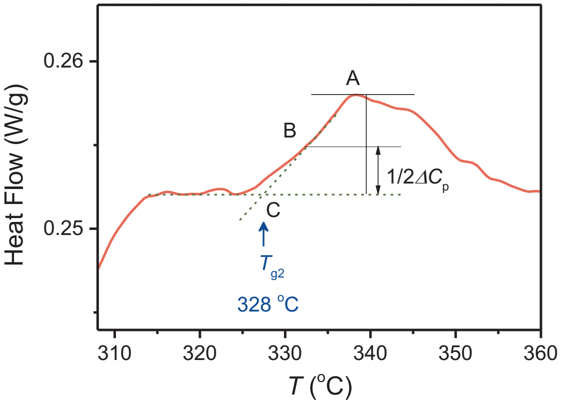

Supplementary Figure 17. Second glass transition point construction.

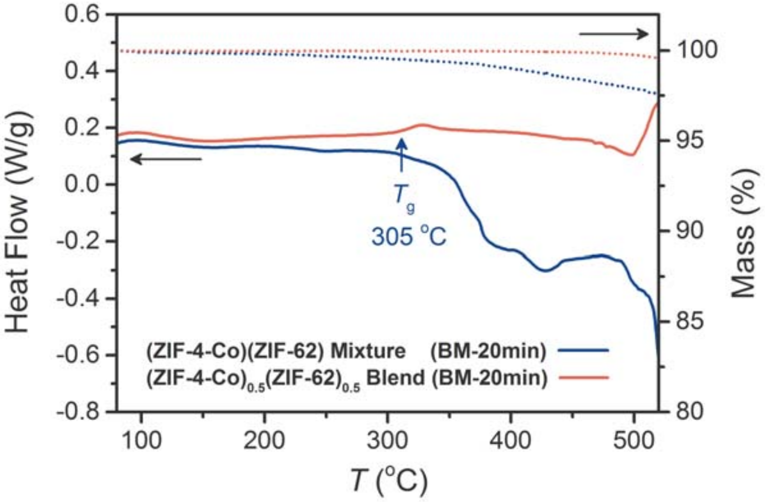

Supplementary Figure 18. DSC scan on a sample of **(**ZIF-4-Co)(ZIF-62)(50/50) formed by 20 minutes of ball-milling, and the resultant glass, conducted at 10 °C min^{-1} heating rate.

PAPER IV

Metal-Organic Framework Glasses with Permanent Accessible Porosity

Chao Zhou,[1,2] Louis Longley,[1] Andraž Krajnc,[3] Glen J. Smales,[4,5] Ang Qiao,[6] Ilknur Eruçar,[7] Cara M. Doherty,[8] Aaron W. Thornton,[8] Anita J. Hill,[8] Christopher W. Ashling,[1] Omid T. Qazvini,[9] Seok J. Lee,[9] Philip A. Chater,[5] Nicholas J. Terrill,[5] Andrew. J. Smith,[5] Yuanzheng Yue,[2,6,10] Gregor Mali,[3] David A. Keen,[11] Shane G. Telfer[9] and Thomas D. Bennett*[1]*

[1]*Department of Materials Science and Metallurgy, University of Cambridge, Charles Babbage Road, Cambridge, CB3 0FS, UK*

[2]*Department of Chemistry and Bioscience, Aalborg University, DK-9220 Aalborg, Denmark*

[3]*Department of Inorganic Chemistry and Technology, National Institute of Chemistry, SI-1001 Ljubljana, Slovenia*

[4]*Department of Chemistry, University College London, Gordon Street, London, WC1H 0AJ, UK*

[5]*Diamond Light Source Ltd, Diamond House, Harwell Science and Innovation Campus, Didcot OX11 0DE, UK*

[6]*State Key Laboratory of Silicate Materials for Architectures, Wuhan University of Technology, Wuhan 430070, China*

[7]*Department of Natural and Mathematical Sciences, Faculty of Engineering, Ozyegin University, Istanbul, Turkey*

[8]*Future Industries, Commonwealth Scientific and Industrial Research Organisation, Clayton South, Victoria 3168, Australia*

[9] *MacDiarmid Institute for Advanced Materials and Nanotechnology, Institute of Fundamental Sciences, Massey University, Palmerston North 4442,* New Zealand

[10] *School of Materials Science and Engineering, Qilu University of Technology, Jinan 250353, China*

[11]*ISIS Facility, Rutherford Appleton Laboratory, Harwell Campus, Didcot, Oxon OX11 0QX, UK*

Email: tdb35@cam.ac.uk S.Telfer@massey.ac.nz

Abstract

To date, only several microporous, and even fewer nanoporous, glasses have been produced, always via post synthesis acid treatment of phase separated dense materials, e.g. Vycor glass. In contrast, high internal surface areas are readily achieved in crystalline materials, such as metal-organic frameworks (MOFs). It has recently been discovered that a new family of melt quenched glasses can be produced from MOFs, though they have thus far lacked the accessible and intrinsic porosity of their crystalline precursors. Here, we report the first glasses that are permanently and reversibly porous toward incoming gases, without post-synthetic treatment. We characterized the structure of these glasses using a range of experimental techniques, and demonstrate pores in the range of 4 – 8 Å. The discovery of MOF glasses with permanent accessible porosity reveals a new category of porous glass materials that are potentially elevated beyond conventional inorganic and organic porous glasses by their diversity and tunability.

Conventional porous glasses are silica-rich materials derived by acid treatment of phase-separated borosilicate glass precursors. They have found widespread applications in electrodes, chromatography and medical devices, and as desiccants, coatings and membranes.[1] In general, they are easily processed and exhibit high mechanical stability. However, these advantages are offset by limitations in their pore sizes, which are typically confined to the macroporous size regime. No porous glass has been fabricated directly by melt-quenching, without post-treatment. Few microporous glasses have been reported, although advances in their synthesis would be particularly attractive for applications based on the selective uptake of gases and small molecules.[2] One of the most well studied microporous glasses is Vycor, which is obtained by first melt-quenching a borosilicate liquid, and then heat treating the glass at a temperature well above T_g, to encourage phase separation. The borate-rich phase is then leached out via acid treatment, to generate pores of over 3 nm radii and Brunauer-Emmett-Teller (BET) surface areas in the range 100-200 m^2g^{-1}.[1] Silica-derived aerogels have also attracted much attention due to their own high BET surface areas and pore sizes of between 0.5 nm and 1 nm.[3] The desire to introduce controllable properties based on organic functional groups has however also spurred the development of amorphous microporous organic materials, such as PIM-1.[4,5] Surface areas verging on 1000 m^2g^{-1} arising from pore sizes of up to 1 nm have been reported. Whilst these organic materials present fewer chemical restrictions on their functionality than their inorganic counterparts, their thermal stability is unfortunately limited and their susceptibility to densification over time (physical aging) is well documented.[5]

In this context, porous materials that combine the advantageous properties of both inorganic and organic glasses are highly sought after. Recent advances in our understanding of the flexible behaviour[6] of soft porous metal-organic frameworks (MOFs)[7] have combined with a surge in research into defects[8] and disorder[9] to redefine our perception of MOFs as ‘perfect’ crystalline materials.[10] We, and others, have drawn on these advances to show that crystallinity is not a prerequisite for many of the attractive properties of MOFs, and to produce liquids and glasses with internal cavities and ion conducting abilities.[11-13]

One sub-set of MOFs that has garnered much attention is the zeolitic imidazolate framework (ZIF) family, numbering over 140 distinct structures containing tetrahedral transition metal ions, linked by imidazolate bis(monodentate) ligands into zeolitic architectures.[14,15] Several members of the family melt upon heating to around 400 °C. For example, in the case of certain polymorphs of ZIF-4 ($[Zn(Im)_2]$, Im = imidazolate, $C_3H_3N_2^-$), this process proceeds on a sub-nanosecond timescale near T_m (melting temperature) and results in a viscous MOF liquid of identical chemical composition to the crystalline solid.[11] Quenching of the liquid results in a 'frozen' structure containing tetrahedral Zn(II) ions bridged by Im ligands. The continuous random network produced is similar to that of $a\mathrm{SiO_2}$, but with the advantage of having both inorganic and organic components.[11,16]

Known hybrid glasses, formed from ZIFs and phosphate coordination polymers,[17,18] are all inaccessible to guest molecules. Here, motivated by the prospect of combining the attractive properties of both inorganic and organic moieties in a porous glass, we sought to develop *accessible* porosity in a melt-quenched MOF glass. We herein report the successful realization of this goal, in the form of glasses derived from ZIFs that reversibly adsorb gas molecules. These materials can be considered prototypical new porous glasses, given that there is no requirement for post-processing treatment. They are synthesized using a straightforward protocol and are stable, retaining their porosity in air over extended periods. These results provide a rational strategy upon which other porous MOF liquid and glass systems can be produced. We anticipate that the stability, processability and chemical diversity of these glasses will underpin their applications in separations, and as components of membranes, catalysts, functional coatings, and thin films.

Results and Discussion

Thermal characterization and vitrification of ZIF precursors

The free energy requirement for breaking the zinc-imidazolate bond has been calculated to be *ca*. 92 kJ mol^{-1} at 865 K.[11] This relatively low bond strength led us to consider ZIFs containing this ligand as primary candidates for melting, followed by quenching of the liquid to produce porous glasses. Limitations exist to the exclusive use of imidazolate however, since close association of the Zn and Im components in the liquid and glass states leads to dense materials.[16] We thus developed a strategy involving the incorporation of sterically congested benzimidazolate (bIm) ligands into the framework, alongside the parent imidazolate linker. We anticipated that the inclusion of a bulky ligand would prevent close packing of the liquid state, and therefore facilitate pore network formation upon quenching. Similar approaches have proven successful in optimizing porosity in both crystalline materials,[19] and amorphous organic polymers.[5] Suitable levels of the imidazolate linker are however still required to facilitate melting, since frameworks constructed exclusively from benzimidazolate ligands do not melt.

To develop our strategy, we initially focused on ZIF-76, $[Zn(Im)_{1.62}(5\text{-ClbIm})_{0.38}]$ (5-ClbIm = 5- chlorobenzimidazolate, $C_7H_4N_2Cl$).[20] This three dimentional framework, formed from Zn^{2+} nodes connected by Im or 5-ClbIm ligands (Figure 1a), possesses the zeolitic LTA topology. In this network architecture, sodalite cages are connected together by rings of 4 Zn ions linked to one another and give rise to a supercage in the centre of the cell.[21] The structure possesses a framework density of 1.03 T/nm^{-3} (T = tetrahedral metal atoms). This is extremely low when compared with ZIF-4 (3.66 T/nm^{-3}), which forms a non-porous glass, and ZIF-8 $[Zn(mIm)_2]$, (mIm = 2-methylimidazolate, $C_3H_5N_2^-$) (2.45 T/nm^{-3}), which does not melt.[22] The structure of ZIF-76 was confirmed by powder X-ray diffraction (PXRD), and the Im:5-ClbIm ratio determined by ^{1}H nuclear magnetic resonance (NMR) spectroscopy on dissolved samples. Desolvation of ZIF-76 resulted in loss of occluded 5-ClbIm from the pores (**Supplementary Figures 1-5**).

Thermogravimetric analysis (TGA) performed on an evacuated sample of ZIF-76 under argon resulted in a featureless trace until thermal decomposition at 525 °C. An accompanying differential scanning calorimetry (DSC) measurement, which quantifies the heat absorption of a sample relative to a reference, revealed an endothermic feature that we ascribe to a melting transition at 451 °C (ΔH_f = 1.8 kJ mol^{-1}) (**Figure 1b**). Cooling of this liquid to room temperature produced a vitreous product, termed a_gZIF-76 (**Supplementary Figure 1**). This terminology identifies an amorphous ('a') product formed by melting, then quenching (subscript 'g' referring to a 'glass'), crystalline ZIF-76. a_gZIF-76 possesses an identical chemical composition to ZIF-76 and (most likely) has the same short range chemical connectivity as that of the ZIF-76 crystal structure. a_gZIF-76 exhibits a glass transition temperature, T_g, of 310 °C upon reheating in a DSC measurement (**Figure 1b, Supplementary Figure 6**).

The isostructural crystal framework [Zn(Im)$_{1.33}$(5-mbIm)$_{0.67}$] (5-mbIm = 5-methylbenzimidazolate, $C_8H_7N_2$), referred to as ZIF-76-mbIm, also forms a glass (a_gZIF-76-mbIm) (**Supplementary Figure 7**).[23,24] A comparison of these with ZIF-76 and a_gZIF-76, allowed us to study the relationship between ZIF structure and the properties of the resulting glass. ZIF-76-mbIm melts at 471 °C (**Supplementary Figure 8**), indicating a higher energy barrier to ligand dissociation due to the electron-donating methyl group. A similar electronic effect was previously pinpointed as the reason why ZIF-8 does not melt.[11] a_gZIF-76-mbIm possesses a T_g of 317 °C (**Figure 1b**, **Supplementary Figure 9)**. The linker ratio of ZIF-76-mbIm, and indeed ZIF-76, are maintained in their respective glasses (**Table 1**, **Supplementary Figures 2-5, 10 and 11**), which is expected on the basis that no mass loss occurs during the melting process. The greater T_g for a_gZIF-76-mbIm is consistent with the greater van der Waals radius of a methyl group compared to chlorine atom, which leads to stronger non-covalent interactions between the framework constituents. This trend is reminiscent of the relationship between T_g and steric side groups in organic polymers.[25,26]

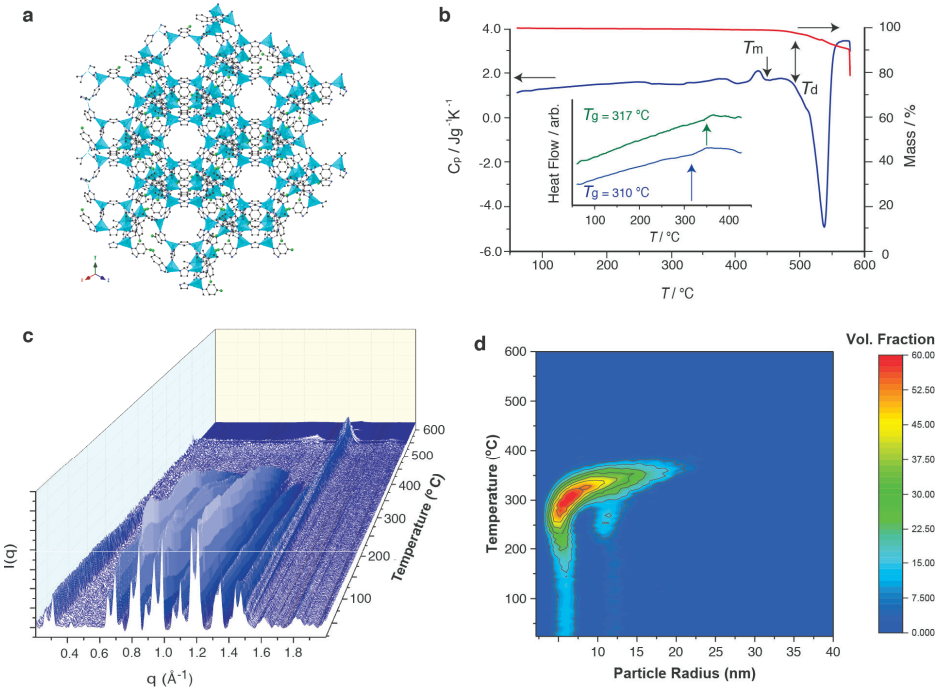

Figure 1. Liquid and Glass Formation of ZIF-76. (a) The structure of ZIF-76, as determined by single-crystal X-ray diffraction.[20] Zn – light blue, Cl – green, C – grey, N – dark blue, H – omitted for clarity. (b) The isobaric heat capacity (C_p) and mass change (%) of ZIF-76 measured during a DSC-TGA upscan at 10 °C/min, highlighting the stable liquid domain between T_m and T_d. Inset – Glass transitions for a_gZIF-76 (blue) and a_gZIF-76-mbIm (green). (c) Temperature resolved WAXS profile of ZIF-76 upon heating from 25 °C to 600 °C. (d) Temperature resolved volume fraction distributions of the different particle sizes of ZIF-76, indicating coalescence into particles of up to 30 nm.

The transformation of ZIF-76 from the crystalline to the liquid state was investigated by small- and wide- angle X-ray scattering (SAXS and WAXS). Bragg diffraction in the variable temperature WAXS pattern decreases sharply around 420 °C, consistent with the melting point from DSC. The resultant diffuse scattering then ceases at *ca*. 520 °C, corresponding to thermal decomposition (**Figure 1c**). The liquid formed from ZIF-76 is therefore stable over a temperature range of approximately 100 °C, consistent with TGA evidence (**Figure 1b**).

Table 1. Summary of the crystalline and glass samples.

	Composition [a]	State	T_m (°C)	T_g (°C)	T_d (°C)
ZIF-76	$[Zn(Im)_{1.62}(5\text{-ClbIm})_{0.38}]$	crystalline	451	-	517
a$_g$ZIF-76	$[Zn(Im)_{1.62}(5\text{-ClbIm})_{0.38}]$	glass	-	310	511
ZIF-76-mbIm	$[Zn(Im)_{1.33}(5\text{-mbIm})_{0.67}]$	crystalline	471	-	596
a$_g$ZIF-76-mbIm	$[Zn(Im)_{1.33}(5\text{-mbIm})_{0.67}]$	glass	-	317	590

The SAXS intensity follows a power law behaviour of the form $Q^{-\alpha}$ at room temperature (**Supplementary Figures 12 and 13**). Fitting gave a value of $\alpha = 3.7$, which decreased to 3.5 at 360 °C, indicating a roughening of internal surface structure upon melting. Similar results were observed in a previous study of the melting of a different material, ZIF-62.[27] The dynamic nature of the liquid phase upon heating was evidenced by a steady increase in α to 3.9 between 360 °C and 500°C, which we associate with a regularization of the internal pore structure of the liquid with both time and temperature. The discontinuity in the SAXS profile at around 550 °C indicates thermal decomposition, in accordance with the WAXS and DSC measurements. The volume weighted fractions of the particles below the observable limit of 315 nm in the sample were extracted from the data (**Figure 1d**), showing crystalline ZIF-76 particles of 5 nm, 12 nm and 20 nm radius, which coalesce at *ca*. 370 °C before melting at higher temperatures.

Linker Positioning in the Vitreous State

The chemical environments, distribution and relative motion of the framework linkers in the liquid state prior to vitrification were studied, to gain insight into phase separation processes and glass homogeneity. Solid-state ^{1}H magic angle spinning (MAS) NMR spectroscopic measurements were carried out for this purpose. Measurements on an evacuated sample of ZIF-76 yielded a single, broad, unresolvable signal at 6-7 ppm arising from both Im and ClbIm protons (**Supplementary Figure 14**). The spectrum of ZIF-76-mbIm featured an additional peak at 1.5 − 2 ppm, belonging to the methyl substituent of the benzimidazolate ring. The ^{13}C MAS NMR spectra of these crystalline samples exhibited several partly resolved signals**,** matching those expected from the chemical structure of the ligand (**Supplementary Figure 15**). Vitrification resulted in little change to the resonances in both the ^{1}H and ^{13}C spectra, aside from a small shift in position of the methyl group resonance to lower field in the ^{13}C NMR spectrum of ZIF-76-mbIm. These MAS NMR results demonstrate that the chemical environments of the ligands in the glasses are broadly similar to those in their crystalline precursors.

The distribution of the organic linkers within both crystal and glass phases was also investigated using spin diffusion NMR spectroscopy. This is a powerful technique, which is able to detect the proximity of different organic components based on the rate of polarization transfer between their protons.[28,29] ^{1}H-detected spin-diffusion experiments were first performed on ZIF-76-mbIm, to track the transfer of proton polarization from the methyl group protons of 5-mbIm (resonance at 2 ppm) to all other protons in the sample (with chemical shifts in the region 6-7 ppm). Off-diagonal peaks at a mixing time of 0 ms are absent, as expected. Their appearance and gradual strengthening in intensity after this time however, is due to polarization transfer (**Supplementary Figure 16**). After mixing times of 10-12 ms, a plateau in the spin-diffusion curve (**Supplementary Figure 17**) was observed, indicating that maximum transfer to both imidazolate and other 5-methylbenzimidazolate protons had been achieved. The detection of a well-resolved and isolated ^{1}H signal from the methyl group protons of 5-mbIm and the ^{13}C signal from **C1'** of the Im ligand (**Figure 2a**) facilitated ^{13}C-detected proton spin-diffusion measurements. This allowed us to track the polarization transfer from the methyl group to **H1** protons of the 5-methyl benzimidazolate (intra-linker transfer) and to **H1'** protons of the imidazolate (inter-linker transfer between the two different linkers) (**Figure 2b**). In crystalline ZIF-76-mbIm, the inter-linker transfer of polarization was observed to be faster than intra-linker transfer, implying that the linkers are well mixed within the framework (**Figure 2c)**. In a_gZIF-76-mbIm, very fast spin-diffusion among the linkers of two different types confirms that the 5-methyl benzimidazolate and imidazolate linkers remain very well mixed and do not separate into domains. Notably, the initial parts of the spin-diffusion curves of the glass are steeper than in the crystal, suggesting that the inter-linker distances between 5-methyl benzimidazolate and imidazolate linkers contract slightly upon vitrification (**Figure 2d**). This is consistent with the downfield shift of the methyl group resonance in the ^{13}C NMR spectrum of a_gZIF-76-mbIm, which may arise from closer contacts with the π electron clouds of neighboring ligands.

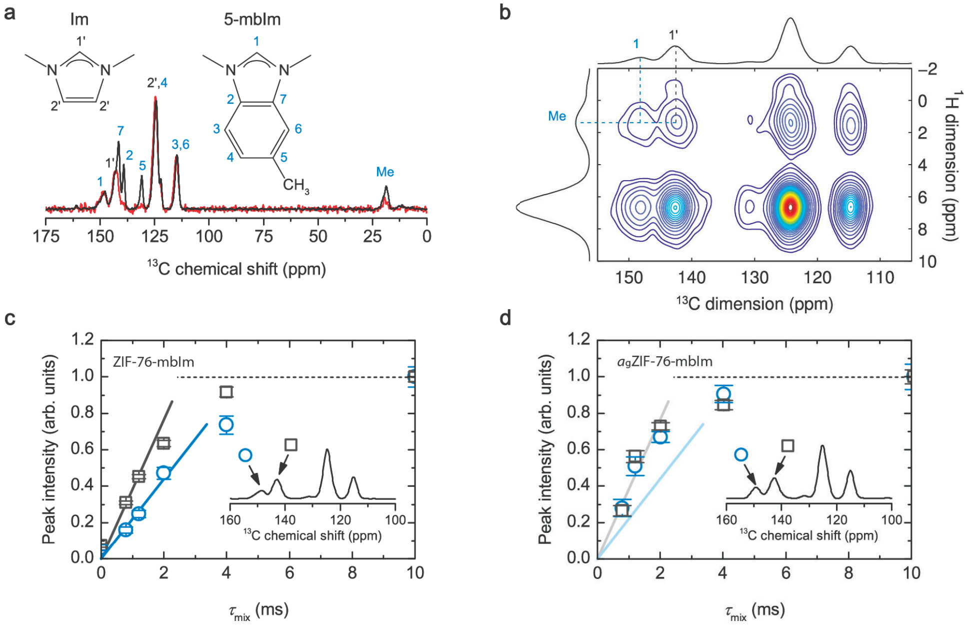

Figure 2. Linker dynamics upon melting. (a) ^{13}C MAS (black solid line) and ^{1}H-^{13}C Lee-Goldburg cross-polarization MAS (red solid line) NMR spectra of crystalline ZIF-76-mbIm. Tentative assignment of individual signals is based on literature data for isotropic chemical shifts from the two molecular fragments. The assignment is further confirmed by comparing the resonances in the ^{13}C MAS and ^{1}H-^{13}C Lee-Goldburg cross polarization MAS NMR spectra. In the latter, only resonances belonging to those carbons with hydrogens attached can be observed. (b) ^{13}C-detected 2D spin-diffusion NMR spectrum, recorded with a mixing time of 10 ms. Cross peaks due to polarization transfer between methyl protons of 5-mbIm on one hand and H1' protons of Im and H1 protons of 5-mbIm on the other are denoted. (c) and (d) Spin-diffusion curves from the ^{13}C-detected measurements on ZIF-76-mbIm and a_gZIF-76-mbIm (squares: inter-linker polarization transfer between methyl protons of 5-mbIm and H1' protons of Im; circles: intra-linker polarization transfer between methyl and H1 protons of 5-mbIm). Solid lines in (c) and (d) indicate the initial slopes of the two spin-diffusion curves for crystalline ZIF-76-mbIm (i.e., lines in (d) are equal to lines in (c)).

Pair Distribution Function Measurements

To further probe the structures of the ZIFs before and after vitrification, synchrotron X-ray total scattering measurements were performed on ZIF-76, ZIF-76-mbIm, a_gZIF-76 and a_gZIF-76-mbIm (**Figure 3a**). The glassy nature of a_gZIF-76 and a_gZIF-76-mbIm was confirmed by the absence of sharp features in their respective structure factors. The corresponding pair distribution functions (PDFs), which are in effect atom-atom distance histograms, of all samples were extracted after appropriate data corrections (**Figure 3b**). The PDFs of all samples are near-identical for distances up to 6 Å. Since the correlations in this range are C-C/C-N (1.3 Å) and Zn-N (2 Å and 4 Å), this implies that the local Zn^{2+} environment is near identical in all four samples. The limit of this order, at 6 Å, corresponds to the distance between two Zn^{2+} centres, and confirms that metal-ligand-metal connectivity is present within both crystalline and glass samples. This is consistent with observations made on other MOF glasses, and it underscores the consistency in the composition of these materials and the similar coordination environment of the zinc(II) ions across the crystalline and amorphous phases.[16]

The PDFs of dense ZIF-glasses are relatively featureless beyond 6 Å,[16] which contrasts with the PDFs of a_gZIF-76 and a_gZIF-76-mbIm. In particular, the feature at 7.5 Å in the *D*(*r*) for a_gZIF-76 (Peak A, **Figure 3b and inset**) (and for a_gZIF-76-mbIm, **Supplementary Figure 18**) is related to a Zn-N^3 distance, where N^3 is the third nearest N atom to a given Zn^{2+} ion. A further feature at 10.8 Å in the *D*(*r*) for a_gZIF-76 is related to the distance between a Zn^{2+} ion and the Cl group on the next nearest neighbour ligand (Peak B, **Figure 3b and inset**). The observation of medium range order (MRO) in the glass state, i.e. **Zn**-Im-Zn-**ClbIm** connectivity, is ascribed to the relative sluggish diffusion kinetics and high viscosities of the liquid phase. Lower viscosities associated with greater ligand movement would result in vastly reduced **Zn**-Im-Zn-**ClbIm** correlations.[11] The extended connectivity here would also render a contiguous pore network possible, as confirmed later by gas adsorption. Similar analysis of the PDFs for ZIF-76-mbIm and a_gZIF-76-mbIm (**Supplementary Figure 18**) also indicates a degree of MRO in the glass, with oscillations persisting to higher *r* values. This is also consistent with the lower position of the first sharp diffraction peak of ZIF-76-mbIm.[30]

Synchrotron X-ray diffraction data were collected during the melting process of ZIF-76 (**Figure 3c**). We observed a reduction in Bragg intensity upon heating, resulting in complete loss of all sharp diffraction peaks in the *S*(Q) at the highest studied temperature of 540 °C. The amorphous pattern is recovered to room temperature on cooling; sharp Bragg peaks do not reappear. In the PDF, features at r values of over 8-10 Å are present in crystalline ZIF-76, but are virtually absent by 540 °C and in the sample at room temperature after heating (**Figure 3d**).

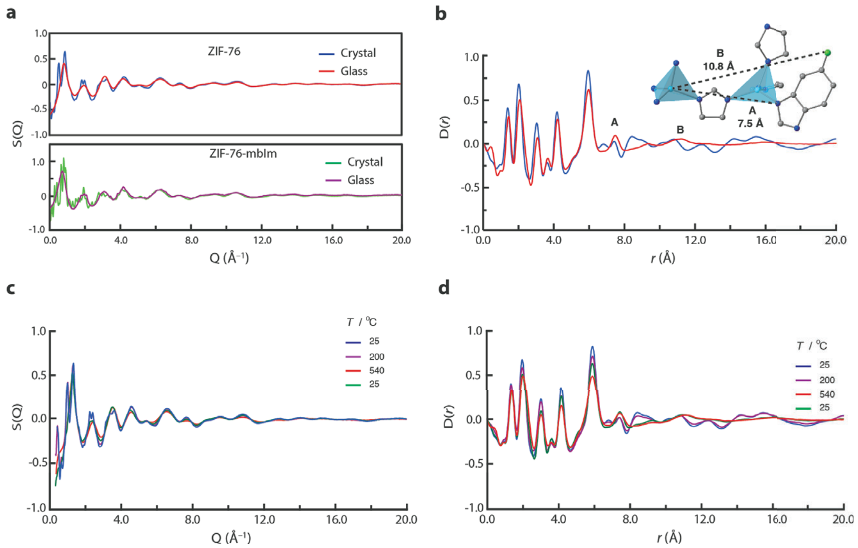

Figure 3. Diffraction in the Crystalline and Glass State. (a) X-ray structure factors *S*(Q) of crystalline ZIF-76 and ZIF-76-mbIm, along with the corresponding glass samples. (b) Corresponding ZIF-76 pair distribution function *D*(r). Inset – medium range order. Zn – light blue, Cl – green, C – grey, N – dark blue, H – omitted for clarity. (c) and (d) X-ray structure factors *S*(Q) and pair distribution functions *D*(r), respectively, of ZIF-76 upon heating and subsequent recovery to room temperature (green curve at 25 °C).

Accessible Porosity in a MOF-glass

We have previously shown that positron annihilation lifetime spectroscopy (PALS) is a useful tool for the mapping of various pore sizes in MOF crystals and glasses.[31] In agreement with the crystal structure of ZIF-76,[20] two cavity diameters of 5.7 Å and 15.7 Å were detected in our ZIF-76 samples (**Supplementary Figure 19**, **Supplementary Table 1**). Upon vitrification to a_gZIF-76, a single pore with a diameter of *ca.* 5 Å was revealed. PALS analysis of crystalline ZIF-76-mbIm also yielded two cavities of diameters 5.8 Å and 15.6 Å. The a_gZIF-76-mbIm glass retains two distinct pores with diameters of 4.8 Å and 7.2 Å (**Supplementary Figure 20**). Although this analysis shows a reduction in porosity due to vitrification, the glasses, and particularly a_gZIF-76-mbIm, still maintain significant porosity.

To prepare samples possessing high pore volumes before conducting gas adsorption experiments, we optimized the synthetic procedures for ZIF-76 and ZIF-76-mbIm, and incorporated larger quantities of the benzimidazolate-derived linker in each case. This strategy borrows the logic employed by Yaghi et al in the synthesis of new high surface area crystalline materials.[19] Samples of ZIF-76 and ZIF-76-mbIm, with stoichiometries of $[Zn(Im)_{1.0}(5\text{-ClbIm})_{1.0}]$ and $[Zn(Im)_{0.93}(5\text{-mbIm})_{1.07}]$, respectively, were thus prepared. The ligand ratios in these materials were determined by ^{1}H NMR spectroscopy on dissolved samples (**Supplementary Figures 21 and 22**). A range of gas adsorption isotherms were measured on crystalline $[Zn(Im)_{1.0}(5\text{-ClbIm})_{1.0}]$ and $[Zn(Im)_{0.93}(5\text{-mbIm})_{1.07}]$. From N_2 adsorption isotherms at 77 K, BET surface areas of 1313 $cm^2\ g^{-1}$ and 1173 $cm^2\ g^{-1}$ were estimated for ZIF-76 and ZIF-76-mbIm, respectively. These values are consistent with those reported in the literature.[23] As expected, these crystalline ZIFs are also porous to a range of other small gases (**Table 2, Supplementary Figures 23-28 and Supplementary Tables 2-4**).

Remarkably, and representing a departure from the dense melt quenched MOF-glasses reported to date,[16] these samples of a_gZIF-76 and a_gZIF-76-mbIm are permanently porous to incoming gases. While a_gZIF-76 reversibly adsorbs in excess of 4 wt% CO_2 at 273 K (**Supplementary Figure 29**), isotherms measured on this glass were accompanied by significant hysteresis in their desorption branches, which persisted with long equilibration times. This indicates restricted diffusion of guest molecules due to constrictions in the pore network, which is consistent with very low uptake of N_2 and H_2 at 77 K. This is to be expected, given the partial collapse of the crystalline porous structure, to the glass state. We therefore turned our attention to the permanent porosity displayed by a_gZIF-76-mbIm, which reversibly adsorbs CO_2 and CH_4 at 273 K and 293 K (**Figure 4a**). In this case, the adsorption isotherms exhibited only very minor hysteresis, implying that diffusion limitations are largely absent for these gases. At 77 K, however, N_2 is prevented from diffusing into the pores, while H_2 is adsorbed but with significant hysteresis (**Supplementary Figure 30**).

The appreciable remnant network of accessible, interconnected pores in a_gZIF-76-mbIm enables it to adsorb 7.0 wt% of CO_2 at 273 K and a pressure of 1 bar (**Table 2**). Micropore volumes and surface areas for ZIF-76-mbIm and a_gZIF-76-mbIm were estimated by NLDFT fitting of their CO_2 adsorption isotherms (**Supplementary Figures 31 and 32**). We note that these are naturally lower than the values derived from N_2 isotherms measured at 77 K, which could only be obtained for ZIF-76-mbIm. The lower CO_2 uptake of a_gZIF-76-mbIm compared to its crystalline precursor can be ascribed to the slight contraction of the overall pore volume of 0.12 cm^3 g^{-1} upon vitrification. The enthalpy of adsorption at Q_{st} for CO_2 indicates that a_gZIF-76-mbIm binds CO_2 more strongly than ZIF-76-mbIm (**Figure 4b, Supplementary Figures 33 and 34**). The modest Q_{st} at zero coverage of the crystalline ZIF (−27.2 kJ mol^{-1}) arises from its largely non-polar pore environment, while the increase in Q_{st} in the glass reveals a pore environment with enhanced interactions with the guest CO_2 molecules (vide infra). We ascribe the higher Q_{st} for binding CO_2 of the glass to a highly contoured pore surface and constricted pore environment, which provide enhanced contacts with the guest. The relatively steep drop-off in Q_{st} with increasing CO_2 loading of the glass indicates that the vitrification process creates regions within the pore network with a particularly high affinity for CO_2.

Table 2. Summary of the textural characteristics of a permanent porous glass derived from ZIF-76-mbIm.

		ZIF-76-mbIm	***a*$_g$ZIF-76-mbIm**
Uptake of CO_2 (1 bar, 273 K)		10.0 wt%	6.7 wt%
Surface area [a]	from N_2 / 77 K data	1173	[d]
	from CO_2 / 273 K data	643	375
Pore volume [b]	from N_2 / 77 K data	0.50	[d]
	from CO_2 / 273 K data	0.17	0.12
Isosteric heat of adsorption, Q_{st} (CO_2) [c]		−26.3	−29.3

[a] In cm^2 g^{-1} using the BET model (N_2) or NLDFT fitting (CO_2). [b] Volume accessible to adsorbate in cm^3 g^{-1} at 1 bar using the density of liquid adsorbate (N_2) or NLDFT fitting. [c] In kJ mol^{-1} at zero loading. [d] Not measurable due to diffusion limitations.

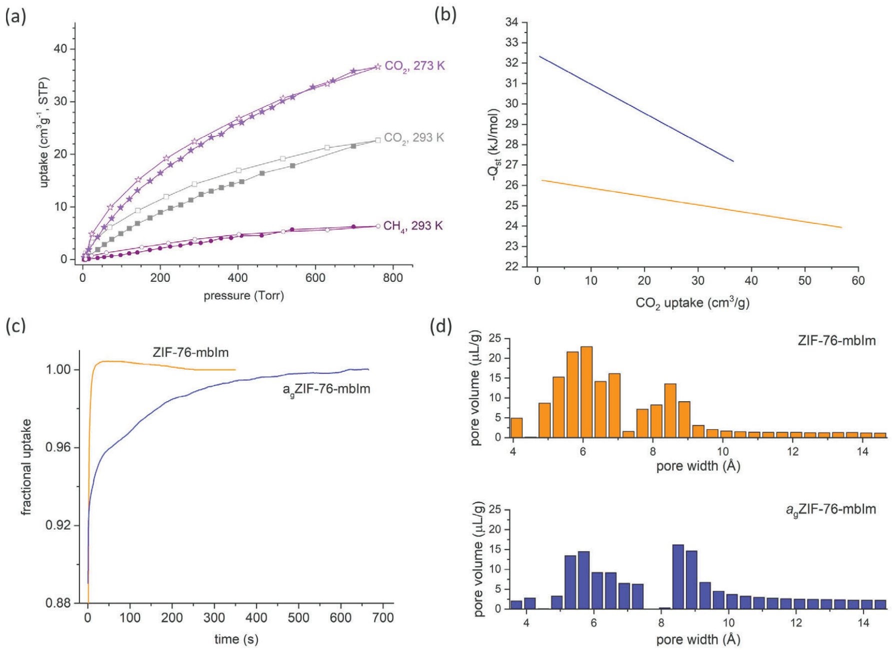

Figure 4. Permanent accessible porosity in *a*$_g$ZIF-76-mbIm and comparisons with ZIF-76-mbIm. (a) Adsorption isotherms of *a*$_g$ZIF-76-mbIm (filled symbols = adsorption, empty symbols = desorption), (b) Calculated isosteric heats of adsorption (Q_{st}) for CO_2 as a function of guest loading, orange – ZIF-76, blue – *a*$_g$ZIF-76-mbIm. (c) Time-dependent CO_2 uptake profiles at 273 K at a pressure of 5 Torr, (d) Pore size distributions as determined by a NLDFT method from CO_2 adsorption isotherms at 273 K.

The kinetic profiles of CO_2 uptake were also measured for ZIF-76-mbIm and a_gZIF-76-mbIm. Over adsorption of CO_2 leads to a fractional uptake above 1, before CO_2 release and equilibration. a_gZIF-76-mbIm takes significantly longer to attain equilibrium between the adsorbed and non-adsorbed gas molecules (**Figure 4c**), which implies that diffusion is more constricted in the glass than its crystalline precursor, and the pore network is more tortuous. This is consistent with the reduced structural regularity, and hindered diffusion inherent in glass, with the remainder of its void space more closely resembling the parent material.

A further illustration of the pore structure is provided by the pore size distribution calculated from CO_2 adsorption isotherms at 273 K, which indicate that the pores contract slightly upon vitrification (**Figure 4d**). Taken together, these observations show that glasses derived from ZIFs have potential in both kinetic and equilibrium-based gas separation processes. Glasses for gas separations may be optimised by matching the pore window sized to the kinetic diameters of target gas pairs. Preliminary experiments indicate that this may be accomplished by varying linker ratios in these glasses. Vitrification of the crystalline frameworks is possible within a broad range of linker ratios to produce porous glasses with finely tuned textural characteristics. The adsorption of gases and the separation of gas mixtures using this suite of materials are the subjects of ongoing investigation.

We note that the network of channels in a_gZIF-76-mbIm is stable for at least three months, a conclusion drawn from the reproducibility of adsorption isotherms measured on samples stored over this period of time. Further, the glasses can be handled in ambient laboratory atmospheres without any detrimental effects on their adsorption capacity. The superior textural characteristics of a_gZIF-76-mbIm compared to a_gZIF-76 can be ascribed to the presence of the methyl group in the former. As indicated by solid-state NMR, these groups anchor the glassy network by noncovalent interactions with neighbouring ligands, which helps to maintain a relatively open and contiguous network of pores and channels.

Discussion

This report describes permanent, accessible, and reversible porosity inherent to glasses derived from metal-organic frameworks. Two precursor crystalline ZIFs were designed, and their high temperature melting monitored *in-situ* by a range of combined diffraction experiments. Notably, these glasses are distinct from those reported by Yaghi and Angell,[13] which are prepared via sol-gel methods, and in which T_g disappears after solvent evaporation. This means that sol-gel glasses cannot be 'formed' by heating to high temperatures. The discovery of accessible porosity in glasses derived from MOFs may serve as the foundation for a new class of porous hybrid inorganic-organic materials. We expect that developments in this field will be enabled by (i) the large number of known MOF or coordination polymer structures that can serve as potential glass precursors,[32] (ii) the ability to combine the chemical diversity of MOFs with established techniques for handling and moulding glasses, (iii) the availability of several techniques for vitrifying crystalline frameworks,[12,33] and (iv) the use of post-synthetic techniques that are employed in other glass families to increase available surface areas.[34]

We envisage a plethora of potential applications will stem from porous MOF glasses, including membranes for chemical separations, catalysis, ion transport, and conductivity.[35] These glasses should not however be placed into competition for the ultra-high surface areas heralded for crystalline MOFs, but seen in the light of ease of processing, mechanical stability and possible use in separations. Additional avenues for research may also arise from their comparison and contextualization with conventional glasses. In this light, MOF glasses may be geared towards applications in optics, where one of their principle advantages will lie in their 'softer' nature and correspondingly lower processing temperatures. The combination of the stimuli responsivity of MOF chemistry[36] with the glass domain will also lead to new, smart applications and a new era of glass technology.[37]

Methods

Synthesis

ZIF-76 [$Zn(Im)_{1.62}(5\text{-}ClbIm)_{0.38}$] and ZIF-76-mbIm [$Zn(Im)_{1.33}(5\text{-}mbIm)_{0.67}$] were prepared via the procedures reported by Peralta et al in the literature.[23] Specifically, imidazole (0.12 g, 17.25 x 10^{-4} mol) and 5-chlorobenzimidazole (0.13 g, 8.66x10^{-4} mol) were mixed together in a solution of DMF (8.28 mL) and DEF (5.73 mL). $Zn(NO_3)_2.6H_2O$ (0.25 g, 8.59 x 10^{-4} mol) was subsequently added, along with NaOH (0.52 mL, 2.5 moldm^{-3}). The turbid solution was then heated to 90 °C for 5 days, and the microcrystalline powder collected by filtration. Occluded solvent was removed by heating under vacuum at 200 °C for 6 h.[38] For the mbIm equivalent, 5-methylbenzimidazole (0.115 g) was used in place of 5-chloroimidazole. Identical procedures were followed for samples of [$Zn(Im)_{1.0}(5\text{-}ClbIm)_{1.0}$] and [$Zn(Im)_{0.93}(5\text{-}mbIm)_{1.07}$] except $NaOH_{(aq)}$ was omitted from the reaction solvent.

Vitrification

Bulk powder samples were placed into a ceramic crucible and then into a tube furnace, which was purged with argon, prior to heating at 10 °C/min to the melting temperatures identified in Table 1. Upon reaching the set temperature, the furnace was turned off and the samples allowed to cool naturally (under argon) to room temperature.

X-ray Powder Diffraction

Data were collected with a Bruker-AXS D8 diffractometer using Cu Kα (λ =1.540598 Å) radiation and a LynxEye position sensitive detector in Bragg-Brentano parafocusing geometry.

Total Scattering measurements

X-ray data were collected at the I15-1 beamline at the Diamond Light Source, UK (λ = 0.161669 Å, 76.7 keV). A small amount of the sample was loaded into a borosilicate glass capillary of 1.17 mm (inner) diameter. Data on the sample, empty instrument and capillary were collected in the region of $\sim 0.4 < Q < \sim 26$ Å^{-1}. Background, multiple scattering, container scattering, Compton scattering and absorption corrections were performed using the GudrunX program.[39,40] Variable temperature measurements were performed using an identical set up, although the capillaries were sealed with araldite. Data were taken upon heating at 25 °C, 100 °C, 200 °C, 280 °C and then in 10 °C steps to 340 °C. Further data were collected in 20 °C intervals to 540 °C, before cooling and a final data set taken at room temperature. Data were corrected using equivalent data those taken from an empty capillary heated to identical temperatures.

Combined small angle – wide angle X-ray scattering

X-ray data were collected at the I22 beamline at the Diamond Light Source, UK (λ = 0.9998 Å, 12.401 keV). The SAXS detector was positioned at a distance of 9.23634 m from the sample as calibrated using a 100 nm period Si_3N_4 grating (Silson, UK), giving a usable Q range of 0.0018 – 0.18 $Å^{-1}$. The WAXS detector was positioned at a distance of 0.16474 m from the sample as calibrated using a standard CeO_2 sample (NIST SRM 674b, Gaithersburg USA), giving a usable Q range of 0.17 – 4.9 $Å^{-1}$. Samples were loaded into 1.5 mm diameter borosilicate capillaries under argon inside a glovebox and sealed to prevent the ingress of air. Samples were heated using a Linkam THMS600 capillary stage (Linkam Scientific, UK) from room temperature to 600°C at 10°C/min. Simultaneous SAXS/WAXS data were collected every 1°C. Data were reduced to 1D using the DAWN package [41,42]and standard reduction pipelines.[43] Values for the power law behavior of the samples were found using the power law model of SASView 4.1.1.[44] Data were fitted over the range $0.003 \le Q \le 0.005$ $Å^{-1}$. Particle size distributions were calculated using the McSAS package,[45,46] a minimal assumption Monte Carlo method for extracting size distributions from small-angle scattering data. Data were fitted over the range $0.002 \le Q \le 0.18$ $Å^{-1}$ with a sphere model.

Nuclear Magnetic Resonance Spectroscopy

Solid-state NMR experiments were carried out on a 600 MHz Varian NMR system equipped with a 1.6 mm Varian HXY MAS probe. Larmor frequencies for ^1H and ^{13}C were 599.50 MHz and 150.74 MHz, respectively, and sample rotation frequency was 40 kHz. For one-dimensional ^1H and ^{13}C magic-angle spinning (MAS) measurements, ^1H and ^{13}C 90° excitation pulses of 1.65 μs and 1.5 μs were used, respectively. In ^1H MAS NMR measurements 8 scans were co-added and repetition delay between scans was 3 s. In ^{13}C MAS NMR measurements number of scans was 5500 and repetition delay was 30 s. Frequency axes of ^1H and ^{13}C spectra were referenced to tetramethylsilane. ^1H-^{13}C cross-polarization (CP) MAS NMR experiment employed Lee-Goldburg (LG) CP block with duration of 100 μs and high-power XiX heteronuclear decoupling during acquisition; number of scans was 660 and repetition delay between scans was 0.4 s. For two-dimensional ^{1}H-^{1}H and ^{1}H-^{13}C spin-diffusion measurements the numbers of scans were 16 and 4000, and numbers of increments in indirectly detected dimensions were 100 and 12, respectively. Repetition delay between scans was 0.5 s. During mixing periods of both measurements, RFDR scheme was used to enhance homonuclear dipolar coupling among protons. ^{1}H-^{13}C experiment employed LG scheme during the CP block.

Solution ^{1}H NMR spectra of digested samples (in a mixture of DCl (35%)/D_2O (0.1 mL) and DMSO-d_6 (0.5 mL)) of samples (about 6 mg) were recorded on a Bruker Avance III 500MHz spectrometer at 293 K. Chemical shifts were referenced to the residual protio-solvent signals of DMSO-d_6. The spectra were processed with the MestreNova Suite.

Differential Scanning Calorimetry and Thermogravimetric Analysis

Characterizations of all the samples were conducted using a Netzsch STA 449 F1 instrument. The samples were placed in a platinum crucible situated on a sample holder of the DSC at room temperature. The samples were heated at 10 °C /min to the target temperature. After cooling to room temperature at 10 °C /min, the second upscan was performed using the same procedure as for the first. To determine the C_p of the samples, both the baseline (blank) and the reference sample (sapphire) were measured.[47]

Gas Adsorption

Isotherms were measured by a volumetric method using a Quantachrome Autosorb iQ2 instrument with ultra-high purity gases. Prior to analysis, the samples were degassed under a dynamic vacuum at 10^{-6} Torr for 10 hours at 150 °C. Accurate sample masses were calculated using degassed samples after sample tubes were backfilled with nitrogen. Where possible, BET surface areas were calculated from N_2 adsorption isotherms at 77 K according to established procedures.[48]

Density Measurements

True densities were measured using a Micromeritics Accupyc 1340 gas pycnometer (1 cm^3 model). The typical mass used was 0.2 g, with the values quoted being the mean and standard deviation from a cycle of 10 measurements.

Positron Annihilation Lifetime Spectroscopy

$^{22}NaCl$, sealed in a thin Mylar envelope, was used as the source of positrons. The samples were packed to 2 mm thickness surrounding the positron source. The ***o***-Ps lifetime measurements were taken under vacuum (1×10^{-5} Torr) at 298 K using an EG&G Ortec spectrometer at a rate of 4.5×10^6 counts per sample. The lifetimes were converted to pore sizes by using the quantum-based formulation assuming a spherical pore geometry.[49] A full description of the technique can be found in a previous study.[31]

Molecular Simulations

Grand canonical Monte Carlo (GCMC) simulations were performed as implemented in the RASPA simulation code[50] to compute single component gas adsorption isotherms of Ar (77 K), CH_4 (273 K), CO_2 (273 K), H_2 (77K), N_2 (77 K) and O_2 (273 K) in ZIF-76 up to 1 bar. The crystal structure of ZIF-76 $[Zn(Im)_{1.5}(clbIm)_{0.5}]$ was taken from the Cambridge Crystallographic Data Center (reference code = GITWEM), and the disorder was removed manually to generate a suitable set of input coordinates for the calculations.[51] Structural properties such as accessible pore volume, pore limiting diameter (PLD) and the largest cavity diameter (LCD) were calculated using Zeo++ software[52] and are listed in **Supplementary Table 4**. For pore volume calculations, the probe radius was set to zero.

Data Availability

The data that support the findings of this study are available from the corresponding authors on request.

Author Acknowledgements

TDB would like to thank the Royal Society for a University Research Fellowship, and for their support (UF150021). We acknowledge the provision of synchrotron access to Beamline I22 (exp. NT18236-1) at the Diamond Light Source, Rutherford Appleton Laboratory UK. We also thank Diamond Light Source for access to beamline I15-1 (EE171151). CZ acknowledges the financial support from the China Scholarship Council and the Elite Research Travel Scholarship from the Danish Ministry of Higher Education and Science. AK and GM acknowledge the support of the Slovenian Research Agency (research core funding No. P1-0021). CMD is supported by the Australian Research Council (DE140101359). LL would like to thank the EPSRC for an allocated studentship. CWA would like to thank the Royal Society for a PhD studentship (RG160498), and the Commonwealth Scientific and Industrial Research Organization (CSIRO) for additional support (C2017/3108). OTQ acknowledges the RSNZ Marsden Fund grant MAU1411. The authors gratefully acknowledge assistance from Dr. Shichun Li in data collection.

Author Contributions

TDB designed the project and wrote the manuscript with SGT, and input from all authors. SAXS/WAXS experiments were performed by TDB, AJS, NJT and GJS, with analysis by AJS and GJS. DSC measurements and sample preparation were carried out by CZ, facilitated by YY. PDF measurements carried out by TDB, DAK, CA, LL, CWA and PAC. All gas adsorption measurements were carried out by SGT, OTQ and SJL. Liquid NMR data were provided by AQ, and solid state NMR measurements carried out and analysed by GM and AK. All simulations were carried out and analysed by IE. PALS data were collected and analysed by CMD, AWT and AJH.

Competing Interests

There are no competing interests.

References

1 Enke, D., Janowski, F. & Schwieger, W. Porous glasses in the 21st century - a short review. *Micropor Mesopor Mat* **60**, 19-30 (2003).

2 Janowski, F. & Enke, D. *Porous Glasses, in Handbook of Porous Solids (eds F. Schüth, K. S. W. Sing and J. Weitkamp)*. (2002).

3 Shimizu, T. *et al.* Transparent, Highly Insulating Polyethyl- and Polyvinylsilsesquioxane Aerogels: Mechanical Improvements by Vulcanization for Ambient Pressure Drying. *Chem Mater* **28**, 6860-6868 (2016).

4 Han, S. H. *et al.* Thermally Rearranged (TR) Polybenzoxazole: Effects of Diverse Imidization Routes on Physical Properties and Gas Transport Behaviors. *Macromolecules* **43**, 7657-7667 (2010).

5 McKeown, N. B. & Budd, P. M. Polymers of intrinsic microporosity (PIMs): organic materials for membrane separations, heterogeneous catalysis and hydrogen storage. *Chem Soc Rev* **35**, 675-683 (2006).

6 Schneermann, A. *et al.* Flexible metal–organic frameworks. *Chem Soc Rev* **43**, 6062-6096 (2014).

7 Horike, S., Shimomura, S. & Kitagawa, S. Soft porous crystals. *Nature Chemistry* **1**, 695-704 (2009).

8 Dissegna, S., Epp, K., Heinz, W. R., Kieslich, G. & Fischer, R. A. Defective Metal-Organic Frameworks. *Adv Mater*, 1704501 (2018).

9 Cliffe, M. J. *et al.* Correlated defect nanoregions in a metal-organic framework. *Nat Commun* **5**, 4176 (2014).

10 Bennett, T. D., Cheetham, A. K., Fuchs, A. H. & Coudert, F. X. Interplay between defects, disorder and flexibility in metal-organic frameworks. *Nature Chemistry* **9**, 11-16 (2017).

11 Gaillac, R. *et al.* Liquid Metal-Organic Frameworks. *Nat Mater* **16**, 1149-1154 (2017).

12 Chen, W. Q. *et al.* Glass Formation of a Coordination Polymer Crystal for Enhanced Proton Conductivity and Material Flexibility. *Angew Chem Int Ed* **55**, 5195-5200 (2016).

13 Zhao, Y., Lee, S.-Y., Becknell, N., Yaghi, O. M. & Angell, C. A. Nanoporous Transparent MOF Glasses with Accessible Internal Surface. *J Am Chem Soc* **138**, 10818–10821 (2016).

14 Phan, A. *et al.* Synthesis, Structure, and Carbon Dioxide Capture Properties of Zeolitic Imidazolate Frameworks. *Accounts Chem Res* **43**, 58-67 (2010).

15 Tian, Y. Q. *et al.* Design and generation of extended zeolitic metal-organic frameworks (ZMOFs): Synthesis and crystal structures of zinc(II) imidazolate polymers with zeolitic topologies. *Chem-Eur J* **13**, 4146-4154 (2007).

16 Bennett, T. D. *et al.* Melt-Quenched Glasses of Metal-Organic Frameworks. *J Am Chem Soc* **138**, 3484-3492 (2016).

17 Umeyama, D., Horike, S., Inukai, M., Itakura, T. & Kitagawa, S. Reversible Solid-to-Liquid Phase Transition of Coordination Polymer Crystals. *J Am Chem Soc* **137**, 864-870 (2015).

18 Nagarkar, S. S. *et al.* Enhanced and Optically Switchable Proton Conductivity in a Melting Coordination Polymer Crystal. *Angew Chem Int Ed* **56**, 4976-4981 (2017).

19 Yang, J. *et al.* Principles of Designing Extra-Large Pore Openings and Cages in Zeolitic Imidazolate Frameworks. *J Am Chem Soc* **139**, 6448-6455 (2017).

20 Banerjee, R. *et al.* High-throughput synthesis of zeolitic imidazolate frameworks and application to CO2 capture. *Science* **319**, 939-943 (2008).

21 Peralta, D. *et al.* Comparison of the behavior of metal-organic frameworks and zeolites for hydrocarbon separations. *J Am Chem Soc* **134**, 8115-8126 (2012).

22 Bennett, T. D. *et al.* Hybrid glasses from strong and fragile metal-organic framework liquids. *Nat Commun* **6**, 8079 (2015).

23 Peralta, D., Chaplais, G., Simon-Masseron, A., Barthelet, K. & Pirngruber, G. D. Synthesis and adsorption properties of ZIF-76 isomorphs. *Micropor Mesopor Mat* **153**, 1-7 (2012).

24 Wu, T., Bu, X. H., Zhang, J. & Feng, P. Y. New Zeolitic Imidazolate Frameworks: From Unprecedented Assembly of Cubic Clusters to Ordered Cooperative Organization of Complementary Ligands. *Chem Mater* **20**, 7377-7382 (2008).

25 Bondi, A. van der Waals Volumes and Radii *The Journal of Physical Chemistry* **68**, 441-451 (1964).

26 Kunal, K., Robertson, C. G., Pawlus, S., Hahn, S. F. & Sokolov, A. P. Role of Chemical Structure in Fragility of Polymers: A Qualitative Picture. *Macromolecules* **41**, 7232-7238 (2008).

27 Longley, L. *et al.* Liquid Phase Blending of Metal-Organic Frameworks. *Nat Commun* **9**, 2135 (2018).

28 Krajnc, A., Kos, T., Logar, N. Z. & Mali, G. A Simple NMR Based Method for Studying the Spatial Distribution of Linkers within Mixed-Linker Metal–Organic Frameworks. *Angew Chem Int Ed Engl* **54**, 10535-10538 (2015).

29 Krajnc, A., Bueken, B., De Vos, D. & Mali, G. Improved resolution and simplification of the spin-diffusion-based NMR method for the structural analysis of mixed-linker MOFs. *Journal of Magnetic Resonance* **279**, 22-28 (2017).

30 Salmon, P. S. & Zeidler, A. Identifying and characterising the different structural length scales in liquids and glasses: an experimental approach. *Phys Chem Chem Phys* **15**, 15286-15308 (2013).

31 Thornton, A. W. *et al.* Porosity in metal–organic framework glasses. *Chem Commun* **52**, 3750-3753 (2016).

32 Moghadam, P. Z. *et al.* Development of a Cambridge Structural Database Subset: A Collection of Metal-Organic Frameworks for Past, Present, and Future. *Chem Mater* **29**, 2618-2625 (2017).

33 Bennett, T. D. & Cheetham, A. K. Amorphous Metal-Organic Frameworks. *Accounts Chem Res* **47**, 1555-1562 (2014).

34 Elmer, T. H. *Engineered Materials Handbook* Vol. 4, Ceramics and Glasses 427-432 (1992).

35 Furukawa, H., Cordova, K. E., O'Keeffe, M. & Yaghi, O. M. The Chemistry and Applications of Metal-Organic Frameworks. *Science* **341**, 974-986 (2013).

36 Coudert, F. X. Responsive Metal–Organic Frameworks and Framework Materials: Under Pressure, Taking the Heat, in the Spotlight, with Friends. *Chem Mater* **27**, 1905-1916 (2015).

37 Morse, D. L. & Evenson, J. W. Welcome to the Glass Age. *Int J Appl Glass Sci* **7**, 409-412 (2016).

38 Prez-Pellitero, J. *et al.* Adsorption of CO2, CH4, and N2 on Zeolitic Imidazolate Frameworks: Experiments and Simulations. *Chemistry: A European Journal* **16**, 1560-1571 (2010).

39 Soper, A. K. GudrunN and GudrunX: Programs for Correcting Raw Neutron and X-ray Diffraction Data to Differential Scattering Cross Section. *Tech. Rep. RAL-TR-2011-013* (2011).

40 Soper, A. K. & Barney, E. R. Extracting the pair distribution function from white-beam X-ray total scattering data. *Journal of Applied Crystallography* **44**, 714-726 (2011).

41 Basham, M. *et al.* Data Analysis WorkbeNch (DAWN). *J Synchrotron Radiat* **22**, 853-858 (2015).

42 Filik, J. *et al.* Processing two-dimensional X-ray diffraction and small-angle scattering data in DAWN 2. *J Appl Crystallogr* **50**, 959-966 (2017).

43 Pauw, B. R., Smith, A. J., Snow, T., Terrill, N. J. & Thünemann, A. F. The modular small-angle X-ray scattering data correction sequence. *Journal of Applied Crystallography* **50**, 1800-1811 (2017).

44 SasView version 4.1 (2017).

45 Pauw, B. R., Pedersen, J. S., Tardif, S., Takata, M. & Iversen, B. B. Improvements and considerations for size distribution retrieval from small-angle scattering data by Monte Carlo methods. *J Appl Crystallogr* **46**, 365-371 (2013).

46 Bressler, I., Pauw, B. R. & Thünemann, A. F. McSAS: software for the retrieval of model parameter distributions from scattering patterns. *Journal of Applied Crystallography* **48**, 962-969 (2015).

47 Yue, Y. Z. The iso-structural viscosity, configurational entropy and fragility of oxide liquids. *J Non-Cryst Solids* **355**, 737-744 (2009).

48 Walton, K. S. & Snurr, R. Q. Applicability of the BET method for determining surface areas of microporous metal-organic frameworks. *J Am Chem Soc* **129**, 8552-8556 (2007).

49 Tao, S. J. Positronium Annihilation in Molecular Substances. *The Journal of Chemical Physics* **56**, 5499 (1972).

50 Dubbeldam, D., Calero, S., Ellis, D. E. & Snurr, R. Q. Raspa: Molecular Simulation Software for Adsorption and Diffusion in Flexible Nanoporous Materials. *Mol. Simul.* **42**, 81-101 (2016).

51 Allen, F. H. The Cambridge Structural Database: a quarter of a million crystal structures and rising. *Acta Crystallogr., Sect. B: Struct. Sci.* **58**, 380-388 (2002).

52 Willems, T. F., Rycroft, C. H., Kazi, M., Meza, J. C. & Haranczyk, M. Algorithms and Tools for High-Throughput Geometry-Based Analysis of Crystalline Porous Materials. *Microporous and Mesoporous Mater.* **149**, 134-141 (2012).

Electronic Supplementary Information for

Metal-Organic Framework Glasses with Permanent Accessible Porosity

Chao Zhou,[1,2] Louis Longley,[1] Andraž Krajnc,[3] Glen J. Smales,[4,5] Ang Qiao,[6] Ilknur Eruçar,[7] Cara M. Doherty,[8] Aaron W. Thornton,[8] Anita J. Hill,[8] Christopher W. Ashling,[1] Omid T. Qazvini,[9] Seok J. Lee,[9] Philip A. Chater,[5] Nicholas J. Terrill,[5] Andrew. J. Smith,[5] Yuanzheng Yue,[2,6,10] Gregor Mali,[3] David A. Keen,[11] Shane G. Telfer[9] and Thomas D. Bennett*[1]*

[1]*Department of Materials Science and Metallurgy, University of Cambridge, Charles Babbage Road, Cambridge, CB3 0FS, UK*

[2]*Department of Chemistry and Bioscience, Aalborg University, DK-9220 Aalborg, Denmark*

[3]*Department of Inorganic Chemistry and Technology, National Institute of Chemistry, SI-1001 Ljubljana, Slovenia*

[4]*Department of Chemistry, University College London, Gordon Street, London, WC1H 0AJ, UK*

[5]*Diamond Light Source Ltd, Diamond House, Harwell Science and Innovation Campus, Didcot OX11 0DE, UK*

[6]*State Key Laboratory of Silicate Materials for Architectures, Wuhan University of Technology, Wuhan 430070, China*

[7]*Department of Natural and Mathematical Sciences, Faculty of Engineering, Ozyegin University, Istanbul, Turkey*

[8]*Future Industries, Commonwealth Scientific and Industrial Research Organisation, Clayton South, Victoria 3168, Australia*

[9] *MacDiarmid Institute for Advanced Materials and Nanotechnology, Institute of Fundamental Sciences, Massey University, Palmerston North 4442,* New Zealand

[10] *School of Materials Science and Engineering, Qilu University of Technology, Jinan 250353, China*

[11]*ISIS Facility, Rutherford Appleton Laboratory, Harwell Campus, Didcot, Oxon OX11 0QX, UK*

Email: tdb35@cam.ac.uk S.Telfer@massey.ac.nz

Table of Contents

1. Vitrification of ZIF-76 3

2. Vitrification of ZIF-76-mbIm 7

3. Small Angle X-ray Scattering 9

4. Solid state NMR Spectroscopy, PDF and PALS measurements 10

5. Gas Adsorption Isotherms 14

6. Simulated Gas Adsorption Isotherms 22

7. References 34

1. Vitrification of ZIF-76

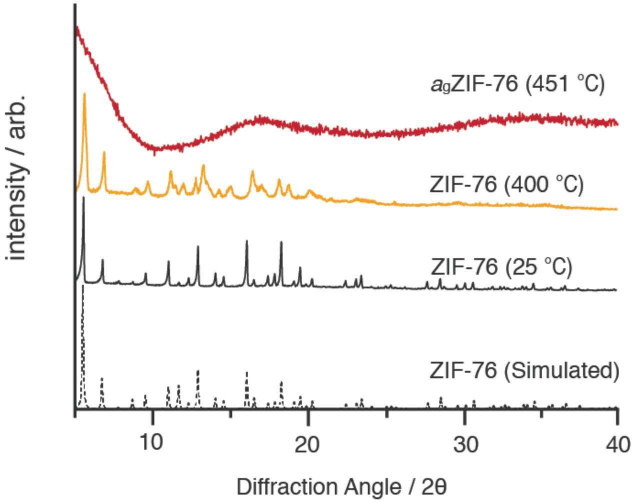

Supplementary Figure 1. X-ray powder diffraction patterns of ZIF-76. Experimental (as-synthesized), and those from samples quenched from 400 °C and 451 °C, are shown alongside the simulated pattern.

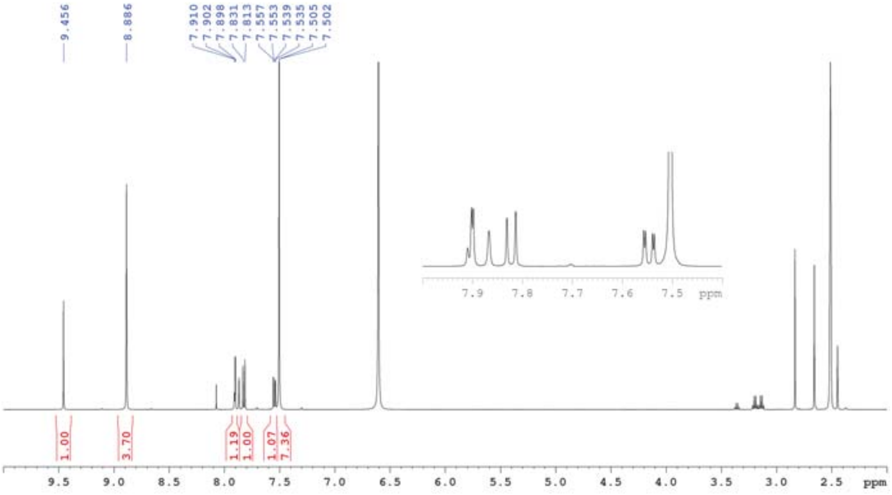

Supplementary Figure 2. ^{1}H NMR spectrum of as-synthesized ZIF-76 digested in DCl/DMSO-d$_6$. NMR peak assignments: Zn(Im)$_{1.62}$(ClbIm)$_{0.38}$. ^{1}H NMR (500 MHz, DMSO-*d*$_6$): 2.5 (DMSO-d$_6$), 7.50 (C***H***C***H***N$_{\mathrm{Im}}$), 7.54 (CC***H***CH$_{\mathrm{ClbIm}}$), 7.82 (CCHC***H***$_{\mathrm{ClbIm}}$), 7.90 (ClCC***H***CC$_{\mathrm{ClbIm}}$), 8.89 (NC***H***N$_{\mathrm{Im}}$), 9.46 (NC***H***N$_{\mathrm{ClbIm}}$).

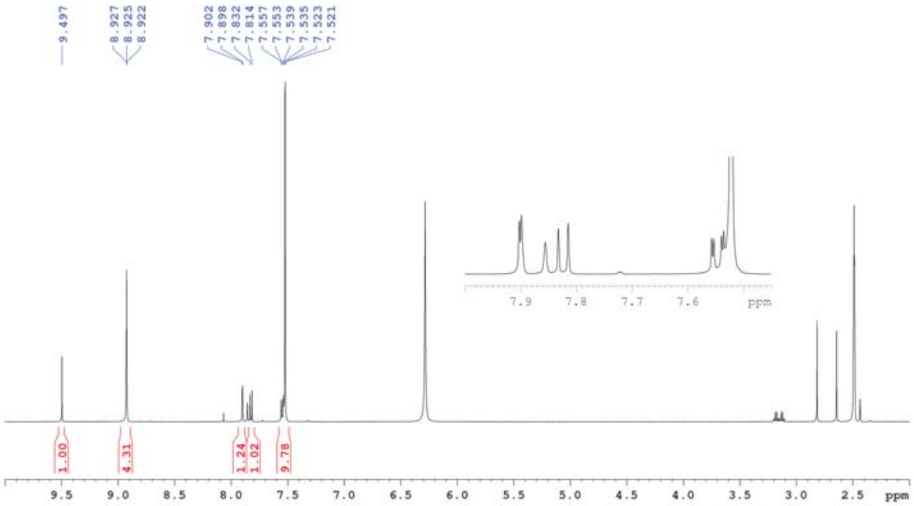

Supplementary Figure 3. ^{1}H NMR spectrum of a sample of ZIF-76 heated to 200 °C and cooled to room temperature, digested in DCl/DMSO-d_6. NMR peak assignments: $\mathrm{Zn(Im)_{1.62}(ClbIm)_{0.38}}$. ^{1}H NMR (500 MHz, DMSO-d_6): 2.5 (DMSO-d_6), 7.52 ($\mathrm{C}\boldsymbol{H}\mathrm{C}\boldsymbol{H}\mathrm{N}_{\mathrm{Im}}$), 7.56 ($\mathrm{CC}\boldsymbol{H}\mathrm{CH}_{\mathrm{ClbIm}}$), 7.82 ($\mathrm{CCHC}\boldsymbol{H}_{\mathrm{ClbIm}}$), 7.90 ($\mathrm{ClCC}\boldsymbol{H}\mathrm{CC}_{\mathrm{ClbIm}}$), 8.93 ($\mathrm{NC}\boldsymbol{H}\mathrm{N}_{\mathrm{Im}}$), 9.50 ($\mathrm{NC}\boldsymbol{H}\mathrm{N}_{\mathrm{ClbIm}}$).

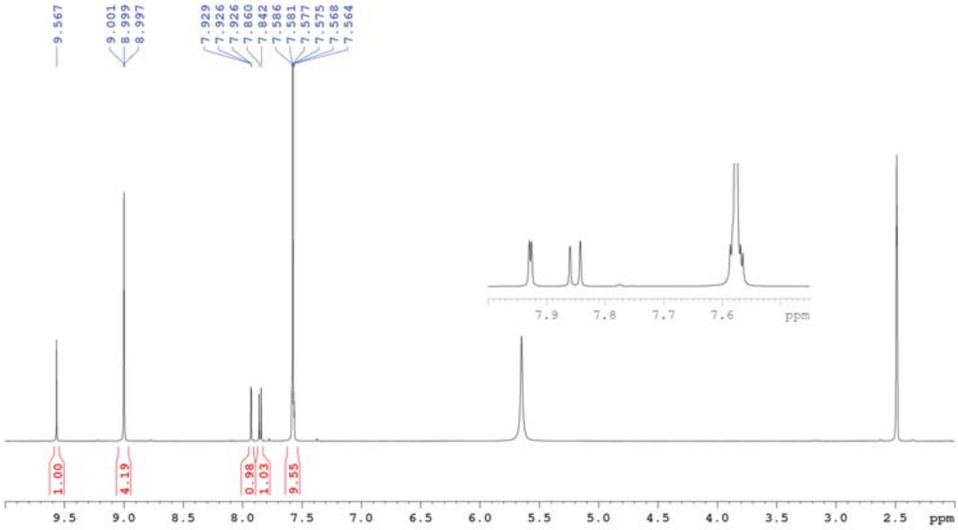

Supplementary Figure 4. ^{1}H NMR spectrum of a sample of ZIF-76 heated to 400 °C and cooled to room temperature, digested in DCl/DMSO-d_6. NMR peak assignments: $\mathrm{Zn(Im)_{1.62}(ClbIm)_{0.38}}$. ^{1}H NMR (500 MHz, DMSO-d_6): 2.5 (DMSO-d_6), 7.56 ($\mathrm{C}\boldsymbol{H}\mathrm{C}\boldsymbol{H}\mathrm{N}_{\mathrm{Im}}$), 7.56 ($\mathrm{CC}\boldsymbol{H}\mathrm{CH}_{\mathrm{ClbIm}}$), 7.85 ($\mathrm{CCHC}\boldsymbol{H}_{\mathrm{ClbIm}}$), 7.93 ($\mathrm{ClCC}\boldsymbol{H}\mathrm{CC}_{\mathrm{ClbIm}}$), 9.00 ($\mathrm{NC}\boldsymbol{H}\mathrm{N}_{\mathrm{Im}}$), 9.57 ($\mathrm{NC}\boldsymbol{H}\mathrm{N}_{\mathrm{ClbIm}}$).

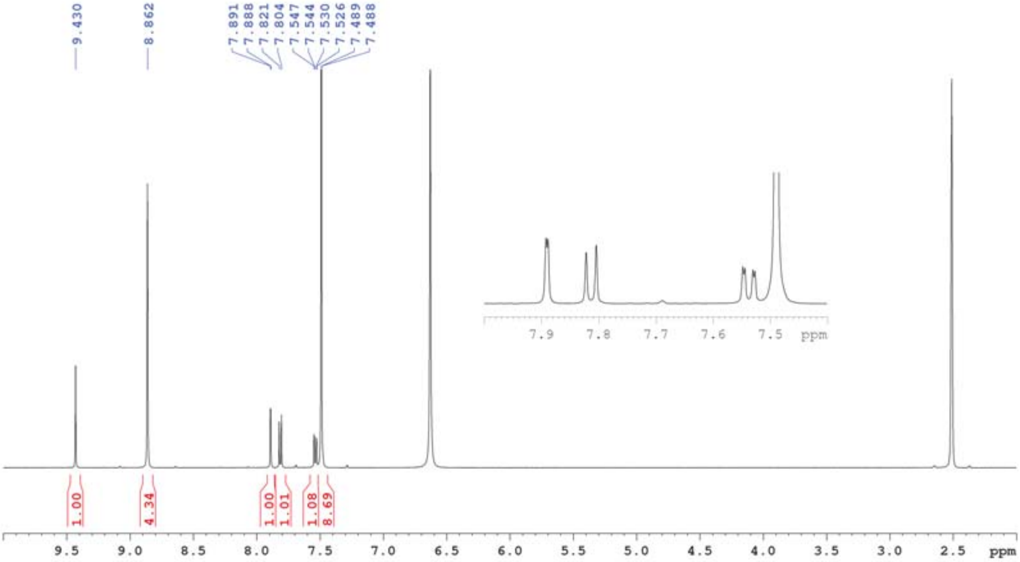

Supplementary Figure 5. ^{1}H NMR spectrum of a_gZIF-76 digested in DCl/DMSO-d$_6$. NMR peak assignments: Zn(Im)$_{1.62}$(ClbIm)$_{0.38}$. ^{1}H NMR (500 MHz, DMSO-d_6): 2.5 (DMSO-d$_6$), 7.49 (C***H***C***H***N$_{\text{Im}}$), 7.55 (CC***H***CH$_{\text{ClbIm}}$), 7.81 (CCHC***H***$_{\text{ClbIm}}$), 7.89 (ClCC***H***CC$_{\text{ClbIm}}$), 8.86 (NC***H***N$_{\text{Im}}$), 9.43 (NC***H***N$_{\text{ClbIm}}$).

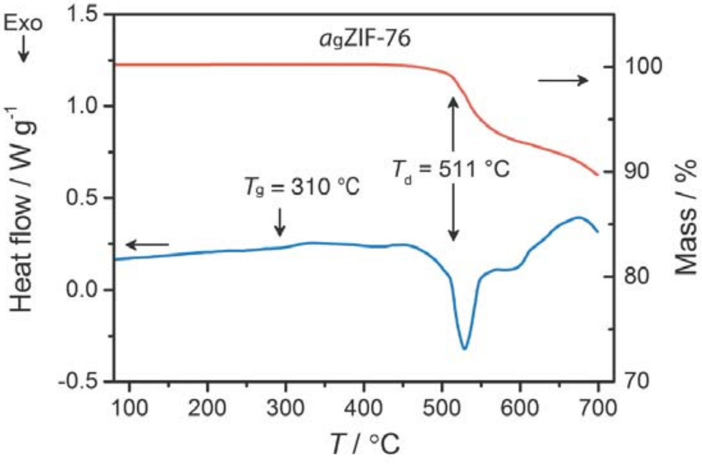

Supplementary Figure 6. Thermal analysis of a_gZIF-76. Isobaric heat capacity (C_p) and mass as a function of temperature (T) for a_gZIF-76. The DSC experiment was conducted in argon at a rate of 10 °C / min, to 700 °C.

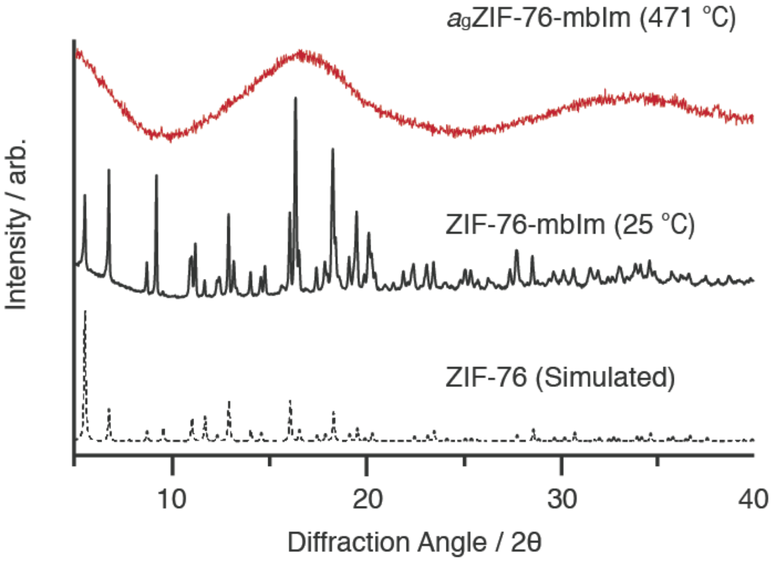

Supplementary Figure 7. X-ray powder diffraction patterns of ZIF-76-mbIm. Experimental (as-synthesized), and that from a sample quenched from 471 °C, are shown alongside the simulated pattern for ZIF-76.

2. Vitrification of ZIF-76-mbIm

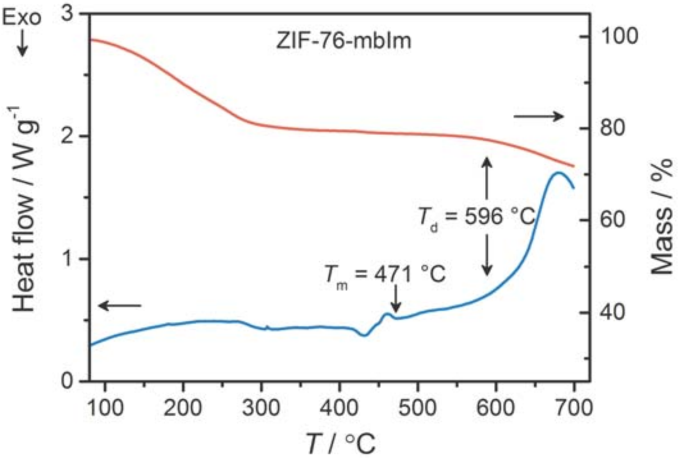

Supplementary Figure 8. Thermal analysis of ZIF-76-mbIm. Isobaric heat capacity (C_p) and mass as a function of temperature (T) for ZIF-76-mbIm. The DSC experiment was conducted in argon at a heating rate of 10 °C / min, to 700 °C.

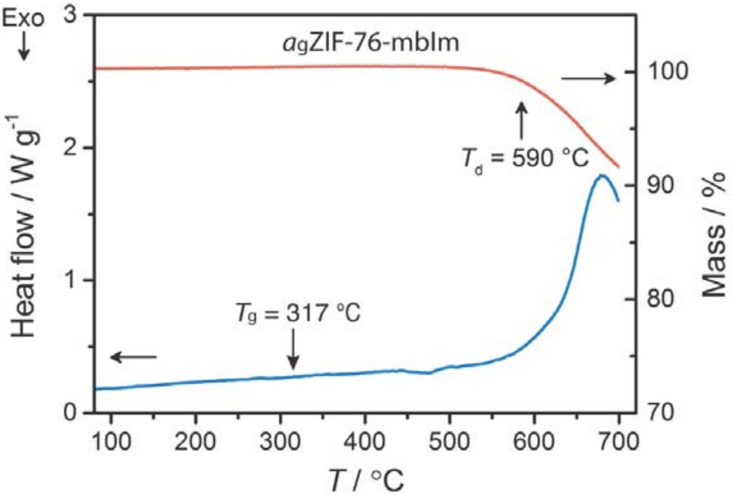

Supplementary Figure 9. Thermal analysis of a_gZIF-76-mbIm. Isobaric heat capacity (C_p) and mass as a function of temperature (T) for a_gZIF-76-mbIm. The DSC experiment was conducted in argon at a heating rate of 10 °C / min, to 700 °C.

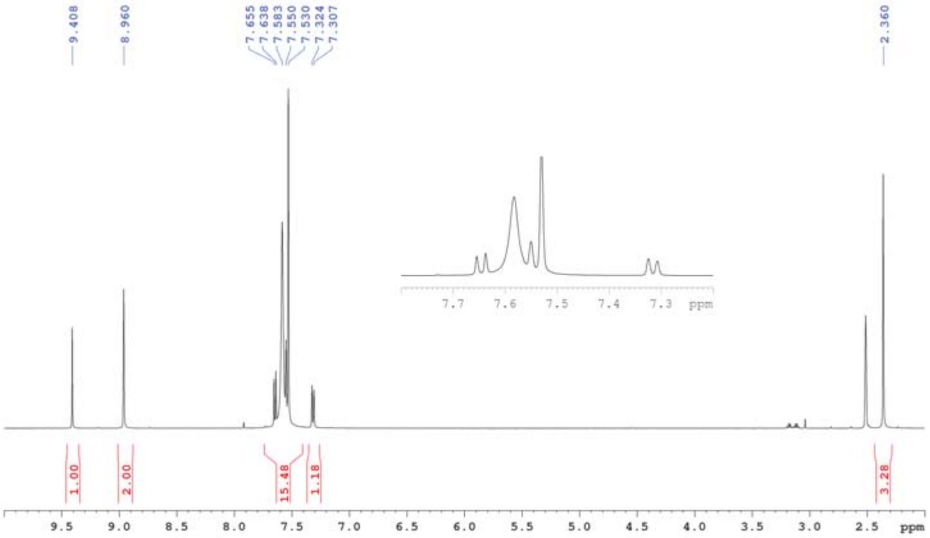

Supplementary Figure 10. ^{1}H NMR spectrum of ZIF-76-mbIm digested in DCl/DMSO-d$_6$. NMR peak assignments: ZIF-76-mbIm. (Zn(Im)$_{1.33}$(mbIm)$_{0.67}$). ^{1}H NMR (500 MHz, DMSO-d_6): 2.36 (C***H***$_{\text{3mbIm}}$), 2.5 (DMSO-d$_6$), 7.32 (CC***H***CH$_{\text{mbIm}}$), 7.54 (C***H***NC***H***$_{\text{Im}}$), 7.55 (CC***H***C(CH$_3$)$_{\text{mbIm}}$), 7.65 (CC**H**C***H***$_{\text{mbIm}}$), 8.96 (NC***H***N$_{\text{Im}}$), 9.41 (NC***H***N$_{\text{mbIm}}$).

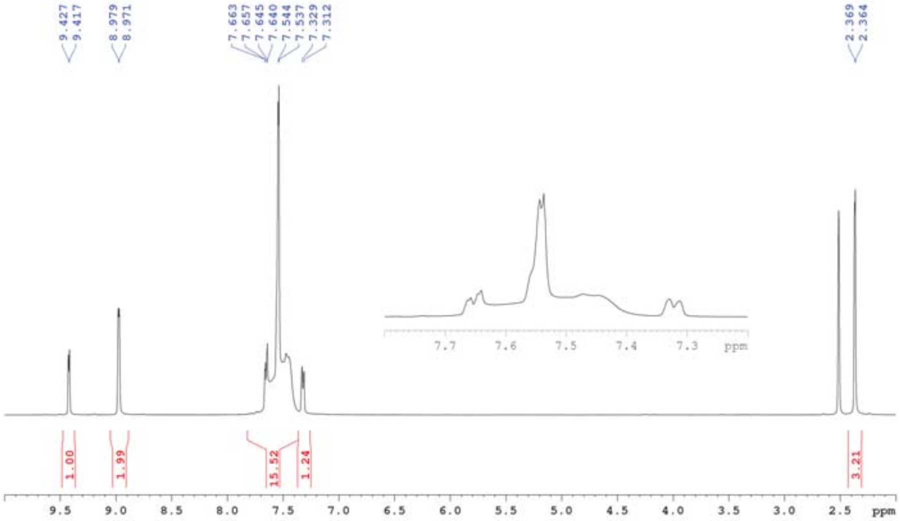

Supplementary Figure 11. ^{1}H NMR spectrum of *a*$_{\text{g}}$ZIF-76-mbIm digested in DCl/DMSO-d$_6$. NMR peak assignments: (Zn(Im)$_{1.33}$(mbIm)$_{0.67}$). ^{1}H NMR (500 MHz, DMSO-d_6): 2.36 (C***H***$_{\text{3mbIm}}$), 2.5 (DMSO-d$_6$), 7.32 (CC***H***CH$_{\text{mbIm}}$), 7.54 (C***H***NC***H***$_{\text{Im}}$), 7.55 (CC***H***C(CH$_3$)$_{\text{mbIm}}$), 7.66 (CCHC***H***$_{\text{mbIm}}$), 8.98 (NC***H***N$_{\text{Im}}$), 9.42 (NC***H***N$_{\text{mbIm}}$).

3. Small Angle X-ray Scattering

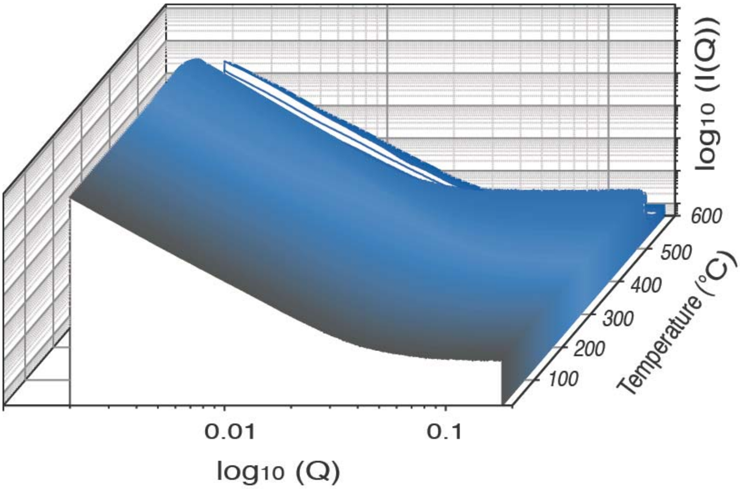

Supplementary Figure 12. Variable temperature resolved SAXS profile for ZIF-76. Heating range from 25 °C to 600 °C.

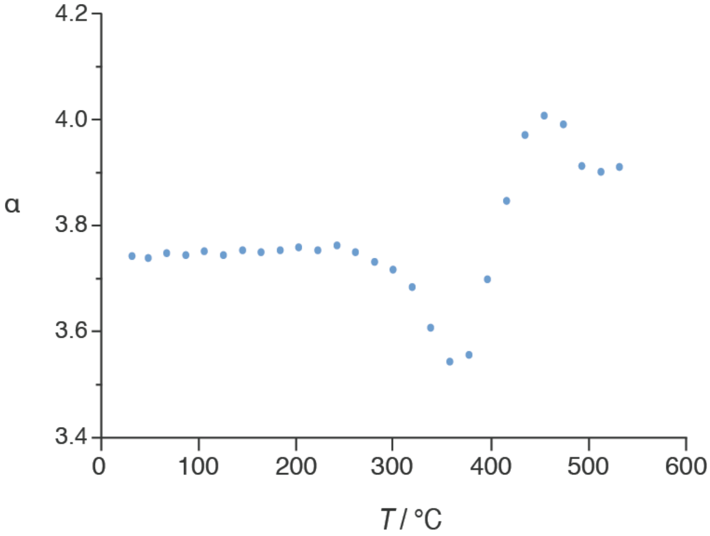

Supplementary Figure 13. Porod fitting of the variable temperature SAXS data. Experiments performed on a sample of crystalline, evacuated ZIF-76.

4. Solid state NMR Spectroscopy, PDF and PALS measurements

Supplementary Table 1. Positron annihilation lifetime spectroscopy data.

	Intensity		Lifetime	
Sample	I3 (%)	I4 (%)	τ3 (ns)	τ4 (ns)
ZIF-76	5.8 ±0.2	6.2 ± 0.1	1.999 ± 0.05	11.934 ± 0.20
a_gZIF-76	6.3 ± 0.1		1.826 ± 0.02	
ZIF-76-mbIm	15.4 ± 0.3	16.6 ± 0.1	2.068 ± 0.03	11.741 ± 0.07
a_gZIF-76-mbIm	9.0 ± 1.6	18.0 ± 1.8	1.554 ± 0.14	2.913 ± 0.08

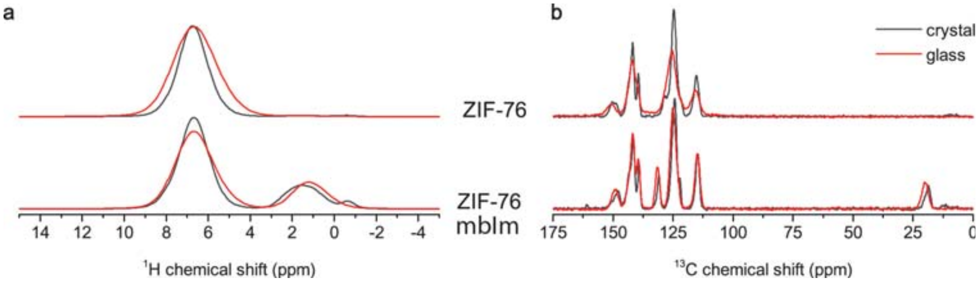

Supplementary Figure 14. Solid-State ^{1}H MAS (a) and (b) ^{13}C MAS NMR spectra.

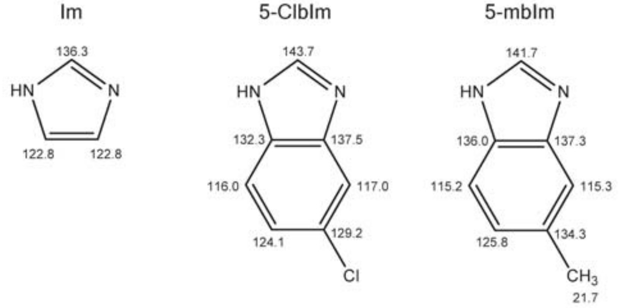

Supplementary Figure 15. ^{13}C isotropic chemical shifts of imidazole ligands. 5-chlorobenzimidazole (5-ClbImH) and 5-methylbenzimidazole (5-mbImH) and imidazole (ImH) species, as found in the literature. These chemical shifts enable tentative assignment of ^{13}C MAS NMR spectra.

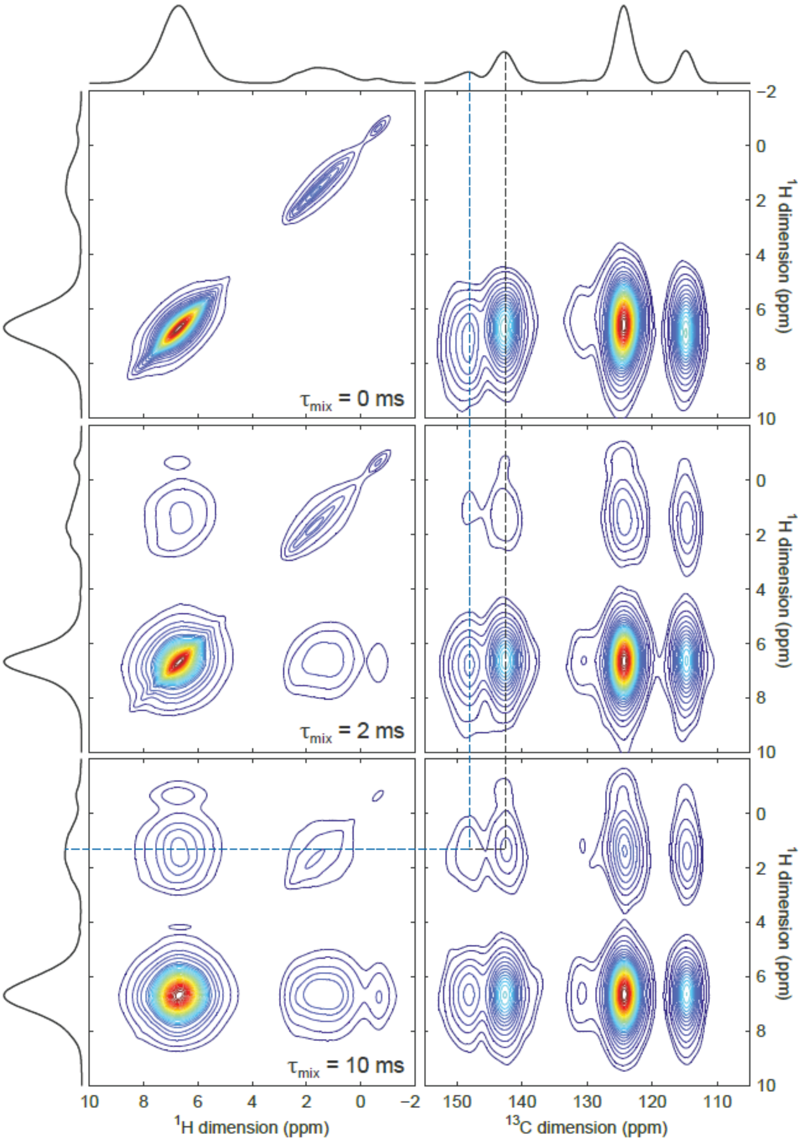

Supplementary Figure 16. Selected ^{1}H-detected and ^{13}C-detected 2D proton spin-diffusion NMR spectra of crystalline ZIF-76-mbIm. The absence of off-diagonal peaks at a mixing time of 0 ms indicates that proton polarization transfer has not occurred, whilst their steady appearance and strengthening in intensity from 2-10 ms is due to the polarization transfer taking place.

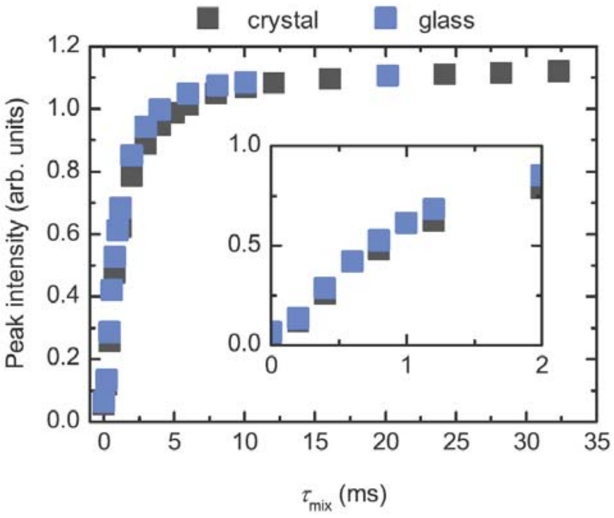

Supplementary Figure 17. Spin-diffusion curves obtained from the ^{1}H-detected measurements in crystalline ZIF-76-mbIm and a_gZIF-76-mbIm.

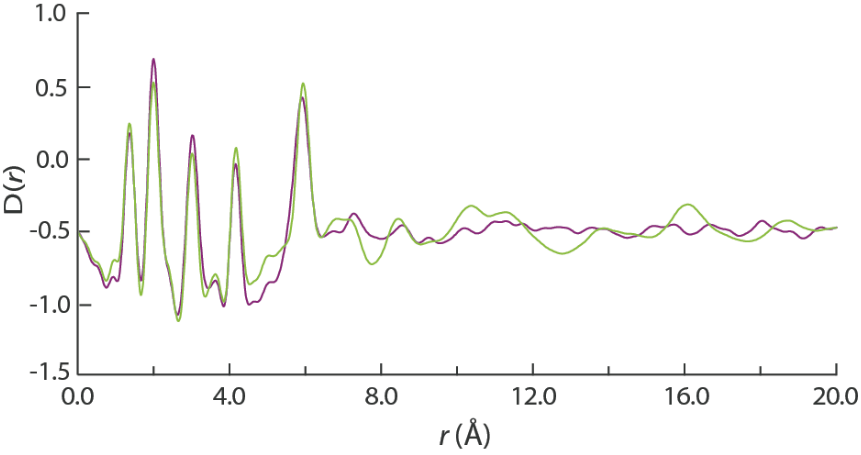

Supplementary Figure 18. Experimental X-ray total pair distribution functions D(*r*). ZIF-76-mbIm (green) and a_gZIF-76-mbIm (purple).

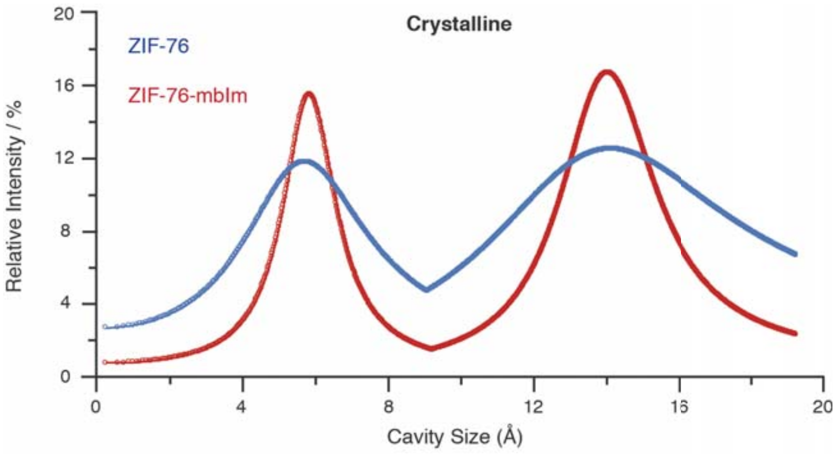

Supplementary Figure 19. PALS measurements on ZIF-76 and ZIF-76-mbIm. Results for the third and fourth components ($\tau3$ and $\tau4$) are represented as Gaussian distributions which correspond to the small and large cavities, respectively, and the Intensity is related to their relative number within the sample (I3 and I4).

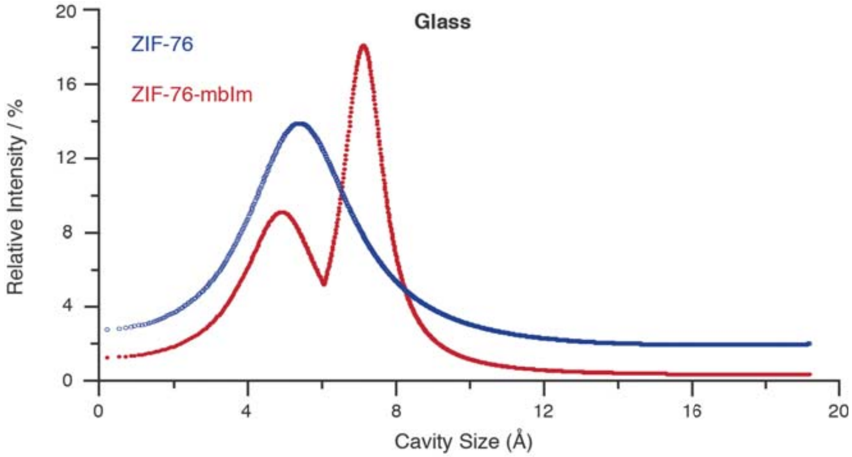

Supplementary Figure 20. PALS measurements on a_gZIF-76 and a_gZIF-76-mbIm. Results for the third and fourth components ($\tau3$ and $\tau4$) are represented as Gaussian distributions which correspond to the small and large cavities, respectively, and the Intensity is related to their relative number within the sample (I3 and I4).

5. Gas Adsorption Isotherms

Supplementary Table 2. Gas adsorption properties for crystalline ZIF-76 and ZIF-76-mbIm. The data are given as volumetric uptake (mL STP / g) at a pressure of 1 bar.

Gas	**H_2**	**CO_2**	**Ar**	**O_2**	**N_2**	**CH_4**
Temperature / K	77	273	77	273	77	273
ZIF-76 [a]						
Experimental	187	59.9	-	-	338	25.2
Simulated	95.5	19.7	268.5	3.4	342	14.6
ZIF-76-mbIm						
Experimental	130.5	54.4	-	27.4	339	44.1

[a] Calculations performed on $[Zn(Im)_{1.5}(5\text{-ClbIm})_{0.5}]$ while experimental isotherms were measured on $[Zn(Im)_{1.0}(5\text{-ClbIm})_{1.0}]$.

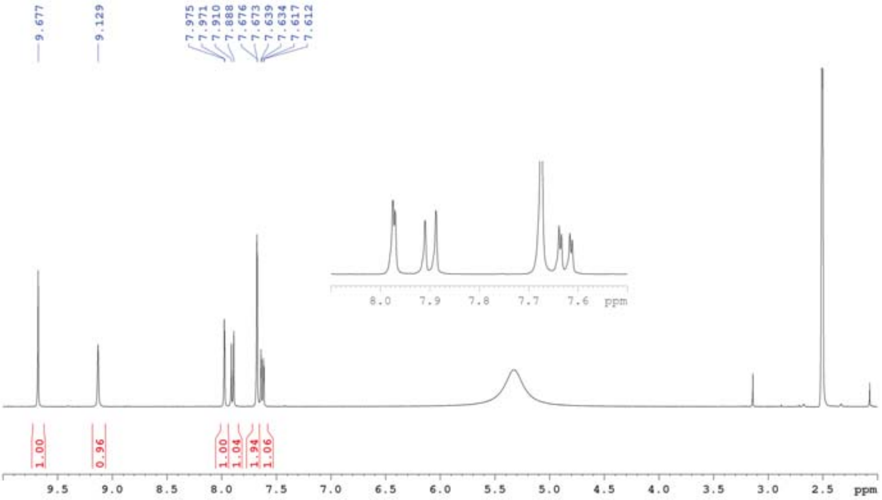

Supplementary Figure 21. ^{1}H NMR spectrum of ZIF-76, [Zn(Im)$_{1.0}$(5-ClbIm)$_{1.0}$], digested in DCl/DMSO-d$_6$. NMR peak assignments: ^{1}H NMR (500 MHz, DMSO-d_6): (Zn(Im)$_{1.0}$(5-ClbIm)$_{1.0}$). 2.5 (DMSO-d$_6$), 7.63 (CC***H***CH$_{\mathrm{ClbIm}}$), 7.67 (C***H***C***H***N$_{\mathrm{Im}}$), 7.90 (CCHC***H***$_{\mathrm{ClbIm}}$), 7.97 (ClCC***H***CC$_{\mathrm{ClbIm}}$), 9.13 (NC***H***N$_{\mathrm{Im}}$), 9.68 (NC***H***N$_{\mathrm{ClbIm}}$).

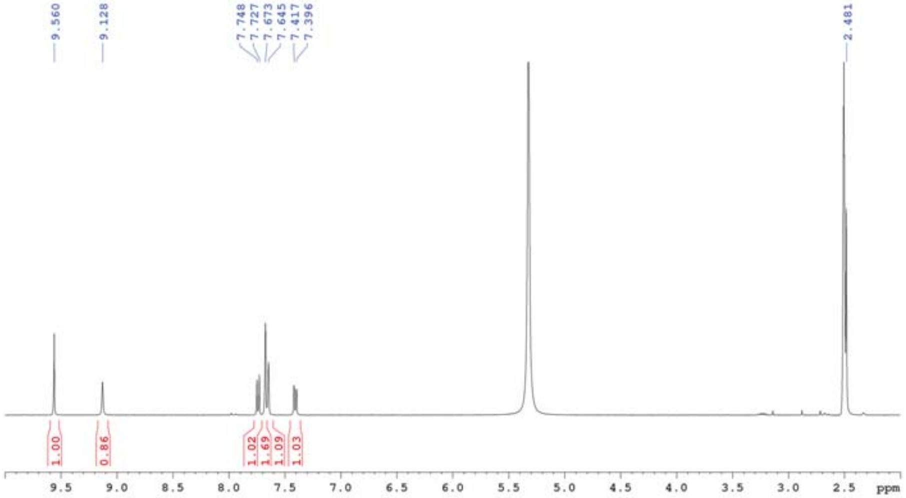

Supplementary Figure 22. ^{1}H NMR spectrum of ZIF-76-mbIm, [Zn(Im)$_{0.93}$(5-mbIm)$_{1.07}$], digested in DCl/DMSO-d$_6$. NMR peak assignments: (Zn(Im)$_{0.93}$(mbIm)$_{1.07}$). ^{1}H NMR (500 MHz, DMSO-d_6): 2.48 (C***H***$_{\mathrm{3mbIm}}$), 2.5 (DMSO-d$_6$), 7.40 (CC***H***CH$_{\mathrm{mbIm}}$), 7.65 (CC***H***C(CH$_3$)$_{\mathrm{mbIm}}$), 7.67 (C***H***NC***H***$_{\mathrm{Im}}$), 7.73 (CCHC***H***$_{\mathrm{mbIm}}$), 9.13 (NC***H***N$_{\mathrm{Im}}$), 9.56 (NC***H***N$_{\mathrm{mbIm}}$).

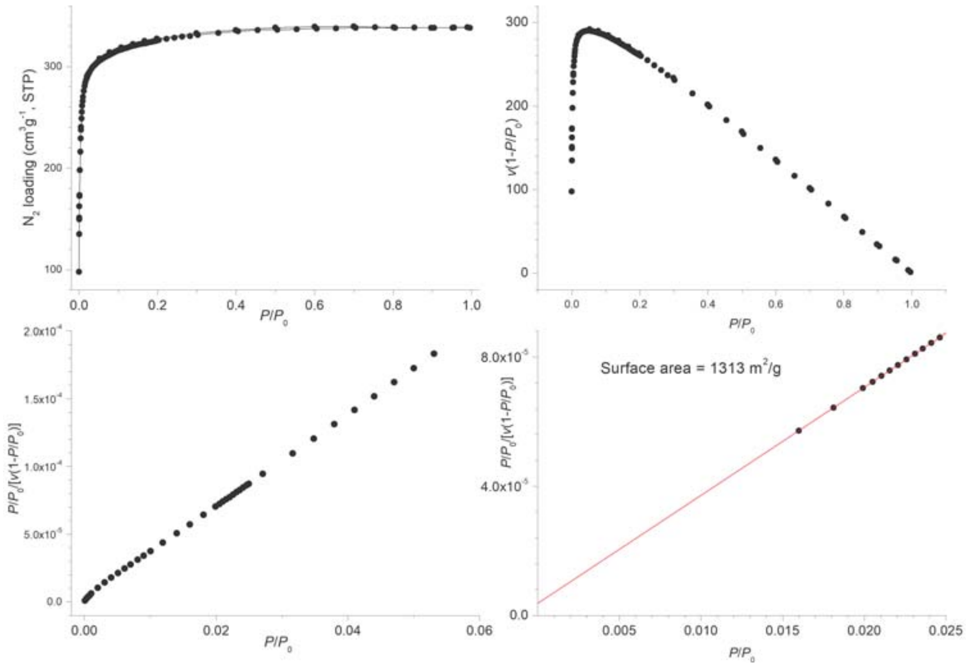

Supplementary Figure 23. N_2 adsorption isotherm at 77 K and BET surface area plots for ZIF-76, $[Zn(Im)_{1.0}(5\text{-ClbIm})_{1.0}]$.

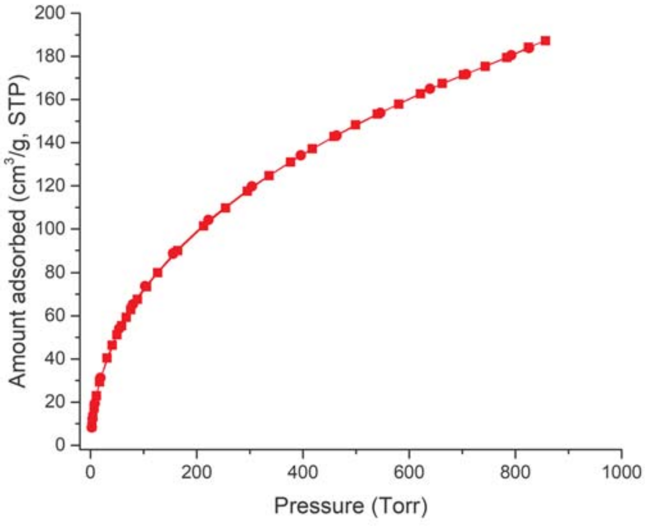

Supplementary Figure 24. H_2 adsorption isotherm at 77 K for ZIF-76, $[Zn(Im)_{1.0}(5\text{-ClbIm})_{1.0}]$ (circles = adsorption; squares = desorption).

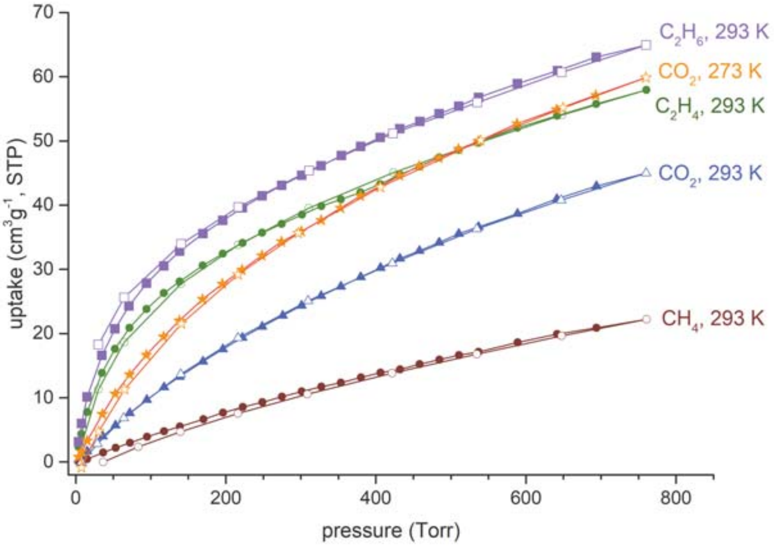

Supplementary Figure 25. Gas adsorption isotherms at 273K and 293 K for ZIF-76, [Zn(Im)$_{1.0}$(5-ClbIm)$_{1.0}$] (filled symbols = adsorption; empty = desorption).

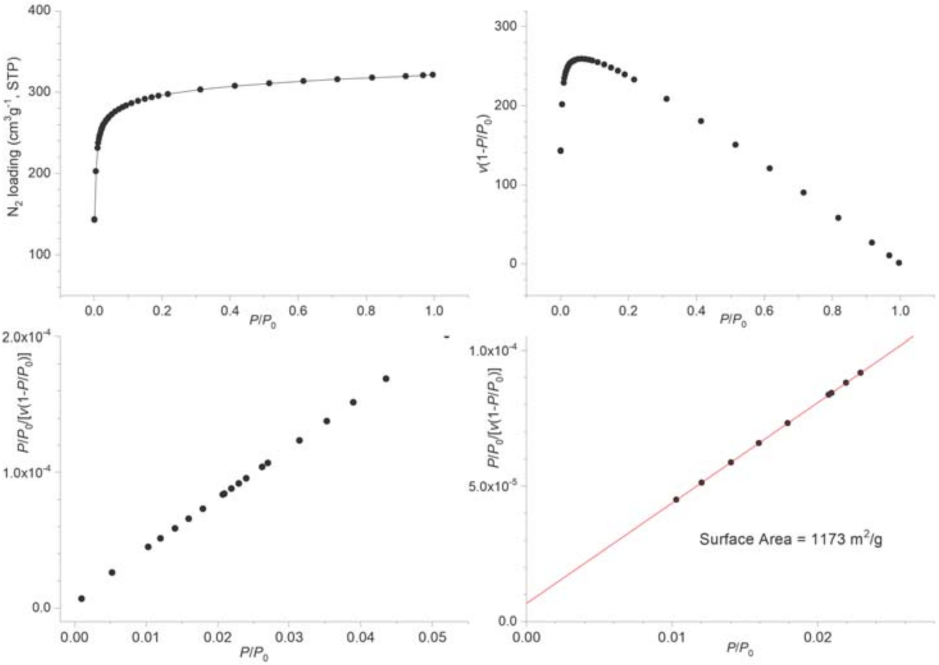

Supplementary Figure 26. N_2 adsorption isotherm at 77 K and BET surface area plots for ZIF-76-mbIm, [Zn(Im)$_{0.93}$(5-mbIm)$_{1.07}$].

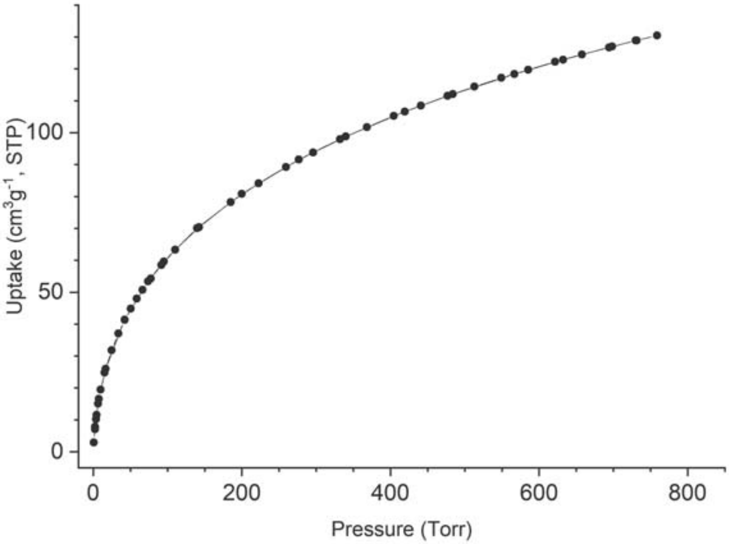

Supplementary Figure 27. H_2 adsorption isotherm at 77 K for ZIF-76-mbIm, $[Zn(Im)_{0.93}(5\text{-}mbIm)_{1.07}]$.

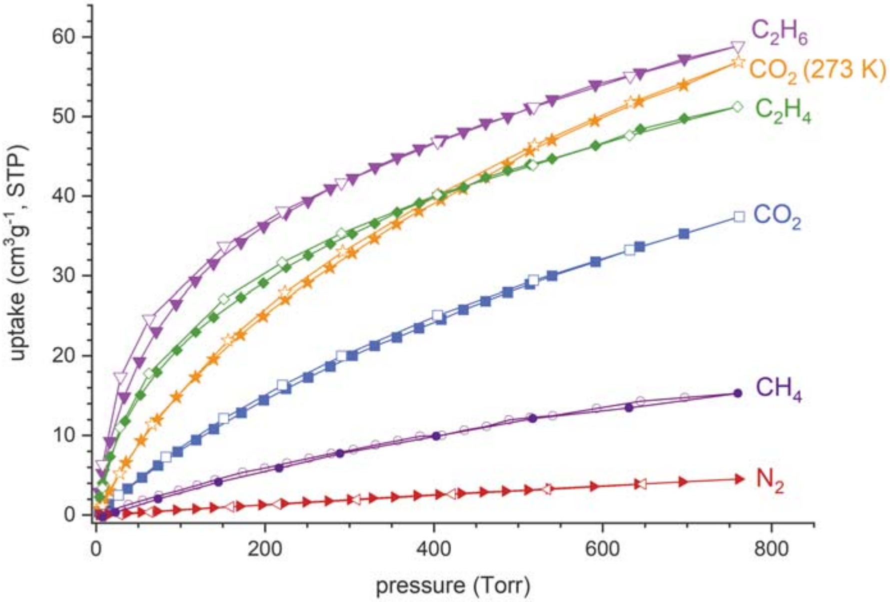

Supplementary Figure 28. Gas adsorption isotherms at 293 K (and 273 K where indicated) for ZIF-76-mbIm, $[Zn(Im)_{0.93}(5\text{-}mbIm)_{1.07}]$ (filled symbols = adsorption; empty = desorption).

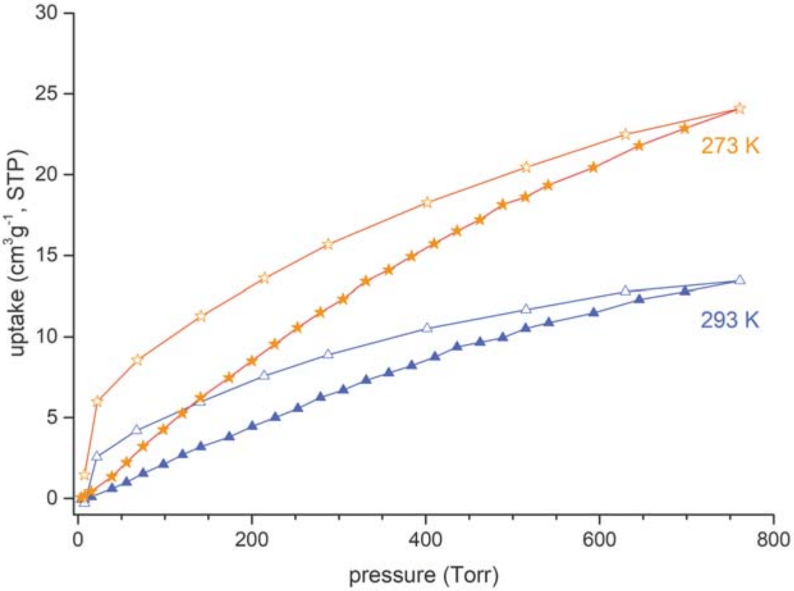

Supplementary Figure 29. CO_2 adsorption isotherms at 273K and 293 K for *a*$_g$ZIF-76, [Zn(Im)$_{1.0}$(5-ClbIm)$_{1.0}$] (filled symbols = adsorption; empty = desorption).

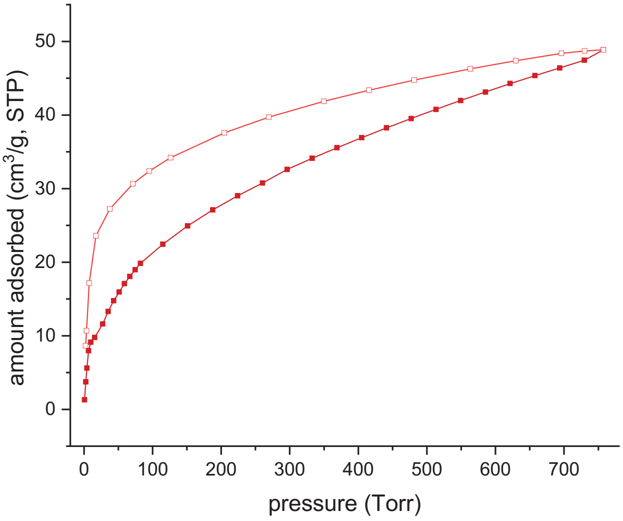

Supplementary Figure 30. H_2 adsorption isotherm for *a*$_g$ZIF-76-mbIm, [Zn(Im)$_{0.93}$(5-mbIm)$_{1.07}$], at 77 K (filled symbols = adsorption; empty = desorption).

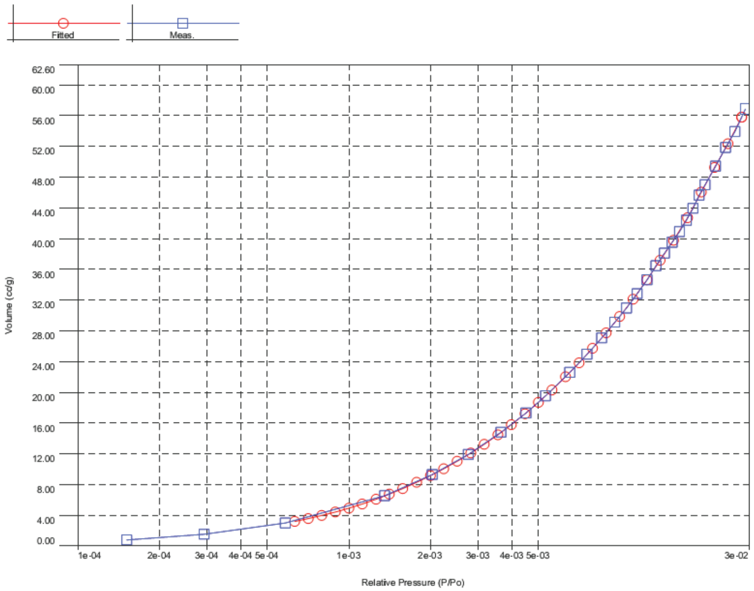

Supplementary Figure 31. NLDFT fitting of the CO_2 adsorption isotherm at 273 K of ZIF-76-mbIm, $[Zn(Im)_{0.93}(5\text{-}mbIm)_{1.07}]$.

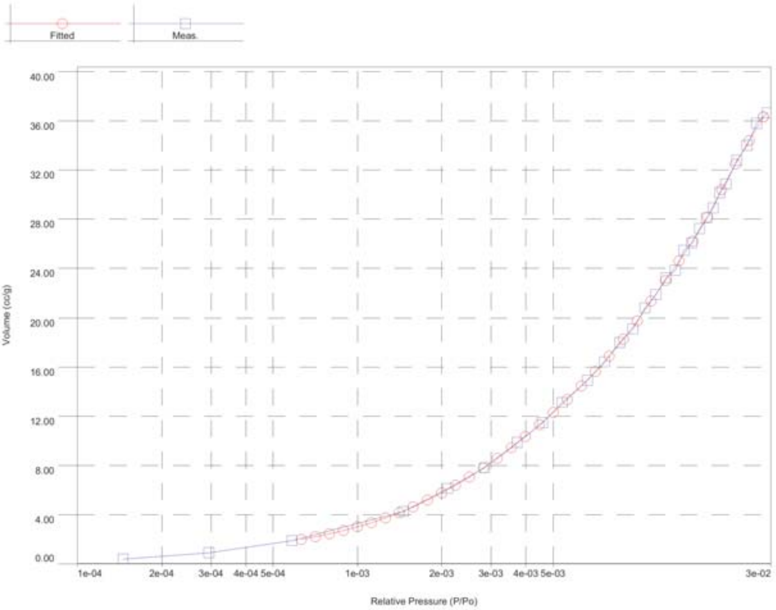

Supplementary Figure 32. NLDFT fitting of the CO_2 adsorption isotherm at 273 K of a_gZIF-76-mbIm, $[Zn(Im)_{0.93}(5\text{-}mbIm)_{1.07}]$.

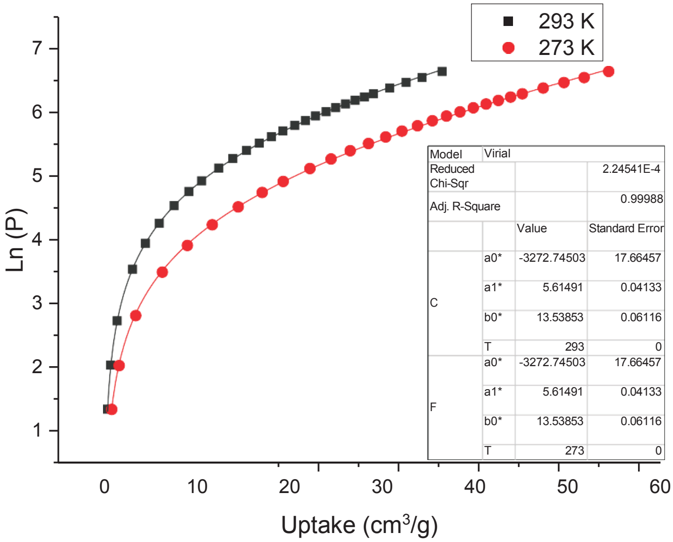

Model	Virial		
Reduced Chi-Sqr			2.24541E-4
Adj. R-Square			0.99988
		Value	Standard Error
C	a0*	-3272.74503	17.66457
	a1*	5.61491	0.04133
	b0*	13.53853	0.06116
	T	293	0
F	a0*	-3272.74503	17.66457
	a1*	5.61491	0.04133
	b0*	13.53853	0.06116
	T	273	0

Supplementary Figure 33. Virial fitting of CO_2 adsorption isotherms at 273 K and 293 K for ZIF-76-mbIm, $[Zn(Im)_{0.93}(5\text{-mbIm})_{1.07}]$, used to calculate the isosteric heat of adsorption (Q_{st}).

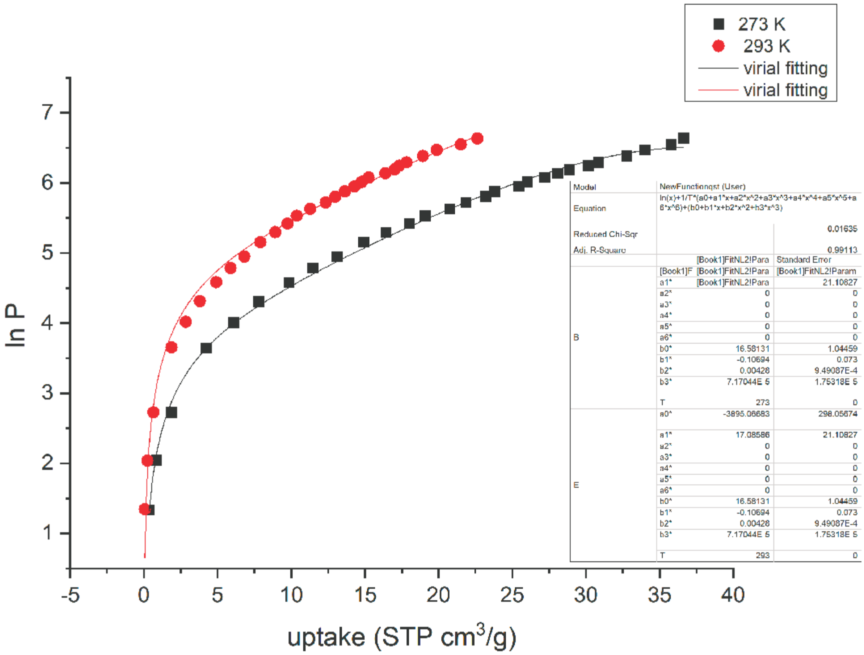

Model	NewFunctionqst (User)		
Equation	ln(x)+1/T*(a0+a1*x+a2*x^2+a3*x^3+a4*x^4+a5*x^5+a6*x^6)+(b0+b1*x+b2*x^2+h3*x^3)		
Reduced Chi-Sqr			0.01635
Adj. R-Square			0.99113
		[Book1]FitNL2!Para	Standard Error
B	[Book1]F	[Book1]FitNL2!Para	[Book1]FitNL2!Param
	a1*	[Book1]FitNL2!Para	21.10827
	a2*	0	0
	a3*	0	0
	a4*	0	0
	a5*	0	0
	a6*	0	0
	b0*	16.58131	1.04459
	b1*	-0.10694	0.073
	b2*	0.00428	9.49087E-4
	b3*	7.17044E 5	1.75318E 5
	T	273	0
E	a0*	-3895.06683	298.05674
	a1*	17.08586	21.10827
	a2*	0	0
	a3*	0	0
	a4*	0	0
	a5*	0	0
	a6*	0	0
	b0*	16.58131	1.04459
	b1*	-0.10694	0.073
	b2*	0.00428	9.49087E-4
	h3*	7.17044E 5	1.75318E 5
	T	293	0

Supplementary Figure 34. Virial fitting of the CO_2 adsorption isotherms at 273 K and 298 K for a_gZIF-76-mbIm, $[Zn(Im)_{0.93}(5\text{-mbIm})_{1.07}]$, used to calculate the isosteric heat of adsorption (Q_{st}).

6. Simulated Gas Adsorption Isotherms

In GCMC simulations, Lennard-Jones (LJ) 12-6 and Coulomb potentials were used to model repulsion-dispersion forces and electrostatic interactions, respectively. The Lorentz-Berthelot mixing rules were used to calculate adsorbent-adsorbate and adsorbate-adsorbate LJ cross interaction parameters. Molecular simulations were performed for 10,000 cycles with the first 5,000 cycles for initialization and the last 5,000 cycles for taking ensemble averages. Three different types of moves including translation, reinsertion and swap of a molecule were considered for spherical molecules. Rotation move was also applied for non-spherical molecules. The cut-off distance was set to 12.8 Å for truncation of the intermolecular interactions and simulation cell lengths were increased to at least 26 Å along each dimension. Periodic boundary conditions were applied in all simulations. Peng-Robinson equation of state was used to convert the pressure to the corresponding fugacity. All molecular simulations were performed using a rigid framework. More details of these simulations can be found in the literature.[1,2]

Single-site spherical Lennard-Jones (LJ) 12-6 potential was used to model H_2,[3] Ar,[4] and CH_4.[5] CO_2 was modeled as a three site linear molecule with three charged LJ interaction sites located at each atom using the EPM2 potential[6]. Similarly, N_2 (O_2) was modeled as a three site molecule with two sites located at two N (O) atoms and the third one located at its center of mass (COM) with partial point charges and the potential parameters of N_2 and O_2 were taken from the literature.[7] The interaction potential parameters for gas molecules were given in Supplementary Table 3. The atomic charges of ZIF-76 were estimated using charge equilibration method as implemented in RASPA simulation code.[8] The Ewald summation method was used to calculate electrostatic interactions. The potential parameters of ZIF-76 atoms were taken from the Dreiding force field.[9] These potentials and force fields were selected based on the results of previous studies which showed good agreement between simulation results and experimentally measured gas uptake data of ZIFs.[10,11]

In order to compare simulation results with the experimentally measured gas uptake data, the absolute gas amount (N_{abs}) obtained directly from GCMC simulations were converted to the excess gas amount (N_{ex}) as follows:

$$N_{ex} = N_{abs} - \rho_g \cdot V_g \qquad (1)$$

where ρ_g is the density of adsorbates in gas phase obtained from the Peng-Robinson equation of state and V_g is the pore volume of ZIF-76.

RASPA was used to compute gas adsorption isotherms. Zeo++ software[12] was used to compute physical properties of ZIF-76 such as density, pore limiting diameter (PLD), the largest cavity diameter (LCD) and pore volume. The accessible pore volume is defined as the volume reachable by the center of the probe and calculated using a Monte Carlo integration technique. Pore volume calculations were performed using a probe radius of 0 Å.

The structure of ZIF-76 is highly disordered, where imidazolate (Im) linker positions are partially occupied by chlorobenzimidazolate (cbIm). The disorder was removed manually to give the literature[13] linker ratio of cbIm/Im = 1/3. The geometry was then optimized prior to molecular simulations. Steepest descent minimization was performed using the Forcite module of Materials Studio 8.0.[14] Note: Perez-Pellitero *et al.*[13] examined different possibilities for the position and orientation of the organic linkers using different configurations and they showed that adsorption results were not affected dramatically.

Cif file for ZIF-76 used as input for molecular simulations

```
data_zif76edited
_symmetry_cell_setting           triclinic
_symmetry_space_group_name_H-M   'P 1'
_symmetry_Int_Tables_number      1
_space_group_name_Hall           'P 1'
loop_
_symmetry_equiv_pos_site_id
_symmetry_equiv_pos_as_xyz
1 x,y,z
_cell_length_a                   22.6702
_cell_length_b                   22.6702
_cell_length_c                   22.6702
_cell_angle_alpha                90.0000
_cell_angle_beta                 90.0000
_cell_angle_gamma                90.0000
_cell_volume                     11651.1
loop_
_atom_site_label
_atom_site_type_symbol
_atom_site_fract_x
_atom_site_fract_y
_atom_site_fract_z
C1 C 0.00624 0.27237 0.27158
H18 H 0.01567 0.23907 0.23874
Zn92 Zn 0.00118 0.18339 0.36792
Zn96 Zn 0.00068 0.36786 0.18137
C6 C 0.15785 0.11609 0.31263
C7 C 0.11376 0.15787 0.30965
N8 N 0.14062 0.07252 0.34907
N9 N 0.06869 0.14037 0.34400
C10 C 0.08624 0.08840 0.36712
H22 H 0.06036 0.06328 0.39835
H23 H 0.19993 0.11768 0.29023
H24 H 0.11544 0.19925 0.28600
C11 C 0.15750 0.31163 0.11432
C12 C 0.11339 0.30905 0.15617
N13 N 0.06853 0.34371 0.13869
N14 N 0.14047 0.34814 0.07075
C15 C 0.08622 0.36659 0.0866
H19 H 0.19945 0.28895 0.11584
```

H20	H	0.11490	0.28535	0.19753
H21	H	0.06056	0.39799	0.06154
N16	N	0.01092	0.45115	0.18872
Zn40	Zn	0.18223	0.00229	0.36786
N17	N	0.01173	0.19055	0.45112
Zn34	Zn	0.18179	0.36778	0.00059
C25	C	-0.00001	0.72589	0.72766
C30	C	0.01842	0.49797	0.82619
C31	C	0.01700	0.82425	0.49919
H37	H	0.06306	0.49856	0.84303
H38	H	0.06190	0.84037	0.50021
H39	H	0.00351	0.76003	0.76080
N35	N	0.06630	0.65209	0.86226
N36	N	0.06708	0.85706	0.65112
C2	C	0.98518	0.35477	0.31055
C3	C	0.98550	0.31246	0.35356
N4	N	0.99863	0.33049	0.25808
N5	N	0.99914	0.25975	0.32997
N47	N	0.81284	0.01310	0.55259
C53	C	0.66771	0.40979	0.02191
C54	C	0.96875	0.32515	0.41146
C55	C	0.58208	0.01750	0.32801
C56	C	0.58628	0.31617	0.03347
C57	C	0.66946	0.02585	0.41599
C58	C	0.96812	0.41271	0.32244
C59	C	0.88934	0.30903	0.15556
C60	C	0.84584	0.11584	0.30832
C61	C	0.69032	0.15293	0.11122
C62	C	0.69200	0.11025	0.15445
C63	C	0.88925	0.15842	0.31021
C64	C	0.84615	0.30671	0.11278
C65	C	0.79881	0.06785	0.53485
C66	C	0.46564	0.06532	0.20259
C67	C	0.79021	0.53139	0.06728
C68	C	0.79099	0.47106	0.06785
C69	C	0.52593	0.06642	0.20274
C70	C	0.79953	0.07006	0.47462
C71	C	0.56657	0.03311	0.38579
C72	C	0.61018	0.03816	0.42954
C73	C	0.95201	0.42704	0.38053
C74	C	0.95226	0.38346	0.42495
C75	C	0.56915	0.37419	0.04661
C76	C	0.60929	0.42111	0.03950
Cl77	Cl	0.58634	0.49369	0.05341
Cl78	Cl	0.59043	0.06237	0.50028
Cl79	Cl	0.92989	0.40177	0.49670
N80	N	0.86130	0.07156	0.34455
N81	N	0.65571	0.06613	0.13869
N82	N	0.93180	0.14095	0.34776
N83	N	0.93141	0.34732	0.13851
N84	N	0.86117	0.34343	0.06874
N85	N	0.65283	0.13561	0.06856
N86	N	0.80935	0.55053	0.01461
N87	N	0.44713	0.01162	0.18579
N88	N	0.81208	0.01619	0.45328
N89	N	0.80862	0.45121	0.01481
N90	N	0.54646	0.01288	0.18766

Zn93	Zn	0.81578	0.36799	0.00296
Zn94	Zn	0.81633	0.00596	0.36966
Zn95	Zn	0.62993	0.00128	0.18358
C100	C	0.63288	0.08259	0.08629
C101	C	0.91374	0.08790	0.36755
C102	C	0.91320	0.36716	0.08549
H131	H	0.54792	0.01021	0.29629
H132	H	0.55553	0.28063	0.03959
H133	H	0.69722	0.44589	0.01417
H134	H	0.96699	0.29150	0.44492
H135	H	0.88930	0.19991	0.28664
H136	H	0.52453	0.38284	0.06131
H137	H	0.55351	0.10371	0.21395
H138	H	0.78979	0.10429	0.56428
H139	H	0.79042	0.10833	0.44763
H140	H	0.71607	0.11228	0.19559
H141	H	0.96573	0.44576	0.28853
H142	H	0.52072	0.04098	0.39665
H143	H	0.43670	0.10180	0.21299
H144	H	0.80484	0.11799	0.28402
H145	H	0.80555	0.28171	0.11461
H146	H	0.77798	0.55988	0.10354
H147	H	0.88964	0.28514	0.19686
H148	H	0.71397	0.19437	0.11133
H149	H	0.70160	0.02672	0.45042
H150	H	0.77887	0.44299	0.10448
H151	H	0.93853	0.47168	0.39089
H153	H	0.93647	0.40033	0.06030
H154	H	0.60011	0.05734	0.06252
H155	H	0.93738	0.06246	0.40026
C165	C	0.68461	0.35122	0.01289
C166	C	0.64432	0.30645	0.01545
N167	N	0.67053	0.25477	0.00327
N168	N	0.73895	0.32910	0.00277
C326	C	0.72562	0.00060	0.27442
C327	C	0.64177	0.01085	0.31450
C328	C	0.68422	0.01382	0.35730
N329	N	0.73814	0.00672	0.33307
N330	N	0.66686	0.00295	0.26128
C103	C	0.26919	0.00696	0.26937
N107	N	0.25869	0.00120	0.32843
C108	C	0.17748	0.01999	0.50100
H152	H	0.23492	0.01702	0.23775
H162	H	0.16151	0.06495	0.50160
Zn369	Zn	0.36411	0.00003	0.17704
C109	C	0.27249	0.27193	0.00202
C114	C	0.49981	0.17672	0.01827
C115	C	0.17644	0.50042	0.02109
H159	H	0.16295	0.49989	0.06686
H161	H	0.49869	0.16521	0.06456
H163	H	0.23928	0.23839	0.00895
C41	C	0.72862	0.00405	0.73058
C46	C	0.49801	0.01782	0.82082
H51	H	0.49781	0.06303	0.83611
H52	H	0.76027	0.01379	0.76492
Zn256	Zn	0.82051	0.00021	0.63557
C121	C	0.30957	0.15688	0.10867

C122	C	0.30593	0.11291	0.15060
N123	N	0.34037	0.06768	0.13371
N124	N	0.34648	0.13942	0.06557
C125	C	0.36415	0.08503	0.08193
H156	H	0.39572	0.05903	0.05736
H157	H	0.28182	0.11483	0.19171
H158	H	0.28741	0.19910	0.10996
Zn127	Zn	0.17838	0.63354	0.00115
Zn252	Zn	0.81873	0.63335	0.00226
N49	N	0.65144	0.06767	0.85994
N50	N	0.86331	0.06753	0.66033
Zn91	Zn	0.63342	0.17803	0.99950
C97	C	0.82077	0.50070	0.98348
C164	C	0.72839	0.27007	0.99689
H270	H	0.76295	0.23816	0.98895
H271	H	0.83838	0.50047	0.93913
C110	C	0.35501	0.31270	0.98511
C111	C	0.31244	0.35535	0.98834
N112	N	0.25942	0.33065	0.99860
N113	N	0.33090	0.25908	0.99442
C169	C	0.41318	0.32685	0.97017
C170	C	0.31815	0.03715	0.59135
C171	C	0.04457	0.40813	0.68842
C172	C	0.32581	0.41472	0.97901
C173	C	0.03167	0.32811	0.59378
C174	C	0.40660	0.03633	0.67945
C175	C	0.30721	0.10763	0.84358
C176	C	0.10987	0.15089	0.69504
C177	C	0.15225	0.30497	0.89225
C178	C	0.10917	0.30677	0.84944
C179	C	0.15260	0.10766	0.69256
C180	C	0.30532	0.15104	0.88613
C181	C	0.19989	0.53159	0.93524
C182	C	0.53205	0.19639	0.93189
C183	C	0.06611	0.20344	0.47070
C184	C	0.47184	0.19517	0.93015
C185	C	0.06651	0.20124	0.53092
C186	C	0.19910	0.47132	0.93430
C187	C	0.05577	0.38436	0.58407
C188	C	0.42637	0.38560	0.95531
C189	C	0.38293	0.42950	0.96055
C190	C	0.41955	0.05655	0.62233
C191	C	0.37554	0.05692	0.57834
C192	C	0.06388	0.42364	0.63154
Cl193	Cl	0.39207	0.08391	0.50774
Cl194	Cl	0.10082	0.49063	0.61999
Cl195	Cl	0.49618	0.40423	0.92769
N196	N	0.06688	0.34485	0.86634
N197	N	0.13674	0.34178	0.93602
N198	N	0.34180	0.13573	0.93026
N199	N	0.13554	0.06578	0.65407
N200	N	0.34503	0.06525	0.86092
N201	N	0.06584	0.13607	0.65822
N202	N	0.18561	0.55045	0.98954
N203	N	0.55028	0.18470	0.98702
N204	N	0.18600	0.45114	0.98850
N205	N	0.01192	0.18880	0.55046

N206	N	0.45094	0.18474	0.98464
Zn207	Zn	0.36736	0.18086	0.99546
Zn208	Zn	0.00033	0.18196	0.63378
C210	C	0.08254	0.08412	0.63428
C211	C	0.36494	0.08338	0.91387
C212	C	0.08464	0.36504	0.91924
H281	H	0.06904	0.39703	0.53997
H282	H	0.20847	0.44351	0.89668
H283	H	0.39356	0.47501	0.95069
H284	H	0.46343	0.07261	0.61241
H285	H	0.06120	0.39833	0.94411
H287	H	0.39791	0.05993	0.93915
H289	H	0.05738	0.06105	0.60095
H309	H	0.10418	0.20897	0.55918
H310	H	0.43985	0.03811	0.71329
H311	H	0.28351	0.10746	0.80217
H312	H	0.44742	0.29458	0.96885
H313	H	0.11175	0.19140	0.72017
H314	H	0.29452	0.44922	0.98638
H315	H	0.19318	0.28051	0.89050
H316	H	0.10918	0.28285	0.80816
H317	H	0.05191	0.43755	0.72499
H318	H	0.19389	0.10723	0.71646
H319	H	0.28092	0.19199	0.88404
H320	H	0.20922	0.56028	0.89828
H321	H	0.10356	0.21235	0.44253
H322	H	0.28408	0.03968	0.55841
H323	H	0.56113	0.20421	0.89489
H324	H	0.02401	0.29954	0.55699
H325	H	0.44455	0.20268	0.89174
C424	C	0.30689	0.01622	0.64817
C425	C	0.34968	0.01582	0.69068
C454	C	0.01683	0.31226	0.65138
C455	C	0.01995	0.35223	0.69639
N456	N	0.00140	0.25883	0.67262
N457	N	0.00272	0.32701	0.74710
C261	C	0.68838	0.11087	0.84270
C262	C	0.69235	0.15238	0.88701
N263	N	0.65812	0.13508	0.93222
C264	C	0.63417	0.08350	0.91457
H273	H	0.71031	0.11252	0.80038
H274	H	0.60265	0.05878	0.94049
H277	H	0.71633	0.19359	0.88531
C265	C	0.84076	0.31135	0.88985
C266	C	0.88509	0.30742	0.84837
N267	N	0.93032	0.34158	0.86573
N268	N	0.85799	0.34820	0.93311
C269	C	0.91262	0.36556	0.91729
H278	H	0.93864	0.39686	0.94219
H279	H	0.88349	0.28324	0.80728
H280	H	0.79850	0.28930	0.88823
Zn33	Zn	0.99846	0.36479	0.82327
C116	C	0.72909	0.72978	0.01197
N119	N	0.67158	0.74347	0.00082
N120	N	0.74304	0.67232	0.00077
H160	H	0.76113	0.76214	0.02597
Zn253	Zn	0.63301	0.81944	0.00346

N126	N	0.55009	0.80998	0.01336
N129	N	0.65593	0.86261	0.07133
N130	N	0.86566	0.65987	0.06606
C98	C	0.49740	0.98058	0.17610
C99	C	0.82170	0.98256	0.50185
H406	H	0.75939	0.99526	0.24115
H407	H	0.83509	0.93678	0.50032
H408	H	0.49826	0.93543	0.16069
C104	C	0.31238	0.98759	0.35008
C105	C	0.35212	0.98264	0.30503
N106	N	0.32643	0.99701	0.25361
C331	C	0.41043	0.66857	0.01989
C332	C	0.32870	0.97635	0.40835
C333	C	0.03186	0.59503	0.32953
C334	C	0.31719	0.58753	0.03672
C335	C	0.04394	0.68993	0.40940
C336	C	0.40841	0.95927	0.31405
C337	C	0.30679	0.88842	0.15094
C338	C	0.10845	0.85080	0.30806
C339	C	0.15551	0.68997	0.11404
C340	C	0.11275	0.69264	0.15723
C341	C	0.15154	0.89361	0.30582
C342	C	0.30522	0.84522	0.10817
C343	C	0.53026	0.79196	0.06616
C344	C	0.06507	0.47067	0.20244
C345	C	0.20427	0.93435	0.53007
C346	C	0.20415	0.93514	0.46979
C347	C	0.46996	0.79220	0.06575
C348	C	0.06515	0.53089	0.20177
C349	C	0.37550	0.57159	0.05089
C350	C	0.06309	0.63322	0.42524
C351	C	0.42216	0.61135	0.04052
C352	C	0.05585	0.58556	0.38595
C353	C	0.42444	0.94334	0.37185
C354	C	0.38535	0.95368	0.41907
Cl355	Cl	0.49178	0.90758	0.38502
Cl356	Cl	0.39011	0.50364	0.08486
Cl357	Cl	0.07742	0.51440	0.40736
N358	N	0.34221	0.86058	0.06448
N359	N	0.06758	0.65788	0.14103
N360	N	0.13712	0.65344	0.07097
N361	N	0.06647	0.86767	0.34652
N362	N	0.13645	0.93745	0.34272
N363	N	0.34490	0.93075	0.13418
N364	N	0.18739	0.98740	0.55023
N365	N	0.01058	0.55060	0.18938
N366	N	0.18886	0.98925	0.45093
N367	N	0.45083	0.80881	0.01213
Zn368	Zn	0.00024	0.63446	0.18370
Zn369	Zn	0.36411	1.00003	0.17704
C373	C	0.08348	0.63503	0.08846
C374	C	0.08453	0.92062	0.36652
C375	C	0.36537	0.91277	0.08137
H385	H	0.28140	0.55761	0.04562
H386	H	0.10812	0.80961	0.28397
H387	H	0.28059	0.80439	0.10981
H388	H	0.10255	0.44248	0.21117

H389	H	0.21466	0.89697	0.55784
H390	H	0.02455	0.55832	0.30072
H391	H	0.55826	0.78074	0.10312
H392	H	0.21488	0.89860	0.44104
H393	H	0.44139	0.78063	0.10218
H394	H	0.19756	0.71250	0.11432
H395	H	0.39843	0.94308	0.46377
H396	H	0.10268	0.55905	0.21047
H397	H	0.46720	0.59838	0.04968
H398	H	0.19217	0.89187	0.28086
H399	H	0.30007	0.98573	0.44480
H400	H	0.43770	0.95022	0.27778
H401	H	0.05065	0.72626	0.43914
H402	H	0.11520	0.71659	0.19843
H403	H	0.44642	0.69784	0.01061
H404	H	0.28251	0.88857	0.19202
H405	H	0.08267	0.62609	0.46821
H415	H	0.06131	0.94563	0.39986
H416	H	0.05697	0.60371	0.06409
H417	H	0.39858	0.93631	0.05648
C419	C	0.35175	0.68473	0.01072
C420	C	0.30714	0.64446	0.01539
N421	N	0.25520	0.67029	0.00320
C468	C	0.01936	0.69767	0.35351
C469	C	0.01621	0.65247	0.31376
N470	N	0.00154	0.74820	0.32834
C25	C	0.99999	0.72589	0.72766
C26	C	0.99260	0.64161	0.68788
C27	C	0.99091	0.68366	0.64462
N28	N	0.99775	0.66723	0.74124
N29	N	0.99620	0.73781	0.66868
C42	C	0.64804	0.98423	0.68729
C43	C	0.69294	0.98153	0.64719
N44	N	0.74416	0.99614	0.67300
N45	N	0.66976	0.99695	0.74125
C117	C	0.69205	0.64985	0.98053
C118	C	0.64926	0.69231	0.98071
C213	C	0.68191	0.59384	0.95714
C214	C	0.98202	0.66836	0.58551
C215	C	0.58987	0.97250	0.67071
C216	C	0.59309	0.68162	0.95787
C217	C	0.68402	0.96093	0.58989
C218	C	0.98782	0.58170	0.67444
C219	C	0.88537	0.69012	0.84558
C220	C	0.84548	0.88832	0.69206
C221	C	0.69097	0.84571	0.89203
C222	C	0.69283	0.88839	0.84873
C223	C	0.88794	0.84486	0.69362
C224	C	0.84197	0.68779	0.88817
C225	C	0.93254	0.79716	0.46718
C226	C	0.46812	0.93228	0.79465
C227	C	0.93451	0.46666	0.79662
C228	C	0.52838	0.93200	0.79637
C229	C	0.93343	0.52693	0.79739
C230	C	0.93164	0.79587	0.52746
C231	C	0.97512	0.56556	0.61613
C232	C	0.57928	0.95231	0.61299

C233	C	0.62651	0.94526	0.57318
C234	C	0.62540	0.58136	0.93493
C235	C	0.97133	0.60879	0.57187
C236	C	0.58101	0.62500	0.93546
Cl237	Cl	0.51099	0.60900	0.90671
Cl238	Cl	0.95073	0.58804	0.50030
Cl239	Cl	0.50725	0.93513	0.59055
N240	N	0.93202	0.86041	0.65721
N241	N	0.86289	0.93092	0.65454
N242	N	0.65586	0.93220	0.86377
N243	N	0.65271	0.86259	0.93418
N244	N	0.93026	0.65527	0.86248
N245	N	0.85955	0.65125	0.93154
N246	N	0.98766	0.44788	0.81476
N247	N	0.98594	0.81507	0.44885
N248	N	0.44846	0.98594	0.81015
N249	N	0.98506	0.81123	0.54808
N250	N	0.54781	0.98603	0.81120
N251	N	0.98648	0.54722	0.81446
Zn254	Zn	0.99686	0.81551	0.63139
Zn255	Zn	0.99719	0.63075	0.81934
Zn257	Zn	0.63112	0.99773	0.81812
C258	C	0.91339	0.63253	0.91482
C259	C	0.63241	0.91542	0.91592
C260	C	0.91575	0.91290	0.63442
H272	H	0.59916	0.94045	0.93926
H275	H	0.94107	0.93659	0.60164
H276	H	0.93940	0.60124	0.93974
H286	H	0.71615	0.56101	0.95481
H288	H	0.98251	0.70034	0.55082
H290	H	0.55346	0.98001	0.69987
H291	H	0.71518	0.80459	0.89235
H292	H	0.55994	0.71557	0.95614
H293	H	0.80019	0.71083	0.88745
H294	H	0.89834	0.43790	0.78475
H295	H	0.99447	0.54783	0.70658
H296	H	0.80413	0.88843	0.71587
H297	H	0.43999	0.89517	0.78429
H298	H	0.61846	0.92863	0.52914
H299	H	0.88582	0.80376	0.71775
H300	H	0.71774	0.88666	0.80807
H301	H	0.55673	0.89484	0.78677
H302	H	0.88350	0.71389	0.80426
H303	H	0.89652	0.55468	0.78538
H304	H	0.89454	0.78385	0.55495
H305	H	0.96856	0.51952	0.60525
H306	H	0.61624	0.53814	0.91681
H307	H	0.89614	0.78676	0.43815
H308	H	0.71992	0.95471	0.55953
C376	C	0.68689	0.88801	0.16038
C377	C	0.69026	0.84580	0.11670
N378	N	0.65022	0.93114	0.14259
C379	C	0.63241	0.91458	0.08833
H410	H	0.70913	0.88702	0.20257
H411	H	0.60111	0.93925	0.06211
H414	H	0.71425	0.80465	0.11887
C380	C	0.88453	0.85113	0.30763

C381	C	0.84060	0.89311	0.31131
N382	N	0.92963	0.86776	0.34235
N383	N	0.85796	0.93600	0.34852
C384	C	0.91226	0.91945	0.36632
H409	H	0.93819	0.94384	0.39808
H412	H	0.88269	0.81018	0.28322
H413	H	0.79848	0.89202	0.28895
Zn32	Zn	0.99746	0.82460	0.36596
Zn48	Zn	0.36526	0.99609	0.81833
Zn128	Zn	0.17861	0.99670	0.63339
Zn370	Zn	0.36783	0.81531	0.99936
C372	C	0.50070	0.82070	0.98131
C418	C	0.27028	0.72792	0.99485
N422	N	0.32933	0.73865	0.99957
H441	H	0.23818	0.76227	0.98675
H452	H	0.50105	0.83761	0.93668
C423	C	0.26868	0.98914	0.72919
N426	N	0.32666	0.99832	0.74243
N427	N	0.25504	0.99898	0.67142
H451	H	0.23614	0.97707	0.76191
C433	C	0.15088	0.69321	0.88933
C434	C	0.10899	0.68971	0.84533
N435	N	0.13438	0.65799	0.93410
C436	C	0.08280	0.63394	0.91646
H445	H	0.11006	0.71234	0.80334
H448	H	0.19179	0.71768	0.88767
H449	H	0.05868	0.60160	0.94194
C428	C	0.31210	0.83903	0.88593
C429	C	0.30840	0.88299	0.84410
N430	N	0.34226	0.92848	0.86141
N431	N	0.34852	0.85678	0.92932
C432	C	0.36586	0.91132	0.91328
H443	H	0.29022	0.79667	0.88450
H444	H	0.28462	0.88093	0.80281
H447	H	0.39687	0.93762	0.93823
C437	C	0.11053	0.83949	0.68754
C438	C	0.15264	0.88330	0.69056
N439	N	0.13553	0.92856	0.65625
C440	C	0.08343	0.91136	0.63310
H442	H	0.05848	0.93747	0.60192
H446	H	0.11179	0.79736	0.70987
H450	H	0.19391	0.88134	0.71439
C209	C	0.97957	0.18095	0.50071
C453	C	0.99302	0.26977	0.73127
H465	H	0.93372	0.16771	0.50057
H466	H	0.98140	0.23579	0.76266
C458	C	0.84579	0.11261	0.69462
C459	C	0.88713	0.15708	0.69083
N460	N	0.93045	0.14007	0.65394
C461	C	0.91484	0.08543	0.63648
H462	H	0.93969	0.05967	0.60494
H463	H	0.80453	0.11415	0.71851
H464	H	0.88525	0.19935	0.71283
C371	C	0.97854	0.50083	0.18018
C467	C	0.99122	0.73204	0.27136
N471	N	0.99979	0.67336	0.26051
H476	H	0.97951	0.76343	0.23755

```
H480 H 0.93267 0.50065 0.16712
C472 C 0.87850 0.71562 0.08127
C473 C 0.92065 0.71455 0.12490
N474 N 0.93446 0.65814 0.13732
C475 C 0.90034 0.62599 0.10078
H477 H 0.94280 0.75254 0.14317
H478 H 0.86111 0.75440 0.05968
H479 H 0.90410 0.57871 0.09616
#END
```

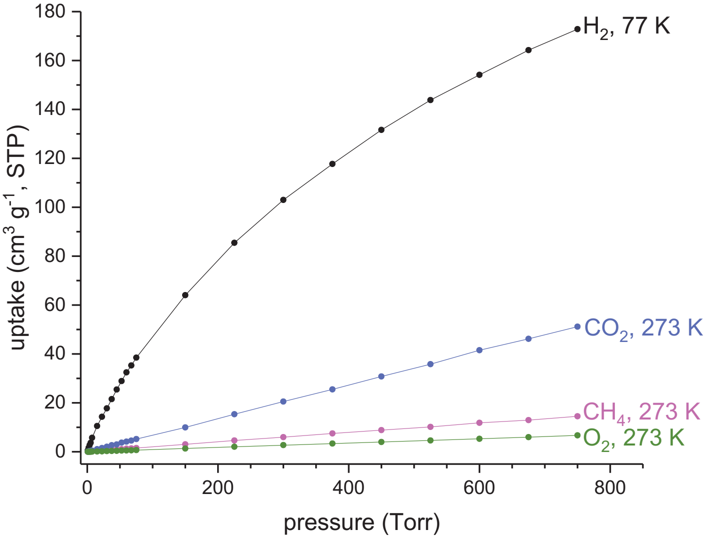

Supplementary Figure 35. Simulated H_2, CO_2, CH_4 and O_2 isotherms for ZIF-76.

Supplementary Table 3. Interaction potential parameters used for gas molecules.

Molecule	Atom	σ (Å)	ε/k_B (K)	q(e)
H_2	H_2	2.96	34.20	-
CH_4	CH_4	3.73	148.00	-
Ar	Ar	3.410	119.50	-
CO_2	C	2.80	27.02	0.700
	O	3.05	79.01	-0.350
N_2	N	3.306	38.298	-0.405
	COM	0.00	0.00	0.810
O_2	O	3.04	53.02	-0.112
	COM	0.00	0.00	0.224

Supplementary Table 4: Calculated textural characteristics of ZIF-76.

Pore volume (cm^3/g)	PLD (Å)	LCD (Å)
0.84	3.24	15.91

7. References

1 Dubbeldam, D., Torres-Knoop, A. & Walton, K. S. On the Inner Workings of Monte Carlo Codes. *Mol. Simul.* **39**, 1253–1292 (2013).

2 Frenkel, D. & Smit, B. *Understanding Molecular Simulation: From Algorithms to Applications*. 2nd edn, (Academic Press, 2002).

3 Buch, V. Path Integral Simulations of Mixed *Para*-D_2 And *Ortho*-D_2 Clusters: The Orientational Effects. *J. Chem. Phys.* **100**, 7610–7629 (1994).

4 Boato, G. & Casanova, G. A self-consistent set of molecular parameters for neon, argon, krypton and xenon. *Physica* **27**, 571-589 (1961).

5 Martin, M. G. & Siepmann, J. I. Transferable Potentials For Phase Equilibria. 1. United-Atom Description of N-Alkanes. *J. Phys. Chem. B* **102**, 2569–2577 (1998).

6 Potoff, J. J. & Siepmann, J. I. Vapor-Liquid Equilibria of Mixtures Containing Alkanes, Carbon Dioxide, and Nitrogen. *AIChE J.* **47**, 1676-1682 (2001).

7 Calero, S., Martín-Calvo, A., Hamad, S. & García-Pérez, E. On the performance of Cu-BTC metal organic framework for carbon tetrachloride gas removal. *Chem. Commun.* **47**, 508-510 (2011).

8 Dubbeldam, D., Calero, S., Ellis, D. E. & Snurr, R. Q. RASPA: molecular simulation software for adsorption and diffusion in flexible nanoporous materials. *Mol. Sim.* **42**, 81-101 (2016).

9 Mayo, S. L., Olafson, B. D. & Goddard, W. A. DREIDING: a generic force field for molecular simulations. *J. Phys. Chem.* **94**, 8897-8909 (1990).

10 Rankin, R. B., Liu, J., Kulkarni, A. D. & Johnson, J. K. Adsorption and Diffusion of Light Gases in ZIF-68 and ZIF-70: A Simulation Study. *J. Phys. Chem. C* **113**, 16906-16914 (2009).

11 Timón, V., Senent, M. L. & Hochlaf, M. Structural single and multiple molecular adsorption of CO2 and H2O in zeolitic imidazolate framework (ZIF) crystals. *Microporous Mesoporous Mater.* **218**, 33-41 (2015).

12 Willems, T. F., Rycroft, C. H., Kazi, M., Meza, J. C. & Haranczyk, M. Algorithms and Tools for High-Throughput Geometry-Based Analysis of Crystalline Porous Materials. *Microporous Mesoporous Mater.* **149**, 134–141 (2012).

13 Pérez-Pellitero, J. *et al.* Adsorption of CO2, CH4, and N2 on zeolitic imidazolate frameworks: experiments and simulations. *Chem. - Eur. J.* **16**, 1560-1571 (2010).

14 Materials Studio v8.0. (Biovia Software Inc., S.D., CA 92121,USA.).

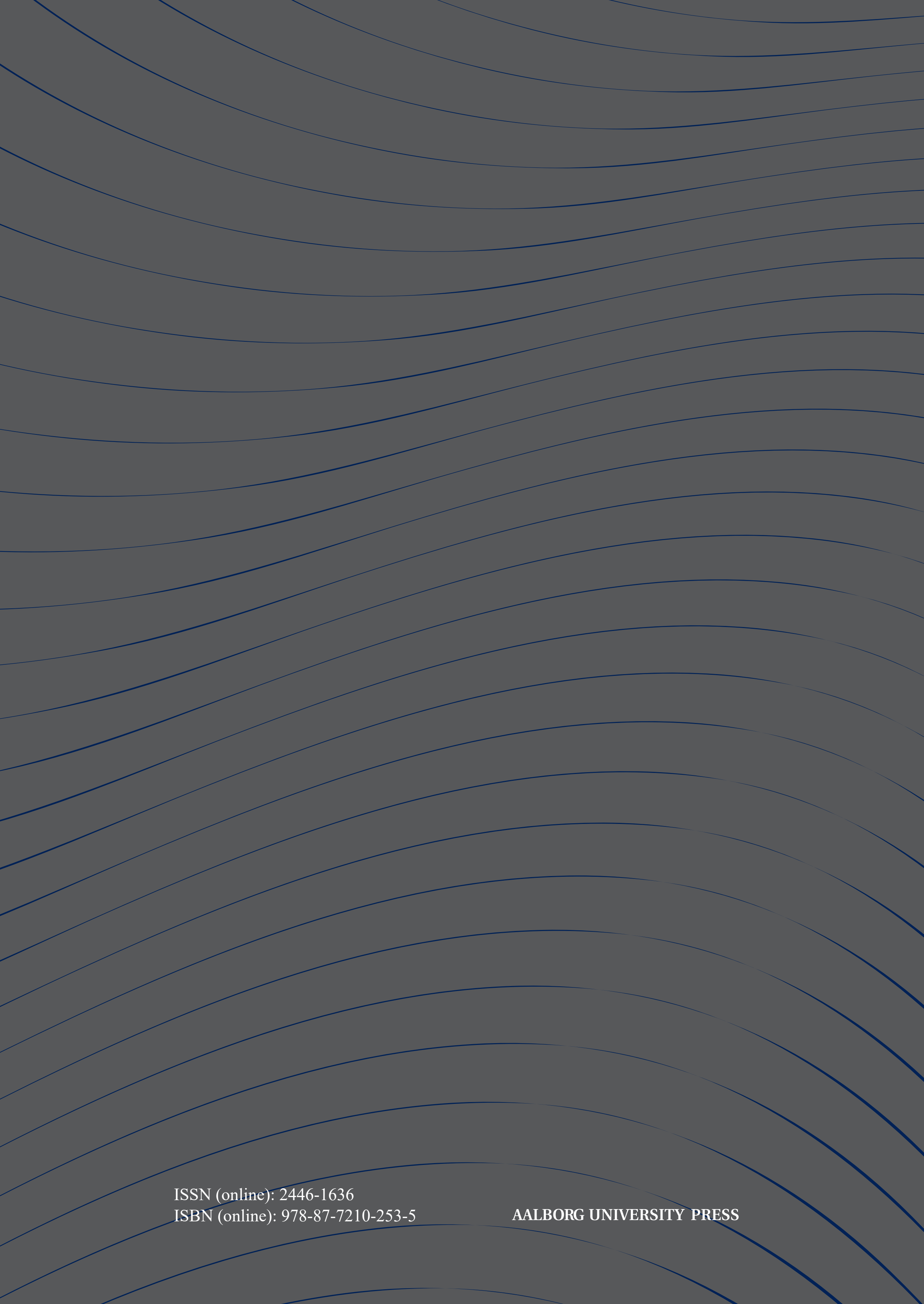

ISSN (online): 2446-1636
ISBN (online): 978-87-7210-253-5

AALBORG UNIVERSITY PRESS